Design and Synthesis of Inhibitor and Imaging Agent for Amyloid Fibrils

THESIS SUBMITTED FOR

THE DEGREE OF DOCTOR OF PHILOSOPHY (SCIENCE)

OF

JADAVPUR UNIVERSITY

October, 2024

By

TAPAS BERA, M.Sc.

DEPARTMENT of CHEMISTRY

INDEX NO: 59/21/Chem./27

DATE OF REGISTRATION: 31st MARCH, 2021

JADAVPUR UNIVERSITY, KOLKATA-700032

WEST BENGAL, INDIA

I would like to dedicate this thesis to my beloved parents and my PhD Supervisor.

Jadavpur University
Department of Chemistry
Organic Chemistry Section
Kolkata-700032, India

Dr. Samit Guha
Assistant Professor
Mobile: +91 9163750994
E-mail: samitfsu@gmail.com;
samit.guha@jadavpuruniversity.in

CERTIFICATE FROM THE SUPERVISOR(S)

This is to certify that the thesis entitled "***Design and Synthesis of Inhibitor and Imaging Agent for Amyloid Fibrils.***" submitted by Sri **Tapas Bera**, who has got his name registered on 31.03.2021 for the award of Ph.D (Science) degree of Jadavpur University, is absolutely based upon his own work under the supervision of **Dr. Samit Guha** and that neither this thesis nor any part of it has been submitted for either any degree / diploma or any other academic award anywhere before.

Samit Guha 21/10/2024

.....

(Signature of the Supervisor(s) date with official seal)

Dr. Samit Guha
Assistant Professor
Department of Chemistry
Jadavpur University
Kolkata-700032, India

Design and Synthesis of Inhibitor and Imaging Agent for Amyloid Fibrils

INDEX NO: 59/21/Chem./27

Abstract: Alzheimer's disease (AD) is a progressive neurodegenerative disorder, presently one of the top 10 reasons for mortality in the world. As of right now, there is no effective molecular toolkit for the early diagnosis of AD, which is not curable or even stops the disease from progressing once symptoms start. The aberrant assembly of amyloid-β (Aβ) peptides that promotes Aβ fibrils or plaque deposition is the primary pathological hallmark of AD. Moreover, considerable evidence suggests that Aβ progressively accumulates in mitochondria and is responsible for mitochondrial dysfunction and oxidative stress, which are accountable for the progression of AD. CT, PET, SPECT, and MRI imaging techniques are generally utilized to diagnose the advanced stage of AD. Nevertheless, the exposure to high energy ionizing radiation and radioactive substances, high cost, inaccessibility of real-time detection, lack of target selectivity, and sensitivity of these probes limit their practical application. The burgeoning technology is targeted fluorescence-based detection and imaging of Aβ, which has several advantages such as extraordinary sensitivity at the molecular level, spatiotemporal resolution, low cost, ability to monitor in real time, no exposure to harmful radiation and radioactive substances, and has become a smart tool for AD diagnosis. Mitochondria targeted AIE molecules with solvatofluorochromic effects to monitor mitochondrial morphology change and dysfunction during Aβ-induced neurotoxicity are still in their infancy. There is an unmet need to design superior mitochondria target selective, rapid responsive functional AIE-based fluorescence imaging diagnostic biomarkers for the early detection of Aβ aggregates in AD. Numerous approaches have been intended and adopted to inhibit Aβ aggregation. Various inhibitory molecules have been constructed to accomplish these tasks, including small molecules, peptides, peptidomimetics, nanoparticles, nanochaperone, and macrocycles. Though these molecules are effectual at both inhibiting and furnishing considerable mechanistic insights in Aβ fibrillation, these approaches have not been permitted yet for clinical application, primarily owing to nonspecific targets of the molecules. Hence, finding superior therapeutics for AD is indispensible. A more convincing AD therapeutic strategy should be inhibition of the formation of prefibrillar soluble oligomers and to maintain $A\beta_{1-42}$ in its nontoxic monomeric form. Specific targeting and inhibiting the formation of neurotoxic prefibrillar soluble oligomers by self-assembly of lipopeptide-based building blocks using the "bottom-up" approach is a promising domain of contemporary research.

Samit Guha 21/10/2024

Signature with Seal of the Supervisor

Dr. Samit Guha
Assistant Professor
Department of Chemistry
Jadavpur University
Kolkata-700032, India

Tapas Bera 21/10/2024

Full Signature of the Candidate

Acknowledgements

I would like to offer my profound gratitude and appreciation to my supervisor, Dr. Samit Guha, Department of Chemistry at Jadavpur University, for his helpful advice, enlightening talks, and helpful suggestions. The thesis could not have been finished without his direction and passion. In addition, Dr. Samit Guha has been a wonderful human being to me during this difficult path, in addition to being a fantastic supervisor. The experience of finishing a research project can be greatly improved by developing a good working relationship with a supervisor. The scientific discussions I had with my supervisor greatly pushed me. In addition to being a great boss, he also assisted me in developing my writing abilities.

I am grateful to our collaborators Dr. Arunima Sengupta (Department of Life Sciences and Biotechnology, Jadavpur University) and Dr. Pradip Kumar Tarafdar (Department of Chemical Sciences, IISER Kolkata) for their spontaneous help related to my research work.

I am grateful to Jadavpur University's administration and the department of chemistry for providing me with a lab, library, and a conducive environment to do my research. I would also like to express my gratitude to all of the faculties in the Organic Chemistry section, Jadavpur University, and the department's support personnel.

I am also appreciative that the Bose Institute and the Indian Institute of Chemical Biology (CSIR-1ICB, Kolkata) allowed me to use confocal microscopy equipment for my research.

I'm proud to acknowledge the kindness and support of my group's members, Dr. Pranab Chandra Saha, Dr. Rabi Sankar Das, Dr. Ayan Mukherjee, Mr. Samiran Kar, Mr. Aniruddha Mondal Dr. Somenath Banerjee and Sucharita Ghara. Additionally, the project students are to be thanked for their assistance with my research.

I am also grateful to the UGC Fellowship for providing me with financial support while I was conducting my research.

I would like to thank all the faculties of the chemistry department, Jadavpur University. Mr. Prantik Saha (confocal microscopy section, Bose Institute), Dr. Arnab Biswas, and all the fellow friends of the Department of Chemistry, Jadavpur University, for their overwhelming help and support throughout my research work.

I believe this is the ideal chance to send my sincere thanks to all of my teachers, especially Dr. Sukumar Guchhait for his support in my early college days.

I'd want to thank all of my friends for their spontaneous assistance with my research, especially Ratul Hore, Sudeshna Mondal, and Subhankar Shee.

Last but not least, I take great pleasure in expressing my gratitude to my parents (Mr. Sarbeswar Bera and Mrs. Nirmala Bera) and my wife (Mrs. Mousumi Das Bera) for their invaluable support, encouragement, and mental support. My decision-making in life is always aided by their blessings and well wishes.

October, 2024 **……..**

Department of Chemistry *(Tapas Bera)*

Jadavpur University,

188, Raja S.C. Mallick Road,

Jadavpur, Kolkata, West Bengal-700032

PREFACE

The research embodied in the present thesis entitled "***Design and Synthesis of Inhibitor and Imaging Agent for Amyloid Fibrils***" deals with the synthesis and characterization of lipopeptide-based nanovesicles to prevent amyloid fibril formation as well as aggregation-induced emission (AIE) probes for fluorescence imaging of Aβ aggregates and to monitor mitochondrial morphology change and dysfunction during Aβ-induced neurotoxicity.

The present investigation described in this thesis has been carried out by the author in the Department of Chemistry, Jadavpur University, Kolkata, during the period July 2019 to October 2024 under the supervision of Dr. Samit Guha, Department of Chemistry, Organic Chemistry Section, Jadavpur University, Kolkata-700032, India.

The five chapters that described the thesis are as follows:

Chapter-1 is a general introduction to Alzheimer's disease (AD), the amyloid cascade hypothesis (ACH), and other AD mechanisms. One of the most important of the misfolding diseases is Alzheimer's disease (AD), where the amyloid deposition is in the brain and causes severe dementia and eventually death. Aβ is a 39-42 residue peptide, most commonly 40 or 42 residues, that is cleaved from a transmembrane protein, the amyloid precursor protein (APP). The Aβ-peptide is an enzymatic cleavage product of the APP, a ubiquitous protein found in different tissues but exists in higher concentrations in the brain. Literature-reported inhibitors and imaging agents for Aβ fibrils have been incorporated in this chapter. Effects of peptidomimetics on aggregation of Aβ40/42 peptides have been incorporated. Diagnostic agents of AD, including aggregation-induced emission (AIE) probes, have been discussed. Interaction mechanisms of AIE probes with amyloid aggregates have been included.

Chapter-2 includes the substances used and the experimental methods needed to successfully finish the entire thesis work .

Chapter-3 deals with the design and synthesis of self-assembling lipopeptide-based nanovesicles that have been utilized to inhibit amyloid fibril formation and reduce the cytotoxicity of the GxxxGxxxGxxxG motif. Alzheimer's disease, a progressive severe neurodegenerative disorder that has been until now incurable, in spite of serious efforts worldwide. We have designed self-assembled myristoyl-KPGPK lipopeptide-based biocompatible nanovesicles, which can inhibit amyloid fibrillation made by the transmembrane GxxxGxxxGxxxG motif of Aβ-protein and

human myelin protein zero as well as reduce their neurotoxicity. Various spectroscopic and microscopic investigations illuminate that the lipopeptide-based nanovesicles dramatically inhibit random coil-to-β-sheet transformation of Aβ25−37 and human myelin protein zero protein precursor, which is the prerequisite of GxxxGxxxGxxxG motif-mediated fibril formation. The Förster resonance energy transfer (FRET) assay using synthesized Cy-3 (FRET donor) and Cy-5 (FRET acceptor)-conjugated Aβ25−37 also exhibits that nanovesicles strongly inhibit the fibril formation of Aβ25−37. The mouse neuro-2a neuroblastoma cell line is used, which revealed the GxxxGxxxGxxxG-mediated cytotoxicity. However, the neurotoxicity has been diminished by co-incubating the GxxxGxxxGxxxG motif with the nanovesicles.

Chapter-4 describes the design and construction of mitochondria targeted aggregation-induced emission (AIE) probe for selective detection of neurotoxic amyloid-β aggregates. A striking issue is the scarcity of imaging probes for the early diagnosis of Alzheimer's disease. For the development of Aβ biomarkers, mitochondria targeting de novo designed intramolecular charge transfer-induced solvatofluorochromic AIE probe Cou-AIE-TPP$^+$ is constructed by engineering the aromatic coumarin framework into the bridge of electron donor-acceptor-donor tethered with a lipophilic cationic triphenylphosphonium (TPP$^+$) group. The synthesized Cou-AIE-TPP$^+$ probe exhibits biocompatibility, noncytotoxicity, and a huge Stokes shift (124 nm in PBS). Cou-AIE-TPP$^+$ has respectable fluorescence augmentation inside the aggregated Aβ40 in comparison to monomeric Aβ40 with high binding affinity (K_d = 83 nM) to Aβ40 aggregates, is capable of detecting the kinetics of amyloid aggregation, and is superior to the gold standard probe thioflavin T. Fluorescence lifetime and brightness are also augmented when the probe Cou-AIE-TPP$^+$ binds with Aβ aggregates in PBS. Cou-AIE-TPP$^+$ (λ_{em} = 604 nm) selectively targets and images neuronal cell mitochondria, is useful to monitor mitochondrial morphology alteration and damage during Aβ40-induced neurotoxicity, recognizes neurotoxic Aβ fibrils, and is highly colocalized with thioflavin T in the human neuroblastoma SH-SY5Y cell line. These findings indicate that the mitochondria targeting de novo designed functional AIE-based solvatofluorochromic Cou-AIE-TPP$^+$ probe is a promising switch on biomarkers for fluorescence imaging of Aβ aggregates and to monitor mitochondrial morphology change and dysfunction during Aβ-induced neurotoxicity, which may offer imperative direction for the advancement of compelling AIE biomarkers for targeted early stage Aβ diagnosis in the future.

Chapter-5 presents the summary of all the investigations described in this thesis. The significance of the results obtained from those investigations has also been discussed in this chapter.

Chapter 3-4 begins with a brief introduction, then moves on to experimental methodology, results & discussion, and conclusions.

The list of Publications has been incorporated at the end of this thesis.

Abbreviations

Abbreviations used for amino acids, peptides, amino acid derivatives, substituents, reagents are largely in accordance with the recommendations of IUPAC–IUB commission on Biochemical Nomenclature, 1974, Pure and Applied Chemistry, 40, 315–331. Other symbols and nomenclature, etc. are based on the list in J. Biol. Chem. 1989, 669–671. Standard three letter coding is used for all the amino acids. Additional abbreviations used in this thesis are listed below–

A	Absorbance
ACN	Acetonitrile
ACQ	Aggregation-caused quenching
AD	Alzheimer's disease
AIE	Aggregation Induced Emission
AFM	Atomic Force Microscopy
Aβ	Amyloid-β
APP	Amyloid precursor protein
BBB	Blood-brain barrier
CLSM	Confocal laser scanning microscopy
CD	Circular dichroism
CR	Congo Red

2-CTC	2-chloro tritylchloride
Cy-3	Cyanine-3
Cy-5	Cyanine-5
DCM	Dichloromethane
DBU	1,8-diazabicyclo[5.4.0]undec-7-en
DD	Death domain
DIPEA	N,N-Diisopropylethylamine
DMSO	Dimethyl sulfoxide
DMEM	Dulbecco's Modified Eagle Medium
DMF	N, N – dimethylformamide
d	doublet
DLS	Dynamic Light Scattering
EOAD	Early-onset AD
ESIPT	Exited-State Intramolecular Proton Transfer
FBS	Fetal Bovine Serum
FDA	Food and Drug Administration
FL	Fluorescence
Fmoc	9-Fluorenylmethoxycarbonyl
FRET	Förster resonance electron transfer
FITC	Fluorescein isothiocyanate
FACS	Fluorescence-activated cell sorting
gCOSY	Gradient-Selected Correlation Spectroscopy
HATU	1-Bis(dimethylamino)methylene]-1H-1,2,3-triazolo[4,5-b]pyridinium 3-oxide hexafluorophosphate

HD	Huntington's disease
HRMS	High-resolution mass spectrometry
HRMS-ESI	High-resolution electrospray ionisation mass spectrometry
HOBT	1- hydroxybenzotriazole
IMM	Inner mitochondrial membrane
J	Coupling constant m Multiplate
MAP	Microtubule-associated protein
MCI	Moderate cognitive impairment
MeOH	Methanol
MMSE	Mini-Mental State Examination
MRI	Magnetic resonance imaging
MTDR	Mitotracker Deep Red FM
MTG	MitoTracker Green FM
MTT	3-(4,5-dimethyl-2-thiazolyl)-2,5-diphenyltetrazolium bromide
MW	Microwave
NMR	Nuclear Magnetic Resonance
NIR	Near-infrared
NIAD	Near-IR Alzheimer's dyes
PDT	Photodynamic therapy
PD	Parkinson's disease
PEG	Poly ethylene glycol
PET	Positron emission tomography
PMT	Photomultiplier Tube
PTT	Photothermal therapy

QDs	Quantum Dots
ROS	Reactive oxygen species
s	Singlet
SEM	Scanning Electron Microscopy
SPPS	Solid phase peptide synthesis
SPs	Senile plaques
SPECT	Single-photon emission computed tomography
SRB	Sulforhodamine B
t	triplet
TCSPC	Time-correlated single photon counting
TLC	Thin layer chromatography
TEM	Transmission Electron Microscopy
TMRE	Tetramethylrhodamine ethyl
TMRM	Tetramethylrhodamine methyl
ThT	Thioflavin T
TPP^+	Triphenylphosphonium cation
TRX	Thioredoxin
TXNIP	Thioredoxin-interacting protein

Contents

Chapter 1

General Introduction

Introduction

Facts of Alzheimer's Disease

Alzheimer's disease (AD) is the utmost reason of dementia in the world.[1,2] It is a progressive neurological illness.[3,4] Currently estimated at 55 million, the global population with dementia is predicted to quadruple every 20 years, with a fresh diagnosis every 7 seconds, and reach 0.14 billion by 2050.[5,6] The UK Alzheimer's Society reports that around 0.85 million people in the UK had dementia in 2019 (with AD accounting for 50–75% of cases). The majority of these individuals resided in England, Scotland, Wales, and Northern Ireland.[7] According to estimates, 1 in 14 adults over 65 in the UK presently have dementia, and at the current rate, there would be more than a million instances by 2025 and 1.5 million cases by 2040.[8] In the US, AD ranks as the sixth most common cause of death. Presently, over 6 million US people are suffering from AD. It is projected that above 12.5 million US individuals will suffer from AD by 2050.[9] Alzheimer's and other dementia patients will cost the US government $355 billion in 2021, and by 2050, that amount is expected to have increased to more than $1.1 trillion.

When AD is diagnosed at age 65, the average life expectancy is 8.3 years; when it is diagnosed at age 90, it is 3.4 years. Patients with AD must face physical and psychological challenges for a considerable amount of time, as must their loved ones and caregivers. This is because patients with AD have a comparatively lengthy surviving span (for instance, the five-year survival rate for lung cancer is < 21%).[10] It has been shown that AD caregivers may have health issues, social disengagement, worry, rage, and insomnia.[11,12] Consequently, AD is a crippling illness that impacts the person, their relatives,

and society at large, making it critical to understand the illness and create efficient therapies.

AD was first systematically studied and described as "A peculiar severe disease process of the cerebral cortex" by German neuroanatomist and psychiatrist Alois Alzheimer on 3rd November, 1906, at the 37th Meeting of South-West German Psychiatrists in Tubingen, Germany.[13,14] When the first signs of hallucinations, paranoia, and amnesia appeared, 51-year-old Auguste Deter was the first patient ever recorded; over the following four years, her condition deteriorated until her death in 1906. Upon studying Auguste Deter's brain, Dr. Alzheimer noticed peculiar fibrillar developments within the cells. This property was later linked to the presence of beta-sheet structures, which were discovered in the 1950's.[15] Emil Kraepelin, a fellow German psychiatrist and colleague of Alois Alzheimer, coined the phrase "Alzheimer's disease" and first identified it as a distinct sickness in the 3rd edition of his Psychiatrie in 1910.[16-18] Fascinatingly, until Terry and Kidd discovered neurofibrillary tangles in the post-mortem brain sections of two AD sufferer in the 1960s, not much attention was given to the disease.[19,20] These odd fibril formations are now called tau tangles, and beta-amyloid (Aβ)[21] peptides have been identified as the "special substance." The primary neuropathological indicators of AD are tau tangles and Aβ plaques, often known as "miliary foci." Even though AD is commonly acknowledged as an age-related condition, it does not only affect the elderly.[22] Early-onset AD (EOAD) is developed in approximately 17% of circumstances earlier than the age of 65.[23] There is data that suggests EOAD progresses more aggressively than late-onset AD, with more severe peripheral and cognitive impairments along with higher loss of neurons and synapses.[24-28] Roughly 13% of EOAD cases have an autosomal dominant mutation linked to AD.[29] Almost all brain functions, e.g., memory, verbal, decision, behavioral, activity,

cognitive, trouble recognizing friends and family members, and life expectancy, are in due course affected.[30] Neuronal deficiencies usually originate in the rhinal cortexes and hippocampus proper, which are arthiocortical medial temporal lobe structures, and then progress to the neo cortex in the basal forebrain.[31,32] Because of this, hippocampal impairment is typically the first deficit observed in AD patients, frequently occurring years before other symptoms of dementia.[33,34] A number of "non-cognitive" symptoms are also linked to AD; despite receiving less research attention than cognitive symptoms, these symptoms could be just as taxing on both patients and those who care for them. For example, most AD patients have motor dysfunctions, which frequently come on before cognitive symptoms. A notable non-cognitive alteration observed in AD patients is their reaction to discomfort. Since it is believed that people with AD have decreased pain sensitivity,[35] fewer pain medications are prescribed to them than to age-matched non-AD controls.[36] However, Cole et al. found higher connectivity and prolonged activation of the brain regions accountable for pain sensation and response, including the thalamus, periaqueductal gray matter, and dorsolateral pre-frontal cortex.[37] In more severe stages of AD, neuropsychiatric impairments e.g., melancholy, anxiety, anger, apathy, euphoria, and disinhibition are also frequently observed, along with psychotic symptoms like hallucinations.[38-41] AD is more common in women in comparison to men, with a 3:1 ratio, for reasons that are now not fully understood.[42-46] Furthermore, compared to males, female patients with AD and moderate cognitive impairment (MCI) exhibit higher rates of brain atrophy.[47-50]

Patients experience behavioral changes, cognitive decline, memory loss, and ultimately death as the condition worsens. There are currently no medicines obtainable to stop the progression of AD or cure this condition. Research on

how to enhance the quality of life for individual with AD and persons who care for them is ongoing on a global scale.

Amyloid Cascade Hypothesis

Multiple factors contribute to the pathophysiology of AD, including inflammation of the brain, protein aggregation, and the immune system.[51,52] The precise mechanism of AD is still up for discussion due to our poor understanding of this complex illness. Many theories have been proposed concerning the potential causes of AD, including the amyloid cascade theory,[53,54] the metal ion hypothesis[55] and the tau hypothesis,[56] each focusing on a disease's pathogenic characteristic (**Figure 1**). These theories form the basis for a large number of therapeutic trials aimed at treating AD.[57] Of them, the amyloid cascade theory has received the greatest research attention in relation to the mechanism underlying AD. David Allsop and John Hardy originally put forth the amyloid cascade theory in 1991.[58] This theory focuses on the amyloid plaques, which are a defining feature of AD. According to histopathological analyses, AD patients' brains exhibit the development of senile plaques (SPs), which are aggregates of the amyloid-β (Aβ) peptide.[59,60]

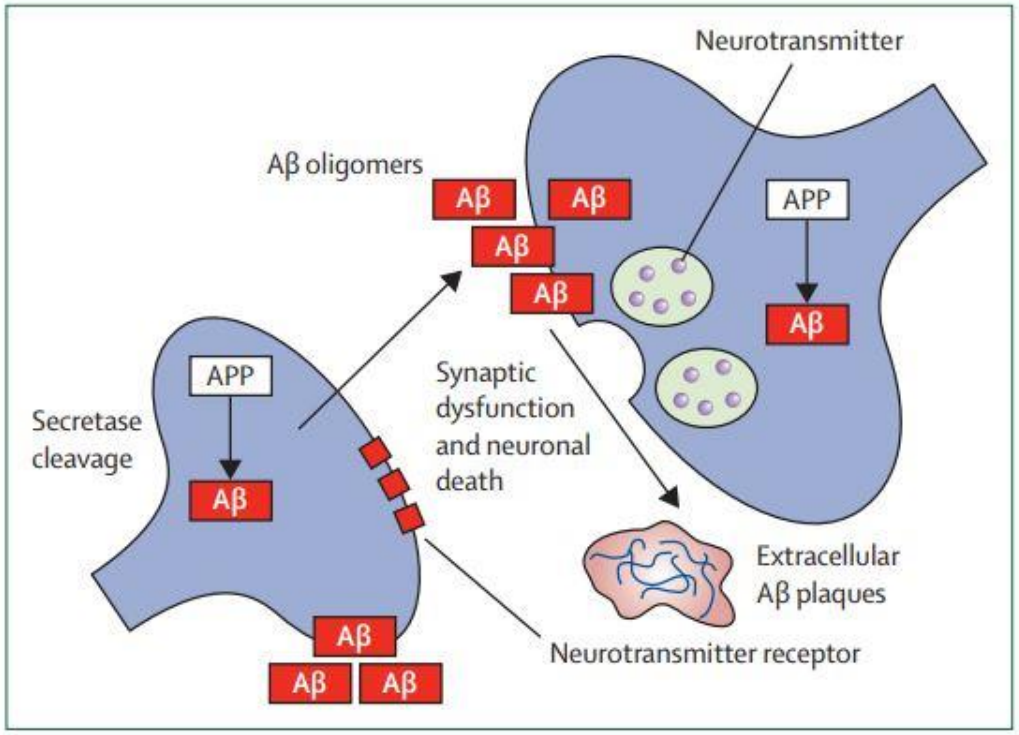

Figure 1. Amyloid cascade hypothesis. Image is taken from *Lancet* **2011**, *377*, 1019-31.[69]

The transmembrane amyloid precursor protein (APP) is the source of the A*β* peptide. β- and γ secretases cleave APP sequentially to produce A*β* monomers of 39–43 amino acid residues.[61-63] A*β*40 and A*β*42, the two main isoforms of the A*β* peptide, have relative lengths of 40 and 42 amino acids. Despite being the more common type, A*β*42 is expected to be more neurotoxic because it aggregates more easily and has two more hydrophobic amino acid residues on its C terminus.[64-67] Research has been done on the A*β*42 peptides' aggregation route from A*β* monomers to mature fibrils. The A*β* peptides encounter an innate transformation from a soluble monomer, soluble oligomer, or frequently partially folded state to self-assembled insoluble oligomers, protofibrils, and

fibrils that are accumulated inside the brain as Aβ plaques. The on-pathway aggregation process consists of a nucleation stage followed subsequently by an elongation stage (**Figure 2**).[68-70] Amyloid fibrils are insoluble and collect in the extracellular space of the brain.[71] They can further aggregate into amyloid plaques, which also have a highly organized β-sheet structure. The amyloid cascade theory states that the build-up of amyloid plaques sets off a sequence of actions, which include pathological alterations in the brain, damage to neuron cells, synapse failure, and the creation of neurofibrillary tangles.[72] Consequently, a great deal of research has been done on amyloid fibrils and plaques as the primary targets for therapeutic approaches, including clinical trials meant to remove Aβ from the brain. There is a growing consensus recently that since they disrupt synaptic function and cell membrane integrity, soluble Aβ oligomers are more hazardous than mature fibrils and senile plaques.[73] The Aβ hypothesis has been the focus of therapeutic trials for AD for the past 25 years; however, recent failures of promising treatment options have cast doubt on this idea.[74] Certain researchers contend that the reason behind the failure of certain anti-amyloid treatments is because the brains were too severely damaged during the clinical trial phase. As a result, early AD identification is becoming increasingly important, and treating the existence of Aβ deposits as a pathology characteristic for imaging rather than a primary focus for therapeutic efforts may be preferable.

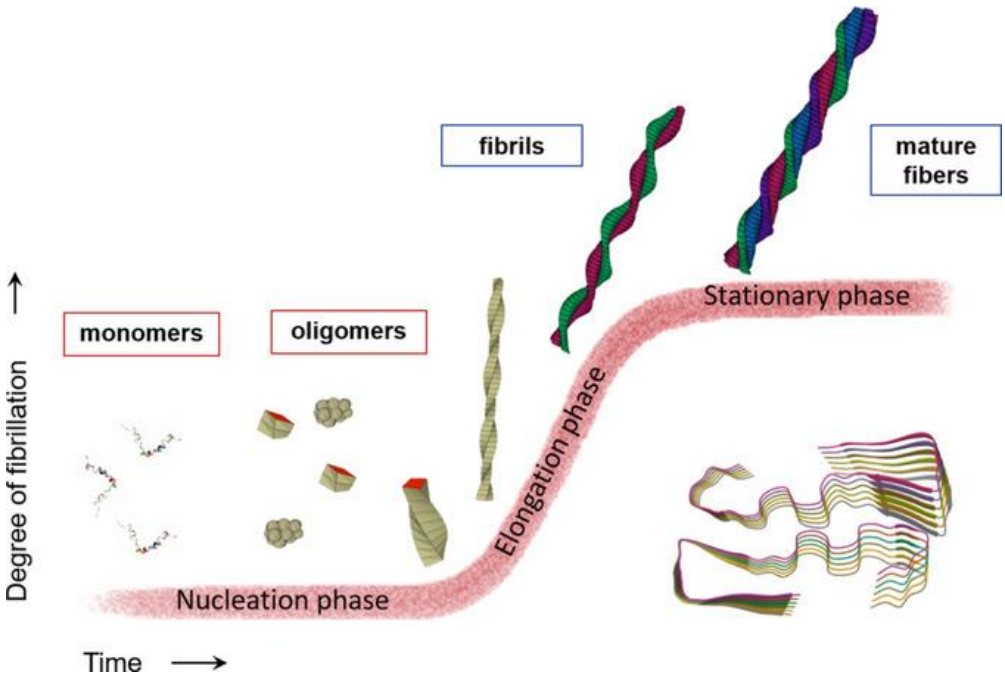

Figure 2. Amyloid aggregation kinetics and biological assembly of Aβ40, (taken from Kollmer et al. *Nat. Commun.* **2019**, *10*, 4760.).[75]

Beta-Amyloid: Rudolph Virchow, a German pathologist, coined the term "amyloid" in 1854 to refer to macroscopic tissue abnormalities. Because Virchow could stain the accumulations with iodine, it is thought that he confused them for starch and coined the term amyloid, which comes from the Latin word for starch, amylum.[76] The current definition of amyloids, which is still under investigation, implicates abnormally folded proteins that form well-ordered and thermodynamically stable β-sheet rich assemblies. These structures are constructed by fibrils that are approximately 7 to 13 nm wide and typically contain 2-6 protofilaments, each of which is 2-5 nm in diameter. These

protofilaments are twisted alongside to construct insoluble aggregates,[79] which could be highlighted with biomarkers like Congo Red[77] and thioflavins (ThT and ThS).[78] The word "amyloid" refers to proteins that have an abundant β-sheet structure that repeats and develops when a properly folded or inherently disordered protein transforms into an amyloid state.[80,81] A protein may also produce distinct amyloids with varying structures based on factors including concentration, temperature, and solvent type.[82,83] Most amyloids are harmful because they either cause functional protein levels to drop or cause amyloid fibrils to acquire pathogenic activities. Amyloids have been connected to a number of illnesses, including lysozyme amyloidosis,[84] aortic medial amyloidosis,[85] Parkinson's[86] and Huntington's diseases.[87] But occasionally, amyloids have developed physiological functions; one example of this is seen in the proteinaceous fibrils of Escherichia coli.[88] The earliest indication that AD is an amyloid illness was in 1984, when Glenner and Wong measured a "novel cerebrovascular amyloid protein" in the beta sheet fibrils that Dr. Alzheimer referred to as "miliary foci" and proposed its role in the pathophysiology of AD. Tanzi, George-Hyslop, and others connected Aβ to the 21st chromosome and a more substantial precursor protein, which is currently referred to as APP.[89-91] After that, in the early 1990s, a number of scholars, including Selkoe, Allsop, and Hardy, developed the cascade hypothesis.[92,93] This theory states that the primary cause of AD is a rising imbalance between the synthesis of Aβ (particularly Aβ42) and its clearance. According to the theory, the build-up of Aβ causes gliosis, oxidative stress, inflammation, tau hyper-phosphorylation, synaptic dysfunction, and ultimately neuronal atrophy.[94,95] The cascade hypothesis is well supported by the findings that Aβ plaques are present in the post-mortem brains of dementia patients and that Aβ42 mutations that elevate Aβ42 levels cause FAD. Moreover, Aβ42 has been demonstrated to be

neurotoxic, with the ability to cause neuronal death 2 h afterward exposure by its binding to the p75 neurotrophin receptor on the cell surface and subsequent activation of its intracellular death domain (DD).[96] Apoptosis is triggered by the DD activating caspase-8, which in turn activates caspase-3.[97,98] Furthermore, research has demonstrated that Aβ42 can bind to and be endocytosed by alpha-7 (α7) nicotinic cholinergic receptors.[99] Intracellular Aβ42 binds to the promoter of p53 and, through a Bax-dependent mechanism, induces apoptosis, increasing p53 expression.[100,101]

In fact, even though the post-mortem brain analyses of DS patients who passed away in their 3rd decade did not exhibit behavioral signs of AD,[102] they do indicate substantial plaque burdens. Additionally, this implies that by the time AD symptoms manifest, neurological destruction has already happened and can't be undone. Hence, by the time a patient sees the doctor, it is already very late to inverse the symptoms via lowering Aβ stages. Lastly, despite the fact that plaques were once thought to be the harmful assemblies of Aβ, it is now widely acknowledged that they are actually the result of Aβ overproduction and that the smaller soluble oligomeric aggregates of Aβ are what cause neurodegeneration.[103,104]

Amyloid Precursor Protein:

Surprisingly little is identified about the normal function of this protein, despite the significant research on the involvement of APP in Aβ formation and, by extension, AD pathology. APP is a single-pass transmembrane protein that ranges in size from 110 to 135 kDa. It is a member of the APLP1 and APLP2 families of amyloid precursor-like proteins, and it has two distinct domains: a longer intracellular domain that contains the C-terminal and a large extracellular domain that contains the N-terminal (**Figure 3**).[105] Eight distinct isoforms of the APP gene can be produced by alternative splicing of its 18

exons. The 695-amino acid (AA) isoform is mostly located in the central nervous system, while the 770 and 751-AA isoforms are present in peripheral tissues and might be utilized as indicators for AD.[106] Though the detailed physiological function or functions of APP remain unclear, there are suggestions that it influences cell development and proliferation positively and may have a role in certain types of cancer.[107,108] Furthermore, it has been established that APP plays a part in the survival and repair of neurons following traumatic brain injury.[109]

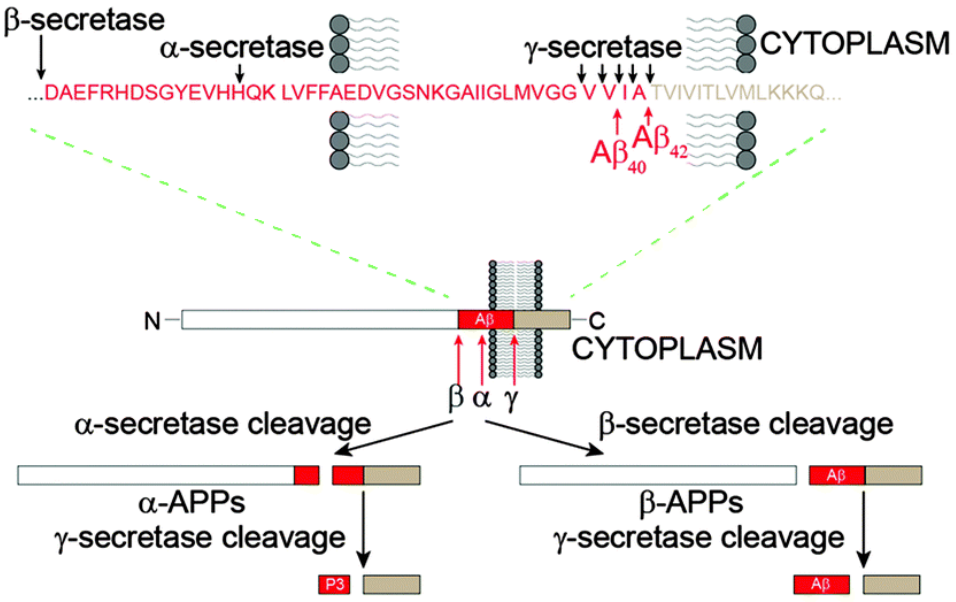

Figure 3. A*β* peptide is produced from APP via the amyloidogenic pathway. (*Chem. Soc. Rev*. **2014**, *43*, 6701-6715.)[110]

Production, Clearance, and Possible Function of Aβ:

The endoplasmic reticulum produces APP in large amounts, which is then quickly processed at the axon terminals by fast axonal transit.[111] As a result, the amount of APP is quite low at any given moment on the surface of the cell.[112] APP can be cleaved and metabolized[113] in a variety of ways, and it is yet unclear what mechanism will take precedence. Alpha (α) and gamma (γ) secretases are involved in the non-amyloid pathway, which occurs in the membrane.[114] APP is first cleaved inside the amyloid sequence by α-secretase, releasing the ectodomain, and then the trans-membrane domain is cleaved by γ-secretase. Moreover, APP can be endocytosed and transported to the Golgi apparatus and endo-lysosomes.[115] There, it is broken down by γ- and beta-secretases at the transmembrane domain and N-terminus, respectively, to produce Aβ peptides with lengths ranging from 38 to 43 amino acid residues and a weight of around 4 kDa.[116] The α- and β-secretases are involved in a third cleavage process that has been reported more recently, resulting in shorter Aβ fragments (15–16 AA long).[117] While the hourly rate of Aβ formation accounts for around 7.6% of total Aβ CSF levels, the clearance rate in brains without AD is approximately 8.3%;[118] variations in these rates, or the quantity of certain Aβ types present, can signify AD disease.[119] There exist various enzymatic and non-enzymatic processes that facilitate the clearance of Aβ from the brain.[120] The nonenzymatic mechanisms include microglia-mediated phagocytosis and drainage via the astrocyte-based lymphatic system, which functions similarly to the peripheral lymphatic system in promoting CSF flow via the cerebral parenchyma and interstitial waste clearance.[121,122] A group of proteases known as Aβ degrading enzymes can break down Aβ proteins to smaller, less harmful pieces that might be eliminated more quickly.[123]

Like APP, the physiological function of Aβ is also unknown. Despite the fact that AD is not subject to natural selection because it arises after the typical age of reproduction, evolutionary biology implies that Aβ might still serve a useful function and boost fitness. Current research indicates that the immune-privileged brain may be using Aβ as an anti-microbial agent.

Characteristics of Amyloid:

The fibrillar shape, cross-β sheet structure, and dye-specific affinity of amyloid are its distinguishing features.[124,125] When examined by transmission electron microscopy (TEM)[126] or atomic force microscopy (AFM),[127] amyloid fibrils discovered in tissue deposits look like unbranched twisted fibers of approximately 7–10 nm in diameter and a few μm in length. X-ray fiber diffraction was utilized in 1968 to investigate the cross-β sheet structure (**Figure 4**).[128] The X-ray fiber diffraction pattern of amyloid fibrils display two reflections: one at 4.7 Å, that represents the separation of two adjacent β stands in the β-sheet packing, and another at roughly 10 Å, that represents β stands inside the β-sheet.

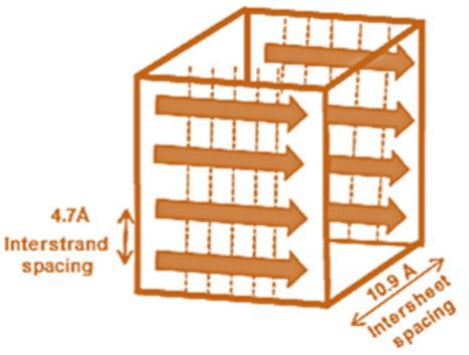

Figure 4. X-ray fiber diffraction pattern of amyloid fibrils.

The latest literature report of high-resolution data from solid-state NMR, small-angle X-ray scattering, and X-ray crystallography complemented the X-ray fiber diffraction pattern nicely. This pattern shows that the intramolecular hydrogen bonds between β-sheet strands arrange the β-sheet secondary structure perpendicular to the fibril axis.[129] When bound to Congo red, amyloid fibril displays apple green birefringence in polarized microscope.[130] When bound to thioflavin T (ThT), amyloid exhibits a strong emission with 440 nm excitation.[131]

Table 1: Amyloid-forming peptides/proteins and their associated diseases and location of affected tissues.[132-136]

Disease	**Aggregating Peptide/Proteins**	**Affected Tissues**
Alzheimer's disease (AD)	Aβ peptides	Brain (hippocampus, cerebral cortex)
Parkinson's disease (PD)	α-Synuclein	Brain (substantia nigra, brain stem)
Prion disease	Pr protein	Brain (gray matter), peripheral nervous system
Huntington's disease (HD)	poly-glutamine	Brain (striatum)
Multiple tauopathies	Tau	Brain (cerebellum)
Type II diabetes	IAPP or "amylin"	Pancreas
Lysozyme amyloidosis	Lysozyme	Kidney, liver, spleen

"Other" AD Mechanisms:

Tau: Lee and Trojanowski discovered deficiencies of neuronal cytoskeleton in AD in connection to the aberrant phosphorylation of tau, on a timetable akin to the ACH's growth.[137] Tau is a microtubule-associated protein (MAP), which was recognized by Weggentron and colleagues.[138] Unlike Aβ, its physiological function is well understood. When microtubules proliferate, they are quite dynamic; however, MAPs like tau, MAP1A, MAP1B, and MAP2 eventually stabilize them. The human microtubule associated protein tau (MAPT) gene spans about 100 kilobases and has a minimum of 16 exons.[139-141] It is found on chromosome 17. Research has demonstrated that tau is important in neurite development, axonal transport,[142] and nucleic acid[143] protection in addition to microtubule stabilization.[144] It's interesting to note that tau knockout mice, like APP knockouts, are alive and only exhibit mild abnormalities in terms of hyperactivity, muscle weakness, and microtubule organization, as well as difficulties in the contextual fear conditioning task.[145] Tau isoforms range in molecular weight from 55 kDa to 62 kDa and are produced via alternate splicing of exons 2, 3, and 10. The microtubule binding site is located in the C terminal, which is impacted by the alternative splicing of exon 10.[146] The three or four repeat (3R and 4R) isoforms are created as a result of either adding or removing an extra binding repeat.[147] The mature human brain has a similar amount of these isoforms, and the alterations in the ratio often identify tauopathies.[148] The 2N4R isoform of tau is a phosphoprotein because it has at least 85 putative phosphorylation sites (80 Ser or Thr and 5 Tyr).[149] Tau separates from microtubules, turns hydrophobic, and begins to aggregate when it is hyperphosphorylated.[150] Tauopathies, a group of neurodegenerative illnesses that include progressive supranuclear palsy, argyrophilic grain disease,

cortico basal degeneration, Huntington's disease, Pick's disease, FTD, and AD, are caused by this aberrant form of tau.[151]

While the precise connection between tau-mediated toxicity and Aβ aggregation remains unclear, multiple in vivo and cell culture investigations have demonstrated the involvement of tau, which may be crucial for Aβ-induced neuronal death.[152-154] Additionally, it appears that tau aggregation contributes to synaptic dysfunction in AD; utilizing neuronal cells, Frandemiche et al. demonstrated that tau is confined to the healthy neurons' axonal dendritic shafts while they are at rest.[155] However, synaptic tau was moved to the synaptic terminals by activity and LTP,[156] where it interacted with actin.

There are some reports that show smaller, soluble aggregates of hyperphosphorylated tau rather than tangles are the harmful type of tau that causes neurodegeneration.[157,158] This notion is comparable to the present notion that Aβ aggregates are the harmful in the form of Aβ rather than the plaques.

Mitochondrial Dysfunction and Oxidative Stress:

As byproducts of aerobic respiration, reactive oxygen species (ROS) are extremely reactive with other molecules because they are rich in free radicals. Numerous ROS, e.g., superoxide ion (O_2^-), hydroxyl radical (OH), and nitric oxide (NO), have a role in physiological cell signaling.[159,160] Nonetheless, it's crucial to maintain a balance between the generation and elimination of ROS because their buildup results in oxidative stress because they attach to and oxidize lipids, proteins, and nucleic acids.[161] There have been reports of both elevated ROS generation and reduced clearance in a number of areas of the AD brain, comprising the amygdala, entorhinal cortex, and hippocampal regions.[162]

Mitochondria always lose electrons during cellular respiration, and they are the main generators of reactive oxygen species (ROS). Indeed, reports of AD have indicated deficiencies in mitochondrial activity.[163] Another important source of intracellular calcium is mitochondria also a part of apoptotic pathways.[164] Therefore, Aβ overload-induced mitochondrial damage is harmful to neurons not only because it reduces energy production but also because it increases oxidative stress, disrupts signaling pathways, and may result in the loss of apoptotic neurons.

Thioredoxin-interacting protein (TXNIP) that binds to and prevents TRX from interacting with ROS, and TRX, which lowers ROS, must be in balance for the thioredoxin (TRX) reduction pathway to work.[165,166] As seen before, Aβ can enhance the expression of TXNIP in the brain by DNA binding and epigenetic processes.[167] Furthermore, it has also been documented that AD patients' brains exhibit TXNIP-associated NLRP3 inflammasome activation.[168] Owing to these connections, TXNIP level increases were the main indicators of oxidative stress used in this research.

Design of Mitochondria Targeting Organic Molecules

Two essential biophysical factors to consider when designing effective mitochondriotropics (mitochondria targeting medicines) are lipophilicity and molecular charge. Furthermore, for efficient mitochondrial localization, organic molecules must penetrate both the plasma and mitochondrial membranes. IMM typically has a lower membrane potential ($\Delta\Psi m$ −150 to −180 mV) than plasma membrane ($\Delta\Psi p$ −30 to −60 mV), allowing for greater accumulation of lipophilic cations within the mitochondrial matrix. Another strategy is to target mitochondrial membrane components, such as negatively charged phospholipid cardiolipin (which is largely found in the IMM) and proteins that reside there. The diverse biological environment makes it difficult to target mitochondria.

Design of Lipophilic Cationic Organic Molecules

Because of their ease of synthesis and high specificity, covalently modified lipophilic cationic compounds have become popular as mitochondria-targeting vehicles in recent decades. The higher the lipophilicity and positive charge density, the easier it is to pass the hydrophobic phospholipid bilayers and accumulate within the mitochondrial matrix. The delocalized lipophilic cationic mitochondriotropics can dissipate the positive charge over a large surface area by either shielding or delocalizing it as it passes through the IMM space, resulting in a decrease in activation energy for transportation through the phospholipid bilayer. The Nernst equation indicates that for every ~61.5 mV increase in ΔΨm, the concentration of lipophilic molecules rises ten times.

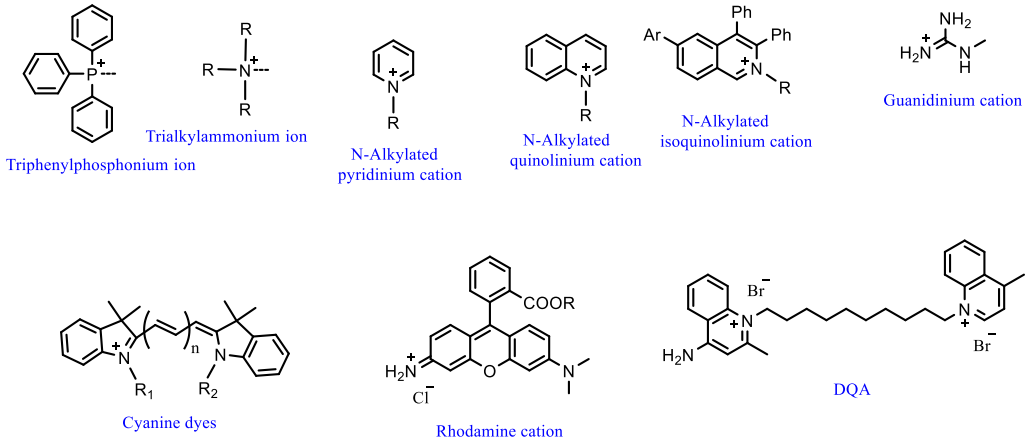

Figure 5. Mitochondria targeting structural scaffolds.

Thus, in response to the ΔΨp of −30 to −60 mV, these compounds first concentrate in the cytosol 5-10 times more than that in the extracellular matrix, and then accumulate within the mitochondrial matrix 100-1000 times greater than cytosolic accumulation in response to the hypernegative IMM potential.

Triphenylphosphonium (TPP^+), ammonium, pyridinium, isoquinolinium, and other mitochondriotropics have been created (**Figure 5**).[169-175] Among these delocalized cationic guanidinium containing arginine, oligomers composed of chiral bicyclic guanidinium moieties, nonpeptidic oligoguanidinium, sorbitol coupled with guanidinium residues, and octa-arginine oligomers for mitochondria targeting have been produced.[176,177] Delocalized cationic rhodamine, cyanine, dequalinium, and berberinium have all been employed.[178,179]

Triphenylphosphonium Ion Conjugated Bioactive Mitochondria Targeting Molecules

Murphy and coworkers were the first to apply triphenylphosphonium (TPP^+)-tethered bioactive compounds for efficient mitochondrial delivery.[180-182] Among the various mitochondria targeting functionalities, TPP^+ bioconjugated mitochondria targeting molecules are the most effective and widely used due to their delocalized cationic character, high lipophilicity, stability in physiological conditions, relatively simple synthetic and purification method, and minimal reactivity toward cellular components.[183,184] The TPP^+ moiety has been bioconjugated with several small organic molecules, including antioxidants like curcumin (Mito-Curcumin), ebselen (Mito-Ebselen), vitamin E (MitoVitE), and ubiquinone (MitoQ). Because of their negative IMM potential, these compounds preferentially accumulate within mitochondria and detoxify them by shielding them from oxidative damage and preventing lipid peroxidation.[185-187] There have also been reports of other physiologically significant TPP^+-conjugated mitochondria that target superoxide spin trapping agents like Mito-DIPPMPO and small molecule superoxide scavengers like Mito-TEMPOL and MitoHE.[188-190]

Commercially Available Mitochondria Targeting Probes

When it comes to live cell imaging, the majority of commercially available Mitotracker probes have a lipophilic cationic cyanine and rhodamine scaffold connected to mitochondrial SH reactive benzyl chloride functionality (**Figure 6**).[191,192] Potential drives the specific accumulation of these lipophilic cationic dyes inside the mitochondria. To track changes in mitochondrial membrane potential, a cyanine-based JC-1 (5,5′,6,6′-tetrachloro-1,1′,3,3′-tetraethylbenzimidazolocarbocyanine iodide) dye is used. Under potential-driven force, it builds up in mitochondria and forms J-aggregates, which cause the emission to shift from green (λ_{em} 529 nm) to red (λ_{em} 590 nm). Green fluorescence is produced when these probes leak into the cytosol during mitochondrial depolarization.

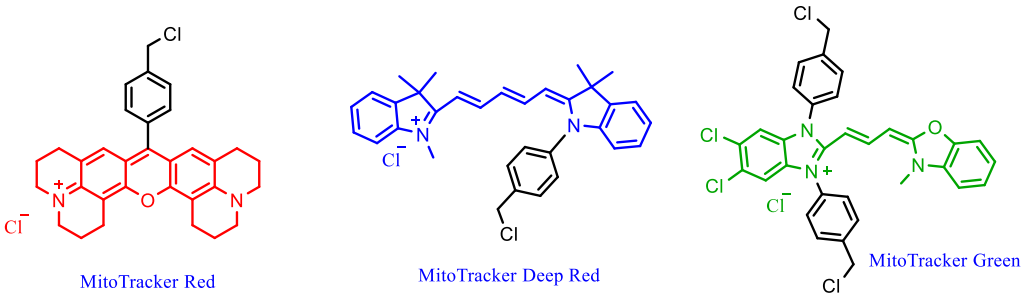

Figure 6. Mitochondrial thiol reactive benzyl chloride group containing commercially available MitoTrackers.

The red/green fluorescence intensity ratio provides a ratiometic measure of depolarization of the mitochondrial membrane potential that is independent of mitochondrial density, size, or shape. As with JC-1, various cyanine dyes were also frequently used to track the depolarization of the mitochondrial membrane potential, including JC-9, DiOC6, Rhodamine-123, tetramethylrhodamine

methyl (TMRM) ester, and tetramethylrhodamine ethyl (TMRE) ester.[193,194] The most reliable and widely used dye among these for measuring mitochondrial depolarization in flow cytometry is JC-1. The main ROS in mitochondria, mitochondrial superoxide ($O_2^{-\bullet}$), is produced as a consequence of oxidative phosphorylation, where O_2 and leaky electrons can combine to generate $O_2^{-\bullet}$. A TPP^+ conjugated fluorogenic probe called MitoSOX Red (ex/em 510/580 nm) is used to measure mitochondrial $O_2^{-\bullet}$ in living cells. Owing to the TPP^+ moiety, it easily gathers in mitochondria, where it is oxidized by $O_2^{-\bullet}$ to produce red fluorescence. Additionally, the MitoSOX Red is inert toward other ROS and RNS but very selective for $O_2^{-\bullet}$.

Diagnosis of Alzheimer's Disease

Documenting memory impairment and conducting mental health assessments are critical components of the clinical diagnosis of AD. The most popular mental cognitive status test for evaluating cognitive decline in the elderly is the Mini-Mental State Examination (MMSE). Neuropathologic analysis of the post-mortem material is used to make the final diagnosis of AD dementia.[195] However, years before cognitive problems manifest, AD-related brain alterations may start. Preclinical AD is the term for this period, in which individuals usually have no symptoms although the brain is going through pathological changes, including Aβ peptide deposition.[196] As a result, the need for diagnostic technologies to detect the disease early on and accurately monitor its progression is growing.

Amyloid Imaging Agents

Since amyloid plaques have been acknowledged as the primary biomarker of AD for the past century and have been the subject of much research, scientists have been designing diagnostic tools based on compounds that have a high

affinity for Aβ plaques. Over the past thirty years, numerous fluorescence probes and radiotracers that are used to diagnose AD have been created.

Fluorescent Imaging Agents

The hydrophobic aromatic molecules, Congo Red (CR) and ThT (**Figure 7**), which are histological dyes, attach only to the cross-β sheet confirmation seen in mature amyloid fibrils.[197-199] Despite their incapability to penetrate the blood-brain barrier (BBB), they remain the gold standard for amyloid detection in vitro, and a number of ligands that are unique to amyloid have been developed as a result of their molecular architectures. As an example, Methoxy-X04 (**Figure 7**), a fluorescent probe based on the Congo Red scaffold, has demonstrated BBB permeability and a high affinity for binding fibrillar β-sheet deposits (K_i = 26.8 nM).[200] A number of ThT analogs have been created by Klunk and collaborators.

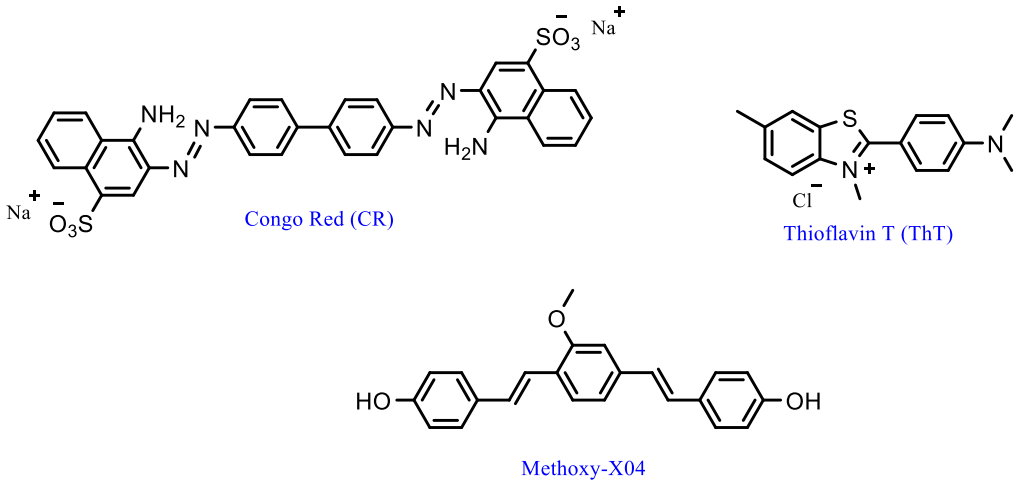

Figure 7. Chemical structures of amyloid imaging agents.

Intramolecular Charge Transfer Based Probe for AD:

Nesterov and associates have constructed a series of near-IR Alzheimer's dyes (NIAD) and described [[5′-(4-hydroxyphenyl)-[2,2′-bithiophen]-5-yl]methylene]-propanedinitrile (NIAD-4) as a probe for amyloid plaques (**Figure 8**).[201] Upon interaction with amyloid fibrils, the UV/Vis absorption of NIAD-4 experiences a bathochromic shift of ~70 nm with a new λ_{max} ~500 nm. The fluorescence maximum remained unchanged, however, established a 400-times escalation in fluorescence intensity.

A dual-functional group containing BODIPY probe was constructed by Ono et al., termed [^{125}I]BODIPY7,[202,203] for ex vivo imaging of Aβ plaques (**Figure 8**). They have incorporated a radioactive isotope (^{125}I) into a BODIPY comprising dye, which can detect Aβ aggregates simultaneously using fluorescence and single-photon emission computed tomography (SPECT) imaging. They have constructed other BODIPY-based probe by incorporating dimethylamino styryl group into the BODIPY core.

Chai and co-workers have developed a BODIPY-containing dye (BD-Oligo), which responds more selectively to Aβ oligomers (**Figure 8**).[204] This dye showed noteworthy light-switching activity at 585 nm (λ_{ex} 530 nm) in the existence of Aβ oligomers, though negligible response was detected in the occurrence of monomeric and fibrillar Aβ. They have utilized this dye in monitoring the creation of Aβ aggregates in real-time and established the consequences by dot blotting with Aβ aggregates and total Aβ antibodies (A11 and 6E10), pelleting assays, and TEM.

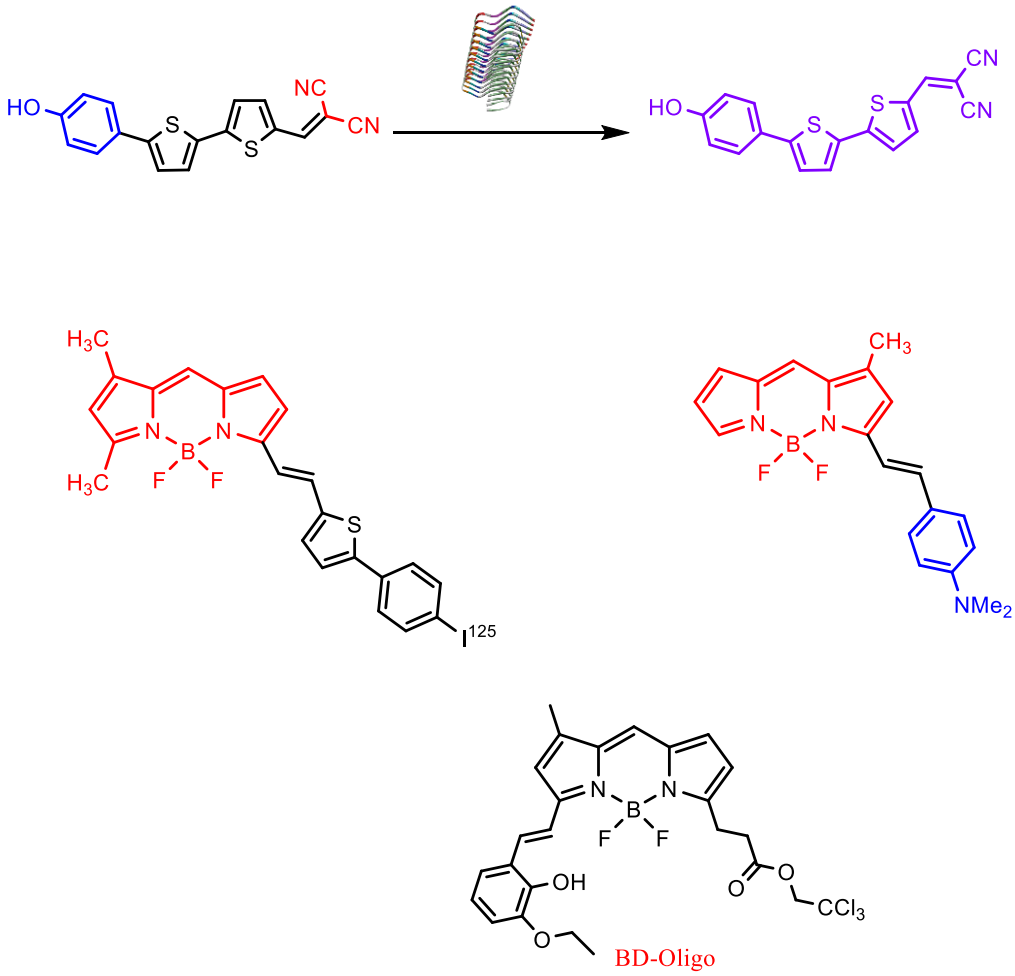

Figure 8. ICT-based dyes used for sensing amyloids.

Förster Resonance Energy Transfer (FRET) for Detection of AD:

Hatai and colleagues created a dye to identify various kinds of Aβ aggregates. ThT, sulforhodamine B (SRB), and sulfo-Cy5 (sCy5) dyes with suitable photophysical characteristics for the formation of FRET pairs were present in the marker (**Figure 9**).[205] Additionally, two peptides that served as recognition units were incorporated to the marker. As the probe interacted with various aggregation forms, it displayed a variety of fluorescence responses. This phenomenon is generated by varying conformations of the dye in contact with distinct amyloid aggregates (i.e., monomers, oligomers, etc.) and is attributed to the differences in FRET efficiency among the three colors. When Aβ monomers are present, the fluorescence is nearly the same. On the other hand, the peak at 680 nm becomes less intense in the presence of low and high molecular weight oligomers, whereas protofibrils and fibrils cause the same peak to become more intense. Using this probe, the researchers were able to determine when important intermediates during aggregation formed.

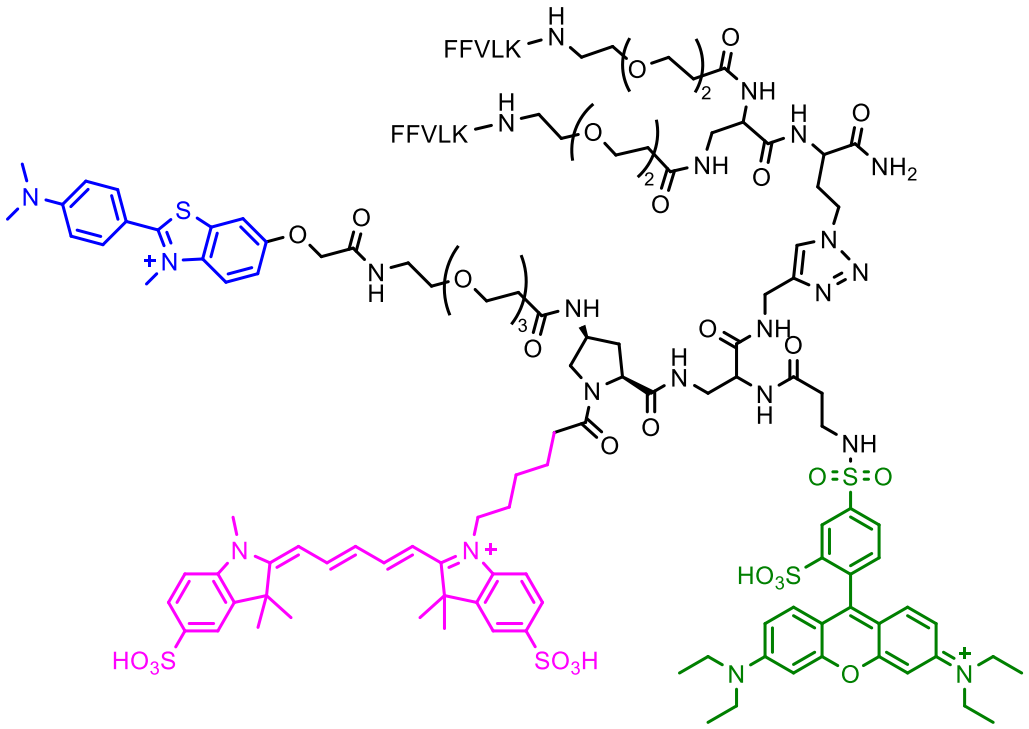

Figure 9. FRET probe for the detection of oligomers.

PET Imaging Agents

Molecular imaging methods have made it possible to assess amyloid plaques in vivo without invasive procedures utilizing PET, SPECT, and MRI.[206] PET is the most sensitive of these imaging techniques, enabling the use of minuscule amounts of imaging agents (from nano to picomolar level) to provide acceptable signal-to-noise ratios and image quality.[207-209]

Radionuclides that undergo positron decay, such as ^{18}F ($t_{1/2}$=109.7 min), ^{15}O ($t_{1/2}$=2.04 min), and ^{11}C ($t_{1/2}$=20.4 min), are found in PET radiotracers. The released positron (β^+) strikes adjacent electrons and generates two γ-rays (511

KeV) that are utilized for diagnostics after being picked up by a specific device.[210] These radioisotopes are used to develop a variety of PET diagnostic agents for AD, such as ^{11}C radiolabeled Pittsburgh Compound-B (^{11}C-PiB) as shown in **Figure 10**, which is a fluorescent probe. PET scanning is frequently used to image fibrillar amyloid load using ^{11}C-PiB.[211] The FDA has permitted three ^{18}F-labelled Aβ tracers, ^{18}F-Florbetaben (Neuraceq), ^{18}F-Florbetapir (Amyvid), and the benzothiazole derivative ^{18}F-Flutemetamol (Vizamyl), for use in estimating detecting Aβ plaque problems in patients with cognitive impairment.[212-216]

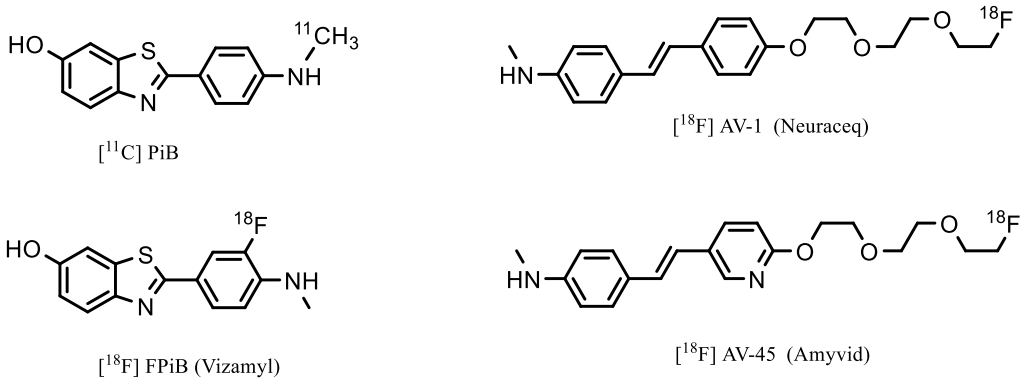

[^{11}C] PiB

[^{18}F] AV-1 (Neuraceq)

[^{18}F] FPiB (Vizamyl)

[^{18}F] AV-45 (Amyvid)

Figure 10. Structures of FDA-approved PET diagnostic agents for AD .

Both ^{11}C and ^{18}F radiotracers have short half-lives when used in clinical settings. Additionally, these radioisotopes are covalently incorporated into the target molecules, necessitating the use of particular synthesis methods and tools. Additionally, the duration of syntheses is constrained by the existence of the quickly disintegrating radionuclides. The use of long-lived radiometals in PET imaging has therefore increased, particularly copper-64 ($t_{1/2}$ = 12.7 h, β^+ = 17.8%; β^- = 38.4%). The extended half-life of ^{64}Cu, in contrast to ^{18}F, permits incorporation in the targeted area and wider clinical applications, particularly for use in places lacking cyclotrons on-site. Furthermore, fast chelation made it simple to include ^{64}Cu into bioactive molecules. $^{64}Cu(II)$ is the typical

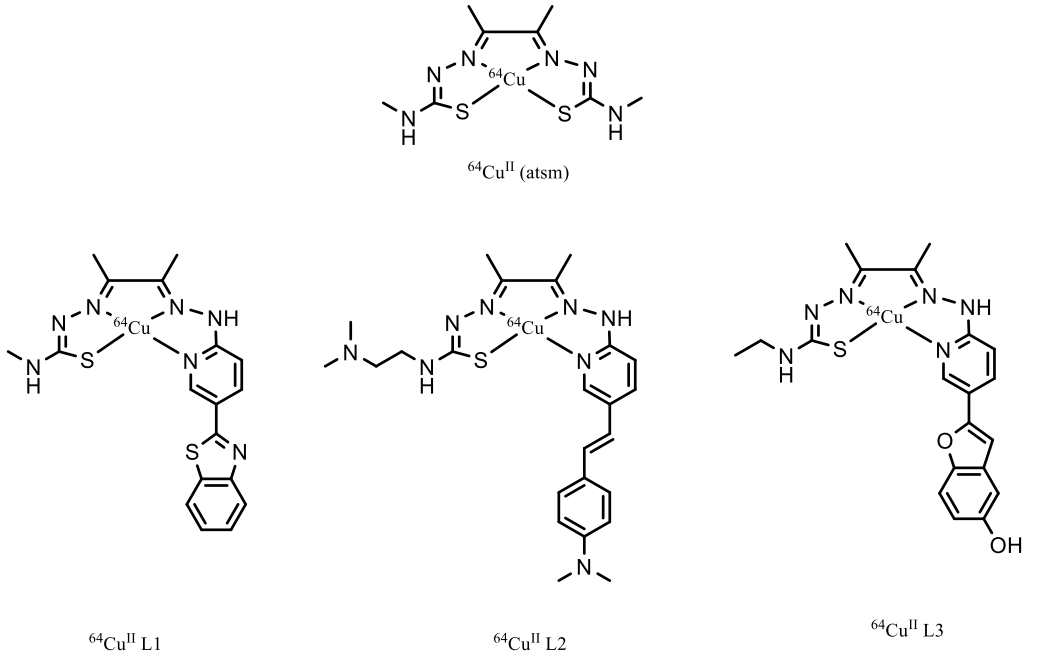

Figure 11. Examples of ^{64}Cu PET imaging agents for detecting Aβ species.

oxidation state of ^{64}Cu in aqueous solution, and its d^9 electronic configuration by employing metal chelators that contain nitrogen donors, anionic oxygen donors, or sulfur donors, allows the development of a wide range of coordination forms, from four-coordinate to six-coordinate.

Cu^{II} (atsm), a radiopharmaceutical for the PET imaging of hypoxia, is coupled with the Aβ targeting motifs, benzothiazole, dimethylaminostyrenyl, and pyridylbenzofuran to generate complexes $Cu^{II}L1$, $Cu^{II}L2$, and $Cu^{II}L3$, respectively (**Figure 11**). Donnelly and colleagues have recently reported the development of ^{64}Cu-based PET imaging of Aβ plaques. In post-mortem human brain tissue, the resulting complexes would bind to Aβ plaques with effectiveness. $Cu^{II}L2$ and $Cu^{II}L3$ also exhibit notable brain uptake in mouse biodistribution tests.[217-220]

MRI Imaging Techniques

Using a therapeutically acceptable MRI contrast agent and non-toxic curcumin, Vithanarachchi et al. created an effective tiny dye for β-amyloid aggregates (**Figure 12**).[221] Research conducted *in vitro* indicates that β-amyloid plaques interact with curcumin-conjugated contrast agents, causing T_1 to shorten and alterations in the wavelength and intensity of fluorescence emission.

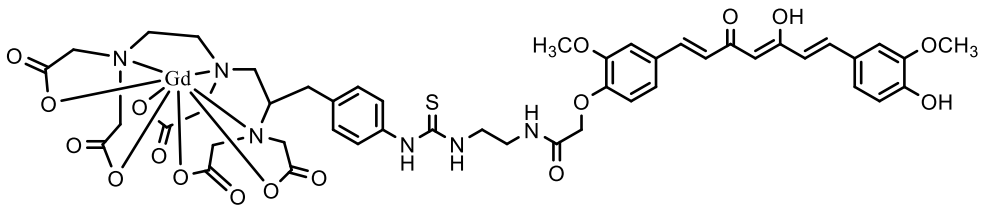

Figure 12. Curcumin-conjugated MR contrast agent for amyloid imaging.

Aggregation-Induced Emission:

The aggregation-caused quenching (ACQ) effect, which occurs when most conventional organic probes are applied at huge concentrations or in the aggregated condition, causes the intrinsic emission to be noticeably reduced or altogether disappear. The structural hydrophobicity of the majority of traditional organic dyes, which results in severe self-quenching, causes them to form irregular aggregates in aqueous environments since they are comprised of many aromatic rings and/or lengthy conjugated chains. For a variety of imaging applications, diluted solutions of organic dyes are utilized as substitutes to reduce the ACQ effect.[222] However, in this case, there are fewer fluorescent molecules, making them more susceptible to high-energy incident light from the outside, which could lead to undesired photobleaching. Furthermore, when the dyes are incorporated inside other loading systems, the ACQ phenomenon also occurs. Therefore, just raising the loading efficiency will not proportionately increase the overall brightness of a single nanoparticle. These disadvantages all significantly reduce the effectiveness of organic dyes in biological applications. Therefore, creating a new class of probes to solve the problems is crucial to revolutionize fluorescence imaging. In 2001, Tang described a particular class of unusual luminogens (silole derivatives) that showed noticeably increased emission when aggregated. He introduced the term "aggregation-induced emission" (AIE) for the first time.[223]

AIE luminogens, also known as AIEgens, are a class of probes that, when aggregated and in solid states, exhibit very high fluorescence, despite being weakly or non-emissive in diluted solutions. As of right now, the main theory to explain the AIE phenomena is the restriction of intramolecular motions (RIM) that comprises the restriction of intramolecular rotations as well as

vibrations. Active intramolecular rotations (in case of propeller-like tetraphenylethene, TPE) as well as vibrations (in case of shell-like 10,10′,11,11′-tetrahydro-5,5′-bidibenzo[a,d][7]-annulenylidene, THBA) significantly deactivate the excitation energy to promote non-radiative relaxation when AIEgens are dissolved in solutions.[224,225] These AIEgens' intramolecular movements are significantly inhibited during aggregation, thereby changing the ingesting routes from non-radiative to radiative relaxation. AIEgens are especially favored for superior-performance bioimaging and long-term fluorescence monitoring. AIE probes often show excellent quantum yields and exceptional photostability in the aggregated and solid phases in contrast to standard organic dyes. The visible spectrum and the near-infrared (NIR) region are now covered by the emission wavelength of several documented AIEgens.

AIE Probes for Amyloid Protein Aggregation Detection

For the purpose of clarifying the various facets of amyloid aggregation, such as (i) monitoring of amyloid aggregation kinetics; (ii) development of inhibitors for amyloid aggregates; (iii) construction of amyloid sensors; and (iv) design of amyloid biomarkers and tracking agents; these are emerging fields of contemporary research.[226] However, these fluorescent compounds always have drawbacks of their own that will restrict their use in specific circumstances. In particular, numerous aromatic rings found in organic dyes (such as ThT, Congo red, resveratrol, rifampicin, morin, etc.) typically result in the common ACQ effect, which means that the energy from intermolecular π-π interactions will be exhausted at the excited (binding or aggregation) states, severely quenching the dyes' fluorescence in the aggregation state. Additionally, the majority of ThT, Congo Red, and associated derivatives have a tendency to identify amyloid

fibrils with a high β-structure (such as less hazardous or off-pathway species), but they have a low sensitivity to amyloid oligomeric aggregates that are thought to be pathogenic species. The cytotoxicity of inorganic nanoparticles, such as carbon dots, quantum dots, and nanodots, to living cells is still up for debate. These particles typically include heavy metals, chelate ions, or chalcogens. Another issue with nanoparticles is that they might aggregate and lose their fluorescence.[227]

At first glance, using AIE to investigate amyloid inhibition, aggregation kinetics, toxicity, and detection mechanisms seems like a sensible choice. This is because the self-aggregation property of amyloid proteins and the AIE of fluorescent molecules complement each other perfectly. This is in contrast to conventional fluorescent molecules, which frequently exhibit the ACQ phenomenon and are utilized at higher concentrations for amyloid-associated applications. AIE molecules have proven to be more effective at addressing the various problems associated with amyloid aggregation. These problems include: (i) a broad emission feedback to an extensive variation of amyloids (Aβ, insulin, α-synuclein, etc.) with extraordinary sensitivity; (ii) high binding propensity to amyloids in comparison to ThT (the gold standard probe for amyloids); (iii) high performance to sense amyloid aggregates; (iv) different detection capability for toxic oligomers at the early stages of amyloid aggregation; (v) pronounced development of amyloid probes from simple buffer solutions, organelles, cells, bacteria, tissues, and even animals; and (vi) simple amalgamation with other imaging modalities (Raman, CT, MRI, and PA) to accomplish multimodal imaging.

Aromatic residues in AIE molecules are responsible for the molecules' strong propensity for attaching amyloids, their "turn-on" properties for photoluminescence, and an improved ratio of signal to background.

Conventional probes (ThT, Congo red and associated derivatives) frequently or exclusively sense β-sheet-rich aggregates due to the extensive range of amyloid aggregates, from oligomers to protofibrils to fibrils. However, AIE probes are able to recognize amyloid aggregates, regardless of their sizes and structures, and as a result, they are demonstrated to have a greater photoluminescence response. Additional structural alterations to AIE probes, such as the substitution of distinct side groups in various positions (QM-FN-SO_3),[228] give them enhanced in vivo and in vitro fluorescence response and detection capabilities, as well as increased resistance to the quenching effect caused by nanoparticles. Labeling of AIE molecules to amyloid proteins allows for the time-lapse monitoring and imaging of the extracellular and intracellular absorption as well as the aggregation of amyloid formation. Therefore, for the purpose of researching amyloid aggregation, toxicity, inhibition, sensing, and imaging, it is equally crucial to build functional AIE molecules.

Interaction Mechanisms of AIE Probes with Amyloid Aggregates

Various AIE processes, such as RIM, TICT, and FRET, have been proposed to explain how AIE molecules interact with amyloid aggregates. RIM is thought to be the primary operating mechanism behind the AIE phenomenon among them. When amyloid aggregates under the right circumstances, AIE molecules interact with the aggregates strongly. These interactions occur primarily through (i) electrostatic attraction among oppositely charged AIE probes and amyloid aggregates, (ii) explicit structural recognition among AIE probes and amyloids, (iii) hydrophobic interaction among the aromatic residues of AIE probes with the hydrophobic pockets of amyloid aggregates, and (iv) chemical reactions that bind AIE probes to amyloids that in turn restrict the

intramolecular motions. It has been shown that bis(triphenylphosphonium)tetraphenylethene (TPE–TPP) exhibits a better emission response to various aggregated states of amyloid proteins, such as α-synuclein oligomers/fibrils, α-lactalbumin ordered aggregates, and oligomeric and fibrillar Aβ, which has been demonstrated to be superior to that of classical ThT.[229,230] TPE-TPP further exhibits exceptional sensitivity to the most harmful oligomeric species and robust resistance to self-quenching.

AIE-Based Molecules for Amyloid Protein Aggregates

Aβ, α-syn, insulin, etc. are among the ~50 distinct amyloid proteins that are pathologically linked to various amyloid disorders.[231] Fluorescent molecules, which do not just include AIE probes, have been comprehensively created for the purpose of detecting amyloid aggregates. However, the majority of these dyes are restricted to single-target or single-mode sensing, which causes these amyloid probes to fail at a high rate in clinical trials.[232] It would be impossible to sense various amyloid proteins, which are pathologically connected to one another, using single-target amyloid probes with single-mode detection. This presents a significant challenge to the development of unique multimodal targeted AIE markers and sensors with enhanced selectivity for the revealing of homo/hetero-aggregates of various amyloid proteins.

One of the best-known AIE-active luminogens, TPE, is characterized by a propeller-shaped architecture with four phenyl rotors centered on an olefin stator.[233]

TPE exhibits significant emission in the aggregated state, however, feeble emission in the dissolved state due to this structural characteristic, which gives TPE AIE features.

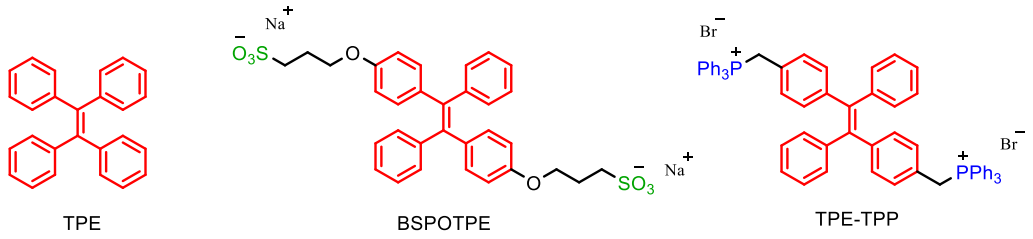

Figure 13. AIE probes for amyloid imaging.

TPE and its derivatives include sodium 1,2-bis[4-(3-sulfonatopropoxyl)phenyl]-1,2-diphenylethene (BSPOTPE)[234] (**Figure 13**), a water-miscible TPE salt that was first created to serve two purposes: (i) to monitor insulin aggregation kinetics (related to type 2 diabetes) and (ii) as an *in situ* inhibitor to prevent the formation of insulin fibrils. BSPOTPE can sense a characteristic nucleation-polymerization aggregation profile of insulin, comprising three different aggregation phases of insulin nucleation, elongation, and saturation.

Additionally, it can show a linear connection among fluorescence signal and insulin concentration in the range of 0–5 mM, which enables BSPOTPE to be utilized as a quantifiable dye for detecting fibrillar insulin. These characteristics make BSPOTPE similar to other fluorescent molecules (such as ThT and CR) for amyloid detection. Tetraphenylethene-triphenylphosphonium, or TPE–TPP, is a novel fluorescent probe that was created to identify distinct amyloid oligomers.[235]

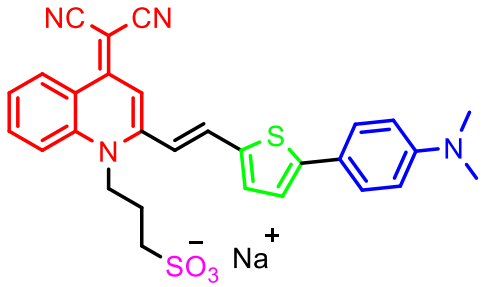

QM-FN-SO_3

Figure 14. AIE molecule for amyloid detection.

When the QM-FN-SO_3 (**Figure 14**) probe binds to Aβ plaques, it can act as a light-up NIR fluorescent dye with a higher signal-to-noise ratio than other common ThT and ThS markers.[228] QM-FN-SO_3 also has the benefit of having acceptable BBB permeability and biocompatibility when used in vivo NIR imaging Aβ plaques. The sulfonate group in QM-FN-SO_3, quinoline-malononitrile (QM), and the lipophilic π-conjugated thiophene-bridge together provide a unique structural combination that can effectively minimize "false-positive" signals resulting from the first aggregation of AIE dyes prior to interaction with Aβ plaques.

Table 2: A summary of different types of molecules used for detecting amyloid aggregates

Compounds	λ_{em} (nm)	K_d (nM)	Reference
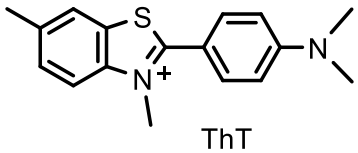 ThT	485 nm	890	236
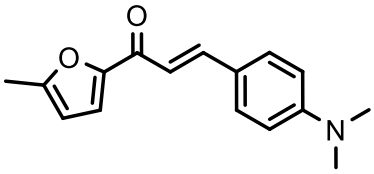	582 nm	2300	237
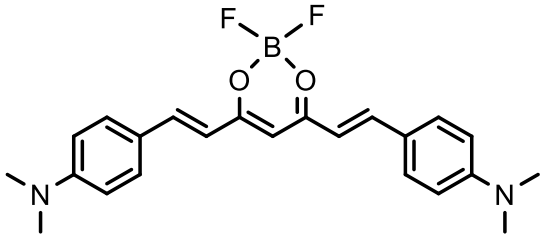	715 nm	38.7	238
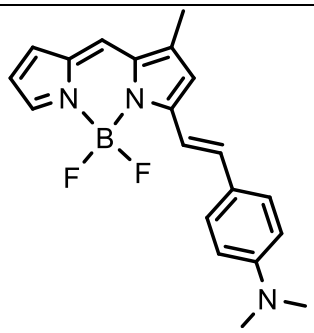	648 nm	44.1	239
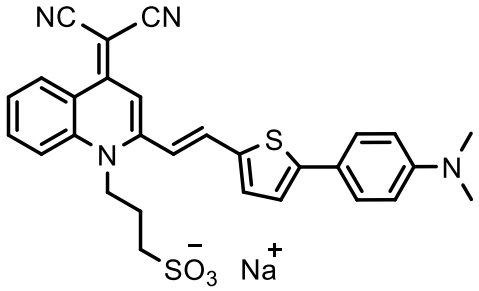	665 nm	NA	228

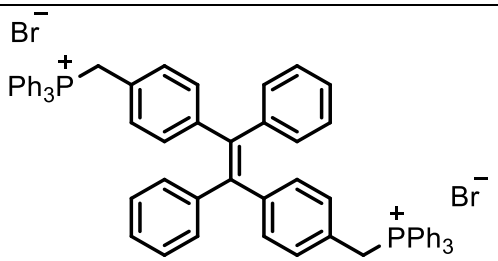	406 nm	8930	235
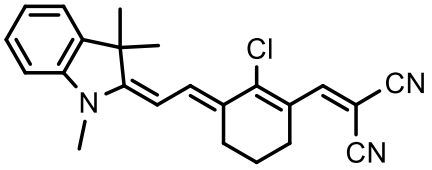	685 nm	59.09	240
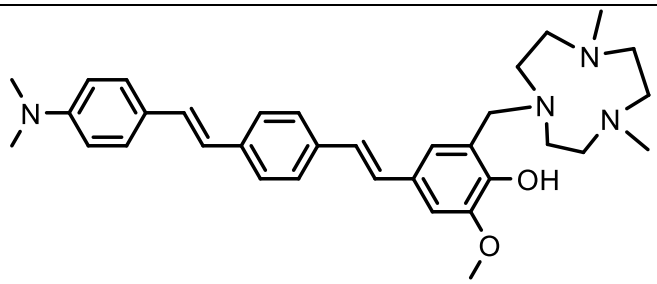	500 nm	58	241
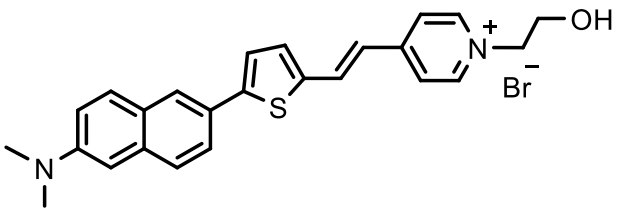	708 nm	143	242
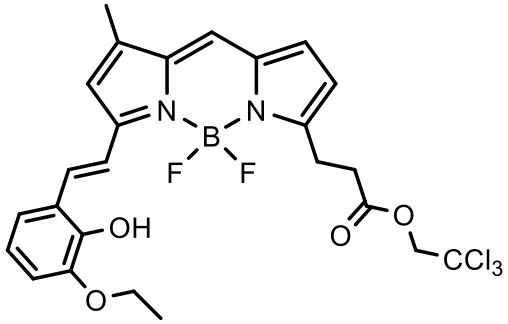	585 nm	480	243

Amyloid Inhibition by Small Molecules:

Even though there aren't any treatments for AD at the moment, things are moving forward. Comprehensive investigations into the structure and biochemistry of amyloid have resulted in the creation of possible treatments to address the underlying illness. There is a thorough analysis of therapy options that address the underlying illness elsewhere.[244] Recently, small-molecule drugs that can inhibit the production, deposition, and accumulation of Aβ aggregates have come to light as a potentially effective means of therapy.[245] During in vitro assays, numerous small compounds that could impact the amyloid aggregation pathway were found. While some of these drug-like compounds stop or lessen the production of non-fibrillar oligomers, others inhibit the creation of amyloid fibrils.[246,247]

Drugs intended to treat Alzheimer's disease (AD) and other neurodegenerative disorders must be capable to cross the blood-brain barrier (BBB) at high enough concentrations to have the desired therapeutic effects, such as blocking the production of amyloid.[248,249] Most of these small compounds have poor BBB penetrating ability and are very cytotoxic, creating them potentially harmful even if they seem to be efficient in inhibiting amyloid aggregates and attenuating amyloid toxicity in cell cultures. Below is a summary of small compounds that prevent amyloid fibrillation both in vivo and in vitro.

A class of chemicals called polyphenols that are found naturally in plants. Due to their capacity to act as antioxidants, polyphenol intake has been shown to be advantageous to health. Polyphenols have drawn more interest as a result of their potential to cure AD. Here, we give a brief summary of the substances curcumin, EGCG, and resveratrol (**Figure 15**), all of which have a strong track record of preventing the formation of amyloid.

Resveratrol reduces amyloid-induced cellular toxicity and prevents the production of Aβ fibrils and islet amyloid polypeptide, which are linked to type II diabetes, in vitro.[250,251] Similarly, EGCG molecules prevent the development of full fibrils and encourage the self-assembly of Aβ[252] and α-synuclein[253] to "off-pathway" oligomers. Micromolar quantities of EGCG are defending against Aβ-induced cell death, according to cell culture research.[254,255] Turmeric's primary ingredient, curcumin, has been shown to prevent Aβ aggregation, with IC_{50} values ranging from 0.1 to 1 μM.[256-259]

Owing to their low toxicity, ability to pass the BBB, and anti-amyloidogenic activity, polyphenols show promise as therapy for AD and other neurodegenerative illnesses. While the in vitro inhibition of amyloid aggregation by EGCG, curcumin, and resveratrol is well established, the exact mechanisms behind these actions remain unclear. The high metabolic activity of these polyphenol compounds in the gastrointestinal tract is a drawback, as it results in inadequate absorption when taken orally. Currently, clinical trials are being conducted to assess their effectiveness in treating AD.[260,261]

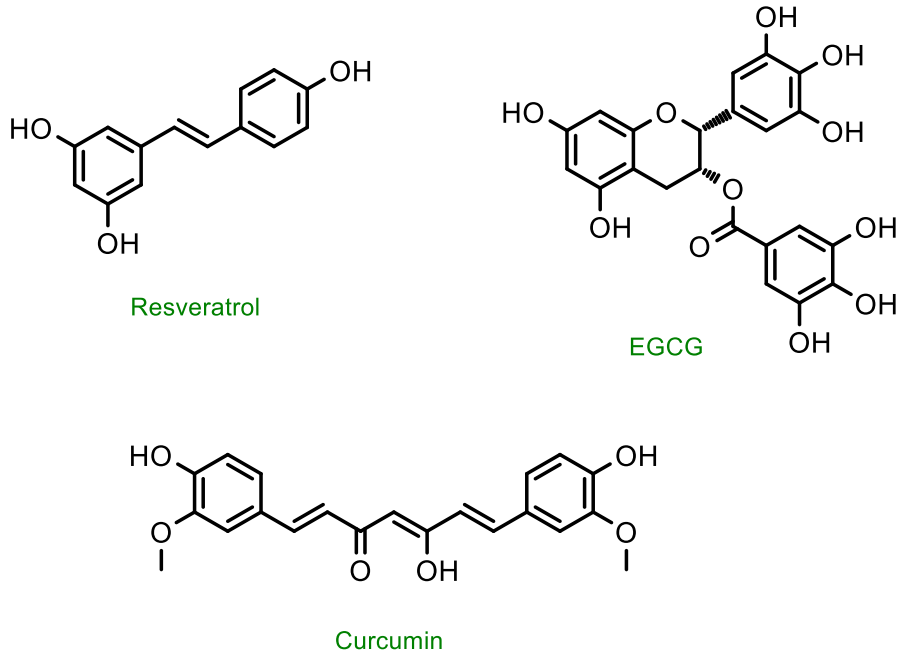

Figure 15. Chemical structures of the resveratrol, EGCG, and curcumin.

Effect of Nanoparticles on Oligomerization of Aβ40/42 Peptides

Many studies investigating the impact of nanoparticles (NPs) on the process of amyloid aggregation have been conducted due to the worry that some NP types may be capable to cross the BBB.[262] Numerous studies showing the opposite effects—from total fibrillation inhibition with NPs to process acceleration—have been reported in the literature. For a thorough explanation of the changing mechanism, it is crucial to take into account the kind of NPs and the precise investigational factors, i.e., concentration, pH, temperature, ionic strength, etc. It was shown that the presence of amino-modified polystyrene NPs strongly violated Aβ40/42 nucleation.[263] By raising the local concentration of the peptide on their surface, NPs can specifically act as a catalytic surface for aggregation at minimal NPs concentration or surface area to peptide ratios.

However, once the concentration or surface area of the NPs exceeds a particular value, the opposite effect is seen (**Figure 16**). As a result, the quantity of peptide molecules adsorbed on the NPs' surface increases, reducing the amount of peptide molecules in solution that can nucleate and preventing the rate of fibrillation.

(a) Low particle surface area

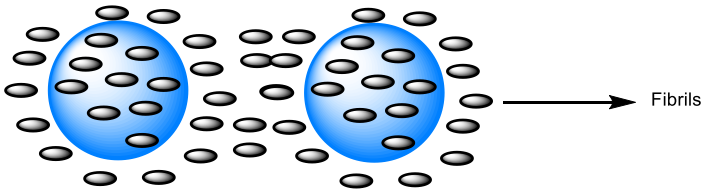

(b) High particle surface area

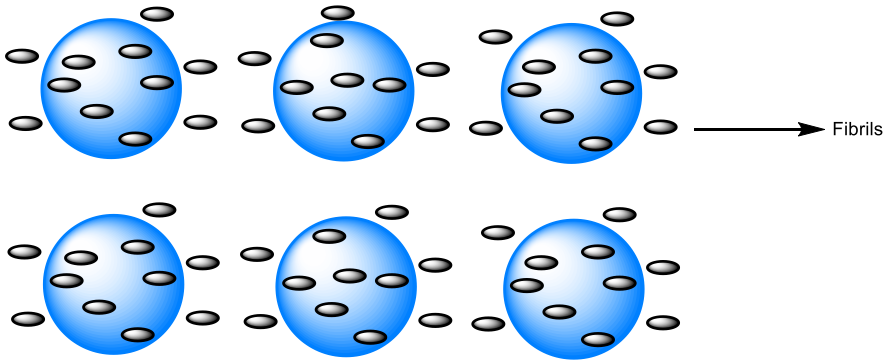

Figure 16. Peptide adsorption on the surface of the NPs. (a) at low particle surface area and (b) at high particle surface area in contrast to peptide concentration.

The way that NPs interact with Aβ40/42 is diverse and involves a range of non-covalent interactions. For example, it was found that the presence of CdTe NPs stabilized with thioglycolic acid inhibited Aβ40 fibrillation.[264] The binding of the Aβ40 monomers and oligomers to the NPs via van der Waals interactions

linked to "high electron density of atoms in the CdTe NPs" was discovered based on STEM, AFM, and a number of 2D NMR investigations. Furthermore, oligomers were able to bind to the NPs more strongly than monomers.[265]

The inhibition mechanism of Aβ40 aggregate mediated by poly(N-acryloyl-L-phenylalanyl-L-phenylalanine methyl ester) (polyA-FF-ME) NPs is similarly thought to include hydrophobic contacts.[266] It is assumed that the F19–F20 motif of Aβ40 and the FF residues of the NPs interact in the purported interactions. It was discussed how hydrogenated and fluorinated nanoparticles affected the Aβ40/42 fibrillation process.[267,268] For instance, complexes of polyampholyte and fluorinated dodecanoic acid inhibit the development of fibrils and encourage the creation of Aβ1–40's β-helical secondary structure. Using TEM, CD spectroscopy, and dynamic light scattering (DLS), hydrogenated counterparts (hydrogenated NPs) stimulate development of the β-sheet secondary structure and improve fibrillation.[270] The increased interactions and reported inhibitory impact on Aβ40 are thought to be caused by the fluorinated NPs' "highly negative zeta potential and hydrophobic fluorinated core." Later, comparable findings were acquired for the Aβ42 instance. Furthermore, the cytotoxicity caused by Aβ1–42 was lessened and increased in the presence of hydrogenated NPs and fluorinated NPs, respectively.[267]

A lot of research has been done on the impact of gold (Au) NPs on the fibrillation pathway.[268-272] It was discovered that bigger AuNPs (36.0 nm and 18.1 nm) promote Aβ40 fibrillation, while smaller L-glutathione-stabilized AuNPs (6.0 nm) suppress the fibril formation. At concentrations of 10 μg/mL and above, L-glutathione-stabilized nanoclusters (AuNCs) measuring 1.9 nm were found to be more potent inhibitors of Aβ40 fibrillogenesis.[272] Moreover, Au-curcumin and gold

nanoparticles functionalized with four curcumin moieties destabilize preformed fibrils and inhibit Aβ40 aggregates in a concentration-dependent way (**Figure 17**).[271] The enhanced water solubility of Au-curcumin NPs is thought to account for its higher inhibitory effectiveness against Aβ40 aggregation as compared to free curcumin. It is assumed that the Au-curcumin NPs engage in multivalent interactions and aromatic stacking with Aβ1–40. The precipitation of Au-curcumin NPs at neutral pH is a limiting factor in their utilization; hence, acidic pH should be used for experimentation.

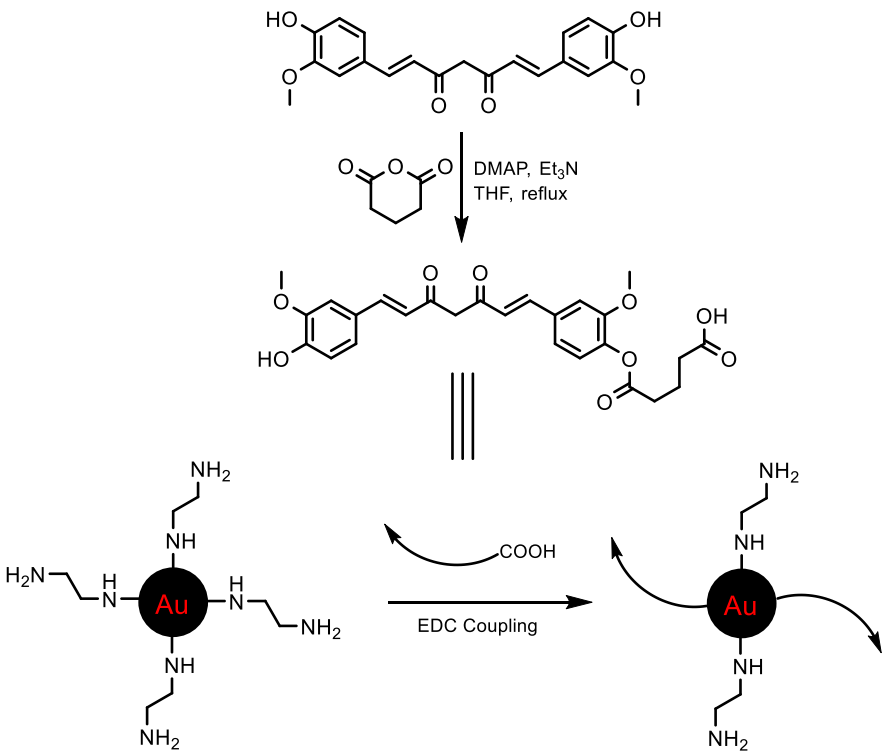

Figure 17. Schematic representation of curcumin-capped Au NPs.

When it came to inhibiting Aβ40 fibrillation, gold nanoparticles with anionic poly(acrylic acid) (PAA) or citrate surface engineering seemed to be more effective than those with cationic surface interactions, such as

cetyltrimethylammonium bromide (CTAB) and polyelectrolytes poly(allylamine)hydrochloride (PAH).[265] Furthermore, ThT-detected fluorescence measurements showed that the PAA-coated NPs were more effectual in comparison to the citrate-coated ones. The TEM findings showed that the only samples that have cationic surface modifications have an impact on the structure of the final aggregates. Whereas PAH-coated NPs encouraged the growth of thin and long fibrils, the addition of CTAB-coated NPs caused the creation of short and thick aggregates. Additionally, at a substoichiometric ratio of 1:2,000,000, the PAA-coated NPs with sizes of 18 nm and 8 nm successfully inhibit Aβ40 aggregate, whereas their 40 nm counterparts were ineffective in suppressing Aβ40 assembly.[270]

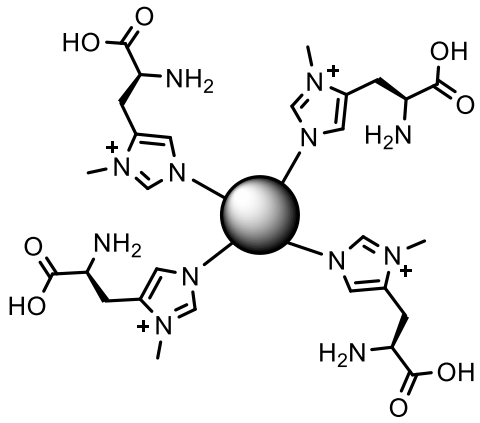

Figure 18. NP coated with a histidine-based polymer.

Therefore, the shape of the resulting aggregates is influenced by the size, surface chemistry, and surface charge of NPs, all of which are significant factors in the development of aggregation. Because the imidazole ring and methylene groups have weak hydrophobicity along with the appropriate combination of anionic and cationic surface charge, the NPs capped with the

histidine-based polymer (**Figure 18**) also exhibit an inhibitory effect against Aβ40 aggregation.[272]

Effect of Proteins and Peptides on Aggregation of Aβ40/42 Peptides

Certain proteins have the ability to block Aβ40/42 self-assembly. Aβ40/42 fibrillation may be effectively moderated by Apolipoprotein E3 (apoE3) through specific interaction Aβ40 oligomers.[273] Small peptides' capacity to inhibit fibrillogenesis has been the subject of numerous articles in current years. According to TEM and ThT assay results, there was a total suppression of Aβ40 aggregation in the presence of the MAQTFWLSIQGKTLYWQIRIYAID (TJ10) peptide (**Figure 19**).[274] Four aromatic amino acids (two Trp and two Tyr) as well as TJ10's β-sheet conformation were thought to have a significant role in the inhibitory process.

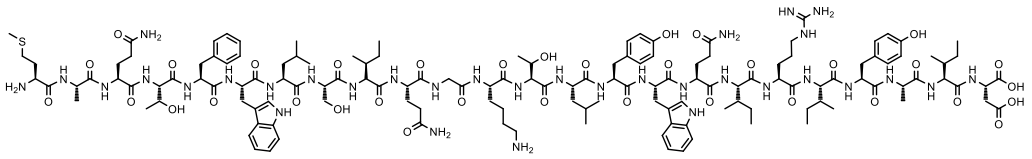

Figure 19. Structure of the TJ10 peptide.

The authors conjectured that TJ10 prevents the protofilaments and oligomers from growing further, which stops the production of mature fibrils. Studying short peptides whose sequence would contain a portion of the protein was prompted by the goal to identify a molecule or family of molecules that would particularly target the amyloidogenic proteins, however, have a simpler structure in comparison to antibodies. For instance, it was found that the peptides RGKLVFFGR (OR1) and RGKLVFFGR-NH2 (OR2) (**Figure 20**)

inhibited the aggregation of Aβ40/42.[275] Included in both OR1 and OR2, the amino acid sequence KLVFF is a component of the hydrophobic region of Aβ40/42. An enzyme-linked immunosorbent assay (ELISA) revealed that while both OR1 and OR2 could stop the development of fibrils, only OR2 could stop the formation of oligomers. Aβ40/42 has also become less toxic to human neuroblastoma cells (SH-SY5Y) when OR2 is present. The amide group at the C-terminus of the OR2 peptide sets it apart from the OR1 peptide. The amide group, according to the authors, makes OR2 more likely for Aβ40/42 to recognize it as a component of its molecule and boost the likelihood of peptide connections.

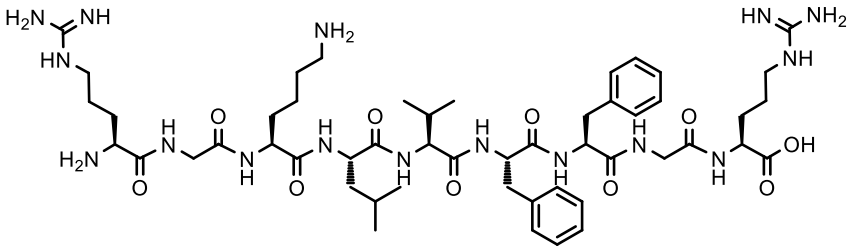

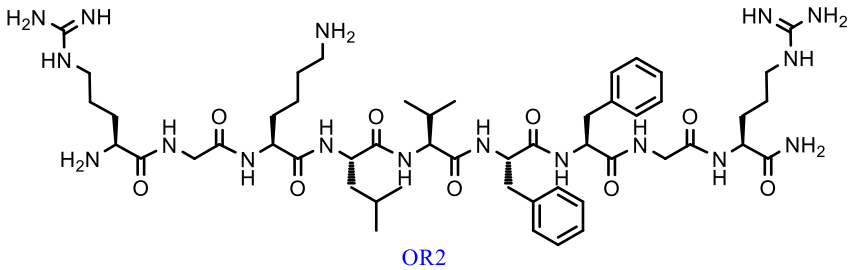

Figure 20. Structure of the OR1 and OR2 peptides.

A set of twenty short peptides with distinct D-amino acid sequences that matched the amino acid residues found at the N-terminus of the Aβ40/42 were examined. It was discovered that the fibrillation process can only be inhibited

by D-peptides containing the KLVFF moiety (Aβ15-20 and Aβ16-22). It was proposed that these peptides bind directly to the corresponding moiety of the Aβ40/42 peptide, just as short L-peptides comprising the KLVFF segment did earlier.[276,277]

Effect of Peptidomimetics on Aggregation of Aβ40/42 Peptides

Hamiton's group demonstrated recently that oligo-pyridylamide-based peptidomimetics (**Figure 21**) prevent Aβ fibrillation and oligomerization by enclosing the peptide in a safe helical shape.[278] They set out to investigate novel approaches for Aβ fibrillation modulation in an effort to broaden the toolkit of peptidomimetic scaffolds. In order to suppress Aβ fibrillation, they have created a small library of cationic N-substituted oligo-pyrrolamides. By trapping monomeric Aβ42 peptides on their surfaces, the amphiphilic N-substituted oligo-pyrrolamides compound, which develops vesicular structures under physiological conditions, suppresses Aβ42 fibrillation.

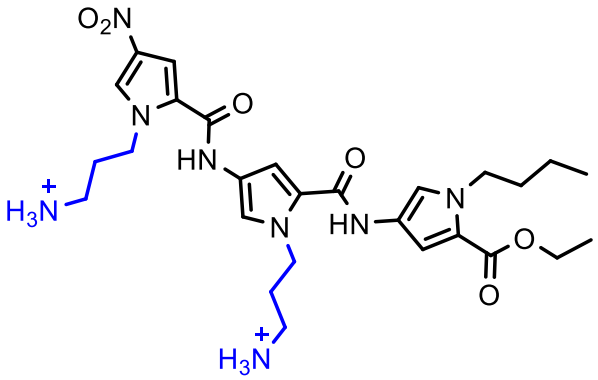

Figure 21. Oligo-pyridylamide-based peptidomimetic for the prevention of Aβ42 fibrillation.

Confocal Laser Scanning Microscopy:

A specialized fluorescence imaging method called confocal laser scanning microscopy (CLSM) is frequently applied in bioimaging applications. In order to create a picture, CLSM uses a concentrated laser beam rather than a lamp or LED lights, following the same principles as a traditional fluorescence microscope. White light laser (WLL) or different wavelength laser excitation sources are also employed in CLSM. The small portion of a specimen is illuminated by laser light, and the light that is emitted is sent through a pinhole (located directly in front of the detector), which eliminates out-of-focus light from neighbouring planes to lower background noise and considerably improve the image quality. A photomultiplier tube (PMT) in CLSM was originally used to detect and amplify the specimen's fluorescence signal. However, as technology developed and after the introduction of the HyD hybrid detector, it now provides better image quality and increased contrast. As opposed to traditional fluorescence microscopy, CLSM has the advantage of being able to lessen the effects of out-of-focus blurring while also enhancing contrast, sharpness, and optical resolution in photos. The primary advantage of CLSM is its ability to create 3D cellular images by selecting the right colors from several Z-stack slices that are taken from the specimen at different depths. This offers more precise information about the structural makeup of cellular organelles.[279,280]

Live Cell Confocal Imaging:

In live cell situations, confocal laser scanning microscopic imaging techniques are frequently used to ensure that a probe is taken up by cells. Moreover, cellular organelle health and morphology alteration can be monitored in real-time using live-cell confocal microscopy.

Figure 22. Specialized instrumentation for live cell confocal laser scanning imaging.

The integrity of the cell membrane may be jeopardized during the fixed cell process, increasing the permeability of the fixed cells to external substances. Moreover, the dynamic behavior of the cells and organelles, which is indispensable biological information is absent from the photos created after cell fixation. On the other hand, live-cell imaging, which shows the dynamic nature of cellular organelles, involves imaging cells over time (time-lapse imaging) at 37 °C and 5% CO_2. Live cell imaging is more challenging and needs a special setup than fixed cell imaging (**Figure 22**). Above all, in order for fluorophores to withstand extended laser irradiation, they must possess exceptional photophysical properties and low toxicity.[281,282]

References

1. Colom-Cadena, M.; Spires-Jones, T.; Zetterberg, H.; Blennow, K.; Caggiano, A.; DeKosky, S. T.; Fillit, H.; Harrison, J. E.; Schneider, L. S.; Scheltens, P.; de Haan, W.; Grundman, M.; van Dyck, C. H.; Izzo, N. J.; Catalano, S. M. *Alzheimers Res. Ther.* **2020**, *12*, 21.

2. Beach, T. G.; Walker, R.; McGeer, E. G. *Glia* **1989**, *2*, 420–436.

3. Pini, L.; Pievani, M.; Bocchetta, M.; Altomare, D.; Bosco, P.; Cavedo, E.; Galluzzi, S.; Marizzoni, M.; Frisoni, G. B. *Ageing Res. Rev.* **2016**, *30*, 25–48.

4. Scheltens, P. *et al*. *Lancet* **2021**, *6736*, 32205–32204.

5. Prince, M.; Ali, G.-C.; Guerchet, M.; Prina, A. M.; Albanese, E.; Wu, Y.-T. *Alzheimers Res. Ther.* **2016**, *8*, 23.

6. Ferri, C. P.; Prince, M.; Brayne, C.; Brodaty, H.; Fratiglioni, L.; Ganguli, M.; Hall, K.; Hasegawa, K.; Hendrie, H.; Huang, Y.; Jorm, A.; Mathers, C.; Menezes, P. R.; Rimmer, E.; Scazufca, M.; *Lancet* **2005**, *366*, 2112–2117.

7. Wittenberg, R.; Hu, B.; Jagger, C.; Kingston, A.; Knapp, M.; Comas-Herrera, A.; King, D.; Rehill, A.; Banerjee, S. *Age Ageing* **2020**, *49*, 264–269.

8. Wittenberg, R.; Knapp, M.; Hu, B.; Comas-Herrera, A.; King, D.; Rehill, A.; Shi, C.; Banerjee, S.; Patel, A.; Jagger, C.; Kingston, A. *Int. J. Geriatr. Psychiatry* **2019**, *34*, 1095–1103.

9. Brookmeyer, R.; Corrada, M. M.; Curriero, F. C.; Kawas, C. *Arch. Neurol.* **2002**, *59*, 1764–1767.

10. Lu, T.; Yang, X.; Huang, Y.; Zhao, M.; Li, M.; Ma, K.; Yin, J.; Zhan, C.; Wang, Q. *Cancer Manag. Res.* **2019**, *11*, 943–953.

11. Dauphinot, V.; Delphin-Combe, F.; Mouchoux, C.; Dorey, A.; Bathsavanis, A.; Makaroff, Z.; Rouch, I.; Krolak-Salmon, P. *J. Alzheimers Dis.* **2015**, *44*, 907–916.

12. Simpson, C.; Carter, P. *Am. J. Alzheimers Dis. Other Demen*. **2015**, *30*, 352–359.

13. Hippius, H.; Neundörfer, G. *Dialogues Clin*. *Neurosci*. **2003**, *5*, 101–108.

14. Hardy, J. *Neuron* **2006**, *52*, 3–13.

15. Eisenberg, D. *Proc. Natl. Acad. Sci. U. S. A.* **2003**, *100*, 11207–11210.

16. Stelzmann, R. A.; Schnitzlein, H. N.; Murtagh, F. R.; Murtagh, F. R. *Clin. Anat*. **1995**, *8*, 429–431.

17. Weber, M. M. *J. Psychiatr. Res*. **1997**, *31*, 635– 643.

18. Ebert, A.; Bär, K.-J. *Indian J. Psychiatry* **2010**, *52*, 191–192.

19. Kidd, M. *Nature* **1963**, *197*, 192–193.

20. Terry, R. D. *J. Neuropathol. Exp. Neurol*. **1963**, *22*, 629–642.

21. Glenner, G. G.; Wong, C. W. *Biochem. Biophys. Res. Commun*. **1984**, *120*, 885–890.

22. Perl, D. P. *Mt. Sinai J. Med.* **2010**, *77*, 32–42.

23. Filley, C. M.; Rollins, Y. D.; Anderson, C. A.; Arciniegas, D. B.; Howard, K. L.; Murrell, J. R.; Boyer, P. J.; Kleinschmidt-DeMasters, B. K.; Ghetti, B. *Cogn. Behav. Neurol.* **2007**, *20*, 149–156.

24. Mendez, M. F. *Continuum (Minneap Minn)* **2019**, *25*, 34–51.

25. Vieira, R. T. *Clin. Pract. Epidemiol. Ment. Health* **2013**, *9*, 88–95.

26. Nochlin, D.; Belle, G. V.; Bird, D.; Sumi, S. M. *Alzheimer Dis. Assoc. Disord*. **1993**, *7*, 212–222.

27. Citron, M.; Vigo-Pelfrey, C.; Teplow, D. B.; Miller, C.; Schenk, D.; Johnston, J.; Winblad, B.; Venizelos, N.; Lannfelt, L.; Selkoe, D. J. *Proc. Natl. Acad. Sci. U. S. A.* **1994**, *91*, 11993–11997.

28. Smits, L. L.; Pijnenburg, Y. A. L.; Koedam, E. L. G. E.; van der Vlies, A. E.; Reuling, I. E. W.; Koene, T.; Teunissen, C. E.; Scheltens, P.; van der Flier, W. M. *J. Alzheimers Dis.* **2012**, *30*, 101–108.

29. Campion, D.; Dumanchin, C.; Hannequin, D.; Dubois, B.; Belliard, S.; Puel, M.; Thomas-Anterion, C.; Michon, A.; Martin, C.; Charbonnier, F.; Raux, G.; Camuzat, A.; Penet, C.; Mesnage, V.; Martinez, M.; Clerget-Darpoux, F.; Brice, A.; Frebourg, T. *Am. J. Hum. Genet.* **1999**, *65*, 664–670.

30. Small, B. J.; Fratiglioni, L.; Viitanen, M.; Winblad, B.; Bächman, L. *Arch. Neurol*. **2000**, *57*, 839–844.

31. Bäckman, L.; Small, B. J.; Fratiglioni, L. *Brain* **2001**, *124*, 96–102.

32. Scoville, W. B.; Milner, B. *J. Neurol. Neurosurg. Psychiatry* **1957**, *20*, 11–21.

33. Humbert, I. A.; McLaren, D. G.; Kosmatka, K.; Fitzgerald, M.; Johnson, S.; Porcaro, E.; Kays, S.; Umoh, E.-O.; Robbins, J. *J. Alzheimers Dis.* **2010**, *19*, 1185–1197.

34. Sato, E.; Hirano, H.; Watanabe, Y.; Edahiro, A.; Sato, K.; Yamane, G.; Katakura, A. *Geriatr. Gerontol. Int.* **2014**, *14*, 549–555.

35. Pickering, G.; Jourdan, D.; Dubray, C. *Eur. J. Pain* **2006**, *10*, 379.

36. Scherder, E. J. A.; Sergeant, J. A.; Swaab, D. F. *Lancet Neurol.* **2003**, *2*, 677–686.

37. Cole, L. J.; Gavrilescu, M.; Johnston, L. A.; Gibson, S. J.; Farrell, M. J.; Egan, G. F. *Eur. J. Pain* **2011**, *15*, 568.e1–568.11.

38. Weintraub, S.; Wicklund, A. H.; Salmon, D. P. *Cold Spring Harb. Perspect. Med.* **2012**, *2*, a006171.

39. Lyketsos, C. G.; Carrillo, M. C.; Ryan, J. M.; Khachaturian, A. S.; Trzepacz, P.; Amatniek, J.; Cedarbaum, J.; Brashear, R.; Miller, D. S. *Alzheimers Dement.* **2011**, *7*, 532–539.

40. Mielke, M. M. *Psychiatr. Times* **2018**, *35*, 14–15.

41. Andersen, K.; Launer, L. J.; Dewey, M. E.; Letenneur, L.; Ott, A.; Copeland, J. R.; Dartigues, J. F.; Kragh-Sorensen, P.; Baldereschi, M.; Brayne,

C.; Lobo, A.; Martinez-Lage, J. M.; Stijnen, T.; Hofman, A. *Neurology* **1999**, *53*, 1992–1997.

42. Beam, C. R.; Kaneshiro, C.; Jang, J. Y.; Reynolds, C. A.; Pedersen, N. L.; Gatz, M. *J. Alzheimers Dis.* **2018**, *64*, 1077–1083.

43. Sala Frigerio, C. S.; Wolfs, L.; Fattorelli, N.; Thrupp, N.; Voytyuk, I.; Schmidt, I.; Mancuso, R.; Chen, W.-T.; Woodbury, M. E.; Srivastava, G.; Möller, T.; Hudry, E.; Das, S.; Saido, T.; Karran, E.; Hyman, B.; Perry, V. H.; Fiers, M.; De Strooper, B. *Cell Rep.* **2019**, *27*, 1293–1306.e6.

44. Seshadri, S.; Wolf, P. A.; Beiser, A.; Au, R.; McNulty, K.; White, R.; D'Agostino, R. B. *Neurology* **1997**, *49*, 1498–1504.

45. Chapman, R. M.; Mapstone, M.; Gardner, M. N.; Sandoval, T. C.; McCrary, J. W.; Guillily, M. D.; Reilly, L. A.; DeGrush, E. *J. Int. Neuropsychol. Soc.* **2011**, *17*, 654–662.

46. Laws, K. R.; Irvine, K.; Gale, T. M. *World J. Psychiatry* **2016**, *6*, 54.

47. Skup, M.; Zhu, H.; Wang, Y.; Giovanello, K. S.; Lin, J. A.; Shen, D.; Shi, F.; Gao, W.; Lin, W.; Fan, Y.; Zhang, H.; *Neuroimage* **2011**, *56* (3), 890–906.

48. Hua, X.; Hibar, D. P.; Lee, S.; Toga, A. W.; Jack, C. R.; Weiner, M. W.; Thompson, P. M.; *Neurobiol. Aging* **2010**, *31*, 1463–1480.

49. Ardekani, B. A.; Convit, A.; Bachman, A. H. *J. Alzheimers Dis*. **2016**, *50*, 847–857.

50. Shinohara, M.; Murray, M. E.; Frank, R. D.; Shinohara, M.; DeTure, M.; Yamazaki, Y.; Tachibana, M.; Atagi, Y.; Davis, M. D.; Liu, C.-C.; Zhao, N.; Painter, M. M.; Petersen, R. C.; Fryer, J. D.; Crook, J. E.; Dickson, D. W.; Bu, G.; Kanekiyo, T. *Acta Neuropathol.* **2016**, *132*, 225–234.

51. Savelieff, M. G.; Nam, G.; Kang, J.; Lee, H. J.; Lee, M.; Lim, M. H., *Chem. Rev*. **2019**, *119*, 1221-1322.

52. Frost, G. R.; Jonas, L. A.; Li, Y. M. *Aging Neurosci*. **2019**, *11*, 337.

53. Selkoe, D. J. *Neuron* **1991**, *6*, 487-98.

54. Hardy, J.; Allsop, D. *Trends Pharmacol. Sci*. **1991**, *12*, 383-8.

55. Frost, B.; Jacks, R. L.; Diamond, M. I. *J Biol Chem* **2009**, *284*, 12845-52.

56. Bush, A. I.; Pettingell, W. H.; Multhaup, G.; Paradis, M. D.; Vonsattel, J. P.; Gusella, J. F.; Beyreuther, K.; Masters, C. L.; Tanzi, R. E. *Science* **1994**, *265*, 1464-1467.

57. Liu, P.-P.; Xie, Y.; Meng, X.-Y.; Kang, J.-S. *Signal Transduct. Target. Ther.* **2019**, *4*, 29.

58. Jakob-Roetne, R.; Jacobsen, H. *Angew. Chem., Int. Ed*. **2009**, *48*, 3030-3059.

59. Savelieff, M. G.; Lee, S.; Liu, Y. Z.; Lim, M. H. *ACS Chem. Biol*. **2013**, *8*, 856-865.

60. Thinakaran, G.; Koo, E. H. *J. Biol. Chem.* **2008**, *283*, 29615-29619.

61. Hardy, J.; Selkoe, D. J. *Science* **2002**, *297*, 353-6. 81. Chen, G. F.; Xu, T. H.; Yan, Y.; Zhou, Y. R.; Jiang, Y.; Melcher, K.; Xu, H. E. *Acta Pharmacol. Sin*. **2017**, *38*, 1205-1235.

62. Pauwels, K.; Williams, T. L.; Morris, K. L.; Jonckheere, W.; Vandersteen, A.; Kelly, G.; Schymkowitz, J.; Rousseau, F.; Pastore, A.; Serpell, L. C.; Broersen, K. *J. Biol. Chem*. **2012**, *287*, 5650-5660.

63. Zhang, Y. W.; Thompson, R.; Zhang, H.; Xu, H. *Mol. Brain* **2011**, *4*, 3.

64. Qiu, T.; Liu, Q.; Chen, Y. X.; Zhao, Y. F.; Li, Y. M. *J. Pept. Sci*. **2015**, *21*, 522-9.

65. Xue, W. F.; Hellewell, A. L.; Hewitt, E. W.; Radford, S. E. *Prion* **2010**, *4*, 20-5.

66. DeToma, A. S.; Salamekh, S.; Ramamoorthy, A.; Lim, M. H. *Chem. Soc. Rev*. **2012**, *41*, 608-21.

67. Cohen, S. I.; Linse, S.; Luheshi, L. M.; Hellstrand, E.; White, D. A.; Rajah, L.; Otzen, D. E.; Vendruscolo, M.; Dobson, C. M.; Knowles, T. P. *Proc. Natl. Acad. Sci. U. S. A.* **2013**, *110*, 9758-9763.

68. Bloom, G. S. *JAMA Neurol*. **2014**, *71*, 505-8.

69. Ballard, C.; Gauthier, S.; Corbett, A.; Brayne, C.; Aarsland, D.; Jones, E. *Lancet* **2011**, *377*, 1019-31.

70. Honig, L. S.; Vellas, B.; Woodward, M.; Boada, M.; Bullock, R.; Borrie, M.; Hager, K.; Andreasen, N.; Scarpini, E.; Liu-Seifert, H.; Case, M.; Dean, R. A.; Hake, A.; Sundell, K.; Poole Hoffmann, V.; Carlson, C.; Khanna, R.; Mintun, M.; DeMattos, R.; Selzler, K. J.; Siemers, E. *N. Engl. J. Med*. **2018**, *378*, 321-330.

71. Ostrowitzki, S.; Lasser, R. A.; Dorflinger, E.; Scheltens, P.; Barkhof, F.; Nikolcheva, T.; Ashford, E.; Retout, S.; Hofmann, C.; Delmar, P.; Klein, G.; Andjelkovic, M.; Dubois, B.; Boada, M.; Blennow, K.; Santarelli, L.; Fontoura, P.; Investigators, S. C. R. *Alzheimer's Res. Ther.* **2017**, *9*, 95.

72. Walsh, D. M.; Klyubin, I.; Fadeeva, J. V.; Cullen, W. K.; Anwyl, R.; Wolfe, M. S.; Rowan, M. J.; Selkoe, D. J. *Nature* **2002**, *416*, 535-9.

73. Shankar, G. M.; Bloodgood, B. L.; Townsend, M.; Walsh, D. M.; Selkoe, D. J.; Sabatini, B. L. *J. Neurosci*. **2007**, *27*, 2866-75.

74. Walsh, D. M.; Klyubin, I.; Fadeeva, J. V.; Rowan, M. J.; Selkoe, D. J. *Biochem. Soc. Trans*. **2002**, *30*, 552-7.

75. Kollmer, M.; Close, W.; Funk, L.; Rasmussen, J.; Bsoul, A.; Schierhorn, A.; Schmidt, M.; Sigurdson, C. J.; Jucker, M.; Fändrich, M. *Nat. Commun.* **2019**, *10*, 4760.

76. Sipe, J. D.; Benson, M. D.; Buxbaum, J. N.; Ikeda, S.; Merlini, G.; Saraiva, M. J. M.; Westermark, P. *Amyloid* **2014**, *21*, 221–224.

77. Yakupova, E. I.; Bobyleva, L. G.; Vikhlyantsev, I. M.; Bobylev, A. G. *Bioscience Reports* **2019**, *39*, 20181415.

78. Rajamohamedsait, H. B.; Sigurdsson, E. M. *Methods Mol. Biol*. **2012**, *849*, 411–424.

79. Chiti, F.; Dobson, C. M. *Annu. Rev. Biochem.* **2006**, *75*, 333–366.

80. Dobson, C. M. *Trends Biochem. Sci.* **1999**, *24*, 329–332.

81. Knowles, T. P. J.; Vendruscolo, M.; Dobson, C. M. *Nat. Rev. Mol. Cell Biol.* **2014**, *15*, 384–396.

82. Pedersen, J. S.; Otzen, D. E. *Protein Sci*. **2007**, *17*, 2–10.

83. Pedersen, J. S.; Dikov, D.; Flink, J. L.; Hjuler, H. A.; Christiansen, G.; Otzen, D. E. *J. Mol. Biol.* **2006**, *355*, 501–523.

84. Pleyer, C.; Flesche, J.; Saeed, F. *Clin. Nephrol. Case Stud*. **2015**, *3*, 42.

85. Peng, S.; Glennert, J.; Westermark, P. *Amyloid* **2005**, *12*, 96–102.

86. Araki, K.; Yagi, N.; Aoyama, K.; Mochizuki, H. *Proc. Natl. Acad. Sci. U. S. A.* **2019**, *116*, 17963–17969.

87. McGowan, D. P.; van Roon-Mom, W.; Holloway, H.; Bates, G. P.; Mangiarini, L.; Cooper, G. J.; Faull, R. L.; Snell, R. G. *Neuroscience* **2000**, *100*, 677–680.

88. Chapman, M. R.; Robinson, L. S.; Pinkner, J. S.; Roth, R.; Heuser, J.; Hammar, M.; Normark, S.; Hultgren, S. J. *Science* **2002**, *295*, 851–855.

89. George-Hyslop, P. H. S. et al. *Science* **1987**, *235*, 885–890.

90. Tanzi, R. E.; Gusella, J. F.; Watkins, P. C.; Bruns, G. A.; St George-Hyslop, P.; Van Keuren, M. L.; Patterson, D.; Pagan, S.; Kurnit, D. M.; Neve, R. L. *Science* **1987**, *235*, 880–884.

91. Selkoe, D. J.; Podlisny, M. B.; Joachim, C. L.; Vickers, E. A.; Lee, G.; Fritz, L. C.; Oltersdorf, T. *Proc. Natl. Acad. Sci. U. S. A.* **1988**, *85*, 7341–7345.

92. Hardy, J.; Allsop, D. *Trends Pharmacol. Sci*. **1991**, *12*, 383–388.

93. Selkoe, D. J. *Sci. Am*. **1991**, *265*, 68–71, 74–76, 78.

94. Selkoe, D. J.; Hardy, J. *EMBO Mol. Med*. **2016**, *8*, 595.

95. Selkoe, D. J. *Physiol Rev.* **2001**, *81*, 741–766.

96. Mann, D. M. A.; Iwatsubo, T.; Ihara, Y.; Cairns, N. J.; Lantos, P. L.; Bogdanovic, N.; Lannfelt, L.; Winblad, B.; Maat-Schieman, M. L.; Rossor, M. N. AJP. *Am. J. Pathol.* **1996**, *148*, 1257–1266.

97. Tanaka, K.; Kelly, C. E.; Goh, K. Y.; Lim, K. B.; Ibáñez, C. F. *J. Neurosci*. **2016**, *36*, 5587–5595.

98. Wang, X. Bauer, J. H.; Li, Y.; Shao, Z.; Zetoune, F. S.; Cattaneo, E.; Vincenz, C. *J. Biol. Chem*. **2001**, *276*, 33812–33820.

99. Nagele, R. G.; D'Andrea, M. R.; Anderson, W. J.; Wang, H.-Y. *Neuroscience* **2002**, *110*, 199–211.

100. Ohyagi, Y.; Asahara, H.; Chui, D.-H.; Tsuruta, Y.; Sakae, N.; Miyoshi, K.; Yamada, T.; Kikuchi, H.; Taniwaki, T.; Murai, H.; Ikezoe, K.; Furuya, H.; Kawarabayashi, T.; Shoji, M.; Checler, F.; Iwaki, T.; Makifuchi, T.; Takeda, K.; Kira, J.; Tabira, T. *FASEB J.* **2005**, *19*, 255–257.

101. Fogarty, M. P.; McCormack, R. M.; Noonan, J.; Murphy, D.; Gowran, A.; Campbell, V. A. *Neurobiol. Aging* **2010**, *31* (10), 1774–1786.

102. Lockrow, J. P.; Fortress, A. M.; Granholm, A. C. E. *Curr. Gerontol. Geriatr. Res.* **2012** *13*.

103. Darocha-Souto, B.; Scotton, T. C.; Coma, M.; Serrano-Pozo, A.; Hashimoto, T.; Serenó, L.; Rodríguez, M.; Sánchez, B.; Hyman, B. T.; Gómez-Isla, T. *J. Neuropathol. Exp. Neurol.* **2011**, *70*, 360–376.

104. De, S.; Klenerman, D. *Biochim. Biophys. Acta Proteins Proteomics* **2019**, *1867*, 870–878.

105. O'Brien, R. J.; Wong, P. C. *Annu. Rev. Neurosci*. **2011**, *34*, 185–204.

106. Vignini, A.; Sartini, D.; Morganti, S.; Nanetti, L.; Luzzi, S.; Provinciali, L.; Mazzanti, L.; Emanuelli, M. *Int. J. Immunopathol. Pharmacol.* **2011**, *24*, 529–534.

107. Oh, E. S.; Savonenko, A. V.; King, J. F.; Fangmark Tucker, S. M.; Rudow, G. L.; Xu, G.; Borchelt, D. R.; Troncoso, J. C. *Neurobiol. Aging* **2009**, *30*, 1238–1244.

108. Lim, G.C.; Aina, E.N.; Cheah, S.K. *et al. BMC Cancer* **2014**, *14*, 212.

109. Plummer, S.; Heuvel, C. V. D.; Thornton, E.; Corrigan, F.; Cappai, R. *Aging Dis.* **2016**, *7*, 163–179.

110. Hayne, D. J.; Lim, S.; Donnelly, P. S. *Chem. Soc. Rev.* **2014**, *43*, 6701–6715.

111. Brunholz, S.; Sisodia, S.; Lorenzo, A.; Deyts, C.; Kins, S.; Morfini, G. *Exp. Brain Res.* **2012**, *217*, 353–364.

112. Koo, E. H.; Squazzo, S. L.; Selkoe, D. J.; Koo, C. H. *J. Cell Sci*. **1996**, *109*, 991–998.

113. Haass, C.; Kaether, C.; Thinakaran, G.; Sisodia, S. *Perspect. Med*. **2012**, *2*, a006270.

114. Nunan, J.; Small, D. H. *FEBS Lett*. **2000**, *483*, 6–10.

115. Tam, J. H. K. H. K.; Seah, C.; Pasternak, S. H. *Mol. Brain* **2014**, *7*, 54.

116. Portelius, E.; Price, E.; Brinkmalm, G.; Stiteler, M.; Olsson, M.; Persson, R.; Westman-Brinkmalm, A.; Zetterberg, H.; Simon, A. J.; Blennow, K. *Neurobiol. Aging* **2011**, *32*, 1090–1098.

117. Lawrence, J. L. M.; Tong, M.; Alfulaij, N.; Sherrin, T.; Contarino, M.; White, M. M.; Bellinger, F. P.; Todorovic, C.; Nichols, R. A. *J. Neurosci.* **2014**, *34*, 14210–14218.

118. Bateman, R. J.; Munsell, L. Y.; Morris, J. C.; Swarm, R.; Yarasheski, K. E.; Holtzman, D. M. *Nat. Med.* **2006**, *12*, 856–861.

119. Hansson, O.; Zetterberg, H.; Buchhave, P.; Andreasson, U.; Londos, E.; Minthon, L.; Blennow, K. *Dement. Geriatr. Cogn. Disord.* **2007**, *23*, 316–320.

120. Yoon, S. S.; Jo, S. A. *Biomol. Ther*. **2012**, *20*, 245.

121. Ries, M.; Sastre, M. *Aging Neurosci*. **2016**, *8*, 210313.

122. Iliff, J. J.; Wang, M.; Liao, Y.; Plogg, B. A.; Peng, W.; Gundersen, G. A.; Benveniste, H.; Vates, G. E.; Deane, R.; Goldman, S. A.; Nagelhus, E. A.; Nedergaard, M. *Sci. Transl. Med*. **2012**, *4*, 147ra111.

123. Sikanyika, N. L.; Parkington, H. C.; Smith, A. I.; Kuruppu, S. *Neurochem. Res*. **2019**, *44*, 1289– 1296.

124. Divry, P.; Florkin, M. *Societe de Biologie. (Fre)*, **1927**, 180-181.

125. Cohen, A. S.; Calkins, E. *Nature*, **1959**, *183*, 1202-3.

126. Eanes, E. D.; Glenner, G. G. *J. Histochem. Cytochem*. **1968**, *16*, 673-7.

127. Cohen, A. S.; Calkins, E. *J. Cell. Biol.* **1964**, *21*, 481-486.

128. Chamberlain, A. K.; Macphee, C. E.; Zurdo, J.; Morozova-Roche, L. A.; Hill, H. A.; Dobson, C. M.; Davis, J. J. *Biophys J.* **2000**, *79*, 3282-93.

129. Knowles, T. P.; Fitzpatrick, A. W.; Meehan, S.; Mott, H. R.; Vendruscolo, M.; Dobson, C. M.; Welland, M. *Eng. Sci.* **2007**, *318*, 1900–1903.

130. Puchtler, H.; Sweat, F.; Levine, M. *J. Histochem. Cytochem.* **1962**, *10*, 355–364.

131. Vassar, P. S.; Culling, C. F. *Arch Pathol*, **1959**, *68*, 487-98.

132. Rambaran, R. N.; Serpell, L. C. *Prion* **2008**, *2*, 112-117.

133. Sweeney, P.; Park, H.; Baumann, M.; Dunlop, J.; Frydman, J.; Kopito, R.; McCampbell, A.; Leblanc, G.; Venkateswaran, A.; Nurmi, A.; Hodgson, R. *Transl. Neurodegener.* **2017**, *6*, 6.

134. Tan, S.; Wong, E., Galluzzi, L.; Bravo-San Pedro, J. M.; Kroemer, G. Eds. *Academic Press*: **2017**, *588*, 245-281.

135. Jellinger, K. A. *J. Alzheimer's Dis.* **2018**, *62*, 1141-1179.

136. Lakshminarayanan, R.; Chaurasia, S. S.; Murugan, E.; Venkatraman, A.; Chai, S.-M.; Vithana, E. N.; Beuerman, R. W.; Mehta, J. S. *Ocul. Surf.* **2015**, *13*, 9–25.

137. Lee, V. M. Y.; Trojanowski, J. Q. *Curr. Opin. Neurobiol.* **1992**, *2*, 653–656.

138. Weingarten, M. D.; Lockwood, A. H.; Hwo, S. Y.; Kirschner, M. W. *Proc. Natl. Acad. Sci. U. S. A.* **1975**, *72*, 1858–1862.

139. Kapitein, L. C.; Hoogenraad, C. C. *Neuron* **2015**, *87*, 492–506.

140. Maccioni, R. B.; Cambiazo, V. *Physiol. Rev.* **1995**, *75*, 835–864.

141. Poorkaj, P.; Kas, A.; D'Souza, I.; Zhou, Y.; Pham, Q.; Stone, M.; Olson, M. V.; Schellenberg, G. D. *Mamm. Genome* **2001**, *12*, 700–712.

142. Caillet-Boudin, M. L.; Buée, L.; Sergeant, N.; Lefebvre, B. *Mol. Neurodegener.* **2015**, *10*.

143. Avila, J.; Lucas, J. J.; Pérez, M.; Hernández, F. *Physiol. Rev.* **2004**, *84*, 361–384.

144. Violet, M.; Delattre, L.; Tardivel, M.; Sultan, A.; Chauderlier, A.; Caillierez, R.; Talahari, S.; Nesslany, F.; Lefebvre, B.; Bonnefoy, E.; Buée, L.; Galas, M. C. *Front. Cell. Neurosci.* **2014**, *8*, 84.

145. Harada, A.; Oguchi, K.; Okabe, S.; Kuno, J.; Terada, S.; Ohshima, T.; Sato-Yoshitake, R.; Takei, Y.; Noda, T.; Hirokawa, N. *Nature* **1994**, *369*, 488–491.

146. Ikegami, S.; Harada, A.; Hirokawa, N. *Neurosci. Lett.* **2000**, *279*, 129–132.

147. Himmler, A.; Drechsel, D.; Kirschner, M. W.; Martin, D. W. *Mol. Cell. Biol.* **1989**, *9*, 1381–1388.

148. Chen, S.; Townsend, K.; Goldberg, T. E.; Davies, P.; Conejero-Goldberg, C. *J. Alzheimers Dis.* **2010**, *22*, 1313–1329.

149. Dujardin, S.; Bégard, S.; Caillierez, R.; Lachaud, C.; Carrier, S.; Lieger, S.; Gonzalez, J. A.; Deramecourt, V.; Déglon, N.; Maurage, C.-A.; Frosch, M. P.; Hyman, B. T.; Colin, M.; Buée, L. *Acta Neuropathol. Commun.* **2018**, *6*, 132.

150. Wang, Y.; Mandelkow, E. *Nat. Rev. Neurosci.* **2016**, *17*, 5–21.

151. Hirata-Fukae, C.; Li, H.-F.; Ma, L.; Hoe, H.-S.; Rebeck, G. W.; Aisen, P. S.; Matsuoka, Y. *Neurosci. Lett.* **2009**, *450*, 51–55.

152. Kovacs, G. G. *Elsevier B.V.* **2018**, *145*, 355–368.

153. Bloom, G. S. *JAMA Neurol*. **2014**, *71*, 505–508.

154. Rapoport, M.; Dawson, H. N.; Binder, L. I.; Vitek, M. P.; Ferreira, A. *Proc. Natl. Acad. Sci. U. S. A.* **2002**, *99*, 6364–6369.

155. Frandemiche, M. L. et al. *J. Neurosci*. **2014**, *34*, 6084–6097.

156. Bliss, T. V. P.; Lømo, T. *J. Physiol*. **1973**, *232*, 331–356.

157. Ward, S. M.; Himmelstein, D. S.; Lancia, J. K.; Binder, L. I. *Biochem. Soc. Trans.* **2012**, *40*, 667–671.

158. Ghag, G.; Bhatt, N.; Cantu, D. V.; Guerrero-Munoz, M. J.; Ellsworth, A.; Sengupta, U.; Kayed, R. *Protein Sci.* **2018**, *27*, 1901–1909.

159. Vara, D.; Pula, G. *Curr. Mol. Med*. **2014**, *14*, 1103–1125.

160. Thannickal, V. J.; Fanburg, B. L. *Am. J. Physiol.- Lung Cell. Mol. Physiol.* **2000**, *279*, L1005–L1028.

161. Kohen, R.; Nyska, A. *Toxicol. Pathol*. **2002**, *30*, 620–650.

162. Wang, X.; Wang, W.; Li, L.; Perry, G.; Lee, H. G.; Zhu, X. *Biochim. Biophys. Acta* **2014**, *1842*, 1240–1247.

163. Wang, W., Zhao, F., Ma, X., Perry, G.; Zhu, X. *Mol. Neurodegener*. **2020**, *15*, 1–22.

164. Giorgi, C.; Baldassari, F.; Bononi, A.; Bonora, M.; De Marchi, E.; Marchi, S.; Missiroli, S.; Patergnani, S.; Rimessi, A.; Suski, J. M.; Wieckowski, M. R.; Pinton, P. *Cell Calcium* **2012**, *52*, 36–43.

165. Yoshihara, E.; O'Connor, C.; Gasser, E.; Wei, Z.; Oh, T. G.; Tseng, T. W.; Wang, D.; Cayabyab, F.; Dai, Y.; Yu, R. T.; Liddle, C.; Atkins, A. R.; Downes, M.; Evans, R. M. *Nature.* **2020**, *586*, 606-611.

166. Zhou, J.; Chng, W. J. *Mitochondrion* **2013**, *13*, 163–169.

167. Fertan, E.; Rodrigues, G. J.; Wheeler, R. V.; Goguen, D.; Wong, A. A.; James, H.; Stadnyk, A.; Brown, R. E.; Weaver, I. C. G. *Am. J. Pathol.* **2019**, *189*, 1435–1450.

168. Li, L.; Ismael, S.; Nasoohi, S.; Sakata, K.; Liao, F.-F.; McDonald, M. P.; Ishrat, T. *J. Alzheimers Dis.* **2019**, *68*, 255–265.

169. Chalmers, S.; Caldwell, S. T.; Quin, C.; Prime, T. A.; James, A. M.; Cairns, A. G.; Murphy, M. P.; McCarron, J. G.; Hartley, R. C. *J. Am. Chem. Soc*. **2012**, *134*, 758−761.

170. Prag, H. A.; Kula-Alwar, D.; Pala, L.; Caldwell, S. T.; Beach, T. E.; James, A. M.; Saeb-Parsy, K.; Krieg, T.; Hartley, R. C.; Murphy, M. P. *Mol. Pharmaceutics* **2020**, *17*, 3526−3540.

171. Chen, H.; Wang, J.; Feng, X.; Zhu, M.; Hoffmann, S.; Hsu, A.; Qian, K.; Huang, D.; Zhao, F.; Liu, W.; Zhang, H.; Cheng, Z. *Chem. Sci*. **2019**, *10*, 7946–7951.

172. Zhang, R.; Niu, G.; Li, X.; Guo, L.; Zhang, H.; Yang, R.; Chen, Y.; Yu, X.; Tang, B. Z. *Chem. Sci*. **2019**, *10*, 1994–2000.

173. Tian, M.; Ge, E.; Dong, B.; Zuo, Y.; Zhao, Y.; Lin, W. *Anal. Chem*. **2021**, *93*, 3602−3610.

174. Chen, W.-H.; Luo, G.-F.; Zhang. X.-Z. *Adv. Mater*. **2019**, *31*, 1802725.

200. Wu, S.; Cao, Q.; Wang, X.; Chenga, K.; Cheng, Z. *Chem. Commun*. **2014**, *50*, 8919–8922.

175. Ferna´ndez-Carneado, J.; Gool, M. V.;Vera, M.; Castel, S.; Prados, P.; de Mendoza, J.; Giralt., E. *J. Am. Chem. Soc*. **2005**, *127*, 869–874.

176. Valero, J.; Van Gool, M.; Perez-Fernandez, R.; Castreno, P.; SanchezQuesada, J.; Prados, P.; de Mendoza, *J. Org. Biomol. Chem*. **2012**, *10*, 5417−5430.

177. D'Souza, G. G. M.; Rammohan, R.; Cheng, S. M.; Torchilin, V. P.; Weissig, V. *J. Controlled Release* **2003**, *92*, 189–197.

178. Cheng, Y.; and Ji, Y. *J. Controlled Release* **2020**, *318*, 38–49.

179. Burns, R. J.; Smith, R. A.; Murphy, M. P. *Arch. Biochem. Biophys*. **1995**, *322*, 60−68.

180. Murphy, M. P. *Trends Biotechnol*. **1997**, *15*, 326−330.

181. Smith, R. A.; Porteous, C. M.; Coulter, C. V.; Murphy, M. P. *Eur. J. Biochem*. **1999**, *263*, 709−716.

182. Huang, Y.; Zhou, Q.; Feng, Y.; Zhang, W.; Fang, G.; Fang, M.; Chen, M.; Xu, C.; Meng, X. *Chem. Commun*. **2018**, *54*, 10495−10498.

183. Li, X.; Tian, M.; Zhang, G.; Zhang, R.; Feng, R.; Guo, L.; Yu, X.; Zhao, N.; He, X. *Anal.Chem*. **2017**, *89*, 3335-3344.

184. Kelso, G. F.; Porteous, C. M.; Coulter, C. V.; Hughes, G.; Porteous, W. K.; Ledgerwood, E. C.; Smith, R. A.; Murphy, M. P. *J. Biol. Chem*. **2001**, *276*, 4588−4596.

185. Filipovska, A.; Kelso, G. F.; Brown, S. E.; Beer, S. M.; Smith, R. A.; Murphy, M. P. *J. Biol. Chem*. **2005**, *280*, 24113−24126.

186. Jameson, V. J.; Cocheme, H. M.; Logan, A.; Hanton, L. R.; Smith, R. A.; Murphy, M. P. *Tetrahedron* **2015**, *71*, 8444−8453.

187. Trnka, J.; Blaikie, F. H.; Logan, A.; Smith, R. A.; Murphy, M. P. *Free Radical Res*. **2009**, *43*, 4−12.

188. Kauffman, M. E.; Kauffman, M. K.; Traore, K.; Zhu, H.; Trush, M. A.; Jia, Z.; Li, Y. R. *React. Oxygen Species* **2016**, *2*, 361−370.

189. Hardy, M.; Poulhe, F.; Rizzato, E.; Rockenbauer, A.; Banaszak, K.; Karoui, H.; Lopez, M.; Zielonka, J.; Vasquez-Vivar, J.; Sethumadhavan, S.; Kalyanaraman, B.; Tordo, P.; Ouari, O. *Chem. Res. Toxicol*. **2014**, *27*, 1155−1165.

190. Johnson, I. D. Molecular Probes Handbook: A Guide to Fluorescent Probes and Labeling Technologies, Life Technologies Corporation, United States, **2010**, DOI: 10.1007/978-1-61779-968-6.

191. Kawazoe, Y.; Shimogawa, H.; Sato, A.; Uesugi, M. *Angew. Chem., Int. Ed*. **2011**, *50*, 5478−5481.

192. Kubi, G. A.; Qian, Z.; Amiar, S.; Sahni, A.; Stahelin, R. V.; Pei, D. *Angew. Chem., Int. Ed*. **2018**, *57*, 17183−17188.

193. Salvioli, S.; Ardizzoni, A.; Franceschi, C.; Cossarizza, A. *FEBS Lett*. **1997**, *411*, 77−82.

194. S Biswas, S.; Dodwadkar, N. S.; Sawant, R. R.; Koshkaryev, A.; Torchilin, V. P. J. *Drug Target.* **2011**, *19*, 552−561.

195. Hardy, J.; Allsop, D. *Trends Pharmacol. Sci*. **1991**, *12*, 383-8.

196. Vallet, P. G.; Guntern, R.; Hof, P. R.; Golaz, J.; Delacourte, A.; Robakis, N. K.; Bouras, C. *Acta Neuropathol* **1992**, *83*, 170-8.

197. Klunk, W. E.; Pettegrew, J. W.; Abraham, D. J. *J. Histochem. Cytochem*. **1989**, *37*, 1273-81.

198. Yakupova, E. I.; Bobyleva, L. G.; Vikhlyantsev, I. M.; Bobylev, A. G. *Biosci. Rep*. **2019**, *39*.

199. LeVine, H. *Protein Sci*. **1993**, *2*, 404-10.

200. Klunk, W. E.; Bacskai, B. J.; Mathis, C. A.; Kajdasz, S. T.; McLellan, M. E.; Frosch, M. P.; Debnath, M. L.; Holt, D. P.; Wang, Y.; Hyman, B. T. *J Neuropathol Exp Neurol* **2002**, *61*, 797-805.

201. Nesterov, E. E.; Skoch, J.; Hyman, B. T.; Klunk, W. E.; Bacskai, B. J.; Swager, T. M. *Angew. Chem. Int. Ed*. **2005**, *44*, 5452−5456.

202. Ono, M.; Ishikawa, M.; Kimura, H.; Hayashi, S.; Matsumura, K.; Watanabe, H.; Shimizu, Y.; Cheng, Y.; Cui, M.; Kawashima, H.; et al. *Bioorg. Med. Chem. Lett*. **2010**, *20*, 3885−3888.

203. Ono, M.; Watanabe, H.; Kimura, H.; Saji, H. *ACS Chem. Neurosci*. **2012**, *3*, 319−324.

204. Teoh, C. L.; Su, D.; Sahu, S.; Yun, S.-W.; Drummond, E.; Prelli, F.; Lim, S.; Cho, S.; Ham, S.; Wisniewski, T.; et al. *J. Am. Chem. Soc*. **2015**, *137*, 13503−13509.

205. Hatai, J.; Motiei, L.; Margulies, D. J. *Am. Chem. Soc*. **2017**, *139*, 2136−2139.

206. Ametamey, S. M.; Honer, M.; Schubiger, P. A. *Chem. Rev*. **2008**, *108*, 1501-16.

207. Shokeen, M.; Anderson, C. J. *Acc. Chem. Res*. **2009**, *42*, 832- 841.

208. Czernin, J.; Phelps, M. E. *Annu. Rev. Med*. **2002**, *53*, 89-112.

209. Moutselos, K.; Maglogiannis, I.; Chatziioannou, A. *BioMed Res. Int.* **2014**, *2014*, 145243.

210. Sedgwick, A. C.; Brewster, J. T.; Harvey, P.; Iovan, D. A.; Smith, G.; He, X.-P.; Tian, H.; Sessler, J. L.; James, T. D. *Chem. Soc. Rev*. **2020**, *49*, 2886-2915.

211. Frederiksen, K. S.; Hasselbalch, S. G.; Hejl, A. M.; Law, I.; Hojgaard, L.; Waldemar, G. *Dementia and Geriatr. Cognit. Disord.* **2012**, *2*, 610-21.

212. Serdons, K.; Terwinghe, C.; Vermaelen, P.; Van Laere, K.; Kung, H.; Mortelmans, L.; Bormans, G.; Verbruggen, A. *J. Med. Chem*. **2009**, *52*, 1428-1437.

213. Choi, S. R.; Golding, G.; Zhuang, Z.; Zhang, W.; Lim, N.; Hefti, F.; Benedum, T. E.; Kilbourn, M. R.; Skovronsky, D.; Kung, H. F. *J. Nucl. Med*. **2009**, *50*, 1887-1894.

214. Uzuegbunam, B. C.; Librizzi, D.; Yousefi, B. H. *Molecules* **2020**, *25*, 977.

215. Kung, H. F.; Choi, S. R.; Qu, W.; Zhang, W.; Skovronsky, D. *J. Med. Chem*. **2010**, *53*, 933-941.

216. Herholz, K.; Ebmeier, K. *Lancet Neurol*. **2011**, *10*, 667-70.

217. Vavere, A. L.; Lewis, J. S. *Dalton Trans*. **2007**, 4893-4902.

218. Hickey, J. L.; Lim, S.; Hayne, D. J.; Paterson, B. M.; White, J. M.; Villemagne, V. L.; Roselt, P.; Binns, D.; Cullinane, C.; Jeffery, C. M.; Price, R. I.; Barnham, K. J.; Donnelly, P. S. *J. Am. Chem. Soc*. **2013**, *135*, 16120-16132.

219. Paterson, B. M.; Donnelly, P. S. *Chem. Soc. Rev*. **2011**, *40*, 3005-3018.

220. McInnes, L. E.; Noor, A.; Kysenius, K.; Cullinane, C.; Roselt, P.; McLean, C. A.; Chiu, F. C. K.; Powell, A. K.; Crouch, P. J.; White, J. M.; Donnelly, P. S. *Inorg. Chem*. **2019**, *58*, 3382-3395.

221. Vithanarachchi, S. M.; Allen, M. J. *Chem. Commun*. **2013**, *49*, 4148-4150.

222. Mei, J.; Huang, Y.; Tian, H. *ACS Appl. Mater. Interfaces* **2018**, *10*, 12217–12261.

223. Luo, J.; Xie, Z.; Lam, J. W.; Cheng, L.; Chen, H.; Qiu, C.; Kwok, H. S.; Zhan, X.; Liu, Y.; Zhu, D. *Chem. Commun*. **2001**, 1740–1741.

224. Chen, J.; Law, C. C.; Lam, J. W.; Dong, Y.; Lo, S. M.; Williams, I. D.; Zhu, D.; Tang, B. Z. *Chem. Mater*. **2003**, *15*, 1535–1546.

225. Hong, Y.; Lam, J. W.; Tang, B. Z. *Chem. Commun*. **2009**, 4332–4353.

226. Aliyan, A.; Cook, N. P.; Martí, A. A. *Chem. Rev*. **2019**, *119*, 11819–11856

227. Nabers, A.; Ollesch, J.; Schartner, J.; Kötting, C.; Genius, J.; Hafermann, H.; Klafki, H.; Gerwert, K.; Wiltfang, J. *Anal. Chem.* **2016**, *88*, 2755–2762.

228. Fu, W.; Yan, C.; Guo, Z.; Zhang, J.; Zhang, H.; Tian, H.; Zhu, W.-H. *J. Am. Chem. Soc.* **2019**, *141*, 3171–3177.

229. Leung, C. W. T.; Guo, F.; Hong, Y.; Zhao, E.; Kwok, R. T. K.; Leung, N. L. C.; Chen, S.; Vaikath, N. N.; El-Agnaf, O. M.; Tang, Y.; Gai, W.-P.; Tang, B. Z. *Chem. Commun.* **2015**, *51*, 1866–1869.

230. Kumar, M.; Hong, Y.; Thorn, D. C.; Ecroyd, H.; Carver, J. A. *Anal. Chem.* **2017**, *89*, 9322–9329.

231. Iadanza, M. G.; Jackson, M. P.; Hewitt, E. W.; Ranson, N. A.; Radford, S. E. *Nat. Rev. Mol. Cell Biol.* **2018**, *19*, 755–773.

232. Zhang, Y.; Ren, B.; Zhang, D.; Liu, Y.; Zhang, M.; Zhao, C.; Zheng, J. *J. Mater. Chem. B* **2020**, *8*, 6179–6196.

233. Zhao, Z. Lam, J. W.; Tang, B. Z. *J. Mater. Chem.* **2012**, *22*, 23726–23740.

234. Hong, Y.; Meng, L.; Chen, S.; Leung, C. W. T.; Da, L.-T.; Faisal, M.; Silva, D.-A.; Liu, J.; Lam, J. W. Y.; Huang, X.; Tang, B. Z. *J. Am. Chem. Soc.* **2012**, *134*, 1680–1689.

235. Das, A.; Gupta, A.; Hong, Y.; Carver J. A.; Maiti, S. *Biochemistry*, **2020**, *59*, 1813–1822.

236. Klunk, W. E.; Wang, Y.; Huang, G. F.; Debnath, M. L.; Holt, D. P.; Mathis, C. A. *Life Sci.* **2001**, *69*, 1471–1484.

237. Jung, S.-J.; Park, S.-H.; Lee, E. J.; Park, J. H.; Kong, Y. B.; Rho, J. K.; Hur, M. G.; Yang, S. D.; Park, Y. D. *Arch. Pharm. Res.* **2015**, *38*, 1992–1998.

238. Ran, C.; Xu, X.; Raymond, S. B.; Ferrara, B. J.; Neal, K.; Bacskai, B. J.; Medarova, Z.; Moore, A. *J. Am. Chem. Soc.* **2009**, *131*, 15257–15261.

239. Ono, M.; Watanabe, H.; Kimura, H.; Saji, H. *ACS Chem. Neurosci.* **2012**, *3*, 319–324.

240. Yan, J.; Zhu, J.; Zhou, K.; Wang, J.; Tan, H.; Xu, Z.; Chen, S.; Lu, Y.; Cui, M.; Zhang, L. *Chem. Commun.* **2017**, *53*, 9910–9913.

241. Sun, L.; Cho, H.-J.; Sen, S.; Arango, A. S.; Huynh, T. T.; Huang, Y.; Bandara, N.; Rogers, B. E.; Tajkhorshid, E.; Mirica, L. M. *J. Am. Chem. Soc.* **2021**, *143*, 10462–10476.

242. Zhang , T.; Chen , X.; Yuan , C.; Pang , X.; Ping , S.; Liu , Y.; Han , L.; Sun , J.; Lam , J. W. Y.; Liu , Y.; Wang , J.; Shi, B.; Tang , B. Z. *Angew. Chem. Int. Ed.*, 2023, **62**, e202211550.

243. Teoh, C. L.; Su, D.; Sahu, S.; Yun, S.-W.; Drummond, E.; Prelli, F.; Lim, S.; Cho, S.; Ham, S.; Wisniewski, T.; Chang, Y.-T. *J. Am. Chem. Soc.* **2015**, *137*, 13503–13509.

244. Salomone, S.; Caraci, F.; Leggio, G. M.; Fedotova, J.; Drago, F. *Br. J. Clin. Pharmacol.* **2012**, *73*, 504–517.

245. Ryan, T. M.; Friedhuber, A.; Lind, M.; Howlett, G. J.; Masters, C.; Roberts, B. R. *J. Biol. Chem.* **2012**, *287*, 16947–16954.

246. Necula, M.; Kayed, R.; Milton, S.; Glabe, C. G. *J. Biol. Chem.* **2007**, *282*, 10311–10324.

247. LeVine, H. *Amyloid* **2007**, *14*, 185–197.

248. Hawkes, C. A.; Ng, V.; McLaurin, J. *Drug Dev. Res.* **2009**, *70*, 111–124.

249. Hubbard, R. E. *Neuropharmacology* **2011**, *60*, 7–23.

250. Ono, K.; Condron, M. M.; Ho, L.; Wang, J.; Zhao, W.; Pasinetti, G. M.; Teplow, D. B. *J. Biol. Chem.* **2008**, *283*, 32176–32187.

251. Feng, Y.; Wang, X. P.; Yang, S. G.; Wang, Y. J.; Zhang, X.; Du, X. T.; Sun, X. X.; Zhao, M.; Huang, L.; Liu, R. T. *Neurotoxicology* **2009**, *30*, 986–995.

252. Ehrnhoefer, D. E.; Bieschke, J.; Boeddrich, A.; Herbst, M.; Masino, L.; Lurz, R.; Engemann, S.; Pastore, A.; Wanker, E. E. *Nat. Struct. Mol. Biol.* **2008**, *15*, 558–566.

253. Bieschke, J.; Russ, J.; Friedrich, R. P.; Ehrnhoefer, D. E.; Wobst, H.; Neugebauer, K.; Wanker, E. E. *Proc. Natl. Acad. Sci. U. S. A.* **2010**, *107*, 7710–7715.

254. Levites, Y.; Amit, T.; Mandel, S.; Youdim, M. B. H. *FASEB J.* **2003**, *17*, 952–954.

255. Bastianetto, S.; Yao, Z.-X.; Papadopoulos, V.; Quirion, R. *Eur. J. Neurosci.* **2006**, *23*, 55–64.

256. Singh, P. K.; Kotia, V.; Ghosh, D.; Mohite, G. M.; Kumar, A.; Maji, S. K. *ACS Chem. Neurosci.* **2013**, *4*, 393–407.

257. Ono, K.; Hasegawa, K.; Naiki, H.; Yamada, M. *J. Neurosci. Res.* **2004**, *75*, 742–750.

258. Hamaguchi, T.; Ono, K.; Murase, A.; Yamada, M. *Am. J. Pathol.* **2009**, *175*, 2557–2565.

259. Kim, H.; Park, B.-S.; Lee, K.-G.; Choi, C. Y.; Jang, S. S.; Kim, Y.-H.; Lee, S.-E. *J. Agric. Food Chem.* **2005**, *53*, 8537–8541.

260. Smith, T. J. *Expert Opin. Drug Discov.* **2011**, *6*, 589–595.

261. Hamaguchi, T.; Ono, K.; Yamada, M. *CNS Neurosci. Ther.* **2010**, *16*, 285–297.

262. Koziara, J. M.; Lockman, P. R.; Allen, D. D.; Mumper, R. J. *Pharm. Res.* **2003**, *20*, 1772–1778.

263. Cabaleiro-Lago, C.; Quinlan-Pluck, F.; Lynch, I.; Dawson, K. A.; Linse, S. *ACS Chem. Neurosci*. **2010**, *1*, 279-287.

264. Yoo, S. I.; Yang, M.; Brender, J. R.; Subramanian, V.; Sun, K.; Joo, N. E.; Jeong, S.- H.; Ramamoorthy, A.; Kotov, N. A. *Angew. Chem. Int. E*d. **2011**, *50*, 5110-5115.

265. Skaat, H.; Chen, R.; Grinberg, I.; Margel, S. *Biomacromolecules* **2012**, *13*, 2662-2670.

266. Saraiva , A. M.; Cardoso , I.; Pereira, M. C.; Coelho, M. A. N.; Saraiva, M. J.; Möhwald, H.; Brezesinski, G. *ChemBioChem* **2010**, *11*, 1905-1913.

267. Rocha, S.; Thünemann, A. F.; Pereira, M. d. C.; Coelho, M.; Möhwald, H.; Brezesinski, G. *Biophys. Chem.* **2008**, *137*, 35-42.

268. Liao, Y.-H.; Chang, Y.-J.; Yoshiike, Y.; Chang, Y.-C.; Chen, Y.-R. *Small* **2012**, *8*, 3631-3639.

269. Moore, K. A.; Pate, K. M.; Soto-Ortega, D. D.; Lohse, S.; van der Munnik, N.; Lim, M.; Jackson, K. S.; Lyles, V. D.; Jones, L.; Glassgow, N.; Napumecheno, V. M.; Mobley, S.; Uline, M. J.; Mahtab, R.; Murphy, C. J.; Moss, M. A. *J. Biol. Eng.* **2017**, *11*, 5.

270. Palmal, S.; Maity, A. R.; Singh, B. K.; Basu, S.; Jana, N. R.; Jana, N. R. *Chemistry* **2014**, *20*, 6184–6191.

271. Gao, G.; Zhang, M.; Gong, D.; Chen, R.; Hu, X.; Sun, T. *Nanoscale* **2017**, *9*, 4107-4113.

272. Palmal, S.; Jana, N. R.; Jana, N. R. *J. Phys. Chem. C* **2014**, *118*, 21630-21638.

273. Smith, T. J.; Stains, C. I.; Meyer, S. C.; Ghosh, I. *J. Am. Chem. Soc.* **2006**, *128*, 14456-14457.

274. Chalifour, R. J.; McLaughlin, R. W.; Lavoie, L.; Morissette, C.; Tremblay, N.; Boulé, M.; Sarazin, P.; Stéa, D.; Lacombe, D.; Tremblay, P.; Gervais, F. *J. Biol. Chem.* **2003**, *278*, 34874–34881.

275. Austen, B. M.; Paleologou, K. E.; Ali, S. A. E.; Qureshi, M. M.; Allsop, D.; El-Agnaf, O. M. A. *Biochemistry* **2008**, *47*, 1984-1992.

276. Tjernberg, L. O.; Lilliehöök, C.; Callaway, D. J. E.; Näslund, J.; Hahne, S.; Thyberg, J.; Terenius, L.; Nordstedt, C. *J. Biol. Chem.* **1997**, *272*, 12601-12605.

277. Tjernberg, L. O.; Näslund, J.; Lindqvist, F.; Johansson, J.; Karlström, A. R.; Thyberg, J.; Terenius, L.; Nordstedt, C. *J. Biol. Chem.* **1996**, *271*, 8545-8548.

278. Maity, D.; Howarth, M.; Vogel, M. C.; Magzoub, M.; Hamilton, A. D. *J. Am. Chem. Soc.* **2021**, *143*, 3086– 3093.

279. Wang, L.; Tran, M.; D'Este, E.; Roberti, J.; Koch, B.; Xue, L.; Johnsson, K. *Nat. Chem*. **2020**, *12*, 165–172.

280. Lukinavicius, G.; Reymond, L.; Umezawa, K.; Sallin, O.;ˇ D'Este, E.; Gottfert, F.; Ta, H.; Hell, S. W.; Urano, Y.; Johnsson, K. *J. Am. Chem. Soc*. **2016**, *138*, 9365−9368.

281. Collot, M.; Fam, T. K.; Ashokkumar, P.; Faklaris, O.; Galli, T.; Danglot, L.; Klymchenko, A. S. *J. Am. Chem. Soc*. **2018**, *140*, 5401−5411.

282. Rhee, H. W.; Zou, P.; Udeshi, N. D.; Martell, J. D.; Mootha, V. K.; Carr, S. A.; Ting, A. Y. *Science* **2013**, *339*, 1328−1331.

Chapter 2

Materials and Methods

Introduction

This chapter provides comprehensive information on fundamental materials and a synopsis of the experimental procedures applied in this thesis to construct a dye and an inhibitor for amyloid aggregates. A number of biological investigations pertinent to this study are also included in the chapter, along with complete information on all spectroscopic measurements and microscopic techniques. Confocal laser scanning microscopy (CLSM) has also received specific attention for imaging live-cell mitochondria, as well as multicolor imaging. Each chapter contains comprehensive details of the biological experiments that were pertinent to the research study as well as the synthetic methods related to the compounds that were the subject of this thesis.

Experimental Procedures

General Materials:

3-methyl-2-butanone, 6-bromohexanoic, phenylhydrazine hydrochloride and DAPI, were obtained from Sigma Aldrich. Acetyl chloride**,** DMF (anhydrous, 99.8%), and all the HPLC grade solvents used for the spectroscopic experiments were procured from Sigma-Aldrich. Rhodamine-B were procured from TCI chemicals. All deuterated NMR solvents were bought from Cambridge Isotope Laboratories, Inc. Fmoc-amino acid building blocks: Fmoc-Gly-OH, Fmoc-Ser(tBu)-OH, Fmoc-Asn(Trt)-OH, Fmoc-Lys(Boc)-OH, Fmoc-Glu(OtBu)-OH, Fmoc-Ala-OH, Fmoc-Ile-OH, Fmoc-Leu-OH, Fmoc-Met-OH, Fmoc-Val-OH, Fmoc-Tyr(tBu)-OH, Fmoc-His(Trt)-OH, Fmoc-Gln(Trt)-OH, Fmoc-Asp(tBu)-OH, Fmoc-Arg(Pbf)-OH, Fmoc-Phe-OH, Fmoc-Pro-OH, Wang Resin LL (100-200 mesh), TLC silica gel 60 F_{254}, and XTT were acquired from Merck. 4-Diethylamino-salicylaldehyde, diethyl malonate,

pyridine, phosphorus oxychloride, 2-(4-Aminophenyl)acetonitrile, 1-[Bis(dimethylamino)methylene]-1*H*-1,2,3-triazolo[4,5-*b*]pyridinium 3-oxide hexafluorophosphate (HATU), *N*,*N*-Diisopropylethylamine (DIPEA), DMF, Thioflavin T, Uranyl acetate, *N,N,N′,N′*-Tetramethyl-*O*-(1*H*-benzotriazol-1-yl)uronium hexafluorophosphate (HBTU), 1-Hydroxybenzotriazole (HOBt), Trifluoroacetic acid (TFA), Triisopropylsilane (TIPS), 1,2-Ethanedithiol, Piperidine, Ethyl iodide, Tetrabutylammonium hydroxide 30-hydrate, Hoechst 33342, all the HPLC grade solvents and spectroscopic grade solvents were bought from Sigma-Aldrich. 1,1,1,3,3,3-Hexafluoro-2-propanol (HFIP) was bought from SRL Chemicals. Rhodamine B was procured from TCI chemicals. N2a and SH-SY5Y cells were obtained from the NCCS, India. 3-(4,5-dimethyl-2-thiazolyl)-2,5- diphenyltetrazolium bromide (MTT), DMEM, Trypsin EDTA mixture, and FBS were procured from HiMedia Laboratories. Mitochondrion targeting commercially available dye MitoTracker Deep Red FM and Ham's F-12K (Kaighn's) medium were acquired from Thermo Fisher Scientific. JC-1-based mitochondrion membrane potential and Annexin V-FITC/PI apoptosis detection kits were procured from BD Biosciences. *Millipore* ultra-pure H_2O was used for all the experiments.

Manual MW Assisted Solid-Phase Peptide Synthesis (SPPS): Peptides were synthesized by manual microwave (MW)-assisted 9-fluorenyl-methoxycarbonyl (Fmoc) solid phase peptide synthesis (Fmoc-SPPS) protocol on Wang resin (LL, 0.60 mmol/g loading density) by a MW peptide synthesizer (*CEM, Discover Bio*). The synthesis of the lipopeptide myristoyl-KPGPK was performed using MW-assisted solid-phase peptide synthesizer at a 0.1 mmol scale on the Wang resin (LL, 0.60 mmol/g loading density). For peptide coupling 5 eq. of the Fmoc-amino acid building blocks were pre-activated with HBTU (4.9 eq.), HOBt (5 eq.), and DIPEA (10 eq.) in DMF.

Handling of Resins and Fmoc Amino Acid Building Blocks: Fmoc amino acid building blocks were stored at –18 ºC. Resins were stored at 4 ºC. Before opening, all the Fmoc amino acid building blocks and resins were warmed to room temperature for 20 minutes.

First Amino Acid Loading on Wang Resin: The Wang resin (0.1 mmol) was swollen in 2 mL DMF for 1 h, then drains the solvent off and washed with DMF (2×). Fmoc-Lys(Boc)-OH (5 eq) or Fmoc-Gly-OH (5 eq), or Fmoc-Val-OH (5 eq), HBTU (4.9 eq.) and HOBt (5 eq.) were dissolved in 2 mL of DCM/DMF (1:1), then DIPEA (10 eq.) was added, and the mixture was taken in the SPE cartridge containing the Wang resin and stirred for 3 h under N_2 bubbling. Drain the solvent, and the resin was sequentially washed with DMF (2×), DCM (2×), and MeOH (2×). After Fmoc-Lys(Boc)-OH or Fmoc-Gly-OH or Fmoc-Val-OH loading on Wang resin, the loading density was calculated by UV/vis analysis of the Fmoc-dibenzofulvene deprotection product.

Estimation of the Loading Density of First Amino Acid on Wang resin: The Fmoc-Lys(Boc)-Wang or Fmoc-Gly-Wang or Fmoc-Val-OH resin (5 mg) and 1,8-diazabicyclo[5.4.0]undec-7-en (DBU) in NMP (2 mL, 2 % in NMP) were taken in a volumetric flask (10 mL). It was stirred for 30 min in a shaker, and the volumetric flask (10 mL) was filled up to the mark with CH_3CN. The solution was diluted with CH_3CN (1/12.5) and transported to an UV quartz cuvette. The cleaved dibenzofulvene was recorded at 304 nm (ε_{304} = 7624 L mol^{-1} cm^{-1}) and compared against reference. The first amino acid Fmoc-Lys(Boc)-OH or Fmoc-Gly-OH or Fmoc-Val-OH loading on the Wang resin was calculated based on Lambert-Beer's law.

ρ(mmol/g) = 163.96×(A – A_0)/m

ρ : loading density of the resin

A : absorption of a sample

A_0 : absorption of reference

m : mass of the analyzed resin in mg.

Protocols for MW-Assisted SPPS:

Before starting the peptide synthesis, the 5 μmol Fmoc-Lys(Boc)-Wang (LL) and Fmoc-Gly-Wang Resins (LL) were individually swollen in DMF (2 mL) for 2 h.

1. Bubbling during the MW-assisted synthesis for all steps: on 3 sec; off 7 sec.

2. **Fmoc deprotection**: 20% piperidine/DMF; time 210 sec, power 20 W, temperature 75ºC, delta temperature 5ºC.

Washing after Fmoc-deprotection: DMF (4×), DCM (4×), DMF (4×) to remove dibenzofulvene by-product.

3. **Coupling**: 0.5 M HBTU/0.5 M HOBt/2 M DIPEA/DMF; time 300 sec, power 20 W, temperature 75ºC, delta temperature: 5ºC.

Washing after coupling: DMF (3×), DCM (3×), DMF (3×)

After the final step, the resin was transferred to a SPE cartridge with frit and washed with DMF (5×), DCM (5×), MTBE (5×), and finally with MeOH (5×). The resins were dried in vacuum and stored at –18°C.

Test Cleavage from Wang Resin: To a pinch of the resin a mixture of TFA/TIPS/EDT (92.5/5.0/2.5 *v/v/v*) [trifluoroacetic acid (TFA), triisopropylsilane (TIPS), and 1,2-ethanedithiol (EDT)] was added, and the cleavage reaction was performed by shaking the resin for 2 h at room temperature. Afterward, the resin beads were filtered off, and the solvent was evaporated under an N_2 stream. Peptides were precipitated by using ice-cold MTBE. The MTBE suspension was centrifuged at −5°C, the supernatant was discarded, and the process was repeated three times. The supernatant was discarded, and the residue was washed with cold MTBE (3×) and dried to obtain the desired compounds with a free carboxy (–COOH) at the C-terminus.

Fmoc-SPPS protocol for peptide synthesis

Working Step	Resin	Reagents	Reaction condition
Coupling	Wang	HBTU/HOBt/DIPEA/DMF	300 sec/75°C/20 W
Washing after coupling	Wang	DMF(5×), DCM(5×), DMF(5×)	
Fmoc deprotection	Wang	20% piperidine/DMF	210 sec/75ºC/20 W
Washing after deprotection	Wang	DMF (4×), DCM (4×), DMF (4×)	
Washing after final coupling	Wang	DMF(5×), DCM(5×), MTBE(5×), MeOH(5×)	
Final Cleavage	Wang	TFA/TIPS/EDT (92.5/5.0/2.5 *v/v*)	2 h/25°C

Characterization

Spectroscopic Measurements:

NMR Spectroscopy: All the cyanine dyes, AIE probe and their intermediate compounds were characterized using 1D (^{1}H, ^{13}C, ^{31}P) and 2D NMR (^{1}H-^{1}H gCOSY) spectroscopy. Bruker DPX300 MHz and Bruker DPX400 MHz spectrometers were used for all NMR investigations, which were conducted at room temperature in appropriate deuterated solutions.

Reversed-Phase High-Performance Liquid Chromatography (RP-HPLC): RP-HPLC was performed on a UFLC, SHIMADZU instrument using a C-18 analytical HPLC column. SPD-M20A prominence diode array detector was used. HPLC run was performed in H_2O- CH_3CN (95% H_2O and 5% CH_3CN) solvent system.

Mass Spectrometry: High-resolution electrospray ionization mass spectrometry (HRMS-ESI) was performed using a Q-TofmicroTM (Waters Corporation) mass spectrometer.

Absorption Spectroscopy: Using a Shimadzu UV-1800 spectrometer and a quartz cuvette with a 1 cm path length, absorption spectra were captured.

Fluorescence Spectroscopy: A Horiba Jobin Yvon FluoroMax-4 spectrofluorometer was used to detect the fluorescence.

Time-correlated single photon counting (TCSPC) experiment: The time-correlated single photon counting (TCSPC) method was used to assess the fluorescence lifetime of the cyanine and AIE probe using Horiba DeltaFlex lifetime equipment (Horiba Jobin Yvon IBH Ltd, Glasgow, Scotland, UK). The fluorescence lifespan of cyanine and AIE probes in various solvents was measured using Delta diode laser excitation sources with 510 nm (Model: DD-510L, Horiba Scientific) and 650 nm (Model: DD-650L, Horiba Scientific)

wavelengths. Horiba EzTime decay analysis software was used to gather lifetime measurements and analyze the results.

Microscopic Studies:

Circular Dichroism (CD) Spectroscopy: CD spectra were acquired on a JASCO instrument (Model J-815–150S) at 25°C. Data were taken using a 1 mm quartz cuvette in the 190-260 nm range with a 0.5 nm step, 2 s collection times per step, and a 1 nm bandwidth.

Fourier Transform Infrared Spectroscopy (FT-IR): FT-IR spectra were acquired on a PerkinElmer Spectrum Two FT-IR spectrometer from 4000 to 400 cm^{-1} at room temperature in ATR mode.

X-Ray Powder Diffraction: The X-ray diffraction from the dried fibers of Aβ40 peptide was recorded on a Bruker D8 Advance X-ray diffractometer by Cu Kα radiation (λ = 1.5418 Å) operating at 40 kV and 40 mA.

Field Emission Scanning Electron Microscopy (FE-SEM): The morphology of the peptides was characterized using FE-SEM. 10 μL of peptide stock solutions (10 μM) were individually drop-cast on a glass cover slip and permitted to dry completely in air at room temperature. Samples were coated with gold, and the images were achieved in INSPECT F50 as well as Zeiss Scanning Electron Microscope instruments with a 10 kV and 5 kV accelerating voltage, respectively.

TEM Experiments: 10 μL of freshly prepared peptide in PBS solutions were pipetted out separately onto 300 mesh carbon-coated copper grids. After 2 m, the solvent on the grid was cautiously blotted by tissue paper. For negative staining, 10 μL of an aqueous solution of uranyl acetate [2 % (w/v)] was added to the grid and allowed to float for 30 s. The excess solution was shocked using a blotting paper. The sample was air dried at room temperature and kept in a

desiccator for 1 day before taking TEM images on a JEOL (Model: JEM 2100F) instrument operated at 120 kV.

Atomic Force Microscopy: 10 μL solution (10 μM) was drop-cast on a freshly cleaved mica film and allowed to dry completely in air for 24 hours before imaging. AFM images were captured on a KEYSIGHT TECHNOLOGIES 5500 AFM instrument (model no: Pico5500) and the images were processed by PicoView 1.10.1 software.

Dynamic Light Scattering (DLS): DLS experimentations were achieved on a Malvern instrument (Malvern, UK) to inspect the hydrodynamic diameter of the nanovesicles in solution. All measurements were performed at a backscattering angle of 173° at 25°C. Three runs were recorded, and the average was taken.

Isothermal Titration Calorimetry (ITC): ITC experimentation was executed on a MicroCal PEAQ-ITC microcalorimeter (Malvern). ITC measures the heat released/absorbed in a biomolecular binding incident in solution and calculates the binding affinity and thermodynamic parameters of molecular interactions in a single test. It helps to understand why the interactions happen, including the binding mechanisms. Binding affinity (K_D), reaction stoichiometry (n), enthalpy (ΔH), and entropy (ΔS) disclose the forces that dictate biomolecular interactions and can also exemplify function and mechanism at a molecular level. The ITC data and plots were examined by MicroCal PEAQ-ITC Analysis Software to measure the heat of interaction and thermodynamic parameters.

Computational Methods:

Density Functional Theory (DFT): The density functional theory (DFT) calculation was performed with Gaussian 09 W software. The ground state geometries were optimized at the Becke 3-parameter exchange functional by the gradient-corrected correlation functional of Lee, Yang, and Parr (B3LYP)

by the 6-31+G* basis set [B3LYP/6-31+G*]. The frontier molecular orbitals (FMOs) were analyzed using Gaussian 09W under the B3LYP/6-31+G* level.

Molecular Docking Simulation: The obtained energy minimized structure using B3LYP/6-31+G* was used for the molecular docking experiment. The crystal structure of Aβ40 fibrils (PDB ID: 2LMP) was achieved from the Protein Database (www.rcsb.org) and optimized by the AutoDock4.2 software. Molecular docking simulation was accomplished with Autodock Vina. Figures were developed through the Discovery Studio Visualizer software package. AutoDock4.2 was exploited for molecular docking experiments with the aid of the Lamarckian procedure inside the grid box of dimensions $60 \times 60 \times 60$ $Å^3$ at the ligand binding pocket. The greatest docking pose of the molecules was anticipated through binding energy, inhibition constant, ligand efficiency, van der Waals forces, intermolecular energy, hydrogen bond, total internal energy, dissolve energy, torsional energy, and unbound energy.

The scoring function was written as: $\Delta G_{binding} = \Delta G_{vdW} + \Delta G_{elec} + \Delta G_{hbond} + \Delta G_{desolv} + \Delta G_{tors}$

Biological Studies:

Cell Culture: SH-SY5Y was a three-time subcloned cell derived from the SK-N-SH human neuroblastoma cell line. The SH-SY5Y cell line was studied as a model for neurodegenerative disorders. A human neuroblastoma cell line SH-SY5Y was maintained in growth media encompassing DMEM:Ham′s F12 (1:1, pH 7.4), glutamine (2 mM), non-essential amino acids (1% NEAA), and 10% FBS. The SH-SY5Y cell line was preserved at 37 °C in the incubator with routine passage of 5% CO_2.

Cell Viability Assay: The cell viability test was performed on SH-SY5Y cells by 2,3-bis-(2-methoxy-4-nitro-5-sulfophenyl)-2*H*-tetrazolium-5-carboxanilide (XTT) reagent. The SH-SY5Y cells (5×10^4 cells/well) were seeded in a 96-well plate in 50% DMEM and F12K media (Invitrogen) with 10% FBS and grown to obtain > 80% confluency before treatment.

Cellular Uptake and Mitochondrial Localization Study: Confocal laser scanning microscopy methods were used for multicolor imaging in living cells as well as to confirm the cellular uptake and organelle selectivity.

Determination of Mitochondrial Membrane Potential Alteration after Incubation with Aβ40 Over Time Using the JC-1 Assay: Amendments in mitochondrial membrane potential were measured using a lipophilic cationic JC-1 probe (mitochondrion membrane potential detection kit) on a fluorescence-activated cell sorting (FACS) flow cytometer. For healthy mitochondria, the $\Delta\Psi_m$ value was highly negative. JC-1 dye was incorporated into the mitochondria, and the J-aggregates of JC-1 were observed. Conversely, when the membrane depolarized, the J-aggregates of JC-1 seepage from the mitochondria into the cytosol as monomers were detected. The excitation of JC-1 was 494 nm, and the emission was detected at 527 nm (green emission, JC-1 monomers) as well as at 596 nm (orange-red emission, JC-1 aggregates). The JC-1 monomers-to-aggregates emission ratio (527/596) was assessed. The greater value of this emission ratio specified larger membrane depolarization.

Annexin V-FITC/PI Apoptosis Detection Assay: The extent of apoptosis was quantitatively acquired by the Annexin V-FITC/PI apoptosis assay kit by FACS. Negatively charged phosphatidylserine (PS) usually exists in the inner leaflet of a healthy cell membrane. In the event of early apoptosis, the PS is flipped from the inner to outer membrane and is exposed. FITC-conjugated Annexin V has a great affinity for PS on the apoptotic cell membrane surface

and is the most sensitive biomarker to identify early apoptosis. The assay kit also comprises propidium iodide (PI) to stain the cellular DNA in necrotic cells. PI cannot penetrate the healthy or early apoptotic intact cell membrane. PI can infiltrate the late apoptotic and necrotic cell membranes and stain these cells.

Chapter 3

Construction of Self-Assembling Lipopeptide-Based Benign Nanovesicles to Prevent Amyloid Fibril Formation and Reduce Cytotoxicity of GxxxGxxxGxxxG Motif

INTRODUCTION

Misfolding and aggregation of proteins into amyloid fibrils through molecular self-assembly are connected with lethal human neurodegenerative disorders and peripheral diseases, comprising Alzheimer's disease (AD), Parkinson's disease, prion, Huntington's, type II diabetes, etc.[1-3] AD is a progressive neurodegeneration and serious brain disorder currently among the top 10 causes of decease worldwide.[4,5] Till now, AD cannot be prevented, cured, or even slowed down once it initiates. A noteworthy factor is the lack of powerful diagnostic and therapeutic tools for the early detection and treatment of AD. The anomalous assembly of amyloid-β (Aβ) peptides into cross-β structure is the key pathological hallmark of AD.[6] According to the estimation made by the WHO, ca. 10 million people worldwide are affected by AD every year and this population will be nearly double by 2030. Contemporary studies have proven that prefibrillar soluble oligomers of Aβ instead of mature fibrils are the key neurotoxic species.[7,8] The Aβ_{1-42} proteins experience an instinctive transition from a soluble, often partially folded form, into insoluble oligomers, protofibrils, and fibrils and deposited in the brain as Aβ plaques.[9,10] Researchers are trying to figure out a way to slow down or even halt AD. Numerous approaches have been intended and adopted to inhibit Aβ aggregation. Various inhibitory molecules have been constructed to accomplish these tasks, including small molecules, peptides, peptidomimetics, nanoparticles, nanochaperone, and macrocycles.[11-22] Though these molecules are effectual at both inhibiting and furnishing considerable mechanistic insights in Aβ fibrillation, these approaches have not been permitted yet for clinical application, primarily owing to nonspecific targets of the molecules. Most of the drugs developed for AD either failed or only offered modest improvement

of the symptoms, and further effort is fundamentally required.[23,24] Hence, finding a superior therapeutics for AD is indispensible. A more convincing AD therapeutic strategy should be inhibition of the formation of prefibrillar soluble oligomers and to maintain Aβ_{1-42} in its nontoxic monomeric form. Specific targeting and inhibiting the formation of neurotoxic prefibrillar soluble oligomers by self-assembly of lipopeptide-based building blocks using the "bottom-up" approach is a promising domain of contemporary research.[25,26] An obvious advantage of lipopeptide-based nano-inhibitors over other inorganic and organic nanoparticles is safety, biodegradability, and biocompatibility issues of the materials they are made of. Generally, lipopeptide-based nanomaterials are biodegradable, biocompatible, and environmentally benign because they are derived from naturally occurring biological building blocks, which have great advantages compared to other types of nano-inhibitors. Lipopeptide can be easily constructed using solid-phase peptide synthesis methods, and the peptide sequence can be specifically modified for driving the self-assembly processes. Nevertheless, the controlled self-assembly processes of lipopeptides into uniform and a well-ordered nanovesicle is a formidable task. We have used a supramolecular strategy based on the self-assembly of naturally occurring biological building blocks that form nanovesicles to inhibit the amyloid fibril growth of GxxxGxxxGxxxG motif of Aβ-protein (Aβ_{25-37}, GSNKGAIIGLMVG) and human myelin protein zero (GVVLGAVIGGVLG) as well as to reduce their neurotoxicity. The GxxxGxxxGxxxG motif is found in the transmembrane (TM) sequences of amyloid precursor protein, prion protein, and human myelin protein zero.[27,28] Gly mutations at positions G163 and G167 in the TM domain of human myelin protein zero produce myelin deficiency and are related with neuropathies like Dejerine–Sottas syndrome and Charcot–Marie–Tooth disease.[29,30] Since protein aggregation is mostly

guided by intermolecular hydrophobic interactions, electrostatic interactions, and hydrogen bonding, the working proposition is the design of myristoyl-KPGPK lipopeptide-based nanovesicles that should interact with the monomer and/or early aggregate seeds through noncovalent interaction to inhibit the formation of neurotoxic prefibrillar soluble oligomers and hence diminish cytotoxicity. Spectroscopic and microscopic studies showed that the synthesized supramolecular nanovesicles can inhibit the amyloid fibril formation made by the TM GxxxGxxxGxxxG motif. Moreover, a mouse Neuro-2a (N2A) neuroblastoma cell line is used, which exhibited GxxxGxxxGxxxG-mediated cytotoxicity of Aβ_{25-37} as well as human myelin protein zero and the cytotoxicity has been diminished by coincubating the GxxxGxxxGxxxG motif with the biocompatible nanovesicles. Our designed self-assembled lipopeptide-based nanovesicles show interesting results to target amyloid fibril-forming peptides, dramatically inhibit random coil to β-sheet transformation, prevent fibril formation, and diminish cytotoxicity to combat protein misfolding and aggregation diseases.

Experimental Section

Materials: Fmoc-amino acid building blocks: Fmoc-Gly-OH, Fmoc-Ser(tBu)-OH, Fmoc-Asn(Trt)-OH, Fmoc-Lys(Boc)-OH, Fmoc-Ala-OH, Fmoc-Ile-OH, Fmoc-Leu-OH, Fmoc-Met-OH, Fmoc-Val-OH, Fmoc-Pro-OH were obtained from Merck. Wang Resin LL (100-200 mesh) and TLC silica gel 60 F254 were also bought from Merck. N,N,N′,N′-Tetramethyl-O-(1H-benzotriazol-1-yl)uronium hexafluorophosphate (HBTU), 1-hydroxybenzotriazole (HOBt), N,N-diisopropylethylamine (DIPEA), N,N-dimethylformamide (DMF, anhydrous, 99.8%), trifluoroacetic acid (TFA), triisopropylsilane (TIPS), piperidine, myristic acid, Congo Red, Thioflavin T, and HPLC grade solvents

were procured from Sigma-Aldrich. Spectroscopic grade solvents were obtained from Sigma-Aldrich to perform all the spectroscopic experiments. DMSO-d_6 was purchased from Cambridge Isotope Laboratories, Inc. and used for NMR spectroscopy. Mouse Neuro-2a (N2A) neuroblastoma cell line was purchased from The National Centre for Cell Science, India. Dulbecco's modified eagle medium (DMEM), trypsin EDTA mixture, fetal bovine serum (FBS), antibiotic antimycotic solution, and 3-(4,5-dimethyl-2-thiazolyl)-2,5-diphenyltetrazolium bromide (MTT) were achieved from Himedia.

METHODS

Microwave Synthesizer: GxxxGxxxGxxxG peptides (GSNKGAIIGLMVG, Aβ_{25-37}; and GVVLGAVIGGVLG, human myelin protein zero protein precursors) and myristoyl-KPGPK lipopeptide were synthesized by manual microwave solid phase peptide synthesizer (CEM corporation, model discover bio, USA make) on Wang resin.

NMR Spectroscopy: ^{1}H and ^{13}C NMR were recorded at 25°C in suitable deuterated solvents on a Bruker DPX300 MHz spectrometer equipped with a BBO probe. Data were processed by Bruker TopSpin 3.6.2 software. Chemical shifts (δ) were mentioned in parts per million (ppm).

High-Resolution Electrospray Ionization Mass Spectrometry (HRMS-ESI): HRMS-ESI was recorded on a Q-Tofmicro (Waters Corporation) mass spectrometer using positive mode. The data were acquired and processed through the manufacturers' supplied mass application software, MassLynx V4.1. The calculated (calc.) and found *m*/*z* ratios were reported for each molecule.

Reversed-Phase High-Performance Liquid Chromatography (RP-HPLC): RP-HPLC of myristoyl- KPGPK lipopeptide was performed on a UFLC, SHIMADZU instrument using a C-18 analytical HPLC column. SPD-M20A prominence diode

array detector was used. HPLC run was performed in H_2O- CH_3CN (95% H_2O and 5% CH_3CN) solvent system.

UV/vis Absorption Spectroscopy: UV/vis spectra were monitored on a JASCO V-730 double-beam spectrophotometer with a quartz cuvette of 1 cm path length. The data were processed by the manufacturers' provided Spectra Manager Version 2 software. The UV/vis absorption data from the appropriate solvent as background was subtracted from the UV/vis data of the sample solution.

Fluorescence Spectroscopy: Fluorescence emissions were measured on a FluoroMax-4 spectrofluorometer (Horiba Scientific) operated by FluorEssence Version 3.9.0.1 software. 5 nm excitation and emission slit widths were used.

Fourier Transform Infrared Spectroscopy (FT-IR): FT-IR spectra were recorded using a PerkinElmer Spectrum Two FT-IR spectrometer from 4000 to 400 cm^{-1} at room temperature in ATR mode. FT-IR spectra of myristoyl-KPGPK lipopeptide in solid state as well as in D_2O solution were acquired. GxxxGxxxGxxxG peptides (GSNKGAIIGLMVG, Aβ_{25-37}; and GVVLGAVIGGVLG, human myelin protein zero protein precursors) at 10 μM concentration in aqueous buffer solution were incubated for 7 days at 37 °C under stirring conditions. Afterward, the formed peptide fibrils were isolated from solution by centrifugation at 12000 g for ten minutes, and the secondary structure of the peptides was monitored using FT-IR.

Circular Dichroism (CD) Spectroscopy: CD spectra were acquired on a JASCO instrument (Model J-815–150S) at 25°C. Data were recorded in a 1 mm quartz cuvette at wavelength range 190–260 nm with a 0.5 nm step, 2 s collection times per step, and 1 nm bandwidth. The CD data from the appropriate solvent as background was subtracted from the CD signal of the sample solution. 1%

TFE in deionized H_2O solution of the GxxxGxxxGxxxG (10 μM) was used for the CD experiment. The secondary structure of GSNKGAIIGLMVG and GVVLGAVIGGVLG peptides at 10 μM concentration in 1% TFE in deionized H_2O solution was monitored at the initial stage (0 hours) and after aged for 7 days at 37°C. CD of GSNKGAIIGLMVG and GVVLGAVIGGVLG peptides were also performed in the presence of the inhibitor myristoyl-KPGPK lipopeptide-based nanovesicles. CD of GSNKGAIIGLMVG and GVVLGAVIGGVLG peptides were also accomplished in the presence of the control molecules KPGPK and myristic acid. The average of three spectra was used for each measurement.

X-Ray Powder Diffraction: GSNKGAIIGLMVG and GVVLGAVIGGVLG peptide solutions (10 μM) were prepared in aqueous phosphate buffer (pH 7.4) and aged for 7 days prior to the X-ray diffraction experiment. Afterward, the formed peptide fibrils were isolated from solution by centrifugation at 12000 g for ten minutes. The X-ray diffraction from the dried fibers of GSNKGAIIGLMVG and GVVLGAVIGGVLG peptides was recorded on a Bruker D8 Advance X-ray diffractometer using Cu Kα radiation (λ = 1.5418 Å) operating at 40 kV and 40 mA.

General Procedure for Preparation of Sample Solutions for FE-SEM, TEM, and AFM: 1 mg of myristoyl-KPGPK lipopeptide as well as GSNKGAIIGLMVG and GVVLGAVIGGVLG peptides were dissolved separately in 1% TFE in deionized H_2O solution. These solutions were diluted with deionized H_2O to make a final concentration of 10 μM each. GSNKGAIIGLMVG and GVVLGAVIGGVLG peptide solutions were aged for 72 h prior to FE-SEM and TEM experiments. The stock solutions were prepared freshly for each of the experiments.

Field Emission Scanning Electron Microscopy (FE-SEM): The morphology of the myristoyl-KPGPK lipopeptide as well as GSNKGAIIGLMVG and

GVVLGAVIGGVLG peptides were characterized using FE-SEM. 10 μL of myristoyl-KPGPK lipopeptide as well as GSNKGAIIGLMVG and GVVLGAVIGGVLG peptide stock solutions (10 μM) were individually drop-cast on a glass cover slip and permitted to dry completely in air at room temperature. Samples were coated with gold, and the images were achieved in INSPECT F50 as well as Zeiss Scanning Electron Microscope instruments with a 10 kV and 5 kV accelerating voltage, respectively.

Transmission Electron Microscopy (TEM): 10 μL of freshly prepared stock solutions of the myristoyl- KPGPK lipopeptide (10 μM) as well as GSNKGAIIGLMVG (10 μM) and GVVLGAVIGGVLG (10 μM) peptides were separately drop-cast on 300 mesh carbon-supported copper grids and waited for 2 min, followed by blotting with filter paper to remove the excess fluid. Finally, for negative staining, an aqueous solution of uranyl acetate [2 % (w/v), 10 μL] was dropped on the grid and waited for 30 s, followed by blotting with filter paper. The grid was allowed to dry absolutely in air, then vacuum dried for 1 day. For the fibril inhibition study, GSNKGAIIGLMVG (10 μM) and GVVLGAVIGGVLG (10 μM) peptides were incubated in the absence or presence of various concentrations of myristoyl-KPGPK lipopeptide with continuous stirring. TEM images of myristoyl-KPGPK lipopeptide as well as GSNKGAIIGLMVG and GVVLGAVIGGVLG peptides in the absence or presence of myristoyl-KPGPK lipopeptide were recorded on a JEM-2100F Field Emission Electron Microscope (JEOL) instrument with an acceleration voltage of 200 kV equipped with a Gatan CCD 2K × 2K camera.

Atomic Force Microscopy: 10 μL of myristoyl-KPGPK stock solution (10 μM) was drop-cast on a freshly cleaved mica film and allowed to dry completely in air for 24 hours before imaging. AFM images were captured on a

KEYSIGHT TECHNOLOGIES 5500 AFM instrument (model no: Pico5500), and the images were processed by PicoView 1.10.1 software.

Dynamic Light Scattering (DLS): DLS experimentations were achieved on a Malvern instrument (Malvern, UK) to inspect the hydrodynamic diameter of the nanovesicles formed by myristoyl-KPGPK lipopeptide in solution. A monodisperse population of the myristoyl-KPGPK lipopeptide based nanovesicles with hydrodynamic diameter of 76 nm and PDI of 0.23 was noticed in deionized water. DLS of the GxxxGxxxGxxxG motif was also performed in the absence or presence of the myristoyl-KPGPK lipopeptide. All measurements were performed at a backscattering angle of 173° at 25°C. Three runs were recorded, and the average was taken.

Congo Red Binding Studies: UV/vis absorption spectra were recorded using Congo Red (a universal diagnostic of amyloid structure) incubated with GSNKGAIIGLMVG (10 μM) and GVVLGAVIGGVLG(10 μM) peptides at different pH values. The broad red-shifted (18 nm) UV-vis absorbance maximum of CR was (λ_{max} shifted from 486 nm to 504 nm from pH 9.0 to 4.5 in ca. 1 h time) from pH 9.0 to 4.5 in the presence of GSNKGAIIGLMVG and GVVLGAVIGGVLG peptides, supporting the existence of a common CR binding mode and amyloid aggregation.[42]

Thioflavin T (ThT) Assay: A stock solution of ThT (50 μM) in PBS (pH 7.4) buffer was prepared and stored at 4°C with appropriate protection to avoid degradation from light. A solution of GSNKGAIIGLMVG (10 μM) as well as GVVLGAVIGGVLG (10 μM) peptides in 20 mmol phosphate buffer (pH 7.4) was prepared. Aliquots of the peptide solution and concentrated solution of ThT were mixed to a solution of 20 mmol phosphate buffers (pH 7.4). For inhibition studies, GSNKGAIIGLMVG (10 μM) and GVVLGAVIGGVLG (10 μM) peptides alone and with inhibitor lipopeptide-based nanovesicles (10 μM)

in PBS (pH 7.4) were incubated at 37°C on a water bath. Fluorescence λ_{em} of ThT was recorded at 485 nm with λ_{ex} at 440 nm. The data were collected at 5 min intervals for 250 min. Three independent experiments were performed for each ThT experiment. Kinetic curves were fitted using the sigmoidal curve fitting. Error bars in **Figure 3(b)** denote standard deviations from the mean of three independent experiments. All samples were stirred continuously using a micro stir bar. ThT assays of GSNKGAIIGLMVG and GVVLGAVIGGVLG (10 μM) peptide aggregation displayed a sigmoidal curve including three phases: lag phase, growth phase, and equilibrium phase. The lag phase normally resembles a lack of mature fibrils; the rapid growth phase designates growing fibril concentration.[43] Lastly, the aggregation process reached equilibrium phase when the maximum of GSNKGAIIGLMVG and GVVLGAVIGGVLG peptides were transformed into mature fibrils.

Preparation of FRET solution: First, Cy-3-Aβ_{25-37} (FRET donor, 0.5 mg) and Cy-5-Aβ_{25-37} (FRET acceptor, 0.5 mg) were dissolved separately in 1 mL HFIP in a centrifuge tube. An equimolar solution of each compound was mixed in three separate tubes, and a stream of N_2 was passed through the solution until complete evaporation of HFIP. The residue of the first two tubes was dissolved in PBS (pH 7.4) (10 μM Cy- 3-Aβ_{25-37} and 10 μM Cy-5-Aβ_{25-37}) whereas the third one was dissolved in PBS containing lipopeptide (10 μM), and the emission spectra of all the solutions were taken at various time intervals.

Fluorescence Lifetime Measurement: The fluorescence lifetimes (τ) of Cy-3-Aβ_{25-37} and Cy-5-Aβ_{25-37} were determined using the time-correlated single photon counting (TCSPC) technique by the Horiba DeltaFlex lifetime machine (Horiba Jobin Yvon IBH Ltd, Glasgow, UK). 510 nm (Model: DD-510L, Horiba Scientific) and 650 nm (Model: DD-650L, Horiba Scientific) Delta

diode laser excitation sources were used to record the τ of Cy-3-Aβ_{25-37} and Cy-5-Aβ_{25-37}, respectively, in DMSO as well as in PBS. Horiba EzTime decay analysis software was used for data analyses and τ measurements.

Quantum Yields of Unsymmetrical Cy-3-Aβ_{25-37} and Cy-5-Aβ_{25-37}: Fluorescence quantum yields (Φ_f) of Cy-3-Aβ_{25-37} and Cy-5-Aβ_{25-37} were calculated by the relative method. The integrated fluorescence intensities of Cy-3-Aβ_{25-37} and Cy-5-Aβ_{25-37} substances were compared with emission intensities of reference molecules by the succeeding equation:

Φ_f (x) = Φ_f (st) × [(A_{st} × F_x × $\eta_x{}^2$) /(A_x × F_{st} × $\eta_{st}{}^2$)]

Φ_f (st): fluorescence QY of the reference molecules

Φ_f (x): fluorescence QY of the synthesized molecules

A_{st} : Absorbance of reference compound at the λ_{ex}

A_x: Absorbance of synthesized compound at the λ_{ex}

F_{st}: Integrated fluorescence areas under the corrected fluorescence spectra for the reference

F_x: Integrated fluorescence areas under the corrected fluorescence spectra for the synthesized compound η_{st} and η_x: Refractive indices of the solvents in which the reference and synthesized compounds were recorded, respectively [here, ($\eta_x{}^2$ / $\eta_{st}{}^2$) = 1].

"st" signifies to the standard and "x" describes the synthesized compound.

Φ_f (st) of Rhodamine-B in absolute EtOH is 0.49 and used as the reference for Cy-3-Aβ_{25-37}.

Φ_f (st) of Zinc pthalocyanine = 0.20 in DMSO, which is used as the reference for Cy-5-Aβ_{25-37}.

Isothermal titration calorimetry (ITC): ITC experiments were conducted on a MicroCal PEAQ-ITC microcalorimeter (Malvern). ITC directly quantifies the heat released or absorbed in a biomolecular binding event in solution and determines the binding affinity and thermodynamic properties of biomolecular interactions in a single experiment, helping to gain a deeper understanding of binding mechanisms and why interactions occur. Binding affinity (K_D), reaction stoichiometry (n), and thermodynamic parameters [enthalpy (ΔH) and entropy (ΔS)] reveal the forces that guide biomolecular interactions and can also illustrate function as well as mechanism at a molecular level. The solution of the Aβ_{25-37} was prepared in nanopure water and filtered using 0.2 μm syringe filters prior to the experiment. The reference cell was filled with the nanopure water. 280 μL of Aβ_{25-37} (20 μM) in nanopure water was kept in the sample cell, and the 7.5 times more concentrated lipopeptide-based nanovesicles (150 μM) in nanopure water was filled in the syringe. In each experiment, 2 μL × 19 injections with a total volume of 38 μL of lipopeptide-based nanovesicles were delivered into a solution of Aβ_{25-37} with a duration of 4 s each injection and 150 s spacing between two injections, and mixing was carried out by stirring the syringe at a speed of 750 rpm at 25°C. The titration experiments were repeated in triplicate at 25°C, and for each case, nearly identical results were obtained. Blank titrations (control runs) were conducted by injecting of nanopure water into nanopure water, nanovesicles into nanopure water, and Aβ_{25-37} dilution was subtracted from Aβ_{25-37}/nanovesicles titration. Binding enthalpy was acquired by fitting the corrected data to a proper

binding model. A titration curve of kcal/mol against molar ratio (nanovesicles/Aβ_{25-37}) was plotted. The upper panels display the raw data for the Aβ_{25-37}/nanovesicles titration, and the bottom panels represent the binding isotherm by plotting integrated peak areas against the molar ratio for titration. The resultant isotherm is best fitted to a binding model to obtain the binding affinity (K_D), stoichiometry (n), enthalpy (ΔH), entropy (ΔS), and ΔG of interaction. The ITC data and profiles were analyzed using MicroCal PEAQ-ITC Analysis Software to determine the heat of interaction as well as thermodynamic parameters.

Docking Studies : The molecular docking study was accomplished using AutoDock 4.2 with the standard method described in the user manual.[41] Here, genetic algorithms with an 80 x 80 x 80 grid box were used for the calculations. For picturing the docking results, Discovery Studio Client 2017 was used. Molecular docking was used to identify and recognize the interaction of myristoyl-KPGPK lipopeptide with Aβ_{1-42} (PDB: 5OQV). Myristoyl-KPGPK lipopeptide binds with Aβ_{1-42} through hydrogen bonding, electrostatic interactions, and hydrophobic interactions with various amino acid residues with ΔG = –6.2 kcal/mol. Molecular docking of the lipopeptide myristoyl-KPGPK with Aβ_{1-42} displays noncovalent interactions between the Gly33, Leu34, Ile32, His14, and Val12 moieties of Aβ_{1-42} with myristoyl-KPGPK.

Cell Culture : Mouse Neuro-2a (N2A) neuroblastoma cells were cultured in DMEM (pH 7.4) supplemented with 10% FBS and antibiotic-antimycotic solution 100×(containing 10000 units penicillin,
10 mg streptomycin, and 25 μg amphotericin B per mL in 0.9% normal saline) in a humidified atmosphere with 5% CO_2 at 37°C and was routinely passaged.

Neuronal Cell Viability Assay: The cytotoxicity of the myristoyl-KPGPK lipopeptide- based nanovesicles as well as GSNKGAIIGLMVG and GVVLGAVIGGVLG peptides on the mouse Neuro-2a (N2A) neuroblastoma cell line was tested by a 3-(4,5-dimethylthiazol-2-yl)-2,5-diphenyltetrazolium bromide (MTT) assay. Myristoyl-KPGPK, GSNKGAIIGLMVG, and GVVLGAVIGGVLG were predissolved in Dulbecco's PBS (D-PBS) buffer (pH 7.4) solution at various concentrations (0.5, 1, 2, 5, 10, and 15 μM). N2A cells were grown and seeded at a density of ~10^4 cells in a 96-well plate and incubated in DMEM at 37°C for 24 h. Subsequently, after 24 h of incubation, myristoyl-KPGPK-based nanovesicles, GSNKGAIIGLMVG, and GVVLGAVIGGVLG peptides were separately treated at various doses (0.5, 1, 2, 5, 10, and 15 μM per well) for 72 h at 37°C. N2A cells were then separately incubated with 10 μL solution of MTT (5 mg mL^{-1} in PBS) for 4 hours in darkness at 37°C. In another set of cell viability assays, GSNKGAIIGLMVG and GVVLGAVIGGVLG peptides (10 μM) were separately co-incubated with the different doses (0.5, 1, 2, 5, 10, and 15 μM) of myristoyl-KPGPK lipopeptide-based nanovesicles in N2A cells (~10^4 cells) for 72 h at 37°C. Subsequently, N2A cells were separately incubated with a 10 μL solution of MTT (5 mg mL^{-1} in PBS) for 4 hours in darkness at 37°C. In individual MTT assay, formazan crystals (purple color) in the wells were dissolved by adding DMSO and the absorbance (*A*) at 575 nm was recorded (measured in triplicate) by an ELISA plate reader. The outcomes were defined by the subsequent equation:

Cell Viability (%) = (*A* of treated cells / *A* of untreated cells) × 100

Synthesis of Myristoyl-KPGPK Lipopeptide, GxxxGxxxGxxxG Peptides (GSNKGAIIGLMVG and GVVLGAVIGGVLG), Cy-3-GSNKGAIIGLMVG, and Cy-5-GSNKGAIIGLMVG

Manual MW Assisted Solid-Phase Peptide Synthesis (SPPS): Myristoyl-KPGPK lipopeptide, GSNKGAIIGLMVG, and GVVLGAVIGGVLG peptides, as well as Cy-3-GSNKGAIIGLMVG (Cy-3-Aβ_{25-37}) and Cy-5-GSNKGAIIGLMVG (Cy-5-Aβ_{25-37}) conjugates, were synthesized by manual microwave (MW)-assisted 9-fluorenyl-methoxycarbonyl (Fmoc) solid phase peptide synthesis (Fmoc-SPPS) protocol on Wang resin (LL, 0.60 mmol/g loading density) by a MW peptide synthesizer (*CEM, Discover Bio*). The synthesis of the lipopeptide myristoyl-KPGPK was performed using a MW-assisted solid-phase peptide synthesizer at a 0.1 mmol scale on the Wang resin (LL, 0.60 mmol/g loading density). The myristic acid and the following Fmoc amino acid building blocks: Fmoc-Lys(Boc)-OH, Fmoc-Pro-OH, and Fmoc-Gly-OH were used as 0.2 M solutions in DMF to synthesize myristoyl-KPGPK. The synthesis of GSNKGAIIGLMVG and GVVLGAVIGGVLG peptides was performed using a MW-assisted solid-phase peptide synthesizer at a 0.1 mmol scale. The following Fmoc-protected amino acid building blocks: Fmoc-Gly-OH, Fmoc-Ser(tBu)-OH, Fmoc-Asn(Trt)-OH, Fmoc-Lys(Boc)-OH, Fmoc-Ala-OH, Fmoc-Ile-OH, Fmoc-Leu-OH, Fmoc-Met-OH, and Fmoc-Val-OH were used as 0.2 M solutions in DMF to synthesize GSNKGAIIGLMVG and GVVLGAVIGGVLG peptides. For peptide coupling, 5 eq. of the Fmoc-amino acid building blocks were pre-activated with HBTU (4.9 eq.), HOBt (5 eq.), and DIPEA (10 eq.) in DMF.

Handling of Resins and Fmoc Amino Acid Building Blocks : Fmoc amino acid building blocks were stored at −18 ºC. Resins were stored at 4 ºC. Before

opening, all the Fmoc amino acid building blocks and resins were warmed to room temperature for 20 minutes.

First Amino Acid Loading on Wang Resin: For the synthesize of myristoyl-KPGPK, the first amino acid Fmoc-Lys(Boc)-OH loading on Wang resin (LL, 0.60 mmol/g loading density) was performed in a SPE cartridge with frit. For the synthesize of GSNKGAIIGLMVG and GVVLGAVIGGVLG peptides, the first amino acid Fmoc-Gly-OH loading on Wang resin was performed in the same protocol. The Wang resin (0.1 mmol) was swollen in 2 mL DMF for 1 h, then drains the solvent off and washed with DMF (2×). Fmoc-Lys(Boc)-OH (5 eq) or Fmoc-Gly-OH (5 eq), HBTU (4.9 eq.), and HOBt (5 eq.) were dissolved in 2 mL of DCM/DMF (1:1), then DIPEA (10 eq.) was added, and the mixture was taken in the SPE cartridge containing the Wang resin and stirred for 3 h under N_2 bubbling. Drain the solvent, and the resin was sequentially washed with DMF (2×), DCM (2×), and MeOH (2×). After Fmoc-Lys(Boc)-OH or Fmoc-Gly-OH loading on Wang resin, the loading density was calculated by UV/vis analysis of the Fmoc-dibenzofulvene deprotection product.

Estimation of the Loading Density of First Amino Acid Fmoc-Lys(Boc)-OH or Fmoc-Gly-OH on Wang resin: The Fmoc-Lys(Boc)-Wang or Fmoc-Gly-Wang resin (5 mg) and 1,8-diazabicyclo[5.4.0]undec-7-en (DBU) in NMP (2 mL, 2 % in NMP) were taken in a volumetric flask (10 mL). It was stirred for 30 min in a shaker, and the volumetric flask (10 mL) was filled up to the mark with CH_3CN. The solution was diluted with CH_3CN (1/12.5) and transported to an UV quartz cuvette. The cleaved dibenzofulvene was recorded at 304 nm (ε_{304} = 7624 L mol^{-1} cm^{-1}) and compared against reference. The first

amino acid Fmoc-Lys(Boc)-OH or Fmoc-Gly-OH loading on the Wang resin was calculated based on Lambert-Beer's law.

m : mass of the analyzed resin in mg.

MW-Assisted SPPS Synthesis of Myristoyl-KPGPK Lipopeptide as well as GSNKGAIIGLMVG and GVVLGAVIGGVLG Peptides: The synthesis of myristoyl-KPGPK lipopeptide as well as GSNKGAIIGLMVG and GVVLGAVIGGVLG peptides was carried out using MW-assisted Fmoc-SPPS protocol at a 5 μmol scale.

Protocols for MW-Assisted SPPS:

Before starting the GSNKGAIIGLMVG and GVVLGAVIGGVLG peptide synthesis, the 5 μmol Fmoc-Lys(Boc)-Wang (LL) and Fmoc-Gly-Wang Resins (LL) were individually swollen in DMF (2 mL) for 2 h.

1. Bubbling during the MW-assisted synthesis for all steps: on 3 sec; off 7 sec.
2. **Fmoc deprotection**: 20% piperidine/DMF; time 210 sec, power 20 W, temperature 75ºC, delta temperature 5ºC.

   Washing after Fmoc-deprotection: DMF (4×), DCM (4×), and DMF (4×) to remove dibenzofulvene by-product.
3. **Coupling**: 0.5 M HBTU/0.5 M HOBt/2 M DIPEA/DMF; time 300 sec, power 20 W, temperature 75ºC, delta temperature: 5ºC.

   Washing after coupling: DMF (3×), DCM (3×), DMF (3×)

After the final step, the resin was transferred to a SPE cartridge with frit and washed with DMF (5×),DCM (5×), MTBE (5×), and finally with MeOH (5×). The resins were dried in vacuum and stored at –18°C.

Test Cleavage from Wang Resin: To a pinch of the resin, a mixture of TFA/TIPS/EDT (92.5/5.0/2.5 *v*/*v*) [trifluoroacetic acid (TFA), triisopropylsilane (TIPS), and 1,2-ethanedithiol (EDT)] was added, and the cleavage reaction was performed by shaking the resin for 2 h at room temperature. Afterward, the resin beads were filtered off, and the solvent was evaporated under N_2 stream. The myristoyl-KPGPK lipopeptide as well as GSNKGAIIGLMVG and GVVLGAVIGGVLG peptides were precipitated by using ice-cold MTBE. The MTBE suspension was centrifuged at −5°C, the supernatant was discarded, and the process was repeated three times. The supernatant was discarded, and the residue was washed with cold MTBE (3×) and dried to obtain the desired compounds myristoyl-KPGPK, GSNKGAIIGLMVG, and GVVLGAVIGGVLG with a free carboxy (−COOH) at the C-terminus.

Fmoc-SPPS protocol for myristoyl-KPGPK lipopeptide as well as GSNKGAIIGLMVG and GVVLGAVIGGVLG peptide synthesis

Working Step	Resin	Reagents	Reaction condition
Coupling	Wang	HBTU/HOBt/DIPEA/DMF	300 sec/75°C/20 W
Washing after coupling	Wang	DMF(5×), DCM(5×), DMF(5×)	
Fmoc deprotection	Wang	20% piperidine/DMF	210 sec/75ºC/20 W
Washing after deprotection	Wang	DMF (4×), DCM (4×), DMF (4×)	
Washing after final coupling	Wang	DMF(5×), DCM(5×), MTBE(5×), MeOH(5×)	
Final Cleavage	Wang	TFA/TIPS/EDT (92.5/5.0/2.5 *v*/*v*)	2 h/25°C

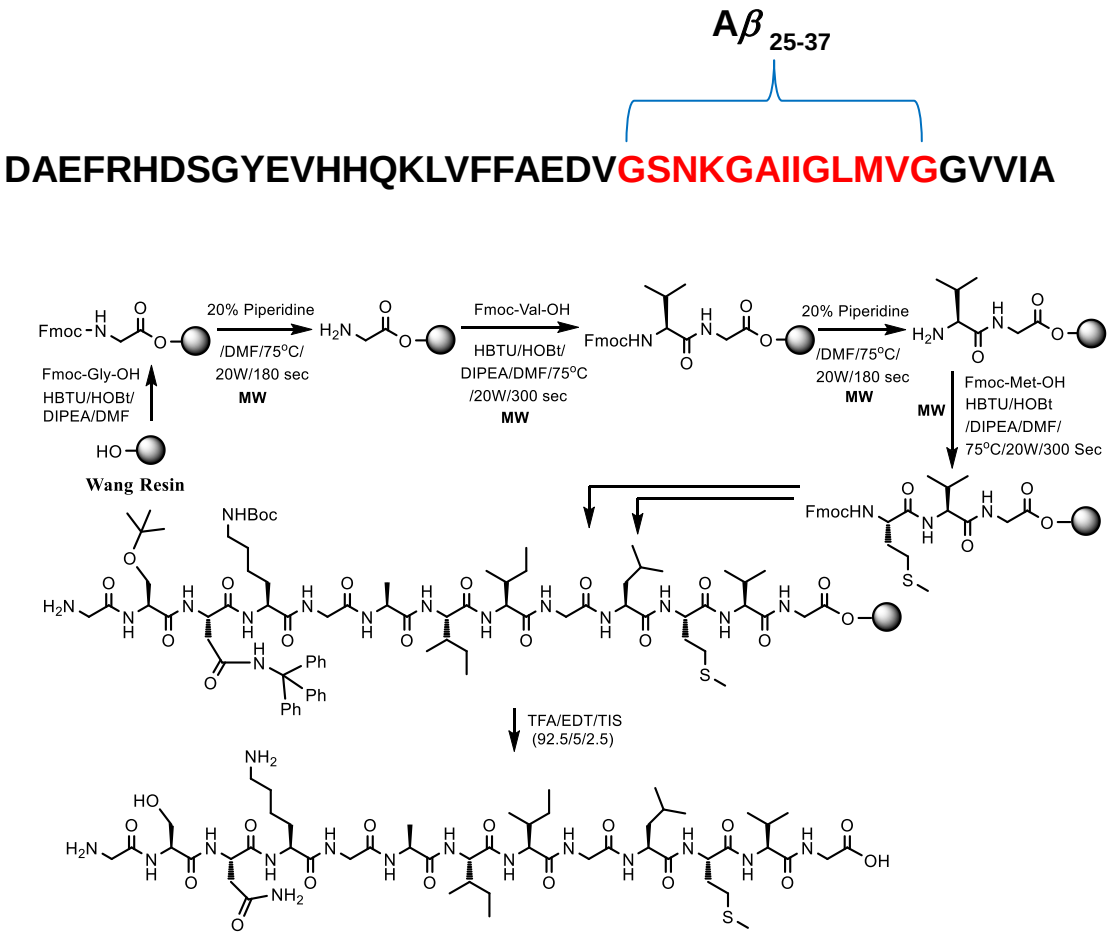

GSNKGAIIGLMVG, A$\beta_{25–37}$ (GXXXGXXXGXXXG motif of A$\beta_{1–42}$)

Figure 1. Synthesis of peptides GSNKGAIIGLMVG (A$\beta_{25–37}$) using MW assisted Fmoc-SPPS protocol on Wang resin.

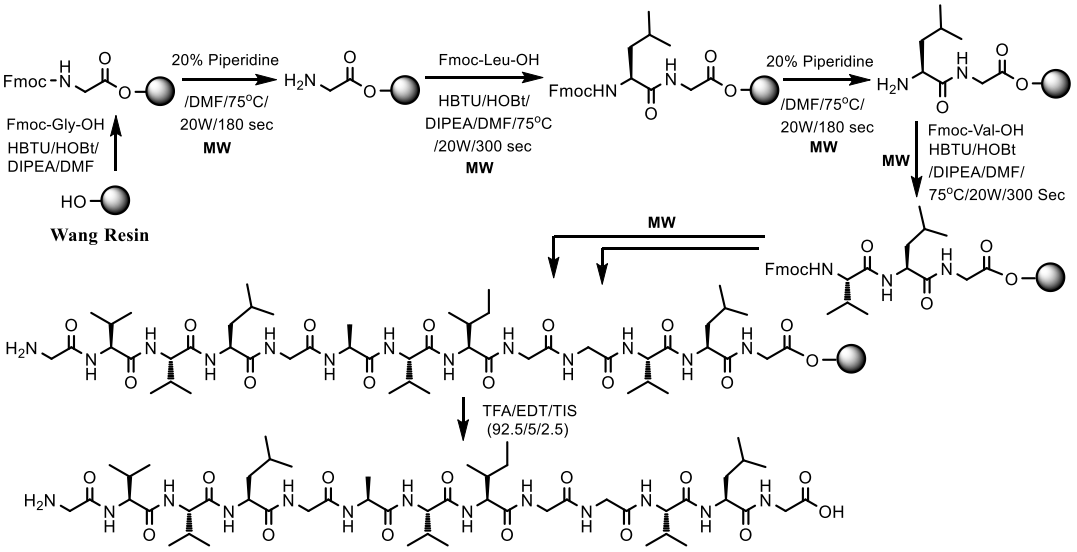

GVVLGAVIGGVLG (GXXXGXXXGXXXG motif of human myelin protein zero)

Figure 2. Synthesis of peptide GVVLGAVIGGVLG (human myelin protein zero protein precursor) using MW assisted Fmoc-SPPS protocol on Wang resin.

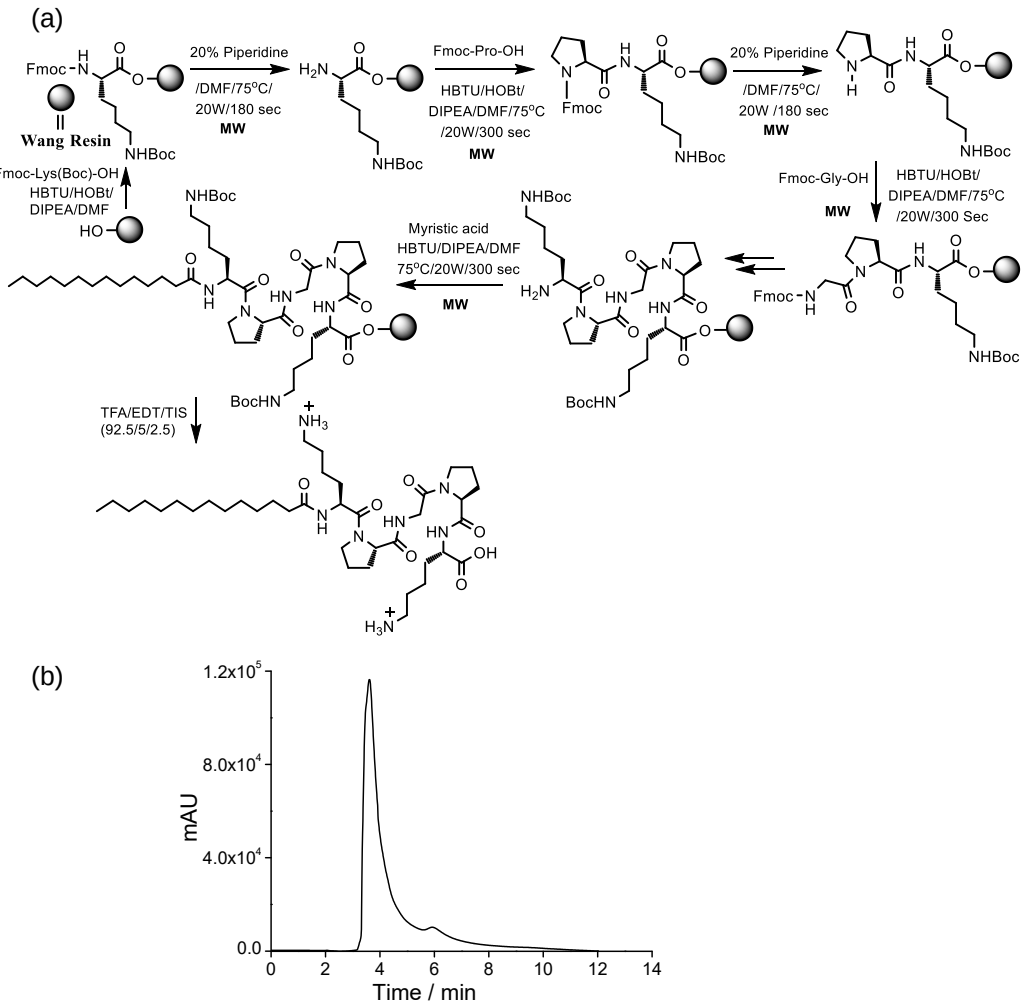

Figure 3. (a) Synthesis of myristoyl-KPGPK lipopeptide using microwave-assisted Fmoc-SPPS protocol on the Wang resin. (b) Analytical HPLC profile of myristoyl-KPGPK lipopeptide.

Peptide KPGPK:

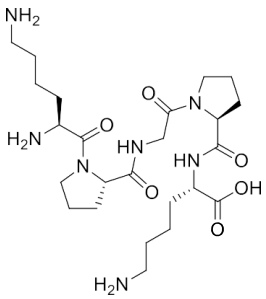

HRMS (ESI +ve) *m*/*z*: Observed for $C_{24}H_{44}N_7O_6^+$ $[M+H]^+$ = 526.3341, $[M+H]^+$calcd = 526.3348.

Lipopeptide myristoyl-KPGPK:

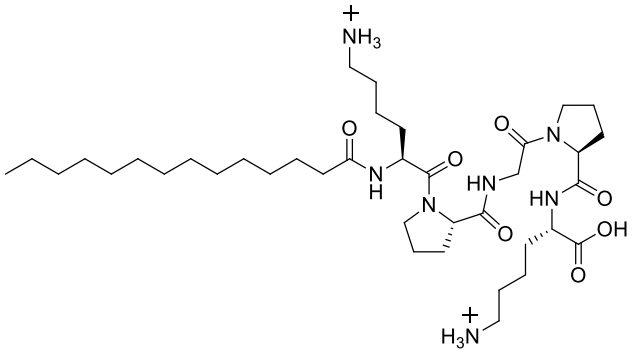

^{1}H NMR (300 MHz, DMSO-d_6, 25°C): δ = 12.61 (1H, br), 8.14 (1H, d, *J* = 6.0 Hz), 7.96–7.91 (2H, m), 7.63 (6H, br), 4.46–4.31 (2H, m), 4.15– 4.09 (1H, m), 3.96–3.91 (1H, m), 3.78 (1H, d, *J* = 6.3 Hz), 3.64 (1H, d, *J* = 6.4 Hz), 2.74–2.69 (6H, m), 2.05–2.00 (6H, m), 1.86–1.82 (6H, m), 1.51–1.45 (6H, m),1.35–1.29 (4H, q, *J* = 6.0 Hz), 1.22–1.20 (24H, m), 0.82 (3H, t, *J* = 5.1 Hz) ppm. ^{13}C NMR (75 MHz, DMSO-d_6, 25°C): δ = 174.0, 172.3, 171.0, 167.4, 65.4, 59.7, 50.3, 47.5, 40.8, 40.5, 35.4, 31.8, 29.5, 29.4, 29.2, 29.1, 26.8, 25.7, 22.6, 14.4 ppm. HPLC (C-18 analytical HPLC column, H_2O-CH_3CN 95:5): Retention time (t_R) = 3.6 min.

FTIR spectrum in solid state: 3279 cm^{-1} (amide A region, N–H stretching), a sharp peak at 1630 cm^{-1}(amide I region, amide CO stretching), 1538 cm^{-1} (amide II region, NH bending).

FTIR spectrum in solution: 1634 cm^{-1} (amide I region, amide CO stretching)

HRMS (ESI +ve) *m*/*z*: Observed for $C_{38}H_{70}N_7O_7^+$ $[M+H]^+$ = 736.4151, $[M+H]^+$calcd = 736.5332.

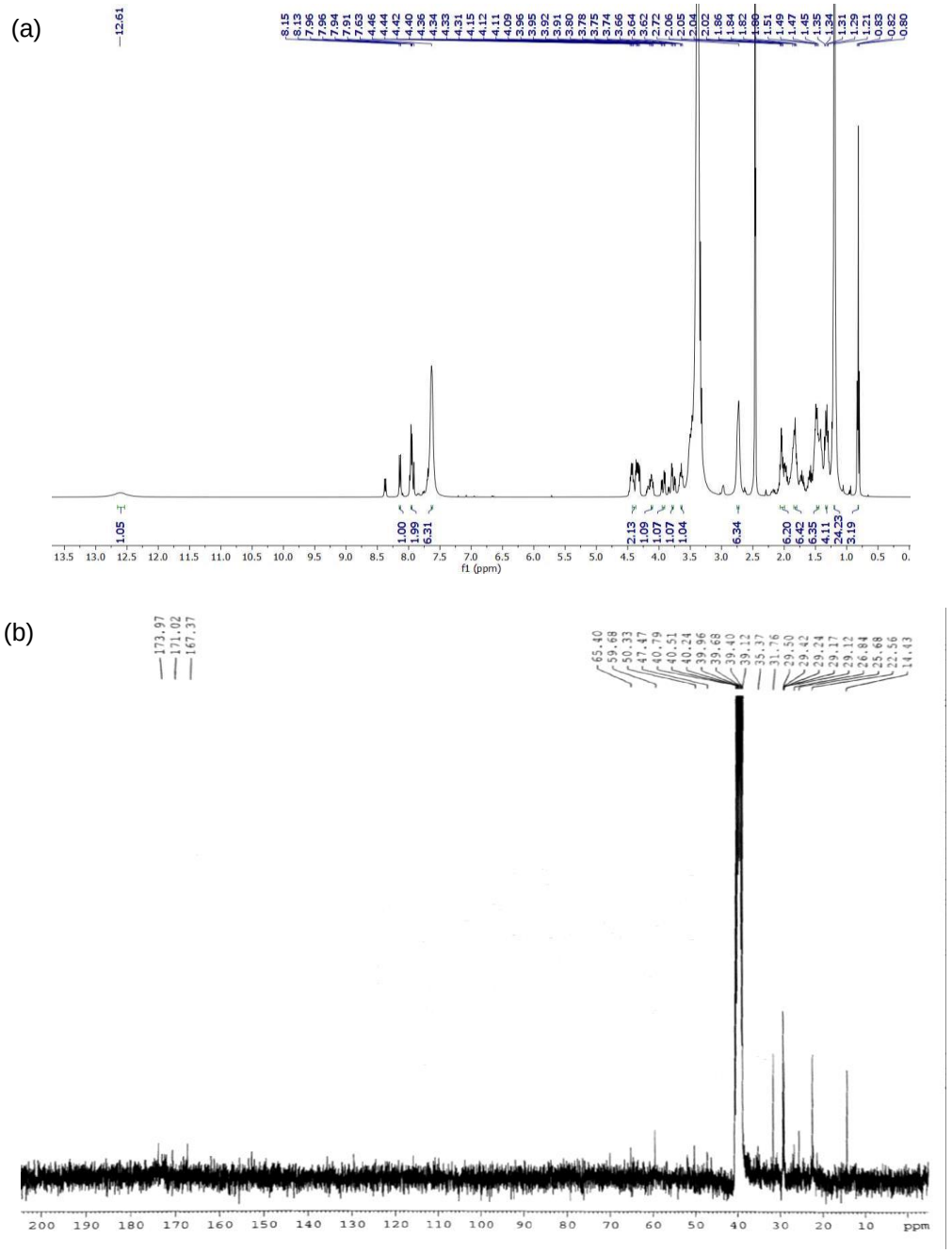

Figure 4. (a) ^{1}H NMR (300 MHz, DMSO-d_6 , 25°C) spectrum and (b) ^{13}C NMR (75 MHz, DMSO-d_6 , 25°C) spectrum of myristoyl-KPGPK lipopeptide.

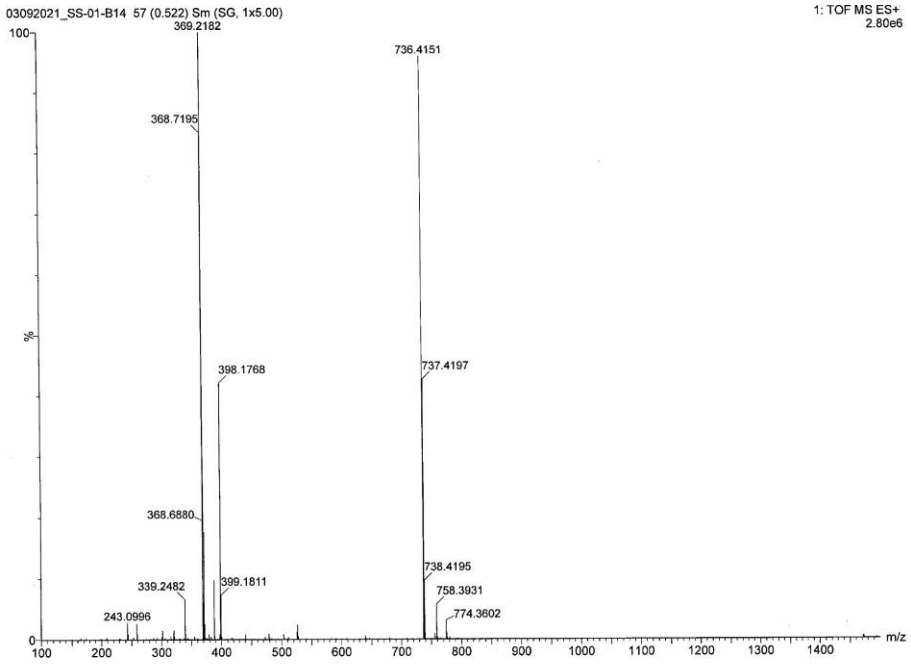

Figure 5. HRMS (ESI +ve) spectrum of myristoyl-KPGPK lipopeptide.

GSNKGAIIGLMVG peptide:

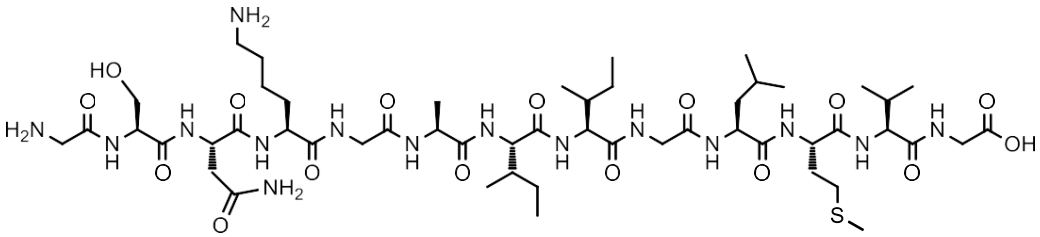

FTIR: 3280 cm^{-1} (amide A region, N–H stretching), a sharp peak at 1627 cm^{-1} (amide I region, amide COstretching), 1532 cm^{-1} (amide II region, NH bending).

HRMS (ESI +ve) *m/z*: Observed for $C_{52}H_{94}N_{15}O_{16}S^+$ $[M+H]^+$ = 1217.5781, $[M]^+$calcd = 1217.4581.

CD: Initially, CD spectrum of GSNKGAIIGLMVG (10 μM) peptide in 1% TFE in deionized H_2O solution typically displays a curve with a negative peak at 198 nm, analogous to a random coil conformation. Time dependent structural transformation in 7 days from random coil to β-sheet ellipticity, characterized by a lower wavelength positive hump at 197 nm and a higher wavelength negative maximum at 215 nm are identified as GSNKGAIIGLMVG continues to aggregate.

X-Ray fiber Diffraction: 4.7 Å (meridional reflection) and 10.9 Å (equatorial reflection).

GVVLGAVIGGVLG:

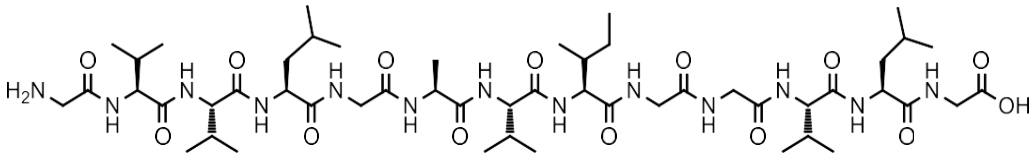

FTIR: 3275 cm^{-1} (amide A region, N–H stretching), a sharp peak at 1626 cm^{-1} (amide I region, amide CO stretching), 1526 cm^{-1} (amide II region, NH bending).

HRMS (ESI +ve) *m/z*: Observed for $C_{51}H_{92}N_{13}O_{14}^{+}$ $[M+H]^+$ = 1110.6956, $[M+H]^+$ calcd = 1110.6882; Observed for $C_{51}H_{93}N_{13}O_{14}^{2+}$ $[M+2H]^+$ = 555.8480, $[M+2H]^+$ calcd = 555.8477.

CD: The CD spectrum of GVVLGAVIGGVLG (10 μM) peptide in deionized H_2O with 1% TFE characteristically exhibits a curve with a negative peak at 198 nm corresponds to random coil that is transformed to a lower wavelength positive hump at 197 nm and the higher wavelength negative maxima at 217 nm after 7 days incubation which is characteristic for *β*-sheet secondary structure.

X-Ray fiber Diffraction: 4.7 Å (meridional reflection) and 10.9 Å (equatorial reflection).

Synthesis of unsymmetrical Cy-3 and Cy-5 dyes: All the intermediate were prepared according to the literature reported procedure.[44]

Cy-3 dye: The compound (*E*)-1-(5-carboxypentyl)-3,3-dimethyl-2-(2-(phenylamino)vinyl)-3*H*-indol-1- ium bromide (0.21 g, 0.45 mmol) was dissolved in pyridine:AcOH (1:1, 1.5 mL each) in a MW vessel equipped with a magnetic stir bar. Compound 1-Hexyl-2,3,3- trimethyl-3*H*-indol-1-ium bromide (0.17 g, 0.51 mmol) was added to it and the MW vessel was sealed with a cap and subjected to MW irradiation for 10 m at 150°C. The reaction mixture was cooled to room temperature and gets a red color residue after addition of Et_2O. The red solid was filtered and washed with Et_2O. Silica gel column chromatography was used for further

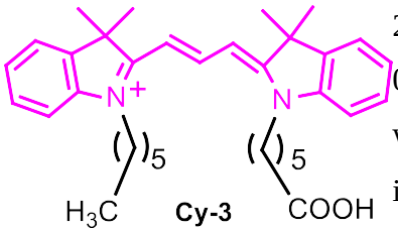

Cy-3

purification in DCM:MeOH (93:7) (R_f = 0.46, visible without staining, pink color) to obtain the desired compound **Cy-3** as a red solid.

Yield: 0.15 g (78%).

^{1}H NMR (500 MHz, DMSO-d_6, 25°C): δ = 12.0393 (1H, br), 8.3692 (1H, t, *J* = 13.5 Hz), 7.6667 (2H, d, *J* = 7.0 Hz), 7.5193–7.4256 (4H, m), 7.3288–7.2999 (2H, t, *J* = 7.5 Hz), 6.5636 (2H, d, *J* = 13.5 Hz), 4.1442 (4H, t, *J* = 6.5 Hz), 2.2326 (2H, t, *J* = 7.3 Hz), 1.7094 (12H, s), 1.5974–1.5356 (4H, m), 1.4707–1.3955 (4H, m), 1.3466–1.2739 (6H, m), 0.8857 (3H, t, *J* = 6.4 Hz) ppm. ^{13}C NMR (125 MHz, DMSO-d_6, 25°C): δ = 174.783, 174.316, 150.377, 142.342, 141.131, 129.152, 125.708, 123.010, 112.067, 103.049, 49.399, 44.308, 33.969, 31.414, 27.937, 27.496, 27.275, 26.248, 24.729, 22.461, and 14.313 ppm.

HRMS (ESI +ve) *m*/*z*: Observed for $C_{35}H_{47}N_2O_2^+$ $[M]^+$ = 527.3956, $[M]^+$calcd = 527.3633.

Photophysical properties in DMSO λ_{abs}= 554 nm, λ_{em}= 573 nm, ε = 1.06 ×10^5 $M^{-1}cm^{-1}$

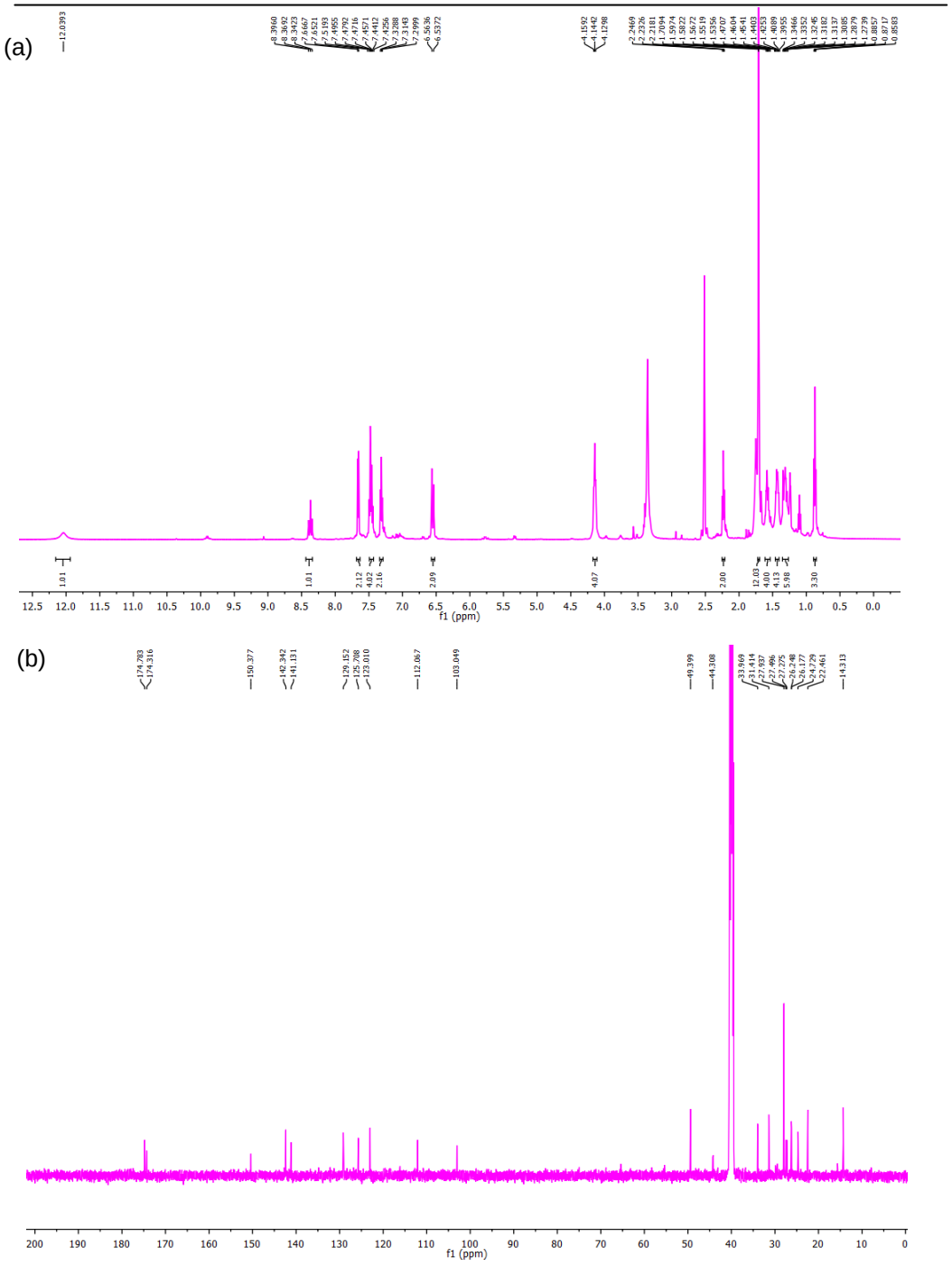

Figure 6. (a) ^{1}H NMR (500 MHz, DMSO-d_6, 25°C) spectrum and (b) ^{13}C NMR (125 MHz, DMSO-d_6, 25°C) spectrum of Cy-3.

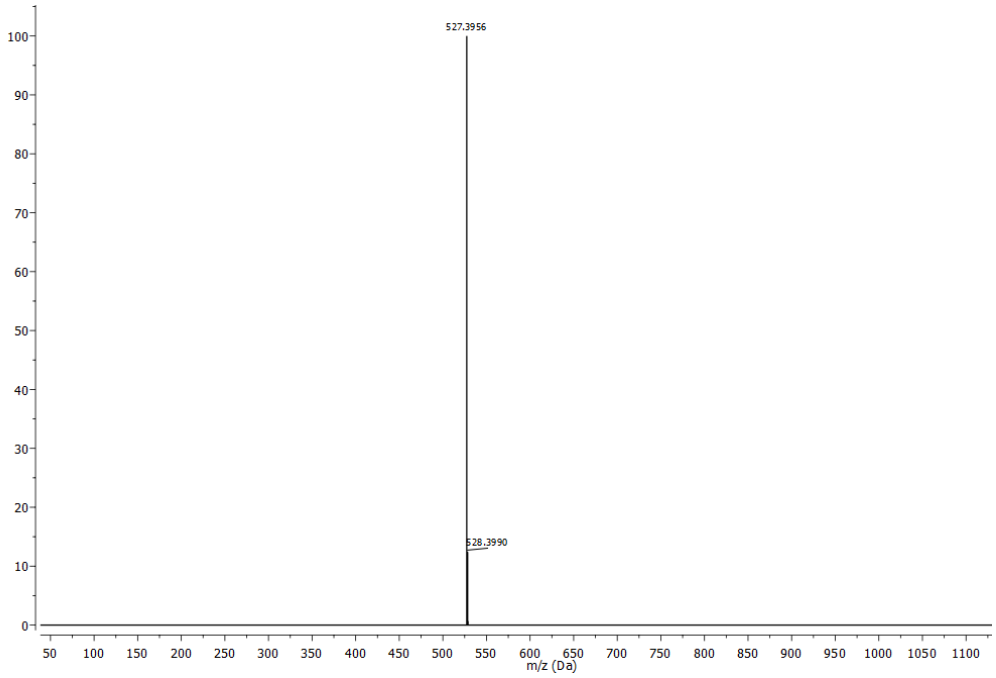

Figure 7. HRMS (ESI +ve) spectrum of Cy-3.

Cy-5 dye: The compound 1-(5-carboxypentyl)-3,3-dimethyl-2-((1*E*,3*E*)-4-(phenylamino)buta-1,3-dien-1- yl)-3*H*-indol-1-ium bromide (0.23 g, 0.45 mmol) was dissolved in pyridine:AcOH (1:1, 2 mL each) in a MW vessel furnished with a magnetic stir bar. Compound 1-Hexyl-2,3,3-trimethyl-3*H*-indol-1-ium bromide (0.17 g, 0.51 mmol) was added and the MW vessel was capped and exposed to MW irradiation at 150°C for 10 min. The reaction mixture was cooled to room temperature and gets a blue colored residueafter addition of Et_2O. The blue solid was filtered and washed with Et_2O. The crude material was purified using column chromatography by DCM:MeOH (95:5) (R_f = 0.55, blue color) to acquire the pure product **Cy-5** as a blue solid.[S4]

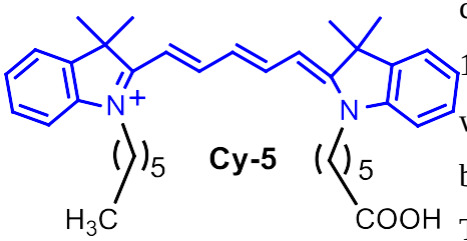

^{1}H NMR (400 MHz, DMSO-d_6, 25°C): δ = 8.3249 (2H, t, *J* = 13.1 Hz), 7.6209 (2H, d, *J* = 7.2 Hz), 7.4020–7.3681 (4H, m), 7.2633–7.2108 (2H, m), 6.5800 (1H, t, *J* = 13.4 Hz), 6.3129 (2H, d, *J* = 13.6 Hz), 4.0979–4.0606 (4H, m), 2.1839 (2H, t, *J* = 7.1 Hz), 1.6689 (12H, s), 1.6180–1.5948 (2H, m), 1.5517–1.5168 (2H, m), 1.3681–1.2223 (10H, m), 0.8533 (3H, t, *J* = 6.4 Hz) ppm.^{13}C NMR (100 MHz,DMSO-d_6, 25°C): δ = 174.262, 172.573, 153.948, 141.948 , 141.046 , 128.365, 125.525, 124.626, 122.379, 111.034 , 103.117 , 48.836, 43.236, 35.718, 33.489, 30.797, 27.103, 26.807, 26.617, 25.627, 24.155, 21.886, and 13.737 ppm.

HRMS (ESI +ve) *m*/*z*: Observed for $C_{37}H_{49}N_2O_2^+$ $[M]^+$ = 553.3744, $[M]^+$calcd =553.3789. Photophysical properties in DMSO λ_{abs}= 650 nm, λ_{em}= 672 nm, ε = 1.19 ×10^5 $M^{-1}cm^{-1}$

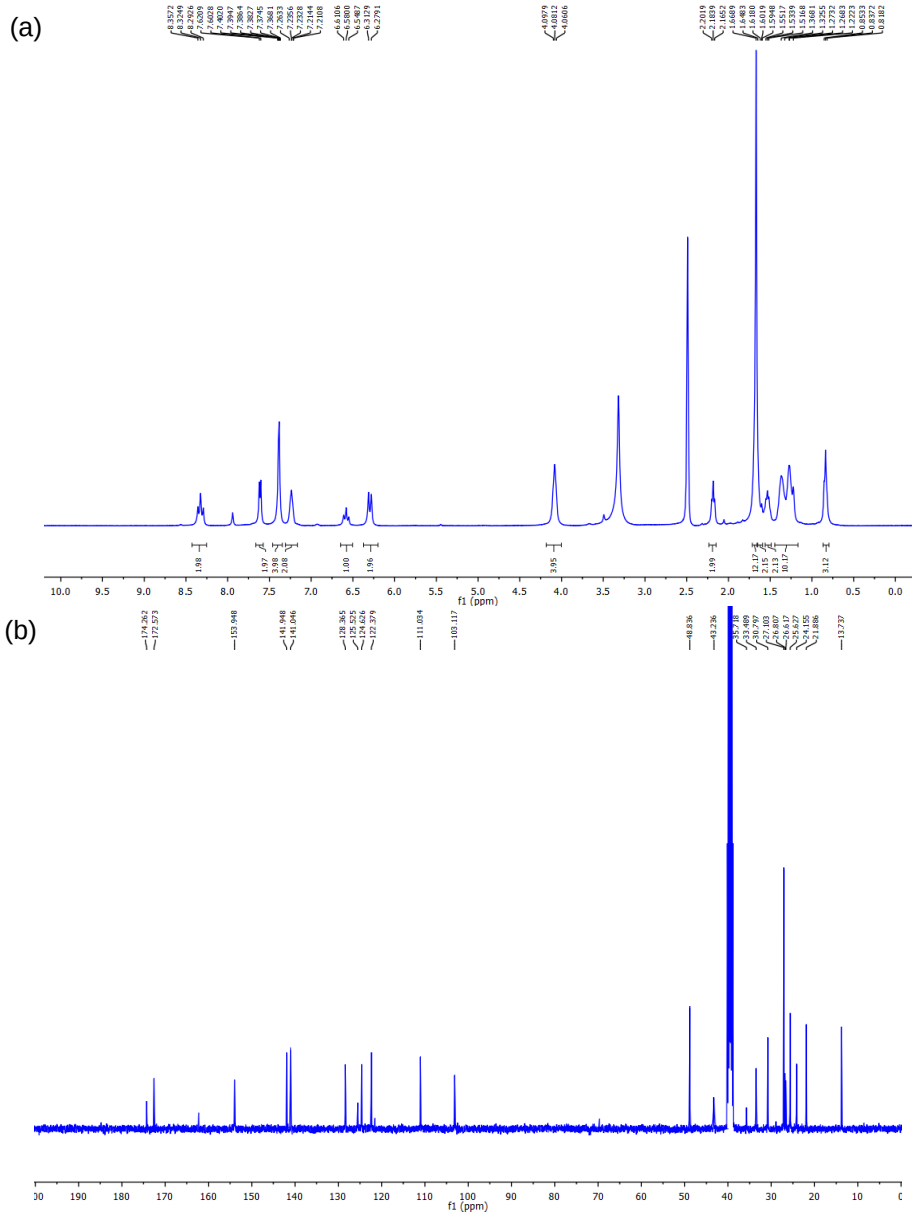

Figure 8. (a) ^{1}H NMR (400 MHz, DMSO-d_6, 25°C) spectrum and (b) ^{13}C NMR (100 MHz, DMSO-d_6, 25°C) spectrum of Cy-5.

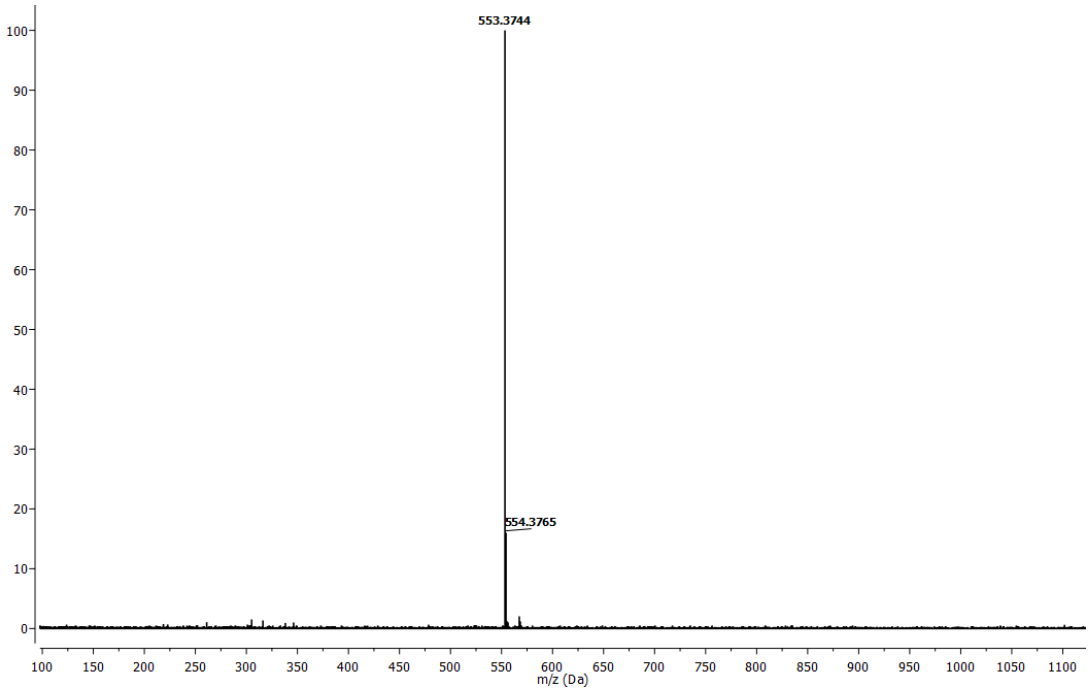

Figure 9. HRMS (ESI +ve) spectrum of Cy-5.

Cy–3-GSNKGAIIGLMVG (Cy-3-A$\beta_{25–37}$) conjugate:

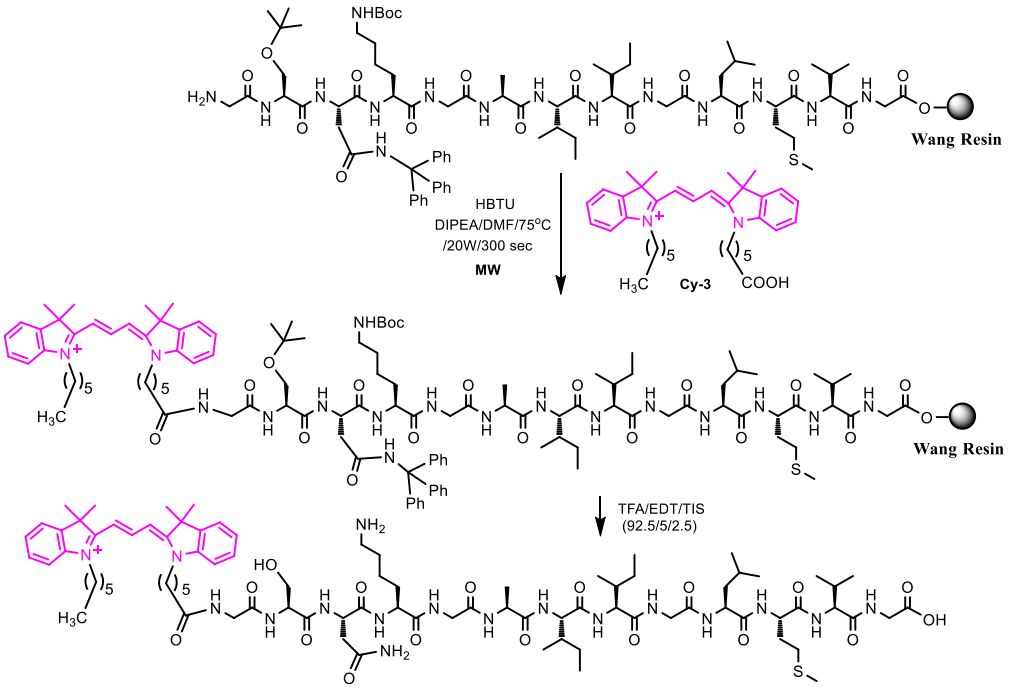

Figure 10. Synthesis of Cy-3-GSNKGAIIGLMVG (Cy-3-A$\beta_{25–37}$) using MW assisted Fmoc-SPPS protocol on Wang resin.

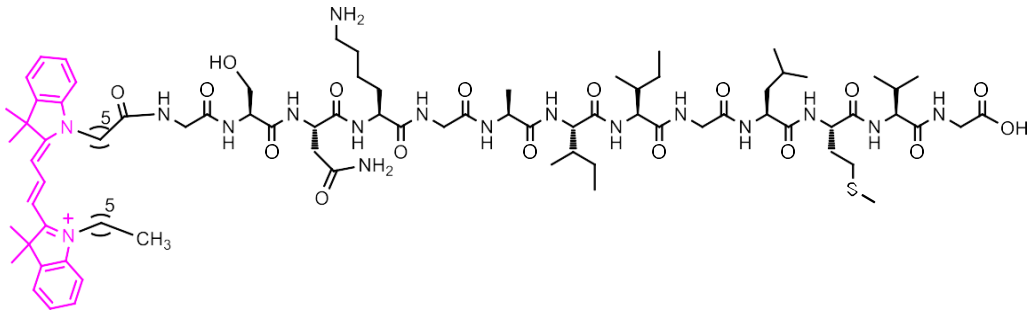

HRMS (ESI +ve) *m/z*: Observed for $C_{87}H_{139}N_{17}O_{17}S^{2+}$ $[M]^{2+}$ =863.0132, $[M]^{2+}$calcd = 863.0123.

Photophysical properties in DMSO: λ_{abs}= 554 nm, λ_{em}= 572 nm, Stokes shift ($\Delta\lambda$) = 18 nm, ε = 1.50 ×10^5 $M^{-1}cm^{-1}$. Φ_f = 0.28 in EtOH [Φ_f of Rhodamine-B (reference) in absolute EtOH = 0.49], Fluorescence lifetime (τ) = 0.14 ± 0.01 ns in PBS and 0.55 ± 0.01 ns in DMSO.

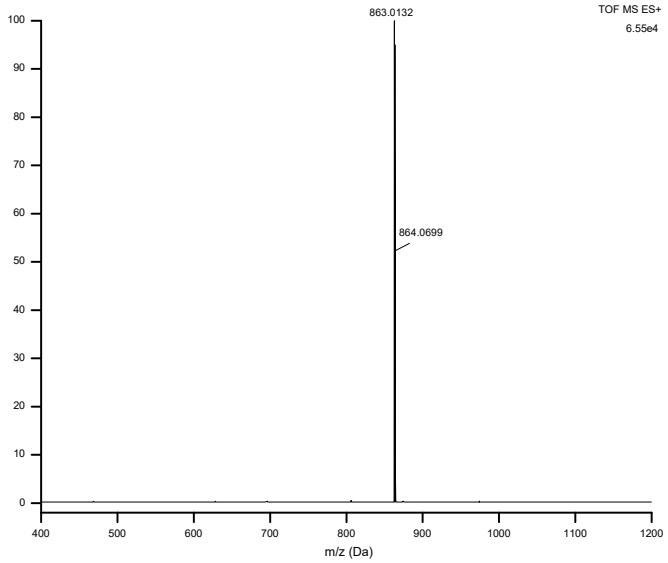

Figure 11. HRMS (ESI +ve) spectrum of Cy-3-GSNKGAIIGLMVG (Cy-3-Aβ_{25-37}).

Cy–5-GSNKGAIIGLMVG (Cy-5-Aβ_{25-37}) conjugate:

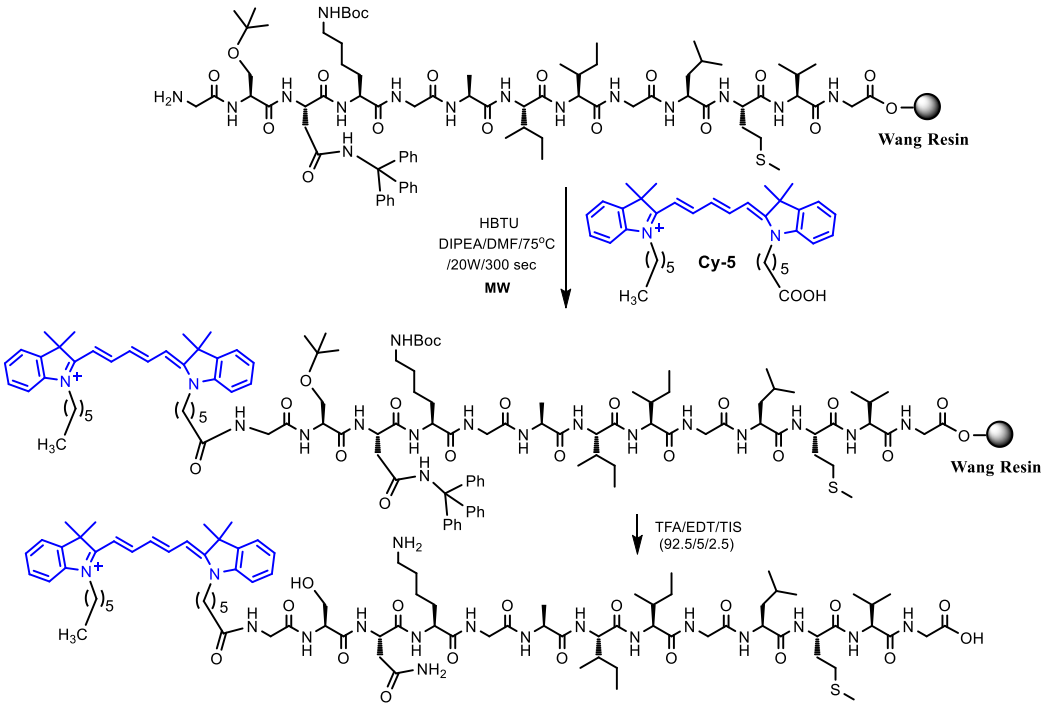

Figure 12. Synthesis of Cy-5-GSNKGAIIGLMVG (Cy-5-Aβ_{25-37}) using MW assisted Fmoc-SPPS protocol on Wang resin.

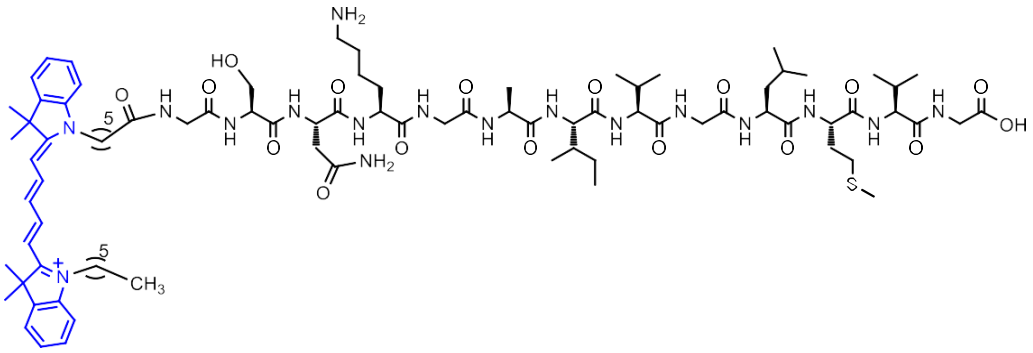

HRMS (ESI +ve) *m/z*: Observed for $C_{89}H_{141}N_{17}O_{17}S^{2+}$ $[M]^{2+}$ = 876.0213, $[M]^{2+}$calcd = 876.0201.

Photophysical properties in DMSO: λ_{abs}= 650 nm, λ_{em}= 671 nm, Stokes shift ($\Delta\lambda$) = 21 nm, ε = 2.2 ×10^5 $M^{-1}cm^{-1}$. Φ_f = 0.47 [Φ_f of Zinc pthalocyanine (reference) in DMSO = 0.20], Fluorescence lifetime (τ) = 0.51 ± 0.01 ns in PBS and 2.55 ± 0.06 ns in DMSO.

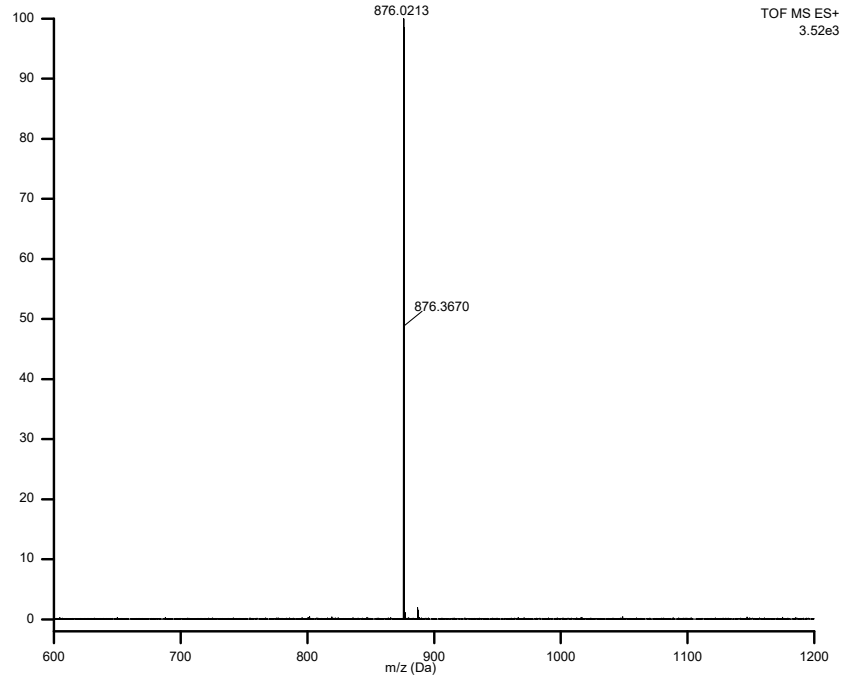

Figure 13. HRMS (ESI +ve) spectrum of Cy-5-GSNKGAIIGLMVG (Cy-5-Aβ_{25-37}).

RESULTS AND DISCUSSION

The designed inhibitor lipopeptide comprises one hydrophobic myristoyl chain to enhance the lipophilicity and a pentapeptide with two hydrophilic Lys residues to improve the electrostatic interaction and water solubility. Pro-Gly-Pro (PGP) is a collagen-derived matrikine that is used at the central position of the pentapeptide. The designed myristoyl-KPGPK lipopeptide has a requisite balance of hydrophilic and hydrophobic residues that may permit it to form a self-assembled specific nanostructure in water, which may interact with the Aβ monomer and/or early aggregate seeds through noncovalent interaction. Particularly, the hydrophobic myristoyl chain and proline ring may interact with the hydrophobic residue of Aβ, whereas the Lys residues may participate in electrostatic interaction and hydrogen bonding with Aβ. We have synthesized the lipopeptide myristoyl-KPGPK by the Fmoc-SPPS protocol on the Wang resin (**Figures 3-5, 14a**). FE-SEM, TEM, and AFM of the myristoyl-KPGPK showed the nanovesicles formation (**Figures 14b-e, 15-17**). The nanovesicles are fairly discrete and homogeneous, with an average diameter of 40 nm. Apparently, the hydrodynamic diameters of the nanovesicles in solution, which include the H_2O-layer acquired in DLS (76 nm), are marginally greater with respect to the nonhydrated diameters found in FE-SEM and TEM (**Figure 14f and Figure 17d**). Moreover, the nanovesicles are stable over a wide range of pH (4-9) (**Figure 18**). FT-IR spectrum of myristoyl-KPGPK in solid state, shows peaks at 1630 cm^{-1} in the amide I region and 1538 cm^{-1} in the amide II region, implying intermolecularly hydrogen-bonded supramolecular β-sheet conformation (**Figure 14g**). The FT-IR data of myristoyl-KPGPK in D_2O shows a peak at 1634 cm^{-1} signifying the presence of β-sheet structure in solution (**Figure 19**). This β-sheet secondary structure of

myristoyl-KPGPK can be closed along two axes of the 2D layer by intermolecular hydrogen bonding, electrostatic interaction, and hydrophobic interaction to form nanovesicles in solution (**Figure 14a**).

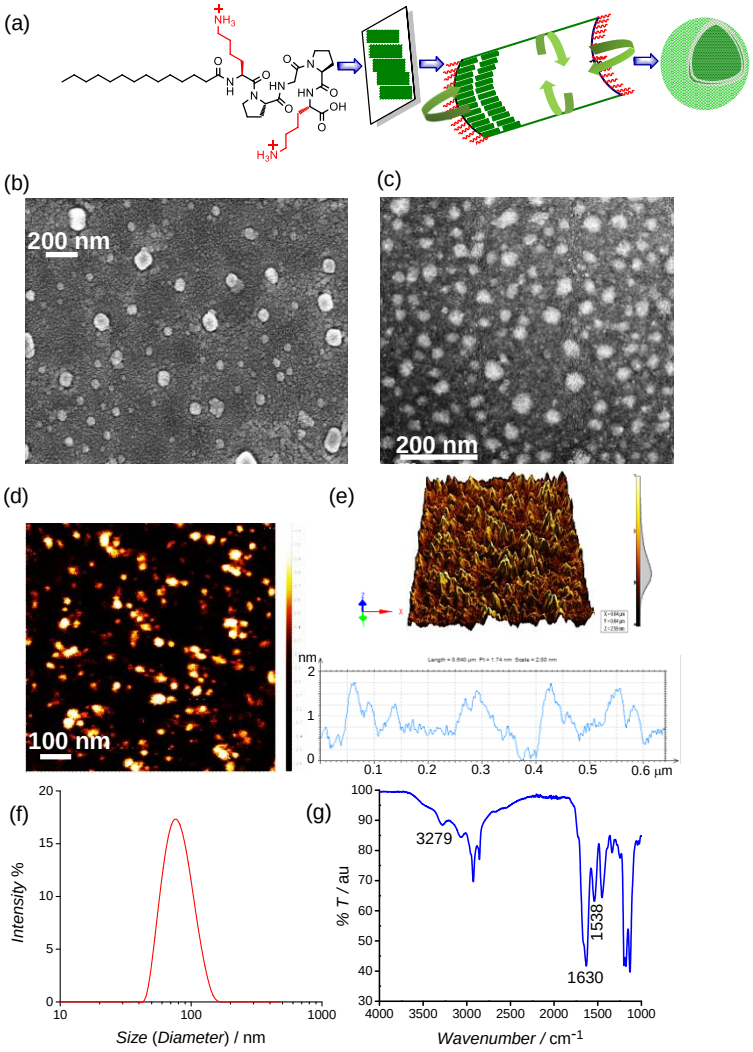

Figure 14. (a) Representation of myristoyl-KPGPK nanovesicle formation. (b) FE-SEM, (c) TEM, (d) AFM, (e) 3D AFM images and height profile of nanovesicles. (f) DLS of the vesicles in DI H_2O. (g) FT-IR spectrum of myristoyl-KPGPK.

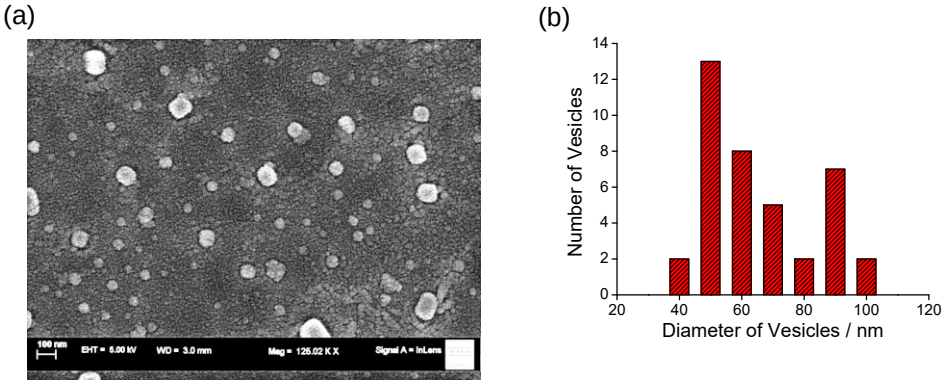

Figure 15. (a) FE-SEM image of myristoyl-KPGPK lipopeptide-based nanovesicles in deionized water used for the statistical analysis. (b) Statistical analysis of vesicles diameters formed by myristoyl-KPGPK lipopeptide.

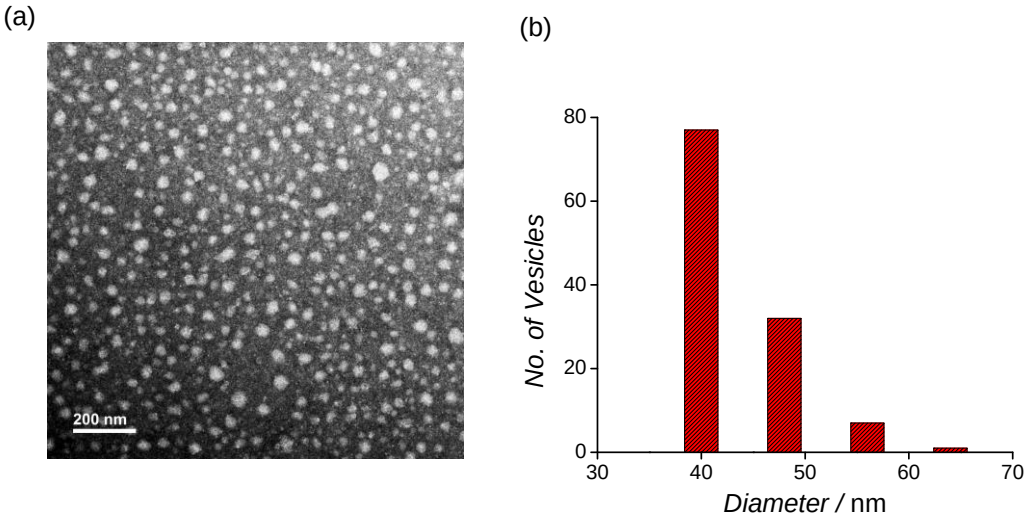

Figure 16. (a) TEM image of myristoyl-KPGPK (10 μM) in deionized water with negatively staining using uranyl acetate indicating vesicles formation. (b) Statistical analyses of nanovesicles diameters made by myristoyl-KPGPK lipopeptide.

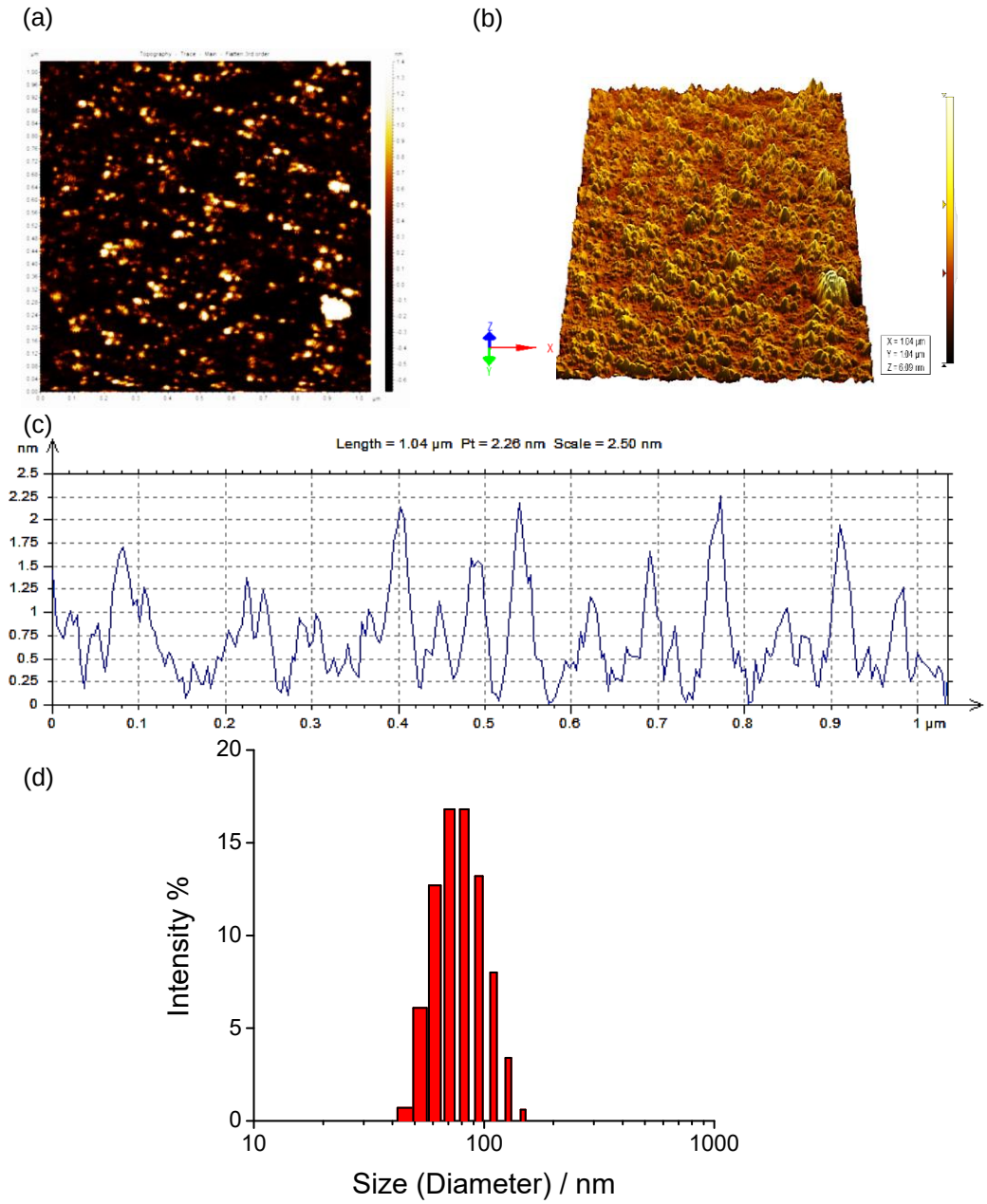

Figure 17. (a) AFM image of the nanovesicles formed by self-assembling myristoyl-KPGPK lipopeptide. (b) 3D AFM image of nanovesicles. (c) Height profile of the myristoyl-KPGPK nanovesicles. (d) Dynamic light scattering (DLS) experiment of the myristoyl-KPGPK based vesicles in deionized H_2O exhibits a monodisperse population (PDI = 0.231) with hydrodynamic diameter of 76 nm.

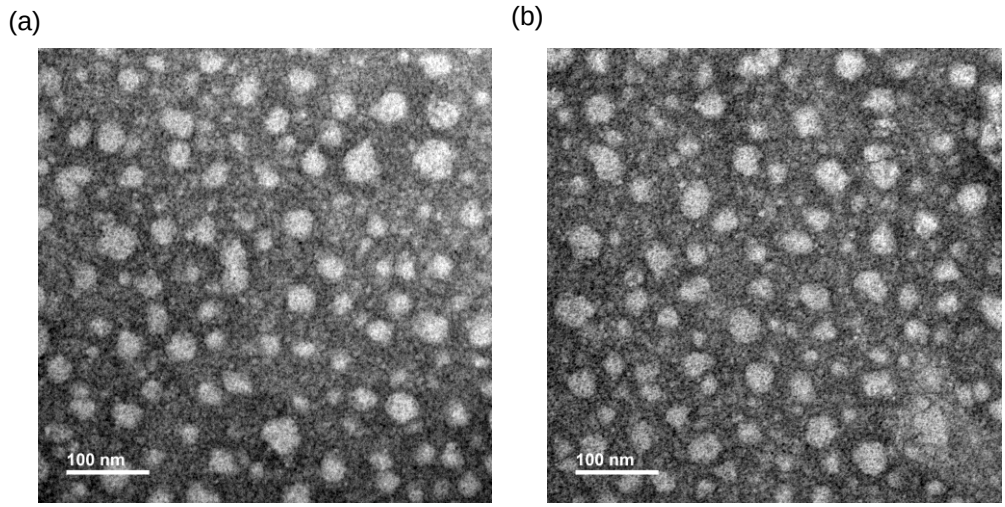

Figure 18. TEM images of myristoyl-KPGPK (10 μM) at (a) pH 4 and (b) pH 9 buffer solution with negative staining indicating the stability of the nanovesicles over a wide range of pH values.

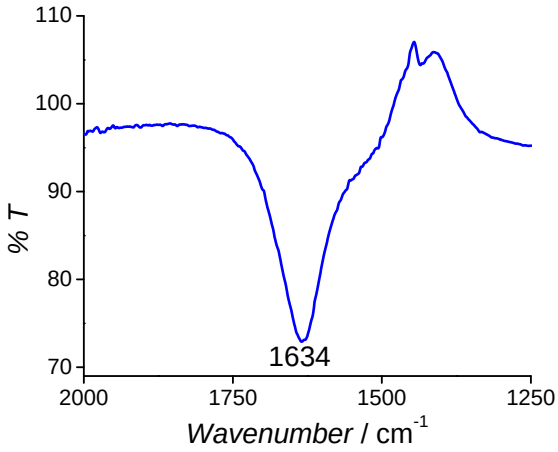

Figure 19. FT-IR spectrum of the myristoyl-KPGPK lipopeptide in D_2O solution.

We have synthesized A$\beta_{25–37}$ (GSNKGAIIGLMVG) and human myelin protein zero protein precursor (GVVLGAVIGGVLG) on Wang resin (**Figures 1, 2, 20a,**). The amyloid fibril formation of TM GxxxGxxxGxxxG is systematically characterized using TEM, FE-SEM, ThT, Congo red (CR), FT-IR, CD, and X-ray fiber diffraction (XRD) assays. FT-IR spectrum of A$\beta_{25–37}$ fiber aged over 7 days shows peaks at 3280 cm^{-1} (amide A), 1627 cm^{-1} (amide I region), and 1532 cm^{-1} (amide II region), demonstrating the formation of intermolecularly hydrogen-bonded β-sheet structure related to with amyloid fibrils (**Figures 20b, 22a**).[31] FT-IR spectrum of GVVLGAVIGGVLG fiber aged over 7 days also exhibited the construction of intermolecularly hydrogen-bonded β-sheet (**Figure 23a**). Initially, the CD spectrum of A$\beta_{25–37}$ (10 μM) in DI H_2O with 1% TFE displays a curve with a negative hump at 198 nm, like a random coil conformation (**Figure 20c**). Time dependent structural conversion in 7 days from random coil to β-sheet ellipticity is characterized by a lower wavelength positive hump at 197 nm and a higher wavelength negative maximum at 216 nm when the A$\beta_{25–37}$ peptide continues to aggregate (**Figures 20c, 22b**).[32] A similar type of time-induced secondary structural transformation from random coil to β-sheet in CD is also noticed for GVVLGAVIGGVLG (10 μM), which is consistent to that of amyloid fibrils of native A$\beta_{1–42}$ (**Figures 22c, 23b**). The peaks acquired from XRD of dried film of GSNKGAIIGLMVG as well as GVVLGAVIGGVLG fiber, feature a cross-β-sheet structure owing to the presence of peaks at 4.7 Å (meridional reflection, resembles to the separation of β-strands within the β-sheets) and 10.9 Å (equatorial reflection, due to the spacing of β-sheets) (**Figures 20d, 23c**).[33] The small amino acid Gly at i and i+4 positions in the GxxxGxxxGxxxG motif provide key packing units and reduce the steric barrier, allowing intermolecular hydrogen bonding and

facilitating the association of β-sheets. The intermolecularly hydrogen-bonded β-sheets are

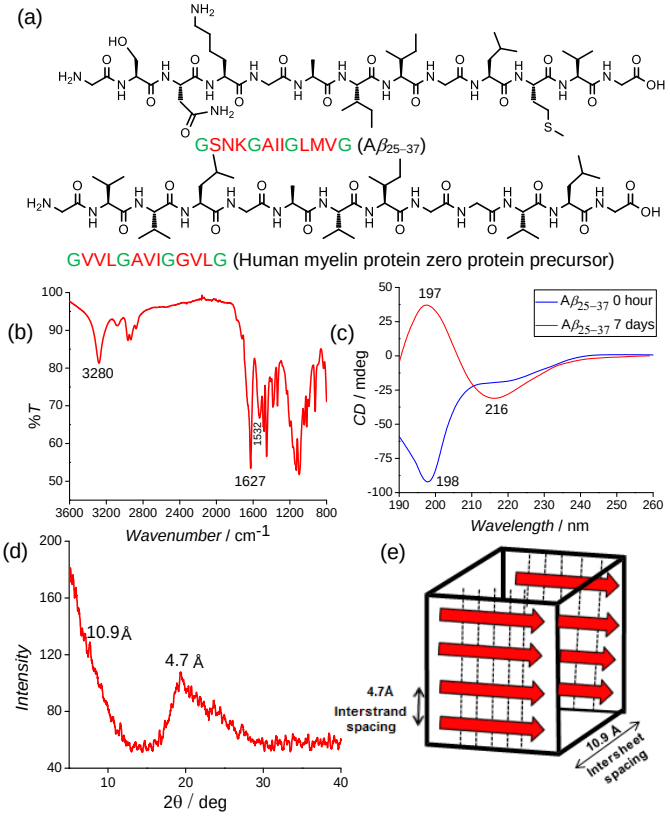

Figure 20. (a) Chemical structures of A$\beta_{25–37}$ and human myelin protein zero protein precursor. (b) FT-IR spectrum of A$\beta_{25–37}$ fibers aged over 7 days. (c) CD spectrum of A$\beta_{25–37}$ (10 μM) in DI H_2O initial (blue) and after 7 days incubation (red curve). (d) XRD of dried film from A$\beta_{25–37}$ fiber. (e) Cross-β structure.

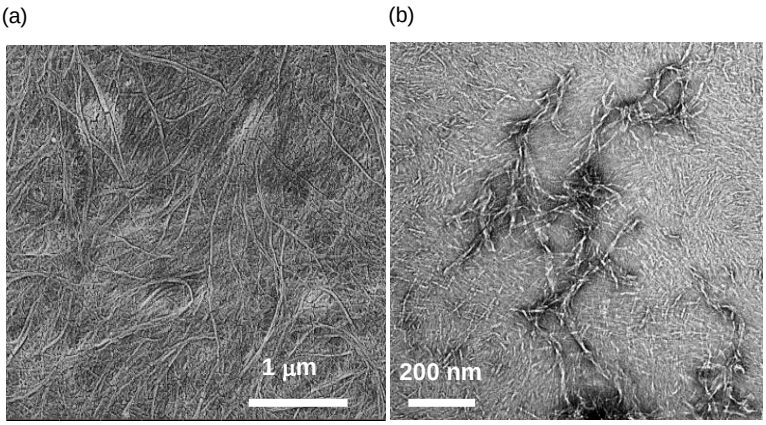

Figure 21. (a) FE-SEM and (b) TEM images of Aβ_{25-37}

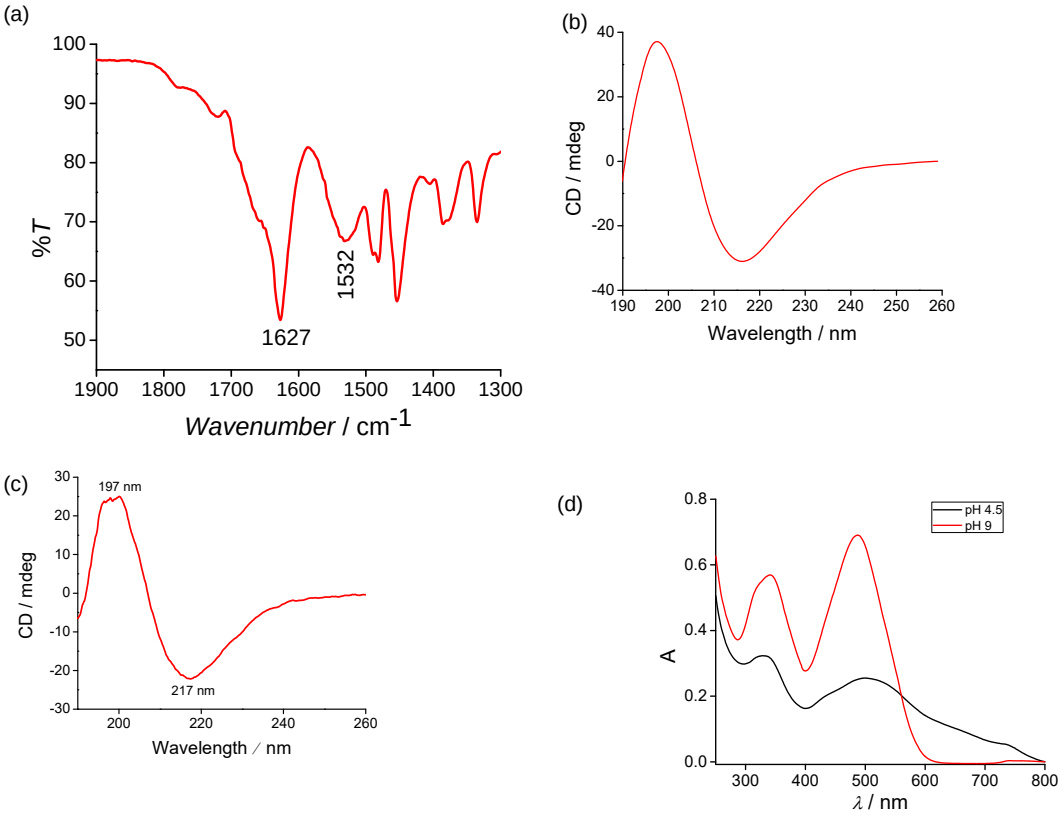

Figure 22. (a) FT-IR spectrum of A$\beta_{25–37}$ fiber aged over 7 days indicating the formation of a intermolecularly hydrogen-bonded β-sheet structure. (b) CD spectrum of A$\beta_{25–37}$ fragment (10 μM) in deionized water after 7 days incubation shows lower wavelength positive peak at 197 nm and higher wavelength negative maxima at 216 nm. (c) CD spectrum of human myelin protein zero protein precursor (GVVLGAVIGGVLG) in deionized water (10 μM) after 7 days incubation shows lower wavelength positive peak at 197 nm and higher wavelength negative maxima at 217 nm. (d) Congo Red binding assay of A$\beta_{25–37}$ (10 μM) peptide at different pH values.

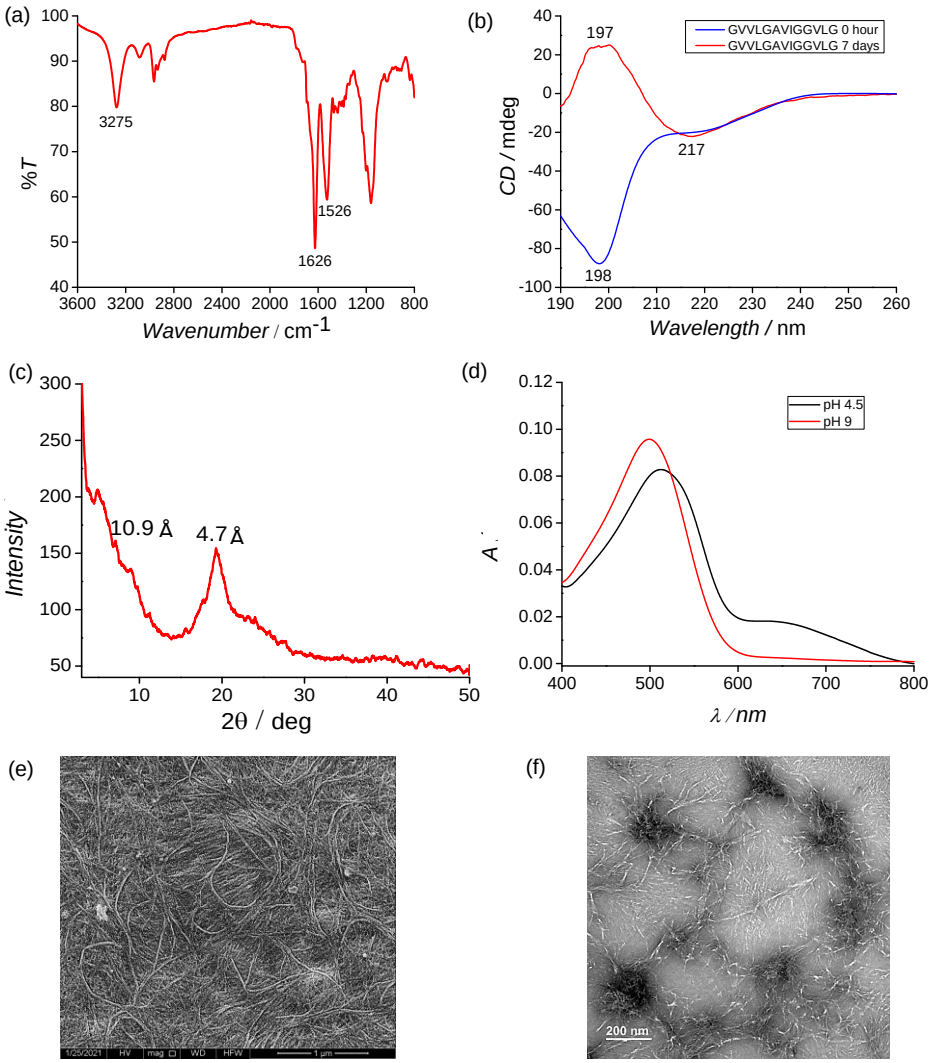

Figure 23. (a) FT-IR spectrum of human myelin protein zero protein precursor (GVVLGAVIGGVLG) fiber, aged over 7 days, shows a peak at 3280 cm^{-1} (N–H stretching, amide A), a sharp peak at 1627 cm^{-1} (amide CO stretching, amide I), 1532 cm^{-1} (NH bending, amide II region), indicating the formation of a intermolecularly hydrogen-bonded β-sheet structure. (b) CD spectrum of GVVLGAVIGGVLG peptide in deionized water (10 μM) after 7 days incubation shows lower wavelength positive peak at 198 nm and higher wavelength negative maxima at 217 nm. (c) X-ray diffraction of dried film of GVVLGAVIGGVLG fiber shows cross-β-sheet structure due to the presence of 4.7Å (meridional reflection) and 10.9Å (equatorial reflection) peaks. (d) Congo Red binding assay of human myelin protein zero protein precursor (10 μM) at

different pH. (e) and (f) FE-SEM and TEM images of GVVLGAVIGGVLG peptide exhibits amyloid fibril formation.

further packed by electrostatic and hydrophobic interaction in a cross-β pattern, which is imperative in the construction and stabilization of amyloid fibrils (**Figure 20e**). CR binding and ThT fluorescence assays show that the amyloid fibrils made of GSNKGAIIGLMVG or GVVLGAVIGGVLG preserve a β-sheet structure (**Figures 22d, 23d, 24b, 25c**).[34] ThT-based amyloid kinetic assays of GSNKGAIIGLMVG and GVVLGAVIGGVLG (10 μM) peptide aggregation characteristically showed a sigmoidal curve comprising three phases: lag phase, growth phase, and saturation phase (**Figure 24b**). The lag phase resembles a lack of mature fibrils, whereas the rapid growth phase designates growing fibril concentration. ThT is a benzothiazole dye that binds to the surface grooves of mature fibrils of the GxxxGxxxGxxxG motif and is accountable for the amplification of ThT fluorescence. Lastly, the aggregation process reached the saturation phase, where most of the GSNKGAIIGLMVG and GVVLGAVIGGVLG peptides are transformed into mature fibrils. FE-SEM and TEM images of GSNKGAIIGLMVG and GVVLGAVIGGVLG show amyloid fibril formation with an average width of 10 nm (**Figures 21a,b and 23e,f**). FT-IR, CD, XRD, FE-SEM, TEM, ThT, and CR binding assays reveal that the GxxxGxxxGxxxG motif forms amyloid fibrils composed of cross β-sheet structure.

As prefibrillar soluble oligomers of Aβ are believed to be the primary neurotoxic, we propose that the lipopeptide-based nanovesicles should inhibit the early stage intermediate formation in the amyloid fibrillation process by noncovalent interaction. The interaction of myristoyl-KPGPK nanovesicles with GxxxGxxxGxxxG motif is examined by CD, TEM, DLS, and ThT assay.

In the presence of nanovesicles, the GxxxGxxxGxxxG motif of Aβ_{25-37} and human myelin protein zero stayed in their initial random coil state even after 7

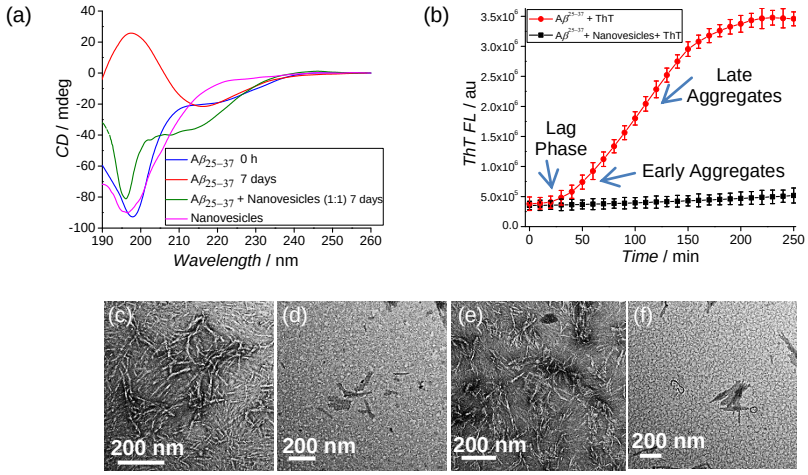

Figure 24. (a) CD of Aβ_{25-37} (10 μM) in the absence and presence of equimolar nanovesicles. (b) ThT kinetic assay of Aβ_{25-37} (10 μM) in the absence and presence of equimolar nanovesicles. TEM images of Aβ_{25-37} (10 μM) and human myelin protein zero protein precursor (10 μM) in the (c,e) absence and (d,f) presence of nanovesicles (10 μM), respectively.

days and inhibits the peptide's transformation to the β-sheet form, which is confirmed by CD (**Figures 24a, 25b**). To further study the inhibitory effect on the GxxxGxxxGxxxG fibrillation; DLS and TEM are used to observe the size distribution and morphological differences of GxxxGxxxGxxxG motif in the presence of nanovesicles. Strikingly, the aggregation pathways of GxxxGxxxGxxxG motif are remarkably controlled by the β-sheet breaker nanovesicles offering distinctive morphological features (wider amorphous structure) than those arising from GxxxGxxxGxxxG fibrils alone (**Figures 24c-f**). The hydrodynamic diameter increases to ~190 nm with a narrow size

distribution in DLS, which indicates the formation of homogeneous mixtures (**Figure 25a**). For only the pentapeptide KPGPK or the myristic acid, we observed random coil to β-sheet transformation and fibril formation of the GxxxGxxxGxxxG motif (**Figure 26a,b**). These results imply that myristoyl-KPGPK nanovesicles strongly prevent the formation of oligomeric intermediates and fibrils of GxxxGxxxGxxxG by preventing the aforementioned transition. To elucidate the influence of nanovesicles on GxxxGxxxGxxxG motif aggregates, the kinetics of fibrillation is tested by ThT assay (**Figures 24b, 25c**). Co-incubation of equimolar concentration of the nanovesicles (10 μM)

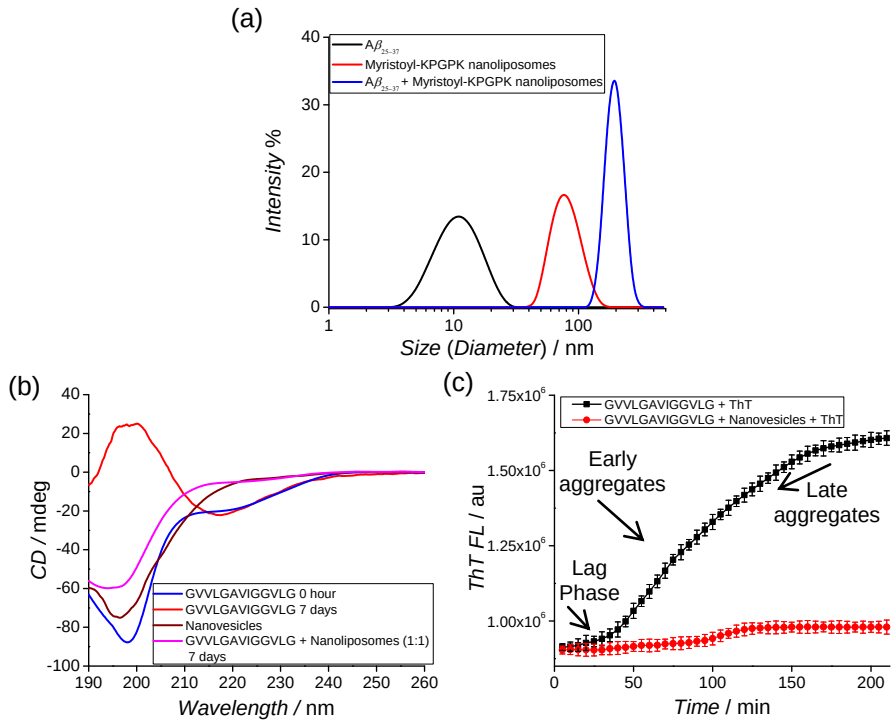

Figure 25. (a) DLS plot of nanovesicles, A$\beta_{25–37}$ fiber as well as equimolar mixture of A$\beta_{25–37}$ and myristoyl-KPGPK lipopeptide based nanovesicles. (b) CD of human myelin protein zero protein precursor GVVLGAVIGGVLG (10 μM) in the presence and absence of equimolar myristoyl-KPGPK nanovesicles. (c) ThT-fluorescence based kinetic study of human myelin protein zero protein precursor GVVLGAVIGGVLG (10 μM) in the absence and presence of equimolar myristoyl-KPGPK lipopeptide based nanovesicles. Error bars shown here represent the mean±standard deviation of three independent experiments.

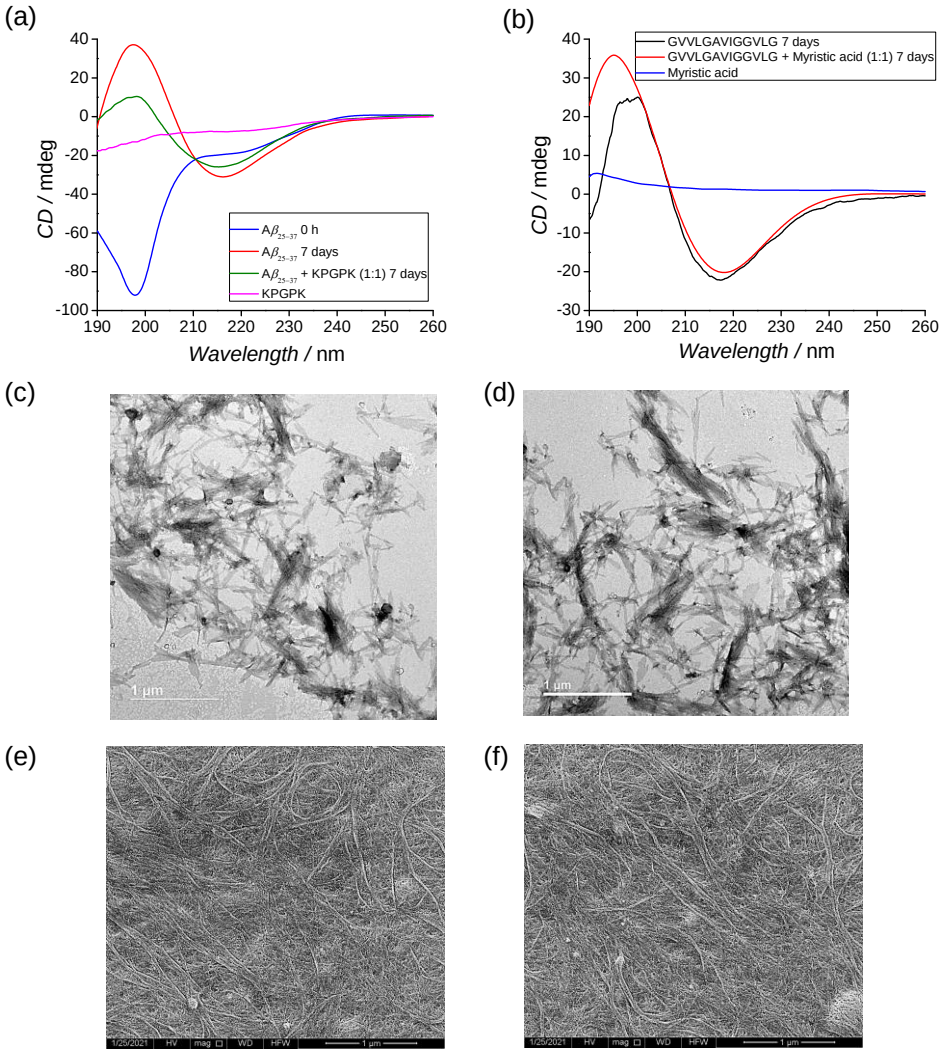

Figure 26. (a) CD of A$\beta_{25–37}$ (10 μM) in the absence and presence of equimolar KPGPK pentapeptide. (b) CD of GVVLGAVIGGVLG (10 μM) in the absence and presence of myristic acid (10 μM). (c) TEM image of A$\beta_{25–37}$ (10 μM) in the presence of equimolar KPGPK pentapeptide. (d) TEM image of human myelin protein zero protein precursor (GVVLGAVIGGVLG) in the presence of equimolar myristic acid. (e) FE-SEM image of A$\beta_{25–37}$ (10 μM) in the presence of equimolar KPGPK pentapeptide. (f) FE-SEM image of GVVLGAVIGGVLG (10 μM) in the presence of myristic acid (10 μM).

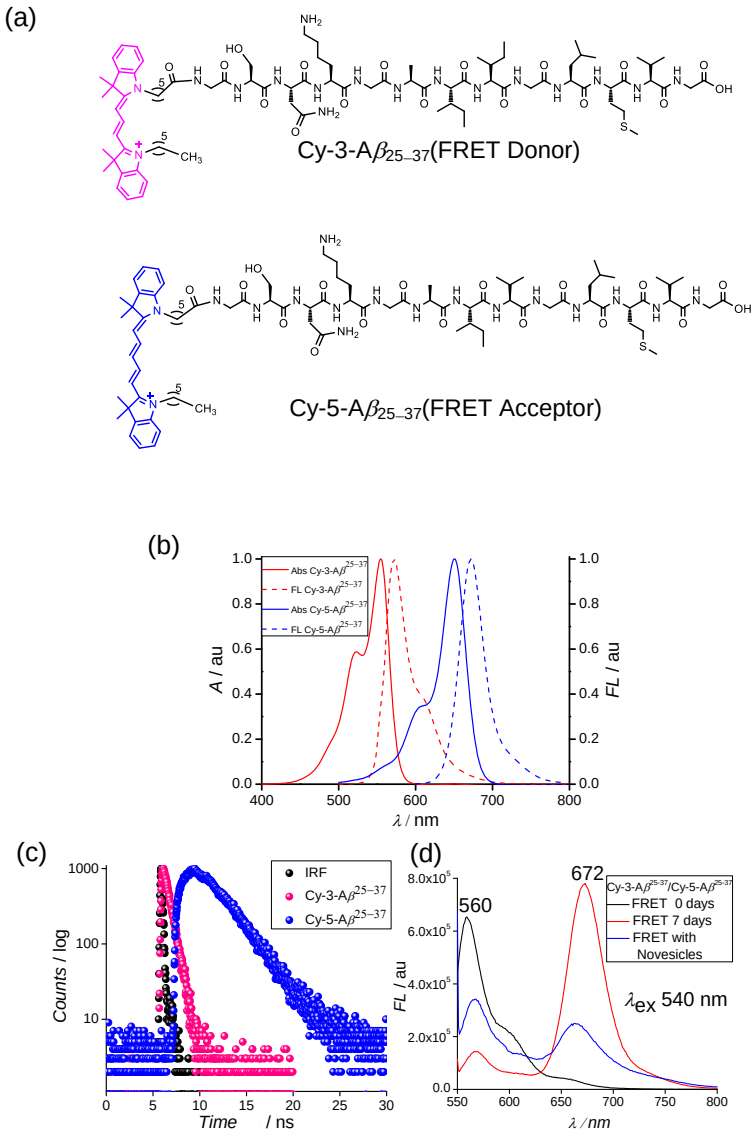

Figure 27. (a) Chemical structures of Cy-3-A$\beta_{25–37}$ FRET donor and Cy-5-A$\beta_{25–37}$ FRET acceptor. (b) Absorption and emission plots of Cy-3-A$\beta_{25–37}$ (10 μM) and Cy-5-A$\beta_{25–37}$ (10 μM) in DMSO. (c) Fluorescence lifetime (τ) of Cy-3-A$\beta_{25–37}$ and Cy-5-A$\beta_{25–37}$ in DMSO (IRF: instrument response function). (d) FRET assay in PBS indicate that nanovesicles strongly inhibit the fibril formation of A$\beta_{25–37}$.

with the GxxxGxxxGxxxG motif (10 μM), causes 6.7-fold lowering of the ThT fluorescence, and GxxxGxxxGxxxG fibrillation is completely inhibited over a 250 min time period resembling the soluble oligomeric native domain. This ability to inhibit GxxxGxxxGxxxG fibrillation is almost retained even after a longer time period (7 days), signifying that the nanovesicles primarily inhibit the fibril growth phase. Förster resonance energy transfer (FRET) pair-based bioconjugates Cy-3-Aβ_{25-37} (FRET donor) and Cy-5-Aβ_{25-37} (FRET acceptor) are synthesized for detecting the oligomeric assemblies of Aβ_{25-37} in a time dependent manner (**Figures 6-13, 27a**).[35,36] Bathochromic shifts of ~100 nm in absorption and emission are observed from Cy-3-Aβ_{25-37} to Cy-5-Aβ_{25-37} (**Figures 27b, 28a,b and Table 1**). The fluorescence lifetime (τ) of Cy-3-Aβ_{25-37} and Cy-5-Aβ_{25-37} are observed at 0.56 ns and 2.6 ns, respectively, in DMSO (**Figures 27c, 29**). Initially, when a 1:1 mixture of Cy-3-Aβ_{25-37} (10 μM) and Cy-5-Aβ_{25-37} (10 μM) in PBS is excited at 540 nm, we observed negligible FRET; however, after 7 days of coincubation, the resulting fluorescence triggers the emission of Cy-5-Aβ_{25-37} at 672 nm due to intermolecular FRET from Cy-3-Aβ_{25-37} to Cy-5-Aβ_{25-37}, signifying efficient oligomerization and fibril formation (**Figures 28c**).[37,38] When we incubated a 1:1 mixture of Cy-3-Aβ_{25-37} and Cy-5-Aβ_{25-37} in the presence of an equimolar concentration of the myristoyl-KPGPK nanovesicles, we observed a decrease in the FRET acceptor fluorescence signal and an increase in the FRET donor signal (**Figure 27d**). The decrease in the FRET signals of Cy-5-Aβ_{25-37} in the presence of nanovesicles is due to the poor FRET communication caused by an increased distance between the Cy-3-Aβ_{25-37} and Cy-5-A$\beta_{25-37,}$ which indicates that nanovesicles strongly inhibit the fibril formation of Aβ_{25-37}. The negative

heat generation in the titration of A$\beta_{25–37}$ monomer with nanovesicles in isothermal titration

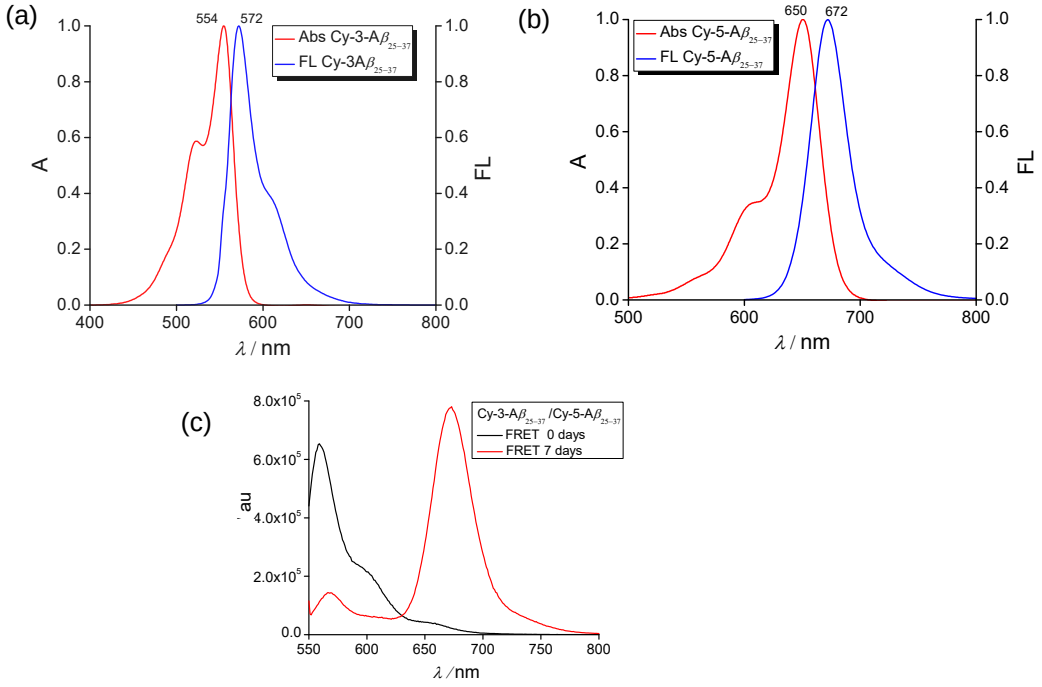

Figure 28. (a) Normalized absorption and emission plots of Cy-3-A$\beta_{25–37}$ (10 μM) in DMSO. (b) Normalized absorption and emission plots of Cy-5-A$\beta_{25–37}$ (10 μM) in DMSO. Nearly 100 nm bathochromic shift in absorption and emission are observed from Cy-3-A$\beta_{25–37}$ to Cy-5-A$\beta_{25–37}$. (c) Fluorescence spectra of 1:1 mixture of Cy-3-A$\beta_{25–37}$ and Cy-5-A$\beta_{25–37}$ at 540 nm excitation initially and after 7 days incubation exhibit FRET signal.

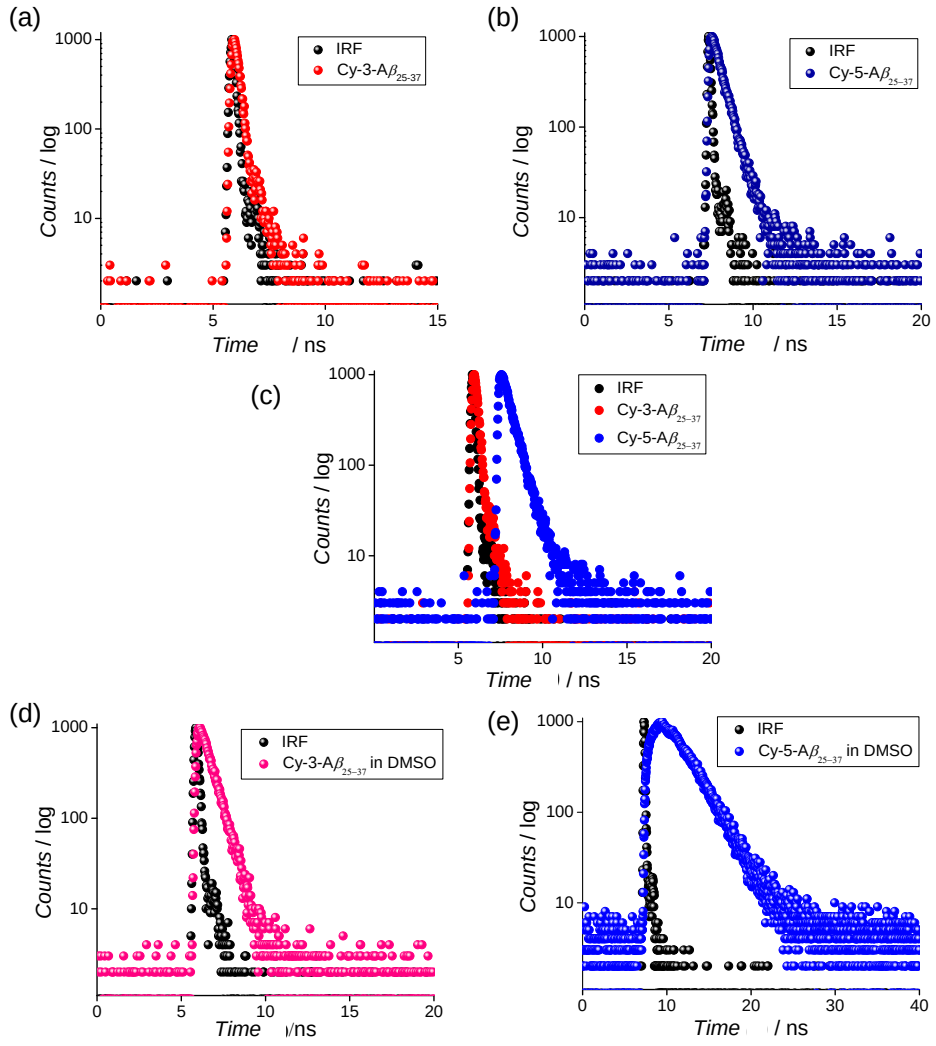

Compound	Life Time in DMSO	Life Time in PBS
Cy-3-Aβ_{25-37}	0.55 ± 0.01 ns	0.14±0.01 ns
Cy-5-Aβ_{25-37}	2.55 ± 0.06 ns	0.51±0.01 ns

Figure 29. (a-c) Fluorescence lifetime (τ) of Cy-3-Aβ_{25-37} and Cy-5-Aβ_{25-37} in PBS after excitation with a delta diode laser at 510 nm and 650 nm, respectively. (d,e) Fluorescence lifetime (τ) of Cy-3-Aβ_{25-37} and Cy-5-Aβ_{25-37} in DMSO after excitation with a delta diode laser at 510 nm and 650 nm, respectively (IRF: instrument response function).

Table 1. Photophysical data of Cy-3-Aβ_{25-37} and Cy-5-Aβ_{25-37}

Compound	λ_{max} (nm)	λ_{em} (nm)	Stokes shift ($\Delta\lambda$)	$\varepsilon \times 10^5$ (M^{-1} cm^{-1})	QY (F)
Cy-3-Aβ_{25-37}	554	572	18	1.50	0.28 in EtOH
Cy-5-Aβ_{25-37}	650	671	21	2.22	0.47 in DMSO

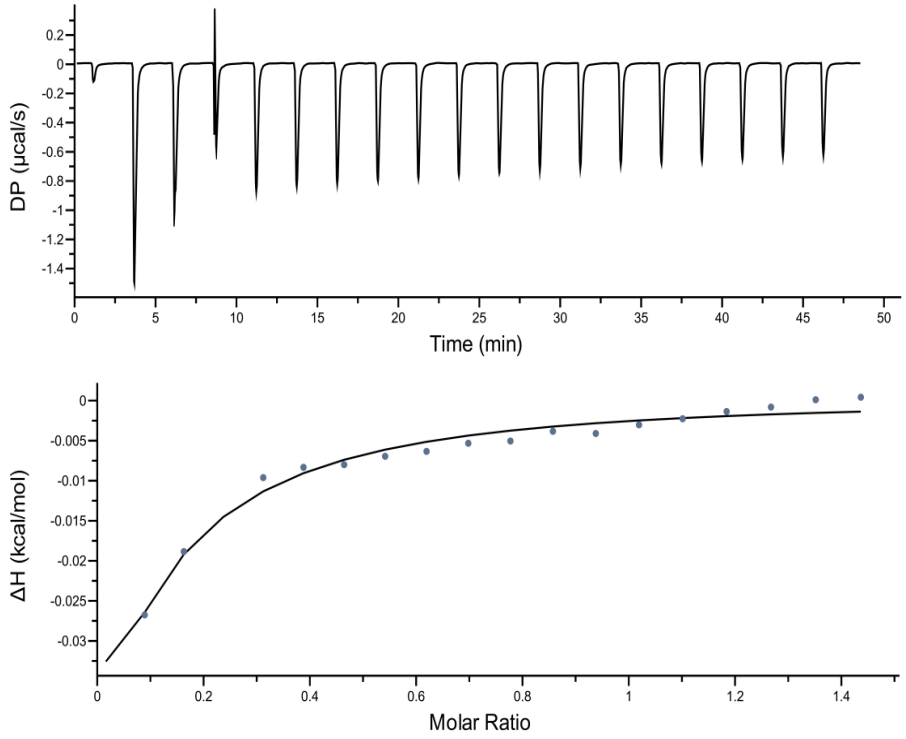

Cell conc.	Syringe conc.	N (Sites)	K_D (M)	ΔH (kcal/mol)	TΔS (kcal/mol)	ΔG (kcal/mol)
20 µM	150 µM	2.2	$7.33e^{-3}$	-6.25	-3.38	-2.87

Figure 30. The upper panels display the raw data for the Aβ_{25-37}/nanovesicles titration and the bottom panels represent the binding isotherm. The resultant isotherm is best fitted to a one site binding model to obtain the binding affinity (K_D), stoichiometry (n), enthalpy (ΔH), entropy (ΔS), and ΔG of interaction.

Docking Analysis

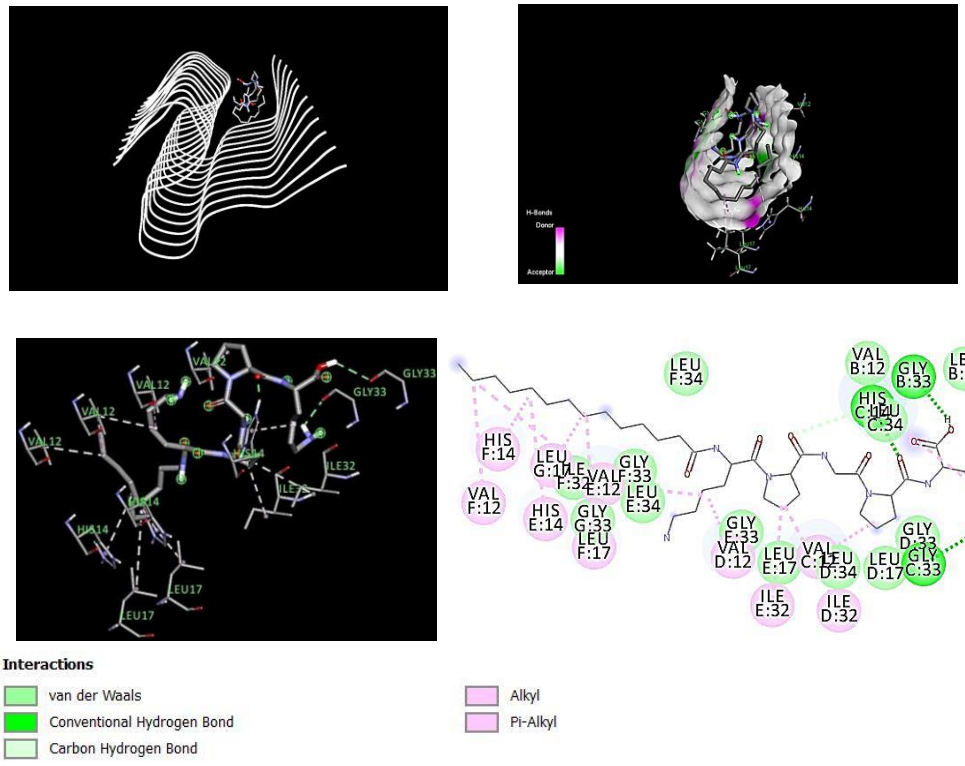

ΔG = –6.2 kcal/mol

Interaction with Gly33, Leu34, Ile32, His14, and Val12 residues of A$\beta_{25\text{-}37}$ with lipopeptide myristoyl-KPGPK

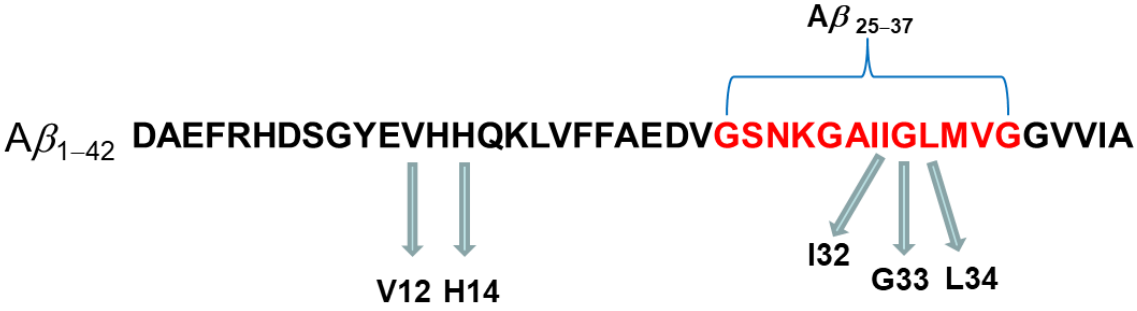

Figure 31. Molecular docking of the lipopeptide myristoyl-KPGPK with Aβ_{1-42} exhibits noncovalent interactions between the Gly33, Leu34, Ile32, His14, and Val12 residues of Aβ_{1-42} with myristoyl-KPGPK with ΔG = –6.2 kcal/mol.

calorimetry (ITC) indicates that the binding is exothermic (**Figure 30**).[39,40] It suggests that Aβ_{25-37}/nanovesicles binding interaction in aqueous solution is primarily enthalpy (ΔH) driven. The free energy change (ΔG) is negative, which confirmed that the interactions between Aβ_{25-37}/nanovesicles are spontaneous in nature. Molecular docking of the lipopeptide myristoyl-KPGPK with Aβ_{1-42} displays noncovalent interactions such as hydrogen bonding, hydrophobic interaction, and electrostatic interaction between the Gly33, Leu34, Ile32, His14, and Val12 residues of Aβ_{1-42} with myristoyl-KPGPK with ΔG = −6.2 kcal/mol (**Figure 31**). Cell viability studies display that the GxxxGxxxGxxxG motif of Aβ_{1-42} and human myelin protein zero exhibit substantial cytotoxicity against mouse N2A cells with IC_{50} values of 4.0 μM and 5.7 μM, respectively (**Figure 32b**). However, we observed negligible cytotoxicity for myristoyl-KPGPK nanovesicles (**Figure 32a**). Remarkably, neurotoxicity of GSNKGAIIGLMVG and GVVLGAVIGGVLG against N2A cells has been diminished by co-incubating the GxxxGxxxGxxxG motif with the nanovesicles (**Figures 32c,d**). The GxxxGxxxGxxxG motif also exhibits cytotoxicity in the presence of only the pentapeptide KPGPK or the myristic acid. It confirms that nanovesicles play a crucial role to inhibit oligomer and fibril formation and diminish neurotoxicity of the TM GxxxGxxxGxxxG motif in a complex cellular environment. The amphiphilic lipopeptide-based nanovesicles exterior may facilitate the trapping of the TM GxxxGxxxGxxxG motif on its lipid layer that may mask its aggregation-prone regions through noncovalent interaction. It plays an important role in inhibiting random coil to β-sheet transformation, disrupting the dynamic equilibrium between monomeric and/or early aggregate seeds of GxxxGxxxGxxxG and toxic oligomeric or prefibrillar species.

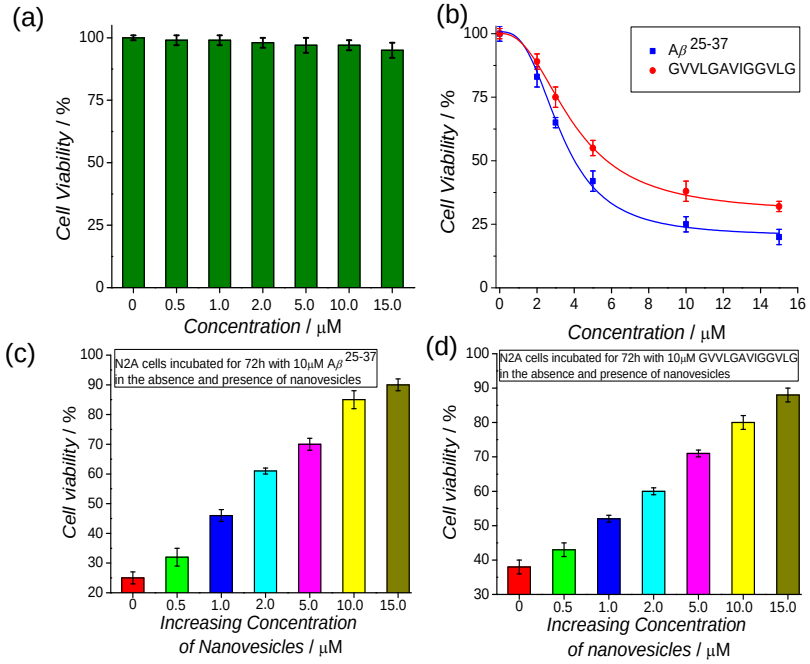

Figure 32. (a) Cell viability of N2A cells at different doses of nanovesicles over 72 h, exhibited negligible cytotoxicity. (b) MTT assay of N2A cells separately treated with different doses of A$\beta_{25—37}$ and human myelin protein zero protein precursor over 72 h. Cytotoxicity of (c) A$\beta_{25—37}$ (10 μM) and (d) GVVLGAVIGGVLG on N2A cells in the presence of different doses of nanovesicles over 72 h (SEM, n=5)

CONCLUSIONS

The synthesized myristoyl-KPGPK has a requisite balance of hydrophilic and hydrophobic residues that permits it to form self-assembled nanovesicles. Various spectroscopic and microscopic analyses indicate that myristoyl-KPGPK nanovesicles dramatically inhibit random coil to β-sheet transformation of TM GxxxGxxxGxxxG motif of A$\beta_{25–37}$ and human myelin protein zero and rescue N2A cells from amyloid aggregate-induced cytotoxicity. Our designed supramolecular nanovesicles offer a stimulating and appealing target for future inhibitor construction to combat protein misfolding and aggregation diseases.

REFERENCES

1. Benson, M. D.; Buxbaum, J. N.; Eisenberg, D. S.; Merlini, G.; Saraiva, M. J. M.; Sekijima, Y.; Sipe, J. D.; Westermark, P. *Amyloid* **2018**, *25*, 215–219.
2. Chiti, F.; Dobson, C. M. *Annu. Rev. Biochem.* **2017**, *86*, 27–68.
3. Ke, P. C.; Zhou, R.; Serpell, L.; Riek, R.; Knowles, T. P. J.; Lashuel, H. A.; Gazit, E.; Hamley, I. W.; Davis, T. P.; Fändrich, M.; et al. *Chem. Soc. Rev.* **2020**, *49*, 5473–5509.
4. Alzheimer's Association Report, 2021 Alzheimer's disease facts and figures. *Alzheimers Dement.* **2021**, *17*, 327−406.
5. Nortley, R.; Korte, N.; Izquierdo, P.; Hirunpattarasilp, C.; Mishra, A.; Jaunmuktane, Z.; Kyrargyri, V.; Pfeiffer, T.; Khennouf, L.; Madry, C.; et al. *Science* **2019**, *365*, eaav9518.

6. Wälti, M. A.; Ravotti, F.; Arai, H.; Glabe, C. G.; Wall, J. S.; Böckmann, A.; Güntert, P.; Meier, B. H.; Riek, R. *Proc. Natl. Acad. Sci.* U.S.A. **2016**, *113*, E4976−E4984.
7. De, S.; Wirthensohn, D. C.; Flagmeier, P.; Hughes, C.; Aprile, F. A.; Ruggeri, F. S.; Whiten, D. R.; Emin, D.; Xia, Z.; Varela, J. A.; et al. *Nat. Commun.* **2019**, *10*, 1541.
8. Haass, C.; Selkoe, D. J. *Nat. Rev. Mol. Cell Biol*. **2007**, *8*, 101−112.
9. Makin, S. *Nature* **2018**, *559*, S4−S7.
10. Michaels, T. C. T.; Šarić, A.; Curk, S.; Bernfur, K.; Arosio, P.; Meisl, G.; Dear, A. J.; Cohen, S. I. A.; Dobson, C. M.; Vendruscolo, M.; et al. *Nat. Chem.* **2020**, *12*, 445–451.
11. Kim, M.; Kang, J.; Lee, M.; Han, J.; Nam, G.; Tak, E.; Kim, M. S.; Lee, H. J.; Nam, E.; Park, J.; et al. *J. Am. Chem. Soc*. **2020**, *142*, 8183−8193.
12. Bartling, C. R. O.; Jensen, T. M. T.; Henry, S. M.; Colliander, A. L.; Sereikaite, V.; Wenzler, M.; Jain, P.; Maric, H. M.; Harpsøe, K.; Pedersen, S. W.; et al. *J. Am. Chem. Soc.* **2021**, *143*, 891–901.
13. Garcia, A. M.; Melchionna, M.; Bellotto, O.; Kralj, S.; Semeraro, S.; Parisi, E.; Iglesias, D.; D′Andrea, P.; De Zorzi, R.; Vargiu, A. V.; et al. *ACS Nano* **2021**, *15*, 3015−3025.
14. Maity, D.; Howarth, M.; Vogel, M. C.; Magzoub, M.; Hamilton, A. D. *J. Am. Chem. Soc.* **2021**, *143*, 3086–3093.
15. Streich, C.; Akkari, L.; Decker, C.; Bormann, J.; Rehbock, C.; Müller-Schiffmann, A.; Niemeyer, F. C.; Nagel-Steger, L.; Willbold, D.; Sacca, B.; et al. *ACS Nano* **2016**, *10*, 7582−7597.
16. Caballero, A. B.; Gamez, P. *Angew. Chem., Int. Ed*. **2021**, *60*, 41–52.
17. Xu, Z.; Jia, S.; Wang, W.; Yuan, Z.; Ravoo, B. J.; Guo, D.-S. *Nat. Chem*. **2019**, *11*, 86−93.
18. Lee, H. H.; Choi, T. S.; Lee, S. J. C.; Lee, J. W.; Park, J.; Ko, Y. H.; Kim, W. J.; Kim, K.; Kim, H. I. *Angew. Chem., Int. Ed*. **2014**, *53*, 7461−7465.

19. Palmal, S.; Maity, A. R.; Singh, B. K.; Basu, S.; Jana, N. R.; Jana, N. R. *Chem. - Eur. J.* **2014**, *20*, 6184–6191.
20. Chaudhary, H.; Iashchishyn, I. A.; Romanova, N. V.; Rambaran, M. A.; Musteikyte, G.; Smirnovas, V.; Holmboe, M.; Ohlin, C. A.; Svedružić, Ž. M.; Morozova-Roche, L. A. *ACS Appl. Mater. Interfaces* **2021**, *13*, 26721−26734.
21. Yan, C.; Wang, C.; Shao, X.; Shu, Q.; Hu, X.; Guan, P.; Teng, Y.; Cheng, Y. *Mater. Today Bio* **2021**, *12*, 100167.
22. Zhang, H.; Hao, C.; Qu, A.; Sun, M.; Xu, L.; Xu, C.; Kuang, H. *Angew. Chem., Int. Ed.* **2020**, *59*, 7131−7138.
23. Doig, A. J.; Castillo-Frias, M. P. D.; Berthoumieu, O.; Tarus, B.; Nasica-Labouze, J.; Sterpone, F.; Nguyen, P. H.; Hooper, N. M.; Faller, P.; Derreumaux, P. *ACS Chem. Nerosci.* **2017**, *8*, 1435–1437.
24. Tolar, M.; Abushakra, S.; Hey, J. A.; Porsteinsson, A.; Sabbagh, M. *Alzheimer's Res. Ther.* **2020**, *12*, 95.
25. Levin, A.; Hakala, T. A.; Schnaider, L.; Bernardes, G. J. L.; Gazit, E.; Knowles, T. P. J. *Nat. Rev. Chem.* **2020**, *4*, 615–634.
26. Wei, G.; Su, Z.; Reynolds, N.; Arosio, P.; Hamley, I.; Gazit, E.; Mezzenga, R. *Chem. Soc. Rev.* **2017**, *46*, 4661–4708.
27. Teese, M. G.; Langosch, D. *Biochemistry* **2015**, *54*, 5125−5135.
28. Anderson, S. M.; Mueller, B. K.; Lange, E. J.; Senes, A. *J. Am. Chem. Soc.* **2017**, *139*, 15774–15783.
29. Roa, B. B.; Dyck, P. J.; Marks, H. G.; Chance, P. F.; Lupski, J. R. *Nat. Genet.* **1993**, *5*, 269–273.
30. Szigeti, K.; Lupski, J. R. *Eur. J. Hum. Genet.* **2009**, *17*, 703–710.
31. Wang, S.-T.; Lin, Y.; Spencer, R. K.; Thomas, M. R.; Nguyen, A. I.; Amdursky, N.; Pashuck, E. T.; Skaalure, S. C.; Song, C. Y.; Parmar, P. A.; et al. *ACS Nano* **2017**, *11*, 8579−8589.
32. Nguyen, P. T.; Zottig, X.; Sebastiao, M.; Arnold, A. A.; Marcotte, I.; Bourgault, S. *Commun. Biol.* **2021,** *4*, 939.

33. Eanes, E. D.; Glenner, G. G. *J. Histochem. Cytochem*. **1968**, *16*, 673–677.
34. Frieg, B.; Gremer, L.; Heise, H.; Willbold, D.; Gohlke, H. *Chem. Commun*. **2020**, *56*, 7589–7592.
35. Saha, P. C.; Bera, T.; Chatterjee, T.; Samanta, J.; Sengupta, A.; Bhattacharyya, M.; Guha, S. *Bioconjugate Chem.* **2021**, *32*, 833–841.
36. Saha, P. C.; Das, R. S.; Chatterjee, T.; Bhattacharyya, M.; Guha, S. *Bioconjugate Chem.* **2020**, *31*, 1301– 1306.
37. Yano, Y.; Kondo, K.; Watanabe, Y.; Zhang, T. O.; Ho, J. J.; Oishi, S.; Fujii, N.; Zanni, M. T.; Matsuzaki, K. *Angew. Chem., Int. Ed.* **2017**, *56*, 1756–1759.
38. Hatai, J.; Motiei, L.; Margulies, D. *J. Am. Chem. Soc*. **2017**, *139*, 2136–2139.
39. Angira, D.; Chikhale, R.; Mehta, K.; Bryce, R. A.; Thiruvenkatam, V. *ACS Chem. Neurosci*. **2019**, *10*, 3868−3879.
40. Li, X.; Zhang, X.; Ladiwala, A. R. A.; Du, D.; Yadav, J. K.; Tessier, P. M.; Wright, P. E.; Kelly, J. W.; Buxbaum, J. N. *J. Neurosci.* **2013**, *33*, 19423–19433.
41. Morris, G. M.; Goodsell, D. S.; Pique, M. E.; Lindstrom, W. L.; Huey, R.; Forli, S.; Hart, W. E.; Halliday, S.; Belew, R.; Olson, A. J. User Guide, AutoDock Version 4.2, Scripps Research, **2012**.
42. Childers, W. S.; Mehta, A. K.; Lu, K.; Lynn, D. G. *J. Am. Chem. Soc*. **2009**, *131*, 10165–10172.
43. Frieg, B.; Gremer, L.; Heise, H.; Willbold, D.; Gohlke, H. *Chem. Commun.* **2020**, *56*, 7589–7592.
44. Saha, P. C.; Das, R. S.; Chatterjee, T.; Bhattacharyya, M.; Guha, S. *Bioconjugate Chem.* **2020**, *31*, 1301–1306.

Chapter 4

A Mitochondria Targeting, de novo Designed, Aggregation-Induced Emission Probe for Selective Detection of Neurotoxic Amyloid-β Aggregates

Introduction

Alzheimer's disease (AD) is a progressive neurodegenerative disorder, presently one of the top 10 reasons for mortality in the world.[1] Almost all brain functions, *i.e*., memory, verbal, decision, behavioural, activity, cognitive, trouble recognizing friends and family members, and life expectancy, are in due course affected.[2,3] The WHO estimates that approximately 10 million individuals globally suffer from AD annually, and that number will be almost doubled within 2030. Albeit the symptoms of AD are often identified in older age, the neurodegeneration undeniably has a long, silent beginning prior to its clinical diagnosis.[4,5] As of right now, there is no effective molecular toolkit for the early diagnosis of AD, which is not curable or even stops the disease from progressing once symptoms start. The aberrant assembly of amyloid-β (Aβ) peptides that promotes Aβ fibrils or plaque deposition is the primary pathological hallmark of AD.[6] The Aβ peptides encounter an innate transformation from a soluble monomer, soluble oligomer, or frequently partially folded state to self-assembled insoluble oligomers, protofibrils, and fibrils that are accumulated inside the brain as Aβ plaques.[7,8] It is believed that these species cause the neurotoxicity and neurodegeneration connected with the development of AD symptoms.[9] Aβ fibrils typically upsurge in the brain as AD progresses.[10] There is budding proof showing that elevated Aβ levels cause severe mitochondrial damage and dysfunction, which is one of the most early and notable hallmarks of vulnerable neurons.[11-13] This is an appealing hypothesis for the pathogenesis of AD. Moreover, considerable evidence suggests that Aβ progressively accumulates in mitochondria and is responsible for mitochondrial dysfunction and oxidative stress, which are accountable for the progression of AD.[14,15] CT, PET, SPECT, and MRI imaging techniques are generally utilized to diagnose the advanced stage of AD.[16-19] Nevertheless, the

exposure to high-energy ionizing radiation and radioactive substances, high cost, inaccessibility of real-time detection, lack of target selectivity, and sensitivity of these probes limit their practical application. The burgeoning technology is targeted fluorescence-based detection and imaging of Aβ, which has several advantages such as extraordinary sensitivity at the molecular level, spatiotemporal resolution, low cost, ability to monitor in real time, no exposure to harmful radiation and radioactive substances, and has become a smart tool for AD diagnosis.[20-22] Thioflavin T (ThT) is a benzothiazole-based fluorescent probe used as a gold standard for Aβ staining.[23] Although it is widely used in identifying Aβ fibrils, ThT and its derivatives have certain restrictions, *e.g.*, a minor Stokes shift, high background fluorescence, low penetration depth, enrichment quenching effect on emission after binding with Aβ fibrils, poor sensitivity, inadequate blood−brain barrier (BBB) penetrability, incapability to target specific cellular organelles, and unclear cytotoxicity.[24] To overcome these pitfalls, several dyes have been reported for the detection of Aβ fibrils.[25-27] Nevertheless, the tedious synthesis, inability of mitochondria targeting, and carcinogenicity limit their use as Aβ markers. Furthermore, most of the organic dyes containing aromatic rings exhibit bright fluorescence in dilute organic solutions and often suffer aggregation-caused quenching (ACQ) effects when dispersed into an aqueous system or aggregated inside live cells.[28,29] ACQ severely hampers their biological applications and is not suitable for cellular mitochondrial imaging as well as Aβ detection. Tang has made a pioneering contribution on aggregation-induced emission (AIE) that is a phenomenon just reverse to the traditional ACQ probe.[30] AIE probes display no emissions or faint fluorescence in solution due to their excited-state energy dissipation through the intramolecular motions; however, they exhibit boosted emission when aggregated or accumulated inside the target and could overcome the

limitations of ACQ probes. Tetraphenyl ethylene (TPE) is the first AIE probe utilized to detect protein aggregation.[31] Next, TPE-TPP is used to analyze early-stage *α*-syn protein aggregation.[32] Tang and associates have reported AIE probes for theranostics of AD.[33] Next, they have used an AIE chromophore to detect protein aggregation in living cells.[34] Liang and co-workers have reported an AIE luminogen for imaging of AD.[35] Hong *et al*. developed an AIE luminogen to identify human serum albumin and insulin fibrillation.[36] Additionally, using water-soluble AIEgens, Guo and co-workers recently accomplished *in vivo* mapping of A*β*40 plaques.[37] Wang's *et al*. have constructed water-soluble AIE-based wash-free A*β* biomarkers.[38] He and Quan have designed an AIE probe for the detection of amyloid fibers and amorphous aggregates.[39] Although there has been a paradigm shift in the development of AIE probes for A*β*, none of them have the ability to target the powerhouse of cells, mitochondria, along with neurotoxic A*β* aggregates.[40,41] Targeting mitochondria is a difficult task owing to the double membrane system and the extremely negative inner mitochondrial membrane (IMM) potential ($\Delta\Psi_m$ −150 to −180 mV).[42,43] Mitochondria targeted AIE molecules with solvatofluorochromic effects to monitor mitochondrial morphology change and dysfunction during A*β*-induced neurotoxicity are still in their infancy. There is an unmet need to design superior mitochondria target selective, rapid responsive functional AIE-based fluorescence imaging diagnostic biomarkers for the early detection of A*β* aggregates in AD.

Herein, the de novo designed mitochondrion targeting and A*β* aggregates detecting functional AIE probe Cou-AIE-TPP$^+$ has six distinctive structural characteristics: (a) an unsymmetrical Cou-AIE-TPP$^+$ probe engineered by aromatic coumarin framework into the bridge of electron donor-acceptor-donor (D-A-D) motif for live cell fluorescence imaging; (b) the intramolecular charge

transfer (ICT) among the D and A residues in the D-A-D chromophore is responsible for the solvatofluorochromic effect, with bathochromic shift of the emission upon the increase of solvent polarity exhibiting a significant Stokes shift of 124 nm in PBS; (c) the probe exhibits AIE phenomena due to restriction of intramolecular motions such as rotation and vibration upon aggregation and targeted binding; (d) a lipophilic cationic triphenylphosphonium (TPP^+) functionality conjugated on the terminal position for targeting living neuronal cells mitochondria by exploiting the highly negative IMM potential,[42,43] (e) Cou-AIE-TPP^+ (λ_{em} = 604 nm) has appropriate lipophilicity and exhibits fluorescence augmentation for aggregated Aβ compared to monomeric Aβ with high specificity, strong binding affinity (K_d = 83 nM), and is superior to the gold standard probe ThT (λ_{em} = 480 nm) for detecting the kinetics of amyloid Aβ aggregation, and (f) the AIE probe with light-up characteristics including fluorescence lifetime and brightness augmentation when Cou-AIE-TPP^+ binds with Aβ aggregates in PBS (**Figure 1**). Selective targeting, 3D cellular imaging, and real-time tracking of human neuroblastoma SH-SY5Y live-cell mitochondria by Cou-AIE-TPP^+ are established by confocal laser scanning microscopy (CLSM). Afterward rapid internalization in the neuronal cell membrane, Cou-AIE-TPP^+ might aggregate inside the mitochondria with an expectation of 500−1000 fold higher concentrations related to the extracellular matrix ($\Delta\Psi_{plasma\ membrane}$ = −30 to −60 mV vs $\Delta\Psi_m$ −150 to −180 mV), thus exhibiting the AIE effect inside the mitochondria. Inspection through SH-SY5Y cell staining demonstrates that the synthesized Cou-AIE-TPP^+ (λ_{em} = 604 nm) effectively recognizes neurotoxic exogenous Aβ fibrils and colocalizes with ThT, showing Pearson's correlation coefficient of 0.91. Moreover, Cou-AIE-TPP^+ is also able to detect mitochondrial morphology change and dysfunction induced by exogenous Aβ.

To the best of the authors' knowledge, this is the first account of a de novo designed, biocompatible, noncytotoxic, D-A-D, solvatofluorochromic, mitochondria targeting, functional AIE-based fluorescent probe capable of monitoring amyloid aggregation kinetics, recognizing neurotoxic exogenous Aβ fibrils, and being useful to monitor mitochondrial morphology alteration and dysfunction during Aβ-mediated neurotoxicity. These findings indicate that the mitochondria targeting de novo designed Cou-AIE-TPP$^+$ probe is a promising biomarker for the fluorescence detection and imaging of Aβ that may offer imperative guidance for the advancement of compelling AIE biomarkers for mitochondria targeted early diagnosis of neurotoxic Aβ in the future.

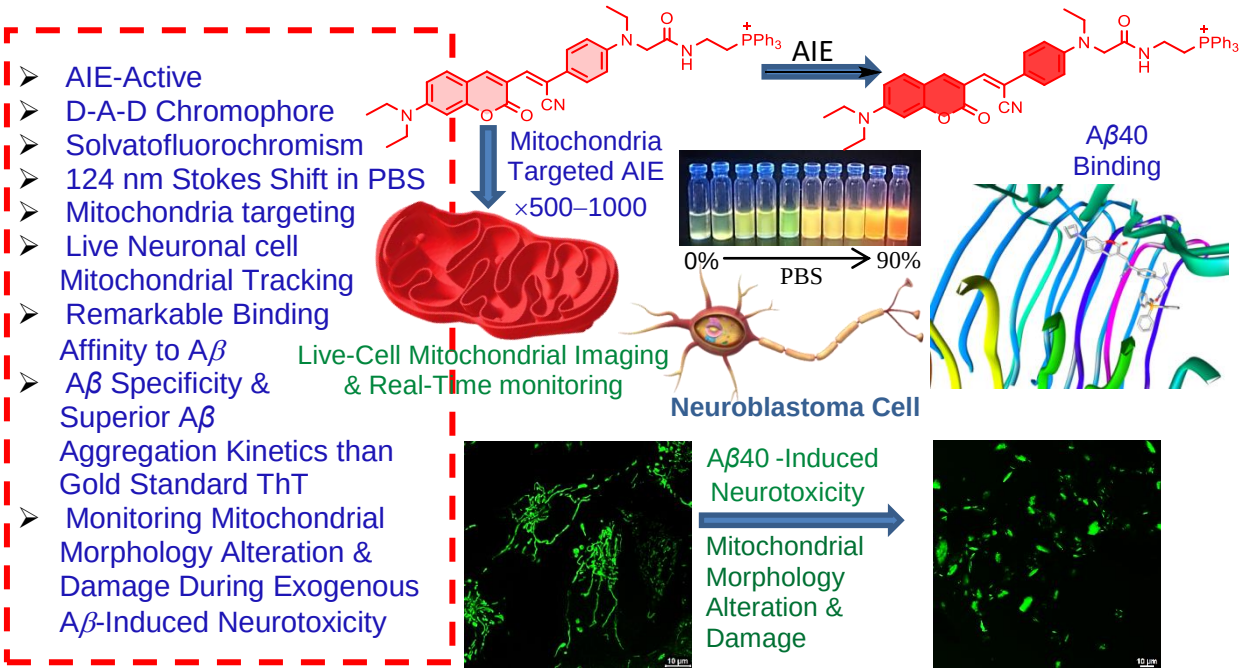

Figure 1. Schematic representation of AIE probe Cou-AIE-TPP$^+$ for mitochondrial targeted imaging, remarkable binding affinity to Aβ, recognizing neurotoxic exogenous Aβ fibrils, and useful to monitor mitochondrial morphology alteration and damage during Aβ-mediated neurotoxicity.

Experimental Methods

General Methods and Materials

Synthesis, Purification, and Characterization of Cou-AIE-TPP$^+$, and Cou-AIE dyes:

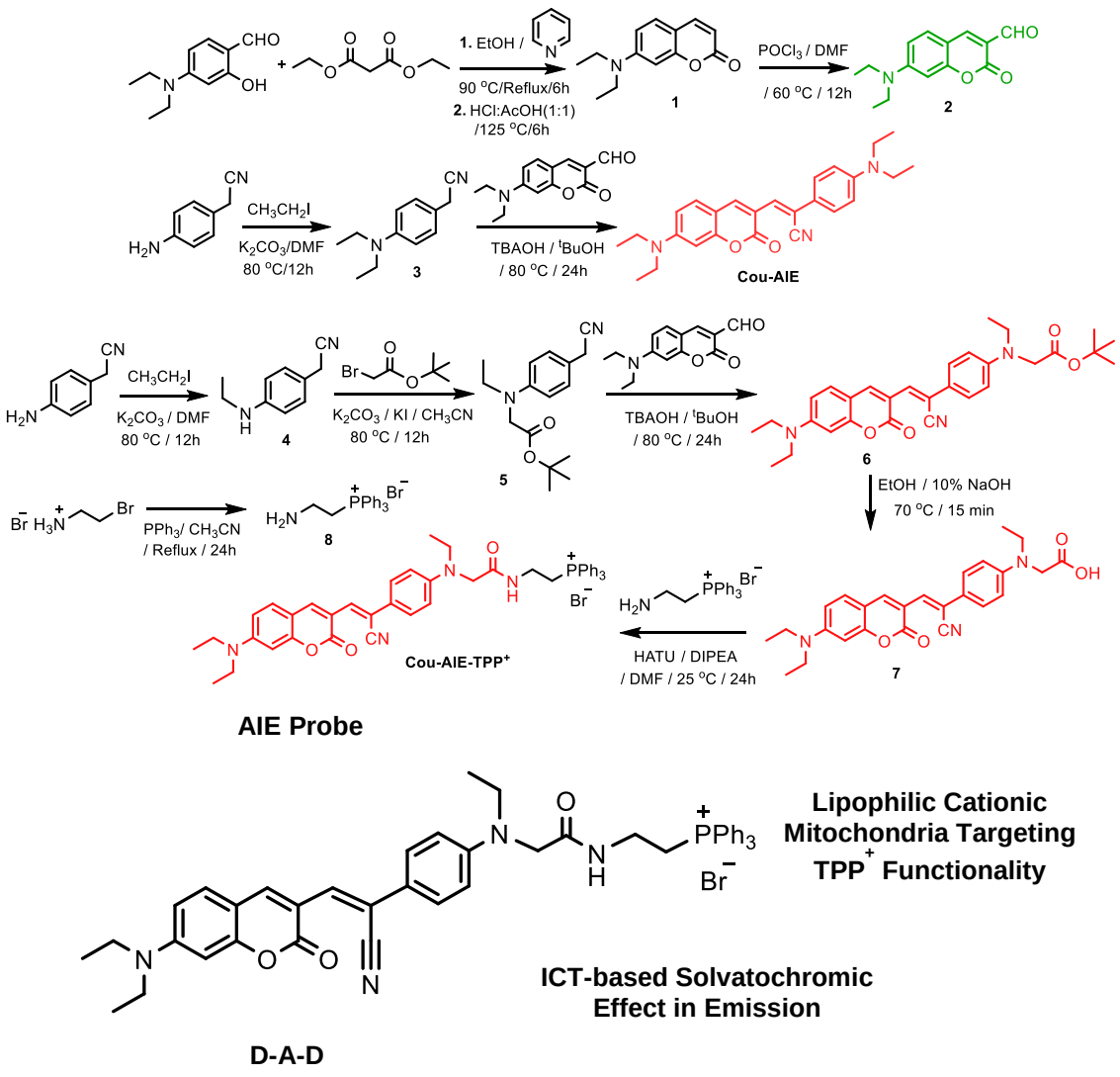

Figure 2. Synthetic schemes of Cou-AIE-TPP$^+$ and a control compound. Cou-AIE, lacking the lipophilic cationic TPP$^+$ functionality

All the compounds were synthesized in oven-dried flasks using dry solvents in an inert N_2 environment, unless otherwise specified. Analytical TLC was performed using aluminium sheets coated with silica gel (TLC silica gel 60 F_{254}), and the corresponding spots were then found using a UV light or the human eye, or by developing with I_2. Column chromatography (silica gel, 100-200 mesh) was used to separate the compound from the raw ingredients as well as side products and eluted with solvents specified. The column chromatography solvents were distilled by the appropriate drying agent before use. A variety of spectroscopic methods were used to characterize each of the molecules.

Synthesis of 7-(diethylamino)-2*H*-chromen-2-one (1): Diethyl malonate (4.16 g, 0.026 mol) and 4-(diethylamino)salicylaldehyde (2.5 g, 0.013 mol) were dissolved in 30 mL of pure EtOH. Next, pyridine (1.29 mL, 0.016 mol) was added, and it was refluxed at 90 °C for 6 h. The solvent was then drawn out in a vacuum once the reaction mixture had been cooled to room temperature. The residue was mixed with 20 mL of HCl (37%) and 20 mL of glacial AcOH, and the mixture was again refluxed at 125 °C for an additional 6 h. After being brought to room temperature, the reaction mixture was dissolved in 100 mL of ice-cold distilled H_2O. By adding 40% aqueous NaOH, the pH of the solution was kept at 5, and the combination remained at room temperature for 30 minutes. It was filtered to obtain a yellow precipitate that was then rinsed with distilled H_2O to acquire a pure, solid yellow compound **1**.

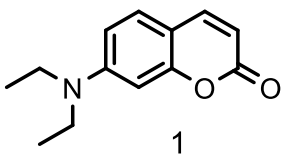

1

Yield: 2.26 g (80%)

^{1}H NMR ($CDCl_3$, 300 MHz, 25 °C): δ = 7.57 (d, J = 9.3 Hz, 1H), 7.28 (d, J = 8.7 Hz, 1H), 6.59 (dd, J = 2.6 Hz, 8.8 Hz, 1H), 6.52 (d, J = 2.5 Hz, 1H), 6.07 (d, J = 9.3 Hz, 1H), 3.45 (q, J = 7.1 Hz, 4H), and 1.24 (t, J = 7.1 Hz, 6H) ppm.
^{13}C NMR ($CDCl_3$, 75 MHz, 25 °C) δ = 162.2, 156.7, 150.6, 143.7, 128.8, 109.2, 108.8, 108.4, 97.6, 44.9, and 12.4 ppm.
HRMS (ESI +ve) *m*/*z*: Observed for $C_{13}H_{16}NO_2^+$ $[M+H]^+$ = 218.1170, $[M+H]^+$ calcd = 218.1176.

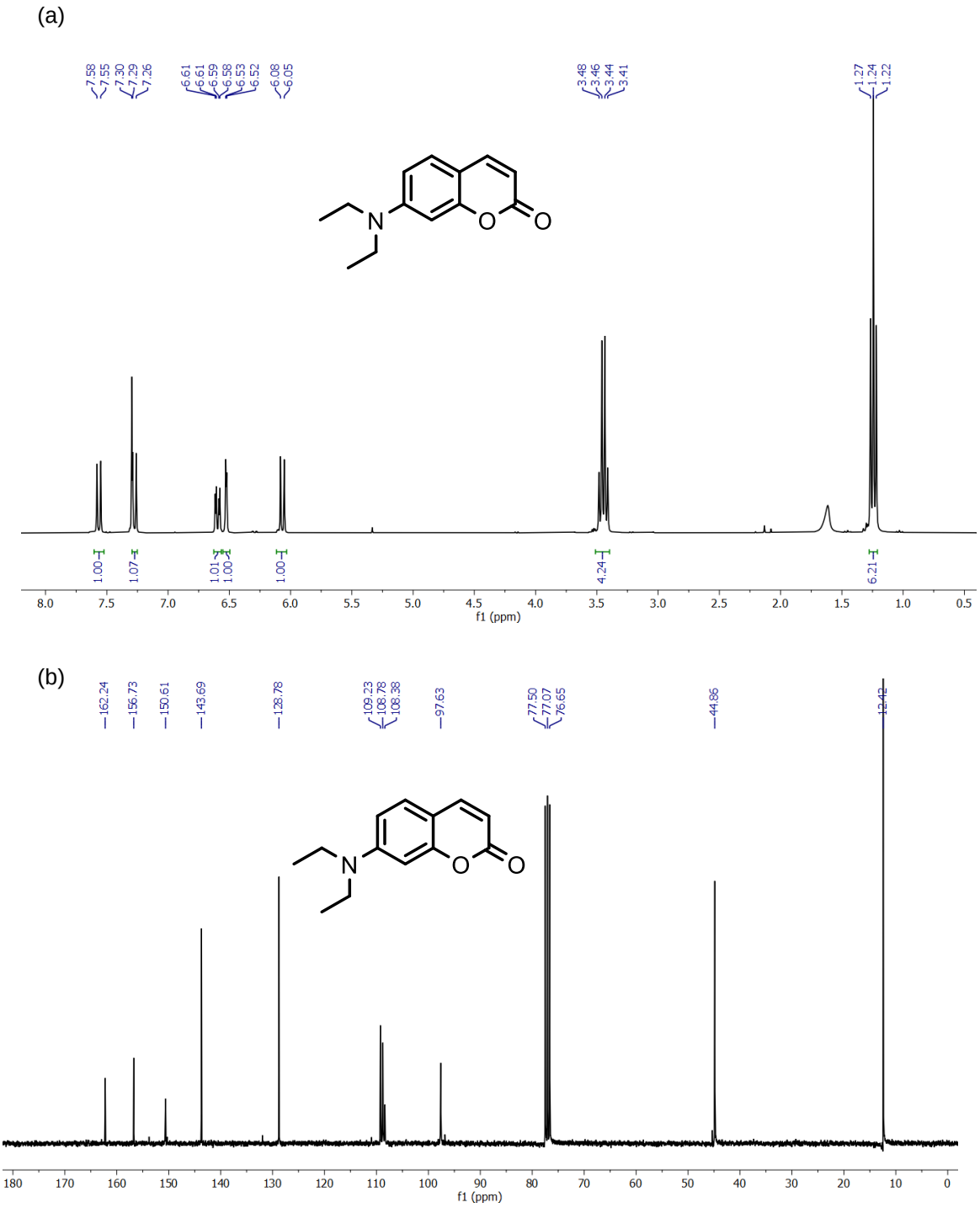

Figure 3. (a) ^{1}H NMR (300 MHz, $CDCl_3$, 25 °C) spectrum and (b) ^{13}C NMR (75 MHz, $CDCl_3$, 25 °C) spectrum of **1**.

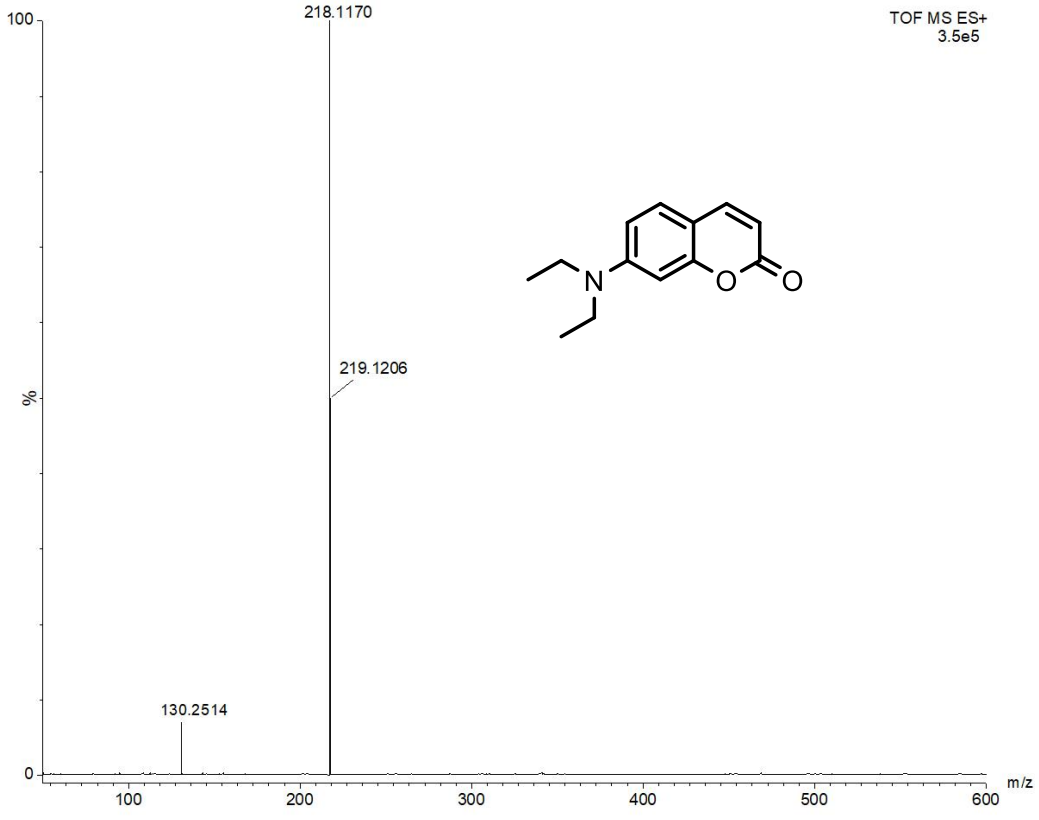

Figure 4. HRMS (ESI +ve) spectrum of compound **1**.

Synthesis of 7-(diethylamino)-2-oxo-2*H*-chromene-3-carbaldehyde (2): Anhydrous DMF (10.8 mL, 0.147 mol) was taken into a 25 mL two-neck round bottomed flask under N_2 atmosphere and $POCl_3$ (2 mL, 0.021 mol) was added dropwise, and the mixture was stirred at 0 °C for 30 min. The solution of 1 (1.5 g, 0.007 mol) in anhydrous DMF (7 mL) was added dropwise to the DMF-$POCl_3$ mixture at 0 °C. After being heated at 60 °C for 12 h, the mixture was cooled and put into ice-cold distilled H_2O. With the addition of a 20% aqueous NaOH solution, the resulting solution's pH was kept at 7. The residue was filtered, and rinsed with distilled H_2O numerous times. The substance was dried using a rotary evaporator to obtain the pure product **2** as an orange solid.

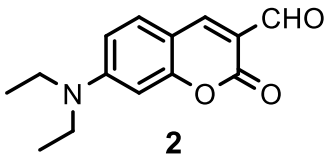

2

Yield: 1.20 g (70%).

^{1}H NMR ($CDCl_3$, 300 MHz, 25 °C): δ = 10.12 (s, 1H), 8.25 (s, 1H), 7.41 (d, J = 9.0 Hz, 1H), 6.63 (dd, J = 2.5 Hz, 9.0 Hz, 1H), 6.48 (d, J = 2.5 Hz, 1H), 3.47 (q, J = 7.1 Hz, 4H), and 1.25 (t, J = 7.1 Hz, 6H) ppm.

^{13}C NMR ($CDCl_3$, 75 MHz, 25 °C) δ = 187.9, 161.9, 158.9, 153.5, 145.4, 132.5, 114.3, 110.2, 108.2, 97.2, 45.3, and 12.5 ppm.

HRMS (ESI +ve) *m*/*z*: Observed for $C_{14}H_{16}NO_3^+$ $[M+H]^+$ = 246.1132 , $[M+H]^+$ calcd = 246.1125.

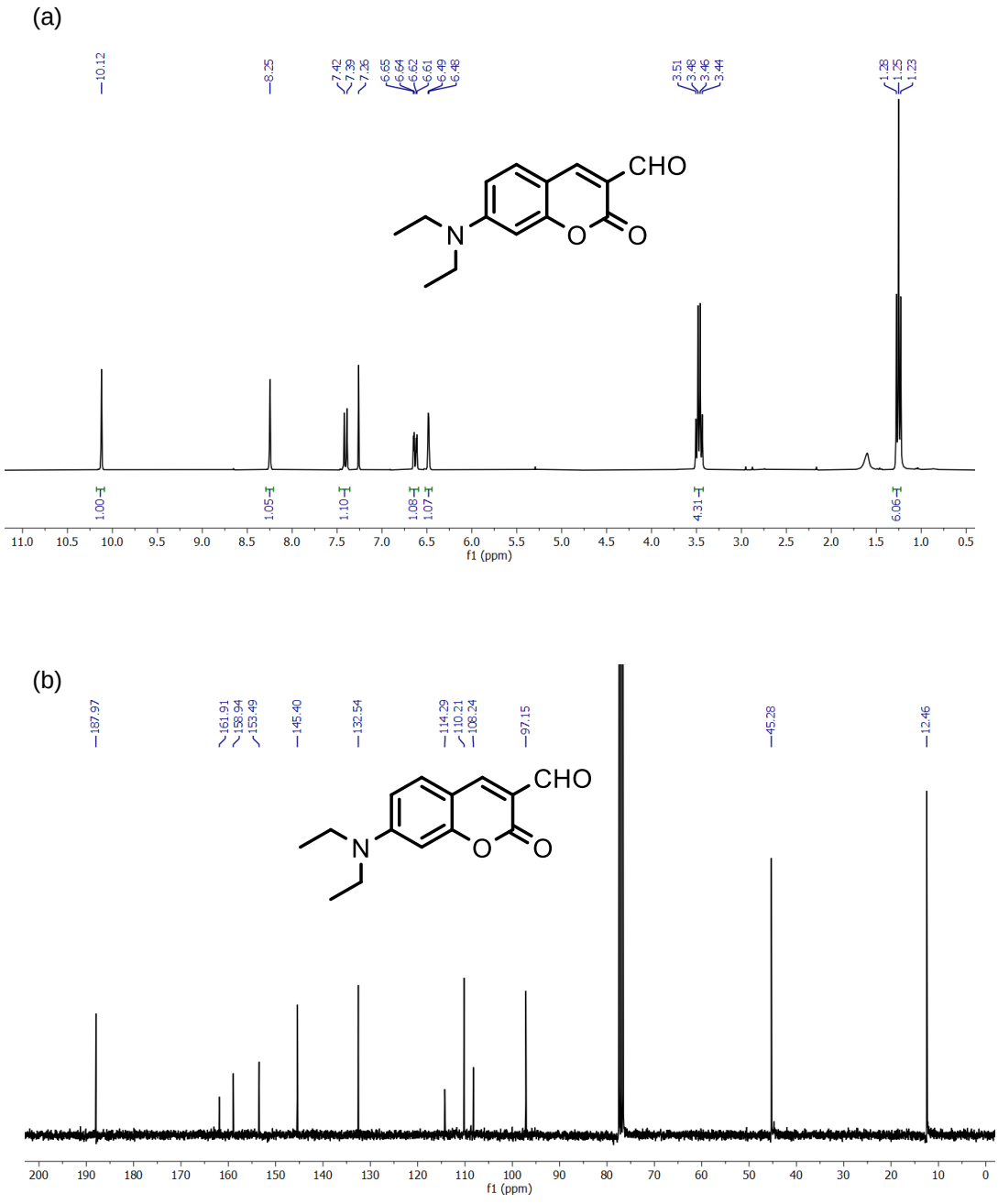

Figure 5. (a) ^{1}H NMR (300 MHz, $CDCl_3$, 25 °C) spectrum and (b) ^{13}C NMR (75 MHz, $CDCl_3$, 25 °C) spectrum of **2**.

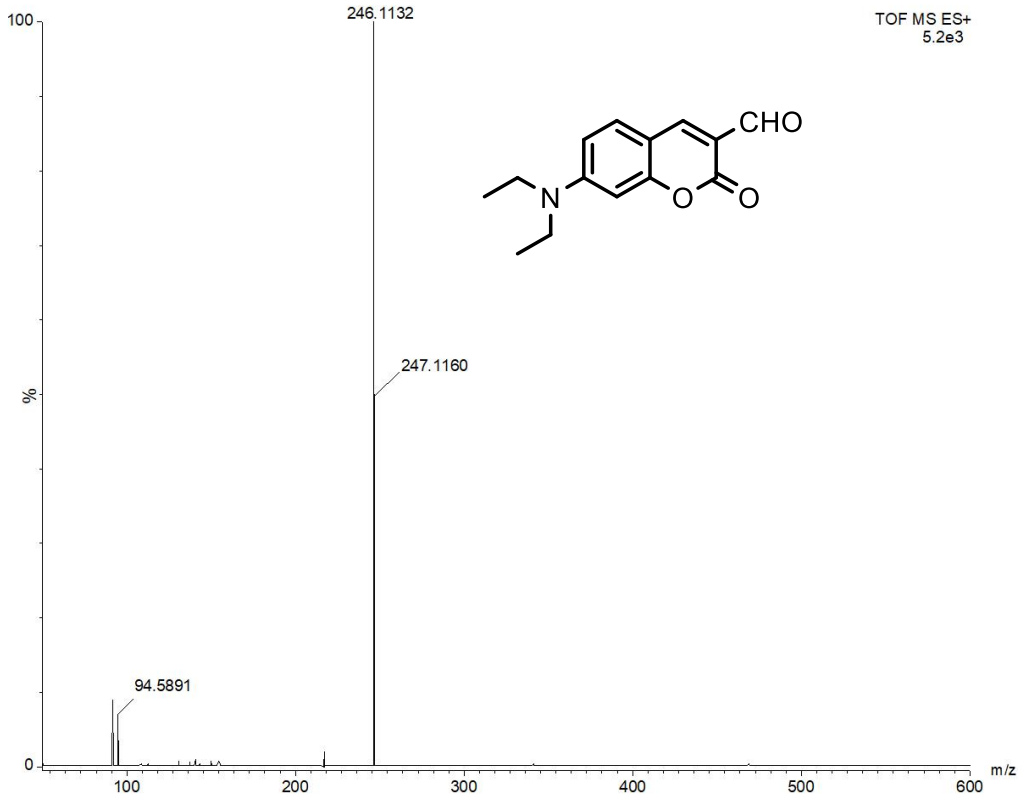

Figure 6. HRMS (ESI +ve) spectrum of compound **2**.

2-(4-(Diethylamino)phenyl)acetonitrile (3): To a solution of 2-(4-aminophenyl)acetonitrile (1 g, 0.008 mol) in dry DMF (20 mL), K_2CO_3 (2.1 g, 0.015 mol) was added, and the solution was stirred at 80 °C. Iodoethane (1.2 mL, 0.015 mol) was slowly added to the reaction mixture, and the reaction was continued at 80 °C for 12 h. DCM was used to extract the mixture after it had been cooled down to room temperature. The organic phase was dried over anhydrous Na_2SO_4, filtered, and the solvent evaporated in a vacuum. EtOAc and n-hexane (5:95 v/v, R_f = 0.7) were used in column chromatography to obtain the pure product **3** as a brown colored liquid.

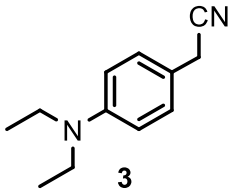

3

Yield: 1.08 g (72%).

^{1}H NMR (300 MHz, $CDCl_3$, 25 °C): δ = 7.16 (d, J = 8.3 Hz, 2H), 6.68 (d, J = 8.3 Hz, 2H), 3.65 (s, 2H), 3.37 (q, J = 7.1 Hz, 4H), and 1.18 (t, J = 7.1 Hz, 6H) ppm.

^{13}C NMR (75 MHz, $CDCl_3$, 25 °C): δ = 147.4, 129.0, 118.8, 115.9, 112.1, 44.4, 22.6, and 12.5 ppm.

HRMS (ESI +ve) *m*/*z*: Observed for $C_{12}H_{17}N_2^+$ $[M+H]^+$ = 189.1386, $[M+H]^+$ calcd = 189.1386.

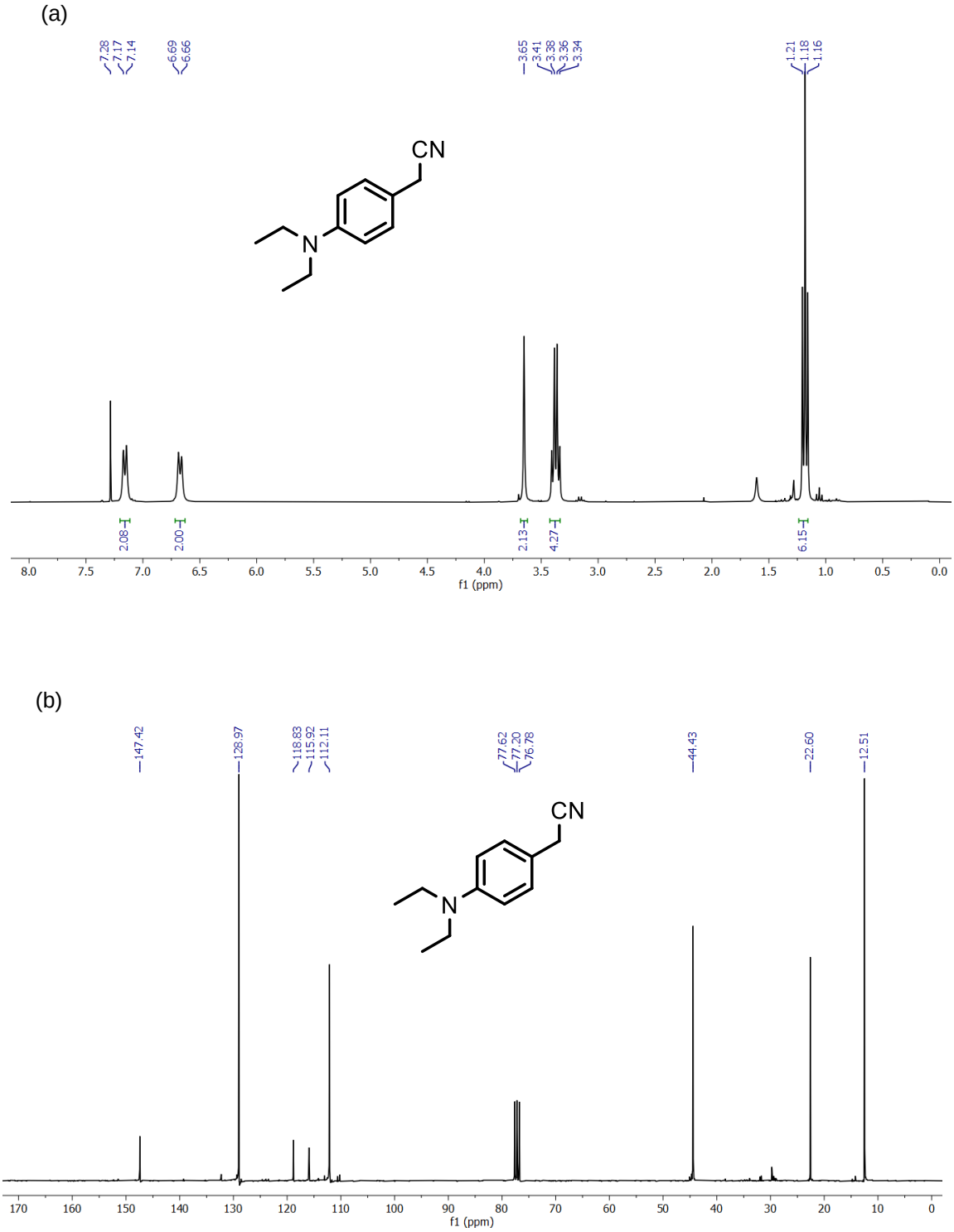

Figure 7. (a) ^{1}H NMR (300 MHz, $CDCl_3$, 25 °C) spectrum and (b) ^{13}C NMR (75 MHz, $CDCl_3$, 25 °C) spectrum of **3**.

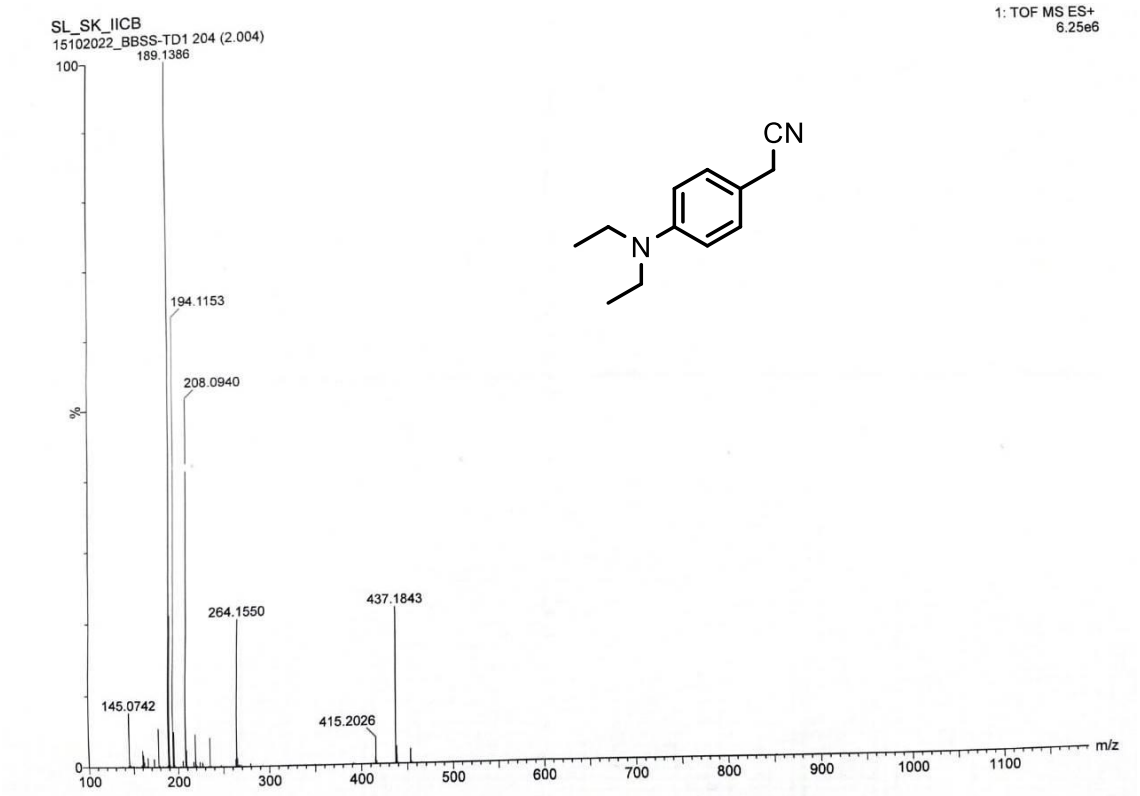

Figure 8. HRMS (ESI +ve) spectrum of compound **3**.

(*Z*)-3-(7-(diethylamino)-2-oxo-2*H*-chromen-3-yl)-2-(4-(diethylamino)phenyl)acrylonitrile (Cou-AIE): Compounds 2 (0.49 g, 0.002 mol), 3 (0.38 g, 0.002 mol), and 20 mL *tert*-BuOH were placed in a round-bottomed flask. Then tetrabutylammonium hydroxide (TBAOH, 25% in Methanol, 0.629 mL) was added dropwise into the mixture. The solution was stirred at 80 °C for 24 h under N_2 atmosphere. It was cooled to room temperature, and the crude product was filtered, washed with MeOH, and dried. The crude material was further purified by silica gel column chromatography using DCM:MeOH (20:1 v/v, R_f = 0.6) to acquire the pure product **Cou-AIE** as red solid.

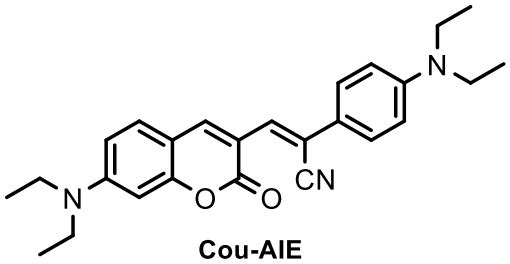

Cou-AIE

Yield: 0.42 g (51%).

^{1}H NMR ($CDCl_3$, 300 MHz, 25 °C): δ = 8.63 (s, 1H), 7.74 (d, J = 8.8 Hz, 1H), 7.65 (s, 1H), 7.57 (d, J = 8.8 Hz, 2H), 6.72–6.64 (m, 3H), 6.51 (d, J = 2.4 Hz, 1H), 3.50–3.41 (m, 8H), and 1.28 (t, J = 7.1 Hz, 12H) ppm.

^{13}C NMR ($CDCl_3$, 75 MHz, 25 °C): δ = 159.5, 140.8, 131.6, 131.3, 130.9, 130.5, 130.3, 128.3, 126.9, 126.7, 126.6, 114.4, 113.6, 111.2, 111.1, 44.5, and 12.6 ppm.

HRMS (ESI +ve) *m*/*z*: Observed for $C_{26}H_{30}N_3O_2^+$ $[M+H]^+$ = 416.2320, $[M+H]^+$ calcd = 416.2333. Observed for $C_{26}H_{31}N_3O_2^{2+}$ $[M+2H]^+$ = 208.6206, $[M+H]^+$ calcd = 208.6203.

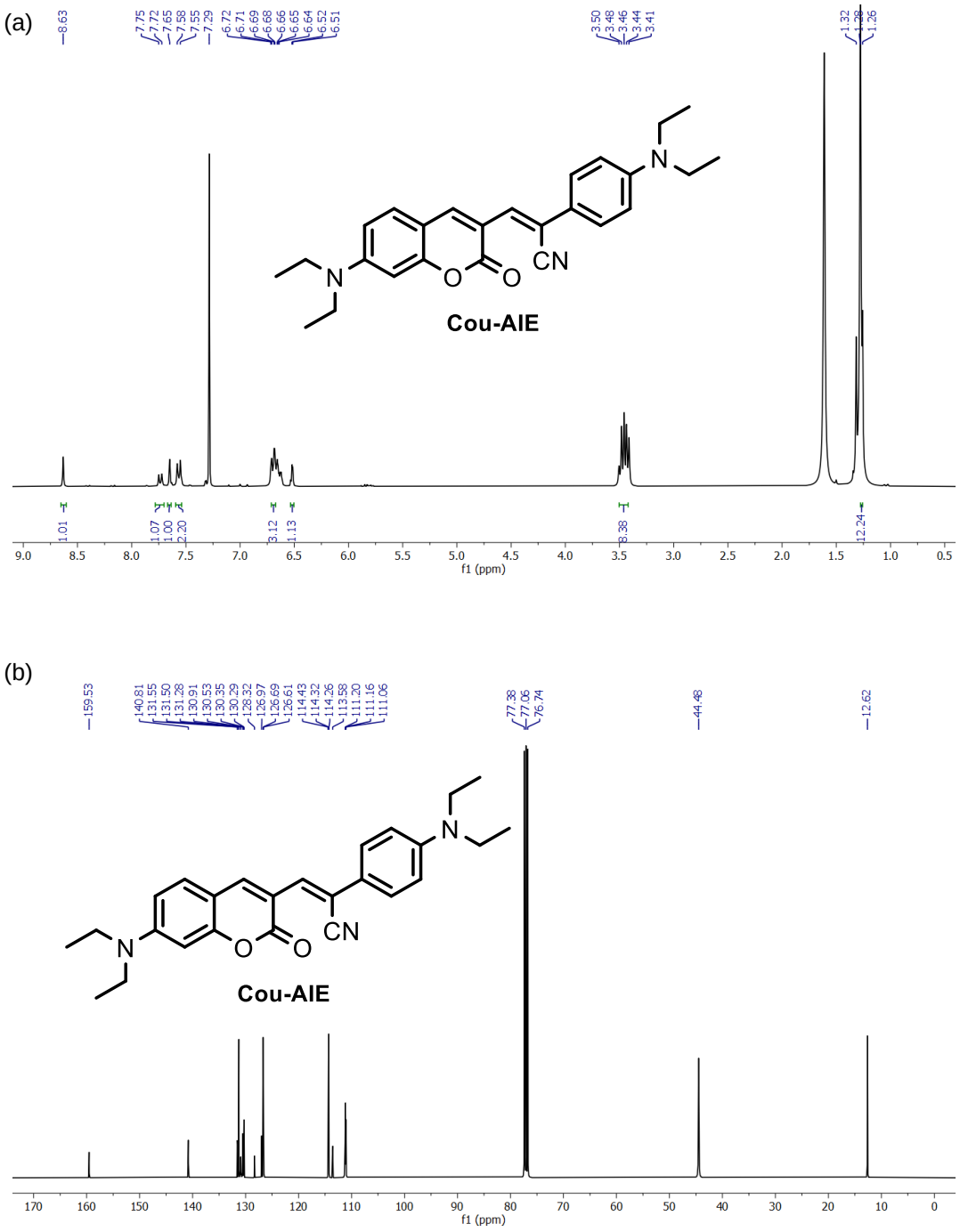

Figure 9. (a) ^{1}H NMR (300 MHz, $CDCl_3$, 25 °C) spectrum and (b) ^{13}C NMR (75 MHz, $CDCl_3$, 25 °C) spectrum of **Cou-AIE**.

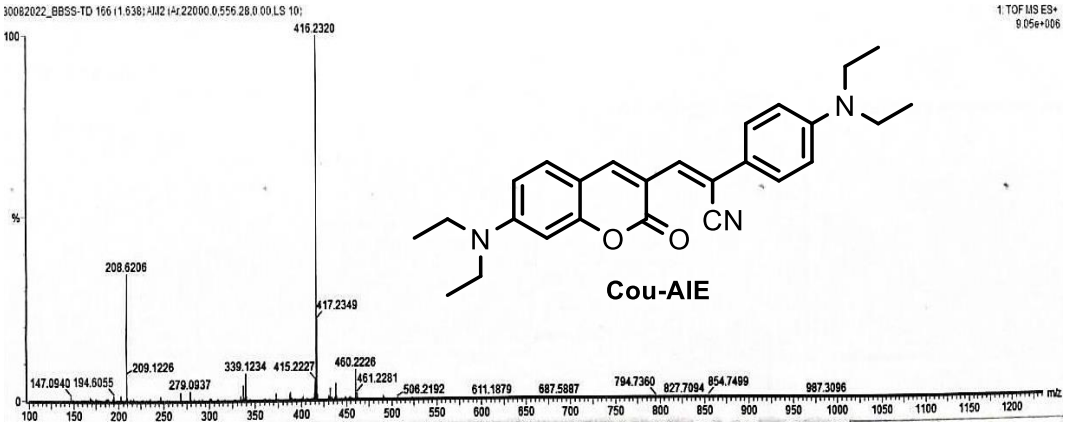

Figure 10. HRMS (ESI +ve) spectrum of Compound **Cou-AIE**.

2-(4-(ethylamino)phenyl)acetonitrile (4): To a solution of 2-(4-aminophenyl)acetonitrile (1.06 g, 0.008 mol) in dry DMF (15 mL), K_2CO_3 (0.97 g, 0.007 mol) was mixed, and the solution was stirred at 80 °C. Then iodoethane (0.6 mL, 0.007 mol) was slowly added to the reaction mixture, and the reaction was continued at 80 °C for 12 h. It was cooled to room temperature, and the mixture was extracted with DCM. The organic phase was dried over anhydrous Na_2SO_4, filtered, and the solvent evaporated in a vacuum. The crude product was purified by column chromatography using EtOAc and n-hexane (10:90 v/v, R_f = 0.3) to obtain the pure product **4** as a brown colored liquid.

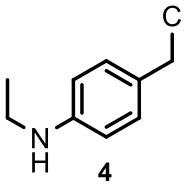

4

Yield: 0.96 g (86%).

^{1}H NMR (300 MHz, $CDCl_3$, 25 °C): δ = 7.13 (d, J = 8.3 Hz, 2H), 6.61 (d, J = 8.6 Hz, 2H), 3.65 (s, 2H), 3.18 (q, J = 7.1 Hz, 2H), and 1.28 (t, J = 7.1 Hz, 3H) ppm.

^{13}C NMR (75 MHz, $CDCl_3$, 25 °C): δ = 148.1, 128.9, 118.7, 117.8, 113.1, 38.5, 22.8, and 14.8 ppm.

HRMS (ESI +ve) *m/z*: Observed for $C_{10}H_{13}N_2^+$ $[M+H]^+$ = 161.1077, $[M+H]^+$ calcd = 161.1073.

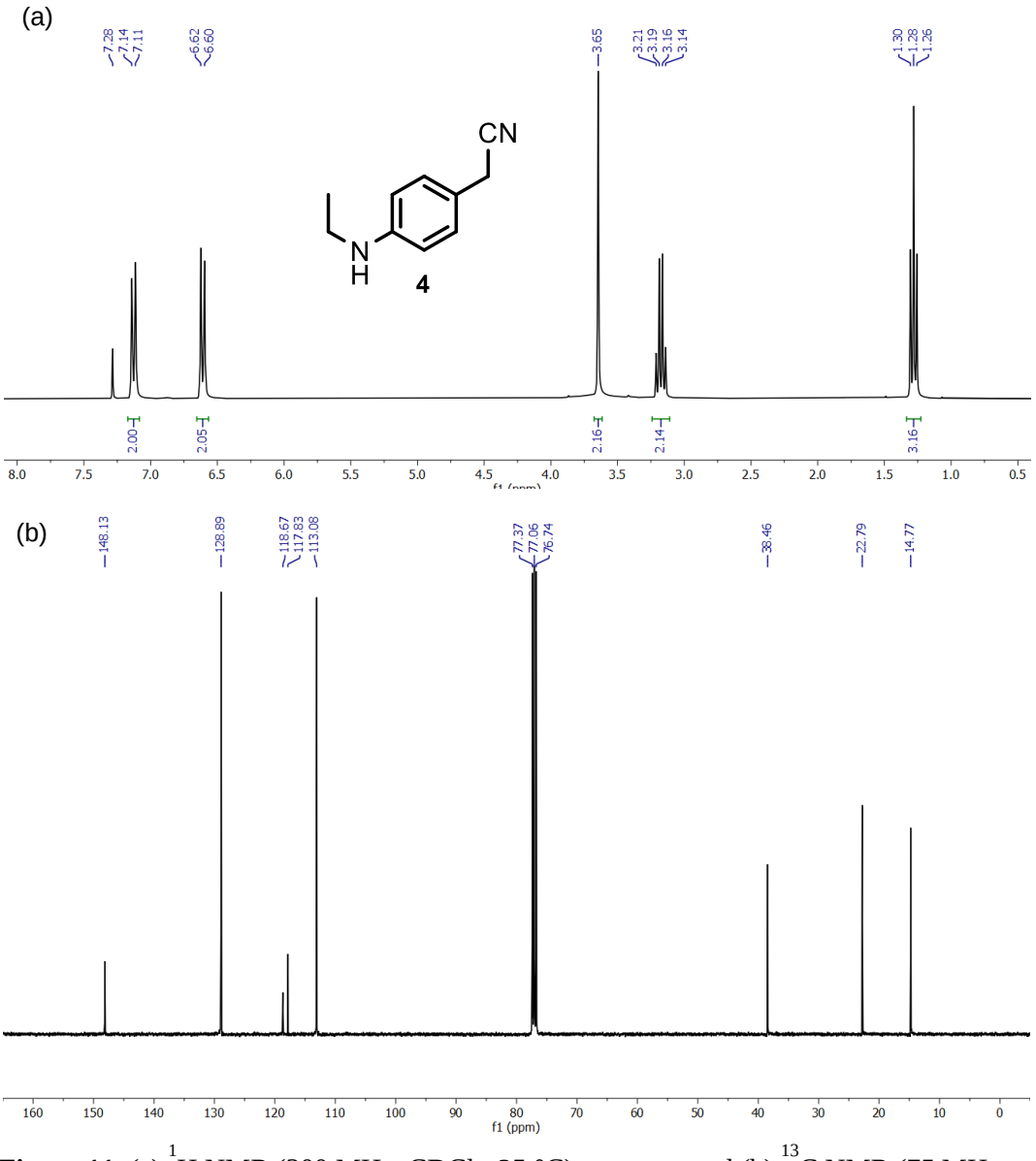

Figure 11. (a) ^{1}H NMR (300 MHz, $CDCl_3$, 25 °C) spectrum and (b) ^{13}C NMR (75 MHz, $CDCl_3$, 25 °C) spectrum of **4**.

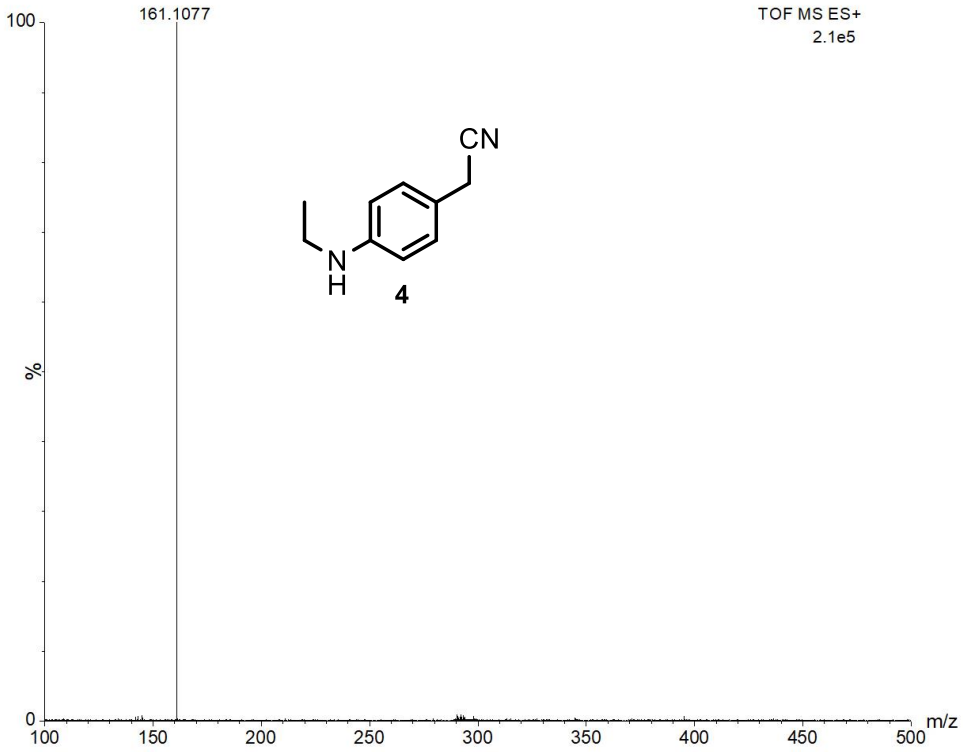

Figure 12. HRMS (ESI +ve) spectrum of compound **4**.

***Tert*-butyl *N*-(4-(cyanomethyl)phenyl)-*N*-ethylglycinate (5)**: A mixture of 2-(4-(ethylamino)phenyl)acetonitrile (0.96 g, 0.006 mol), *tert*-butyl bromoacetate

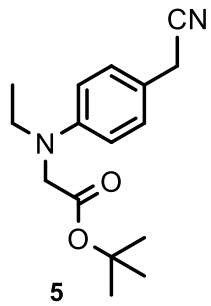

5

(1.37 mL, 0.009 mol), K_2CO_3 (2.49 g, 0.018 mol), and KI (0.15 g, 0.0009 mol) in CH_3CN (20 mL) was heated to reflux for 12 h. The solvent was evaporated off, after which DCM (50 mL) and H_2O (50 mL) were added, and the organic layer was extracted. The DCM layer was dried with anhydrous Na_2SO_4. After removal of the solvents using a rotary evaporator, the crude product was purified over silica gel using n-Hexane:EtOAc (95:5, R_f = 0.7) as the eluent to yield the pure compound **5** as a brown liquid.

Yield: 1.51 g (92%).

^{1}H NMR (300 MHz, $CDCl_3$, 25 °C): δ = 7.16 (d, J = 8.6 Hz, 2H), 6.63 (d, J = 8.6 Hz, 2H), 3.93 (s, 2H), 3.64 (s, 2H), 3.47 (q, J = 7.1 Hz, 2H), 1.47 (s, 9H), and 1.22 (t, J = 6.8 Hz, 3H) ppm.

^{13}C NMR (75 MHz, $CDCl_3$, 25 °C): δ = 170.3, 147.6, 128.9, 118.7, 117.2, 112.2, 81.6, 53.1, 46.3, 28.1, 22.6, and 12.5 ppm.

HRMS (ESI +ve) *m*/*z*: Observed for $C_{16}H_{22}N_2O_2Na^+$ $[M+Na]^+$ = 297.1570, $[M+Na]^+$ calcd = 297.1573.

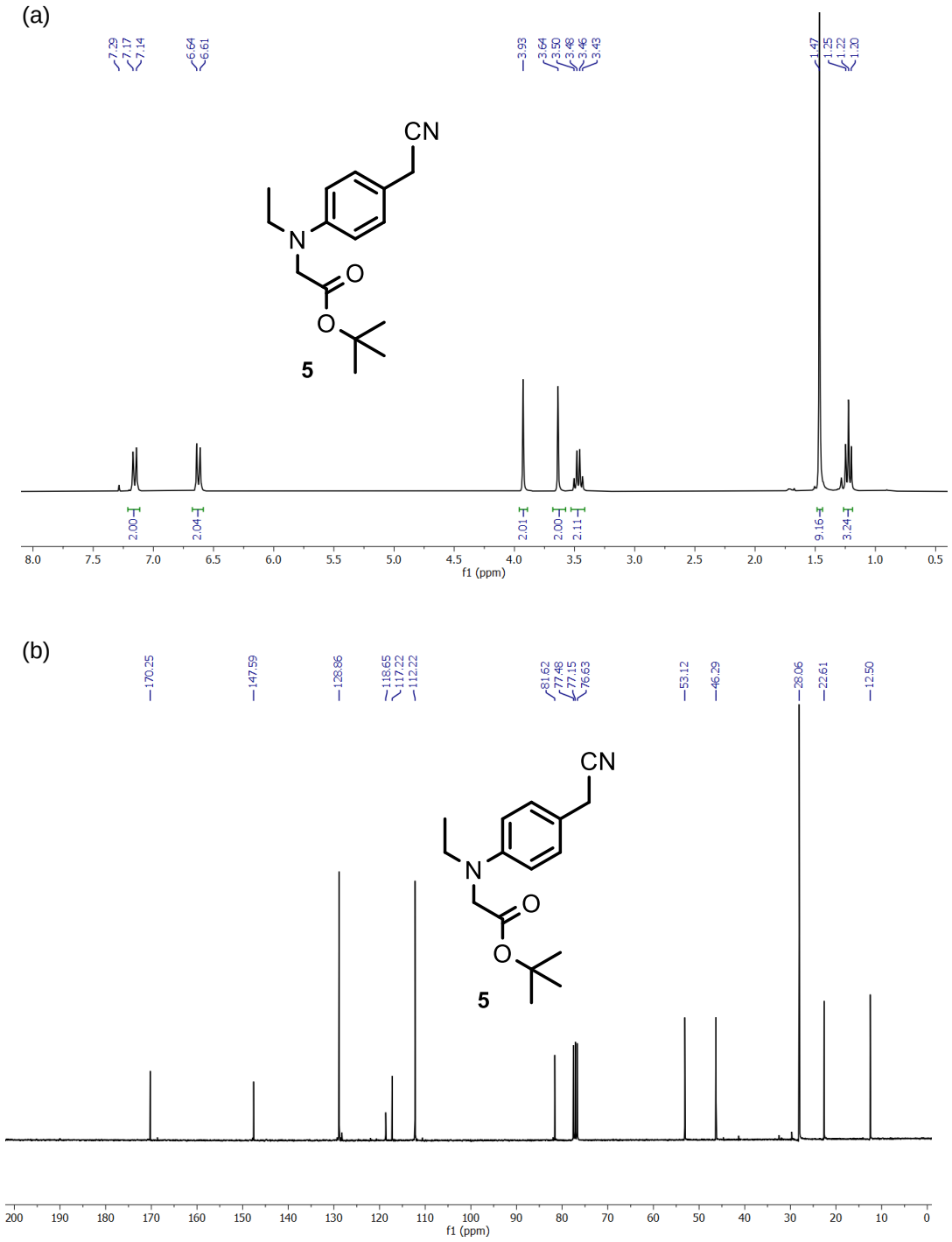

Figure 13. (a) ^{1}H NMR (300 MHz, $CDCl_3$, 25 °C) spectrum and (b) ^{13}C NMR (75 MHz, $CDCl_3$, 25 °C) spectrum of **5**.

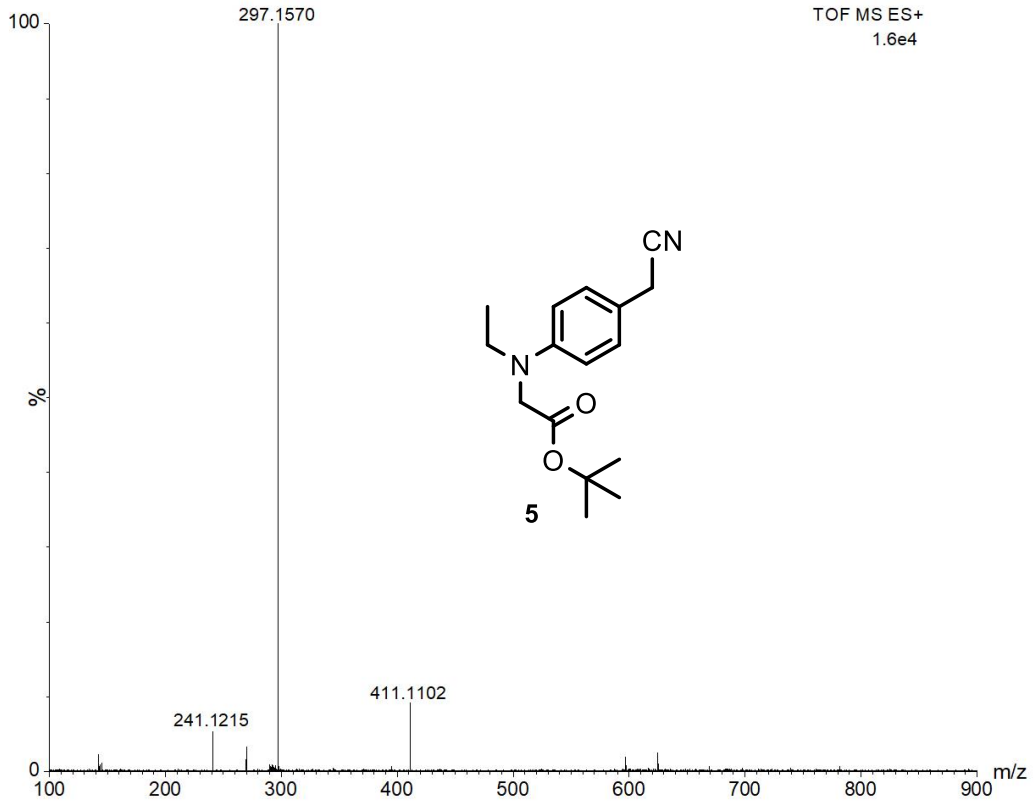

Figure 14. HRMS (ESI +ve) spectrum of compound **5**.

***Tert*-butyl (*Z*)-*N*-(4-(1-cyano-2-(7-(diethylamino)-2-oxo-2*H*-chromen-3-yl)vinyl)phenyl)-*N*-ethylglycinate (6)**: Compounds 2 (0.49 g, 0.002 mol), 5 (0.55 g, 0.002 mol), and ^{t}BuOH (20 mL) were placed in a round-bottomed flask. Then tetrabutylammonium hydroxide (TBAOH, 25% in Methanol, 0.629 mL) was added dropwise into the mixture. Next, the solution was refluxed for 24 h under N_2 atmosphere. The solution was cooled to room temperature, and the crude product was filtered. The residue was washed with MeOH and then dried. The crude residue was further purified by column chromatography utilizing Hexane/EtOAc (5:1, R_f = 0.6) as the eluent to acquire the pure material **6** as a red solid.

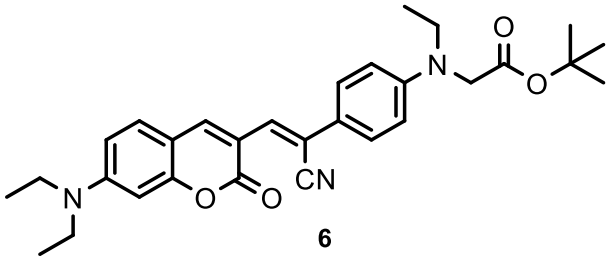

6

Yield: 0.4 g (40%).

^{1}H NMR ($CDCl_3$, 400 MHz, 25 °C): δ = 8.63 (s, 1H), 7.67 (s, 1H), 7.57 (d, J = 9.0 Hz, 2H), 7.40 (d, J = 9.0 Hz, 1H), 6.67–6.62 (m, 3H), 6.51 (d, J = 2.5 Hz, 1H), 3.97 (s, 2H), 3.54–3.42 (m, 6H), 1.48 (s, 9H), and 1.25 (t, J = 7.3 Hz, 9H) ppm.

^{13}C NMR (101 MHz, $CDCl_3$, 25 °C): δ = 169.9, 162.1, 156.3, 151.5, 148.5, 139.5, 130.3, 129.9, 127.1, 122.5, 118.7, 114.7, 111.9, 110.1, 109.6, 108.7, 97.2, 81.9, 53.1, 46.4, 45.0, 29.7, 28.1, and 12.5 ppm.

HRMS (ESI +ve) *m*/*z*: Observed for $C_{30}H_{35}N_3O_4Na^+$ $[M+Na]^+$ = 524.2524, $[M+Na]^+$ calcd = 524.2520.

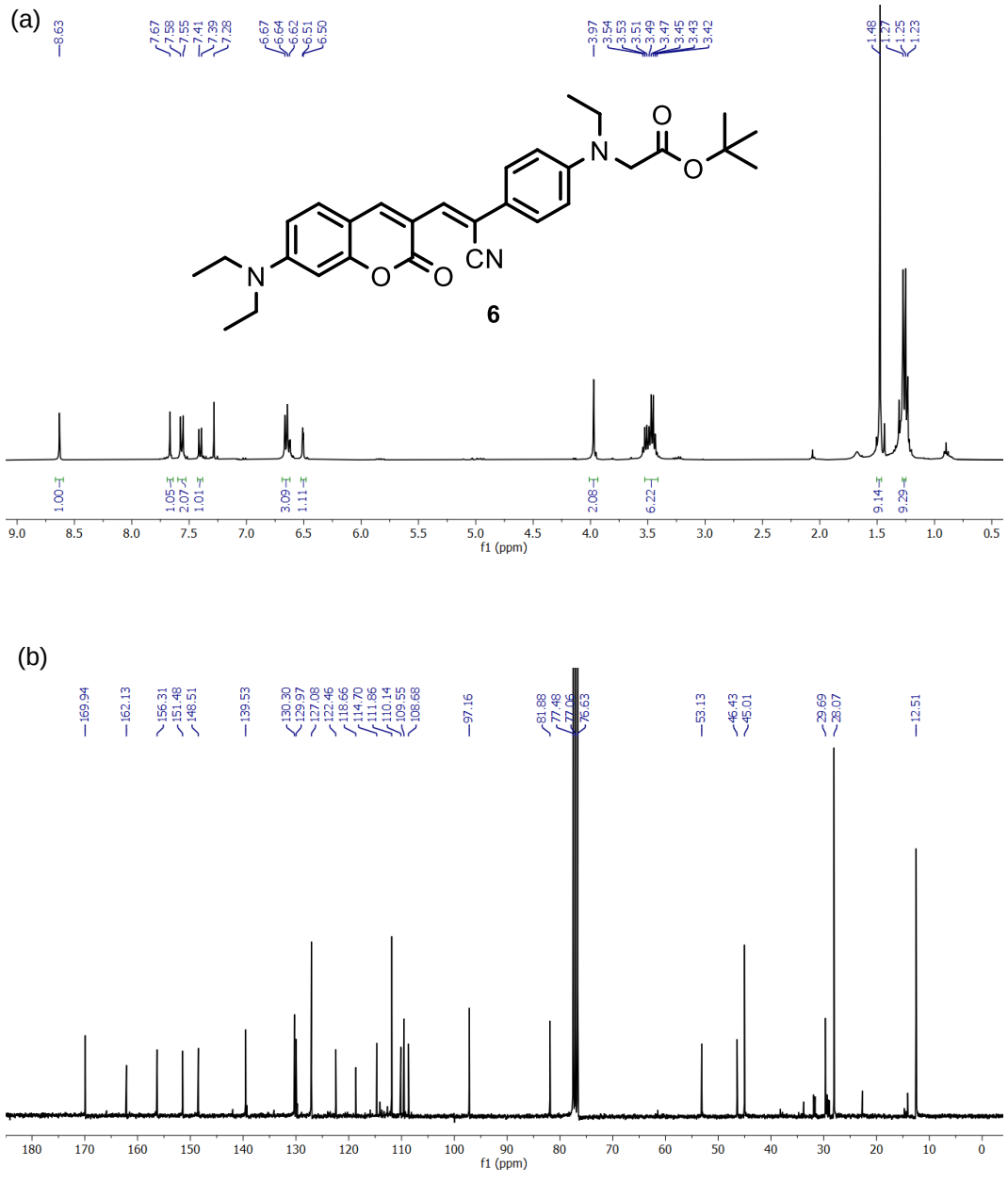

Figure 15. (a) ^{1}H NMR (400 MHz, $CDCl_3$, 25 °C) spectrum and (b) ^{13}C NMR (101 MHz, $CDCl_3$, 25 °C) spectrum of **6**.

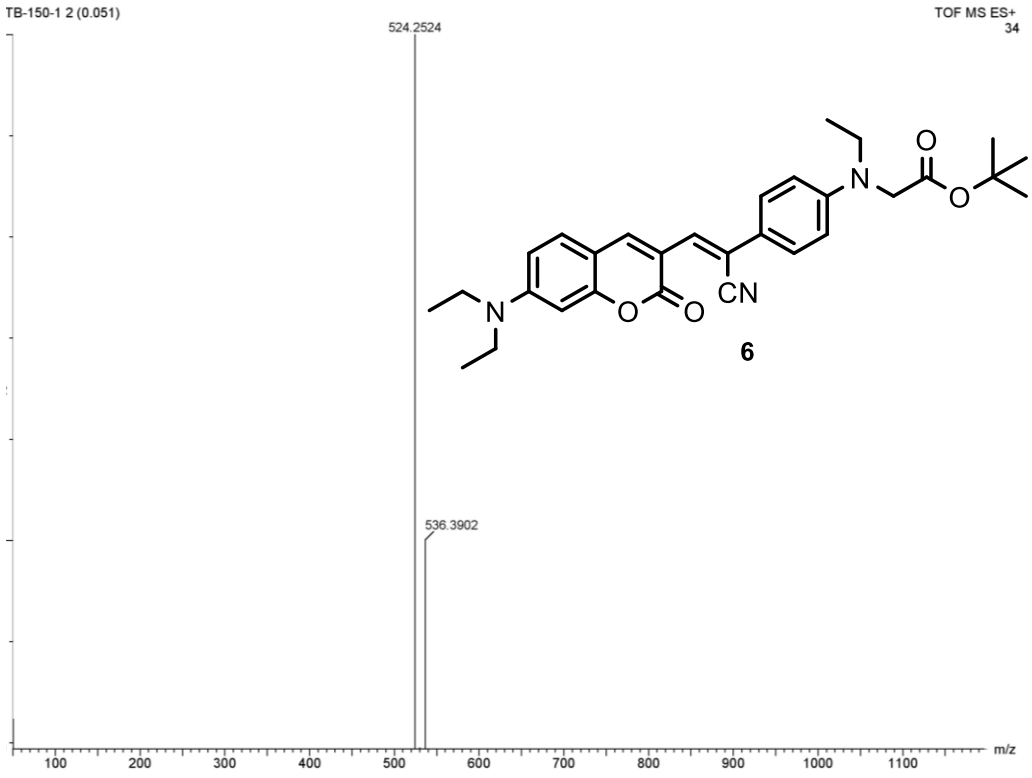

Figure 16. HRMS (ESI +ve) spectrum of compound **6**.

(*Z*)-*N*-(4-(1-cyano-2-(7-(diethylamino)-2-oxo-2*H*-chromen-3-yl)vinyl)phenyl)-*N*-ethylglycine (7): To a solution of **6** (0.5 g, 0.001 mol) in EtOH (10 mL), 10 mL of 10% NaOH was mixed, and the solution was heated to reflux for 15 min. The solution was acidified to pH 2 using conc. HCl and cooled to 0 °C, giving a large amount of precipitate. The product was filtered and thoroughly washed with water, dried, and recrystallized in absolute EtOH to give **7** as a reddish solid.

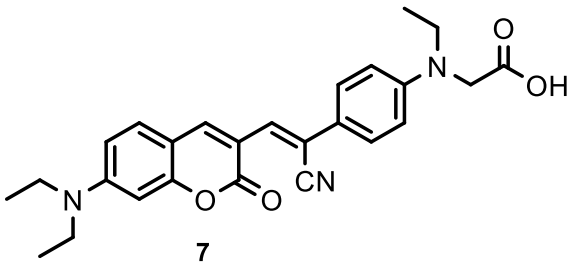

7

Yield: 0.31 g (70%).

^{1}H NMR (400 MHz, $CDCl_3$, 25 °C): δ = 10.15 (s, 1H), 8.64 (s, 1H), 7.67 (s, 1H), 7.57 (d, J = 7.8 Hz, 2H), 7.44 (d, J = 9.2 Hz, 1H), 6.67–6.65 (m, 3H), 6.52 (d, J = 2.4 Hz, 1H), 3.97 (s, 2H), 3.53–3.46 (m, 6H), and 1.28 (t, J = 7.5 Hz, 9H) ppm.

^{13}C NMR (101 MHz, $CDCl_3$, 25 °C) δ = 190.3, 176.8, 165.9, 159.7, 158.1, 149.9, 145.4, 141.8, 127.2, 118.9, 118.5, 117.8, 111.9, 110.2, 98.7, 61.5, 45.3, 45.0, 12.6, and 12.5 ppm.

HRMS (ESI +ve) m/z: Observed for $C_{26}H_{27}N_3O_4$ $[M]^+$ = 445.2008, $[M]^+$ calcd = 445.2002.

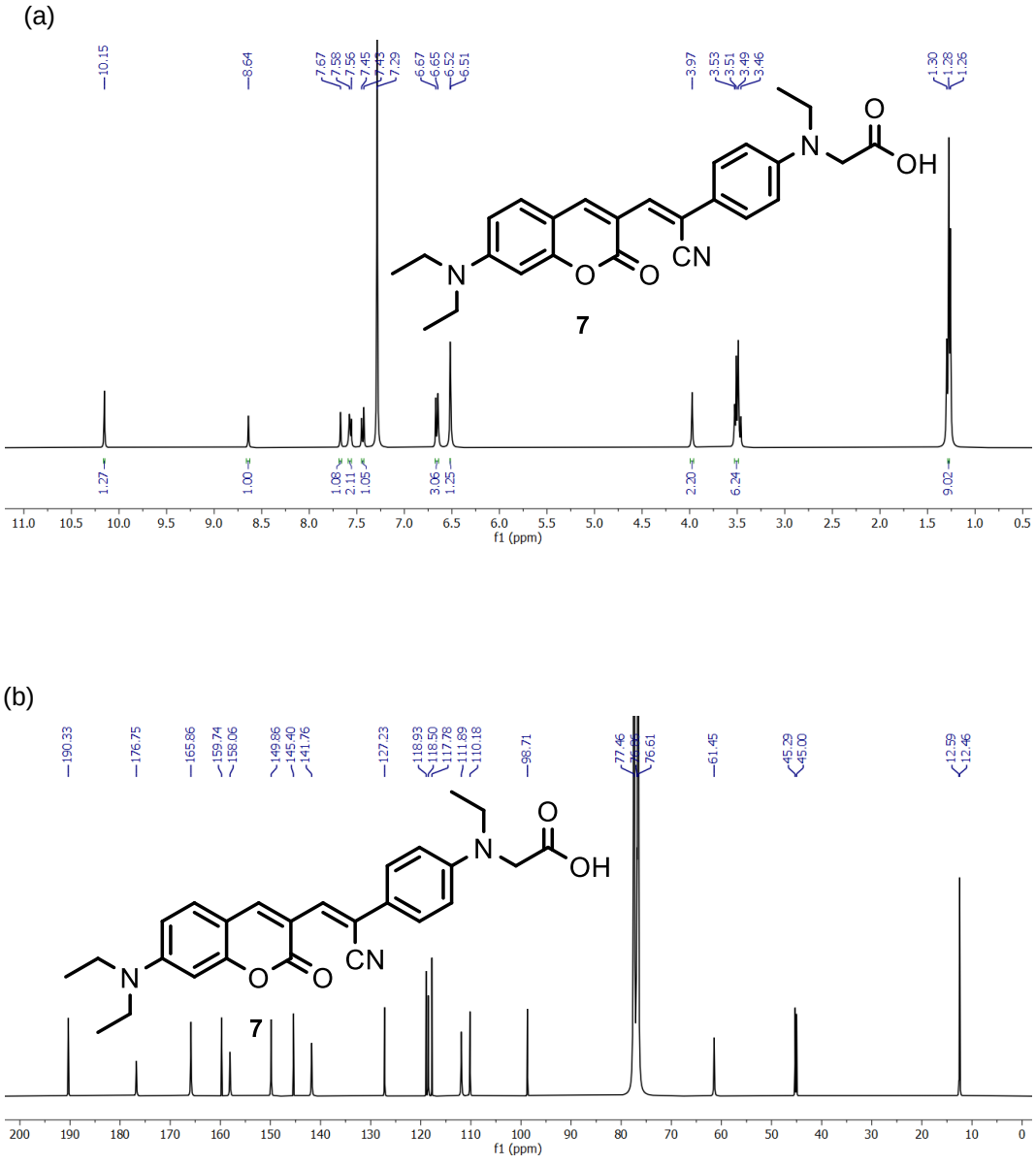

Figure 17. (a) ^{1}H NMR (400 MHz, $CDCl_3$, 25 °C) spectrum and (b) ^{13}C NMR (101 MHz, $CDCl_3$, 25 °C) spectrum of **7**.

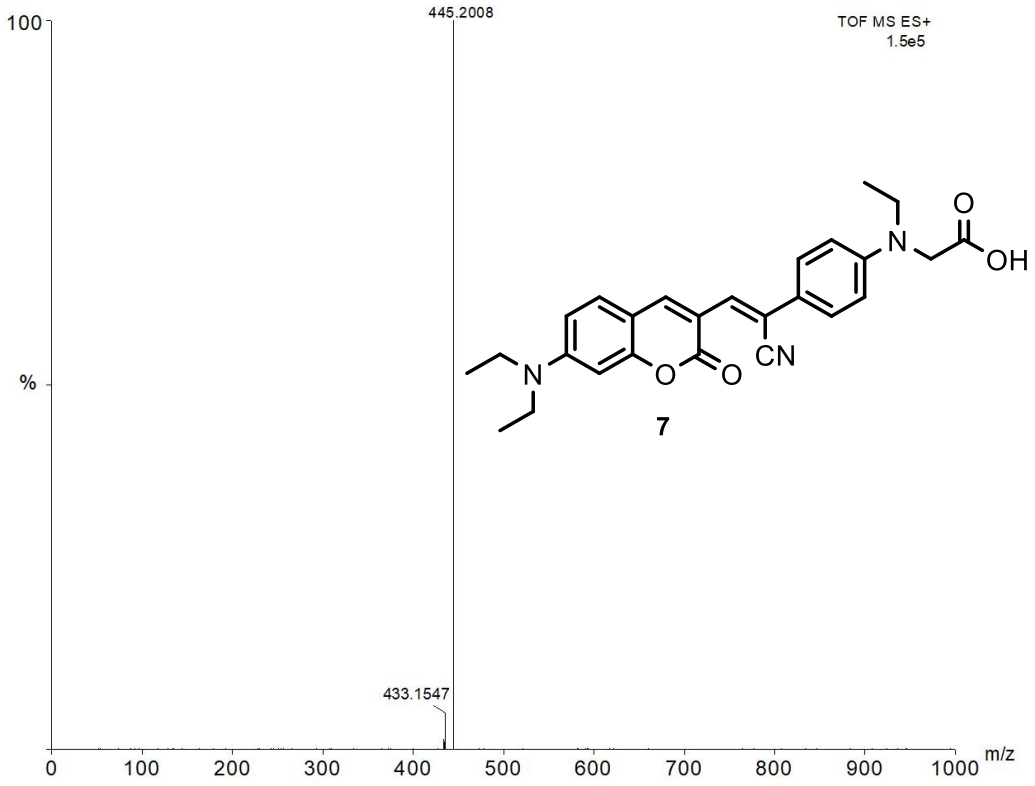

Figure 18. HRMS (ESI +ve) spectrum of compound **7**.

(2-Aminoethyl)triphenylphosphonium bromide (8): 2-Bromoethylamine hydrobromide (2.05 g, 0.01 mol) and PPh_3 (2.62 g, 0.01 mol) was stirred in CH_3CN (15 mL) at 80 °C for 24 h in a N_2 atmosphere. A white precipitate was obtained and it was filtered. The residue was dissolved in water, and K_2CO_3 was added until the pH of the solution reached 10-11. DCM was mixed, and the extracted organic layer was rinsed with brine (3×). The organic portion was dried with anhydrous Na_2SO_4, filtered, and evaporated using a rotary evaporator to achieve a white residue. The residue was rinsed with Et_2O (3×) to acquire a white solid pure product (2-aminoethyl)triphenylphosphonium bromide.

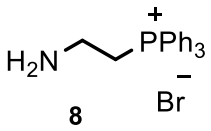

8

Yield: 3.67 g (95%).

^{1}H NMR (300 MHz, $CDCl_3$, 25 °C): δ = 7.83–7.64 (m, 15H), 3.84–3.75 (m, 2H), 3.15–3.07 (m, 2H), and 2.81 (br, 2H) ppm.

^{13}C NMR (75 MHz, $CDCl_3$, 25 °C): δ = 134.7, 133.8, 130.5, 119.0, 117.9, 41.7, and 23.9 ppm.

ESI-HRMS (+ve) *m/z*: Observed for $C_{20}H_{21}NP^+$ $[M]^+$ = 306.1407, $[M]^+$ calcd = 306.1406.

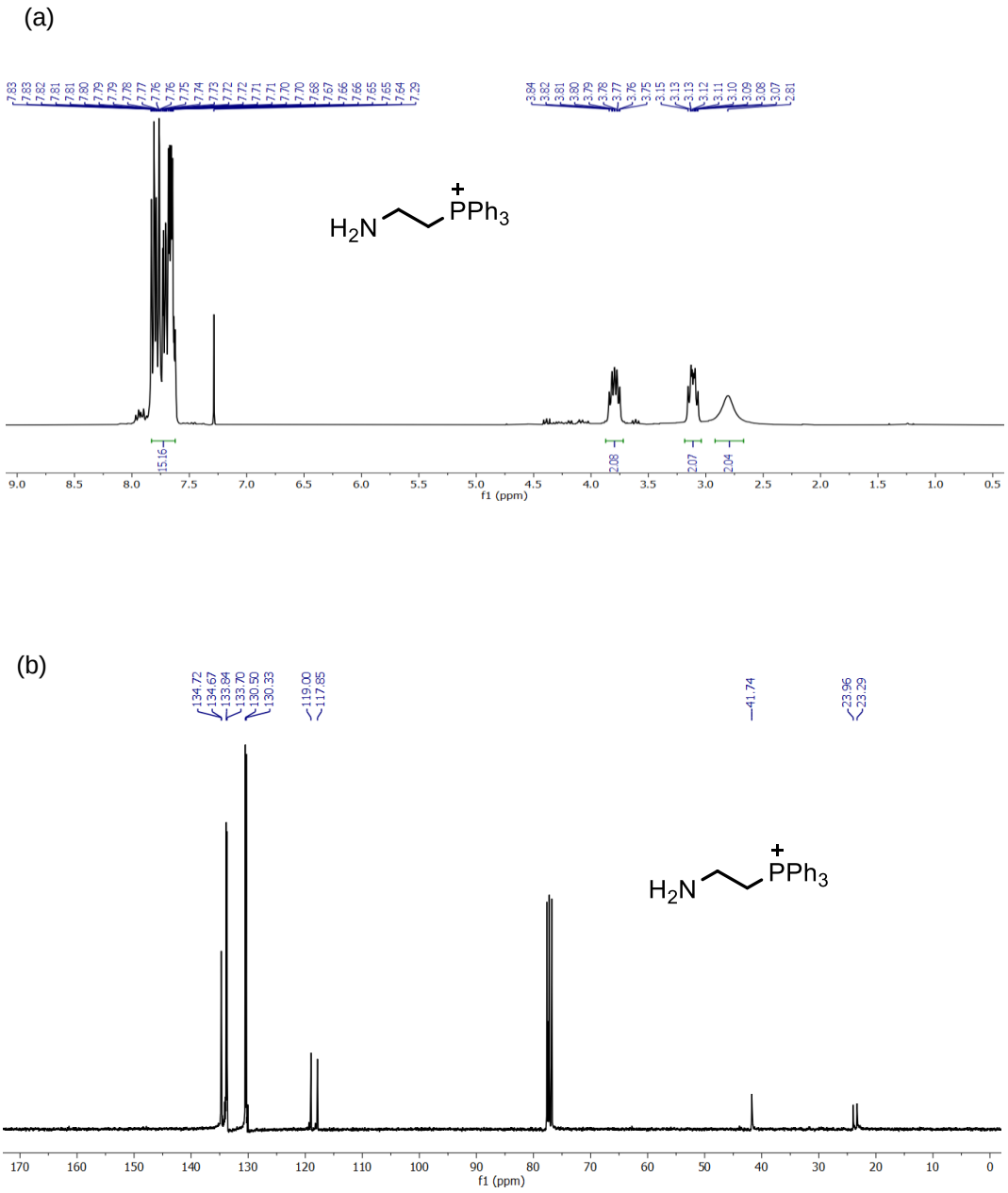

Figure 19. (a) ^{1}H NMR (300 MHz, $CDCl_3$, 25 °C) spectrum and (b) ^{13}C NMR (75 MHz, $CDCl_3$, 25 °C) spectrum of (2-aminoethyl)triphenylphosphonium bromide.

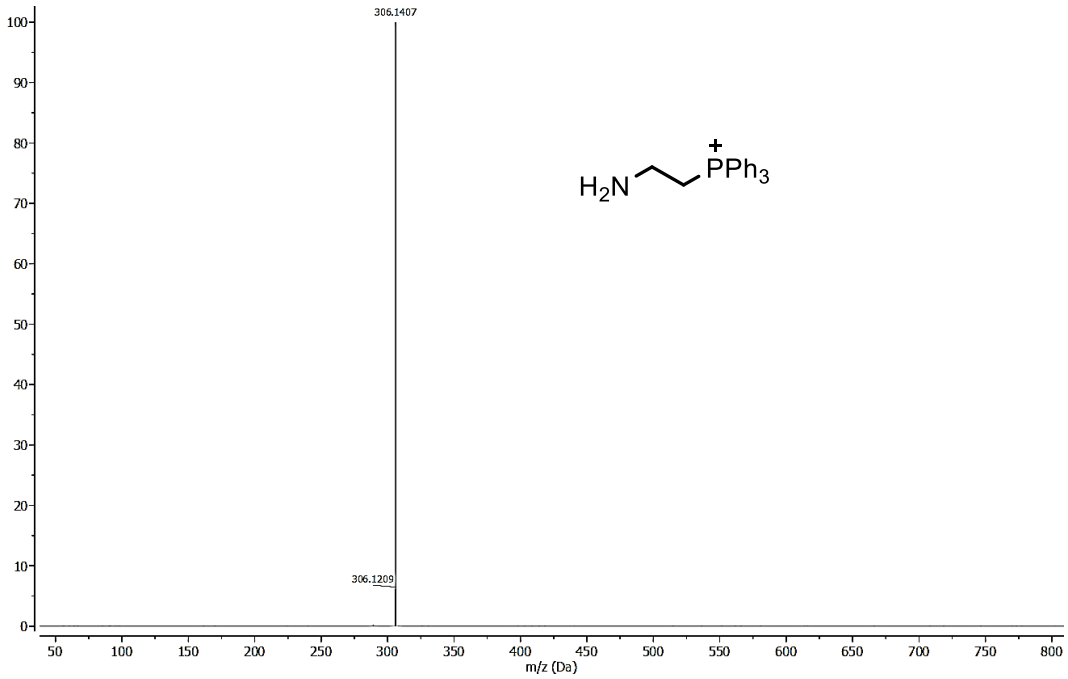

Figure 20. HRMS (ESI +ve) spectrum of compound (2-aminoethyl)triphenylphosphonium bromide.

(*Z*)-(2-(2-((4-(1-cyano-2-(7-(diethylamino)-2-oxo-2*H*-chromen-3-yl)vinyl)phenyl)(ethyl)amino)acetamido)ethyl)triphenylphosphonium bromide (Cou-AIE-TPP$^+$): (*Z*)-*N*-(4-(1-cyano-2-(7-(diethylamino)-2-oxo-2*H*-chromen-3-yl)vinyl)phenyl)-*N*-ethylglycine (Compound 7, 0.16 g, 0.35 mmol), DIPEA (60 μL, 0.35 mmol), and HATU (0.13 g, 0.35 mmol) were dissolved in 5 mL of DMF under N_2 atmosphere and stirred for 30 m at 25 °C. The synthesized compound (2-aminoethyl)triphenylphosphonium bromide (Compound 8, 0.16 g, 0.42 mmol) was mixed to this solution and stirred for 24 h. The resultant solution was evaporated under reduced pressure. Cold Et_2O was mixed to obtain a red colored crude product, which was collected by filtration. This crude compound was purified via column chromatography utilizing CH_2Cl_2:CH_3OH (95:5, R_f = 0.65) to get the red colored solid pure product **Cou-AIE-TPP$^+$**.

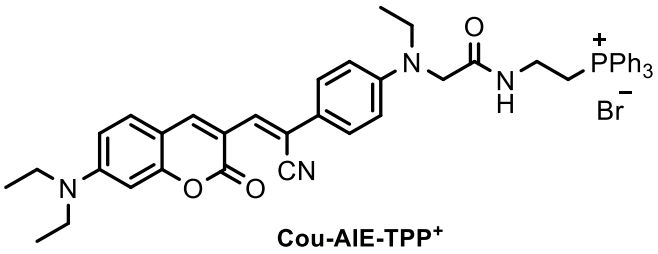

Cou-AIE-TPP$^+$

Yield: 0.19 g (67%).

^{1}H NMR (300 MHz, $CDCl_3$, 25 °C): δ = 8.62 (s, 1H), 7.91–7.64 (m, 16H), 7.55 (d, J = 8.9 Hz, 2H), 7.40 (d, J = 8.9 Hz, 1H), 6.66–6.60 (m, 3H), 6.50 (d, J = 2.4 Hz, 1H), 3.97 (2H, s), 3.86–3.75 (2H, m), 3.52–3.39 (6H, m), 3.17–3.12 (2H, m), and 1.29 (9H, t, J = 6.1 Hz) ppm.

^{13}C NMR (101 MHz, $CDCl_3$, 25 °C): δ = 169.9, 162.1, 156.3, 151.5, 148.5, 139.5, 134.6, 134.0, 133.9, 130.5, 130.4, 130.3, 130.0, 128.9, 128.8, 127.1, 122.5, 119.0, 118.2, 114.7, 112.2, 111.9, 109.6, 108.7, 97.2, 53.1, 46.4, 46.3, 45.0, 29.7, and 12.5 ppm.

DEPT-135 (101 MHz, $CDCl_3$, 25 °C): δ = 169.9 (disappear), 162.1 (disappear), 156.3 (disappear), 151.5 (disappear), 148.5 (disappear), 139.5 (positive), 134.6 (positive), 134.0 (positive), 133.9 (positive), 130.5 (positive), 130.4 (positive), 130.3 (positive), 130.0 (positive), 128.9 (positive), 128.8 (positive), 127.1 (positive), 122.5 (disappear),, 119.0 (disappear), 118.2 (disappear), 114.7 (disappear), 112.2 (positive), 111.9 (positive), 109.6 (positive), 108.7 (disappear), 97.2 (positive), 53.1 (negative), 46.4 (negative), 46.3 (negative), 45.0 (negative), 29.7 (negative), and 12.5 (negative) ppm.

^{31}P NMR (121 MHz, $CDCl_3$, 25 °C): δ = 23.9 (s) ppm.

2D NMR: ^{1}H–^{1}H COSY (Correlation Spectroscopy) NMR (300 MHz, $CDCl_3$, 25 °C) spectrum of Cou-AIE-TPP^{+} probe confirmed the coupling connectivity.

HRMS (ESI +ve) *m*/*z*: Observed for $C_{46}H_{47}N_4O_3P^{2+}$ $[M+H]^{2+}$ = 367.1695, $[M+H]^{2+}$ calcd = 367.1687.

Photophysical properties of Cou-AIE-TPP^{+} in PBS: λ_{abs}= 480 nm, λ_{em}= 604 nm, Stokes shift ($\Delta\lambda$) = 124 nm, ε = 1.68 ×10^{4} M^{-1}cm^{-1}, Φ_f = 0.45 in PBS [Φ_f of Rhodamine-B (reference) in EtOH = 0.49]. Fluorescence lifetime (τ) = 2.168 ± 0.126 ns in PBS.

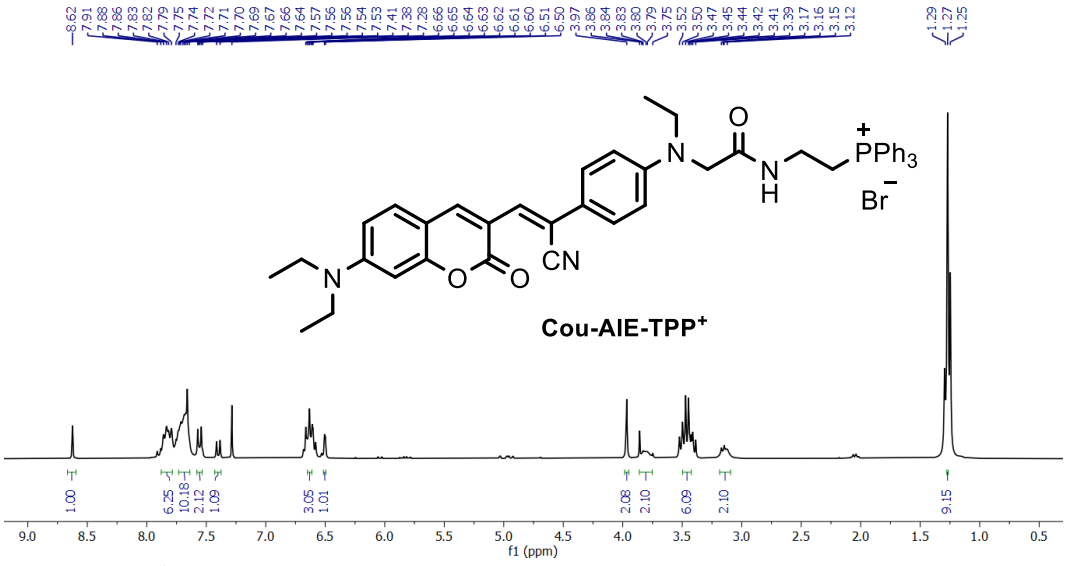

Figure 21. ^{1}H NMR (300 MHz, $CDCl_3$, 25 °C) spectrum of compound **Cou-AIE-TPP**$^{+}$.

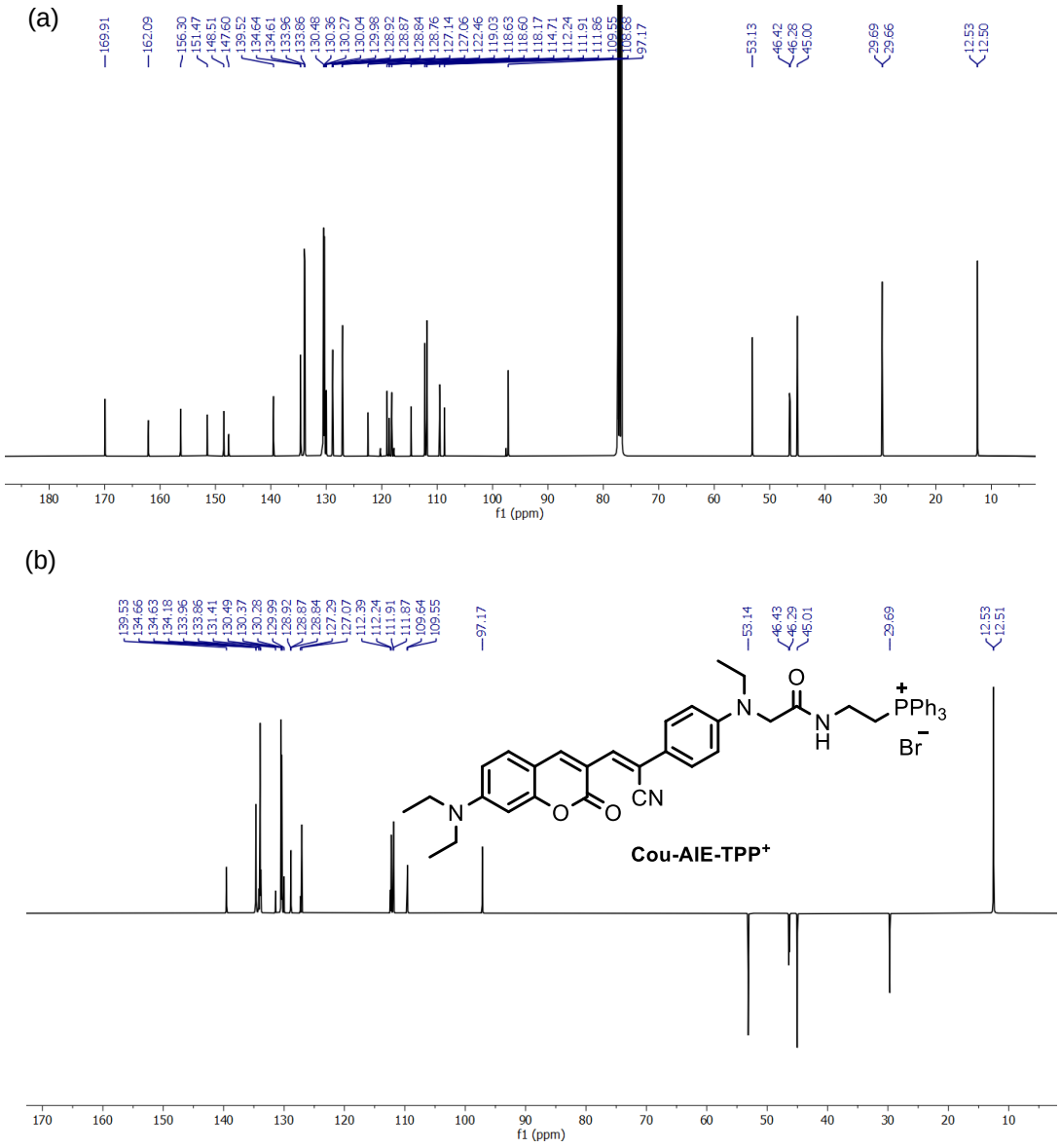

Figure 22. (a) ^{13}C NMR (101 MHz, $CDCl_3$, 25 °C) spectrum and (b) DEPT-135 (101 MHz, $CDCl_3$, 25 °C) spectrum of compound **Cou-AIE-TPP**$^{+}$.

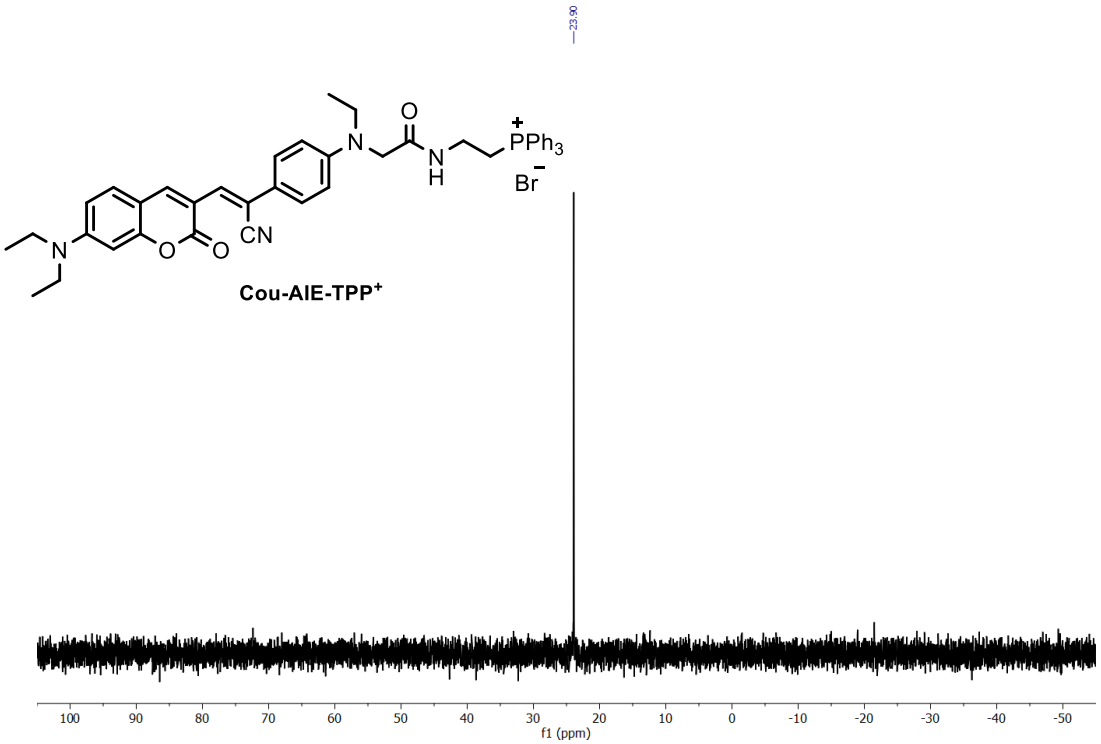

Figure 23. ^{31}P NMR (121 MHz, $CDCl_3$, 25 °C) spectrum of **Cou-AIE-TPP**$^{+}$ probe.

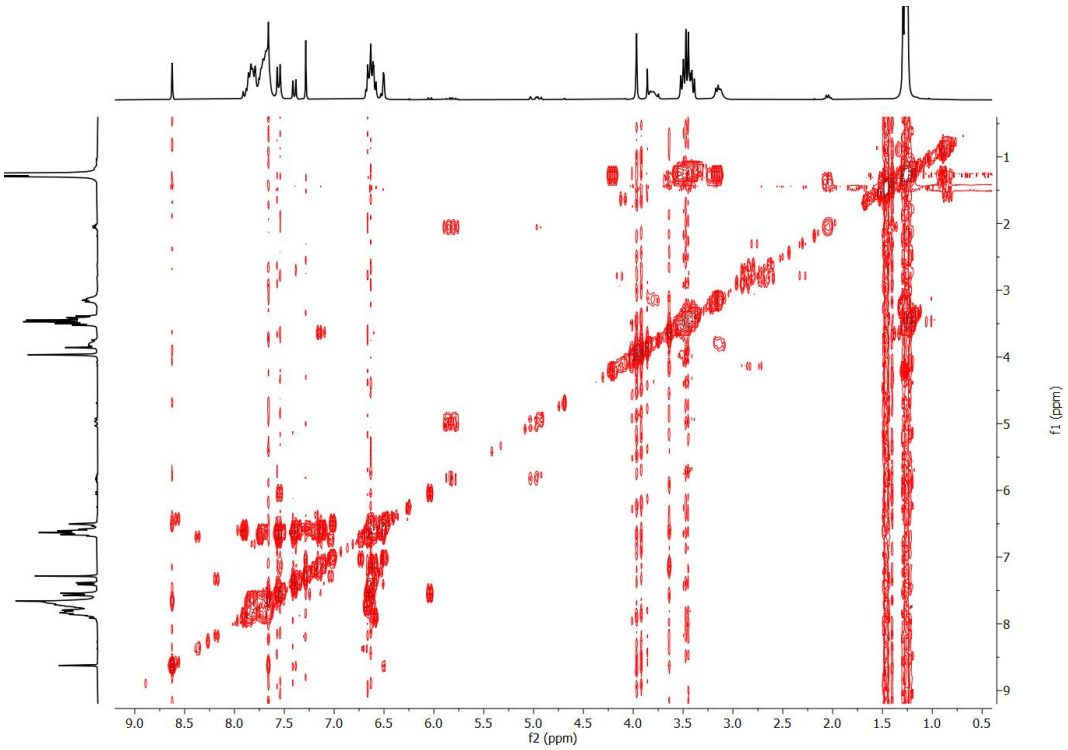

Figure 24. ^{1}H-^{1}H COSY (Correlation Spectroscopy) NMR (300 MHz, $CDCl_3$, 25 °C) spectrum of the probe **Cou-AIE-TPP**$^{+}$.

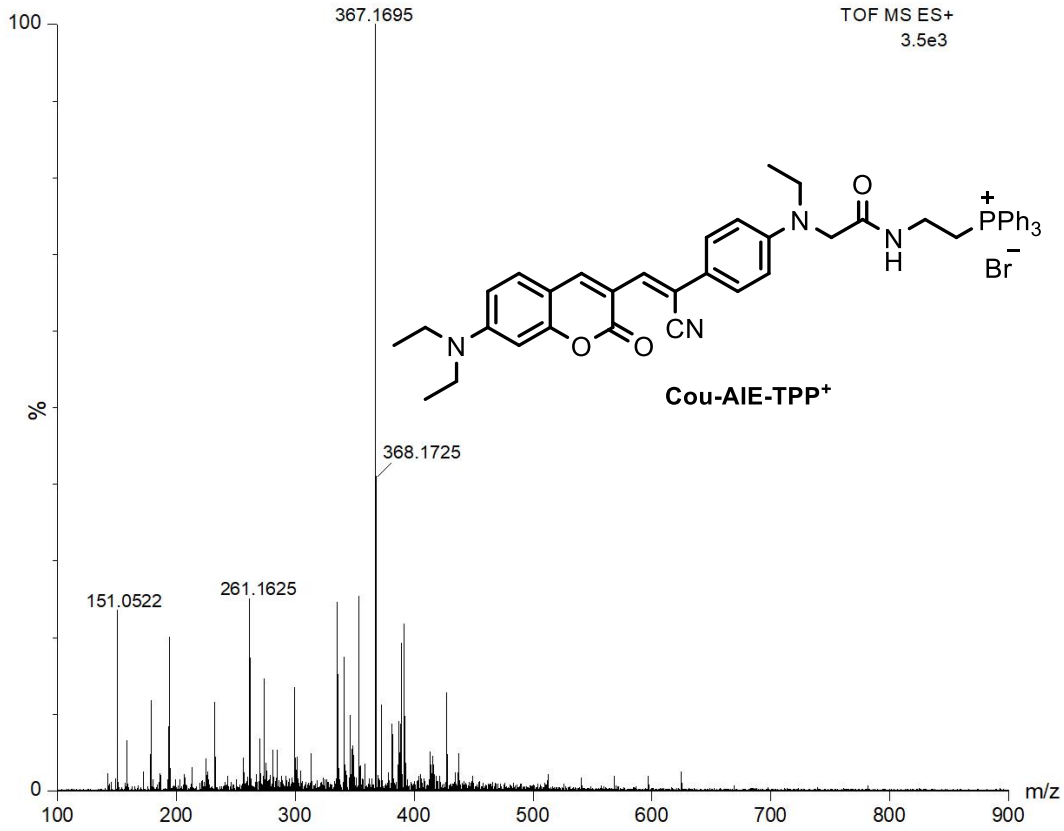

Figure 25. HRMS (ESI +ve) spectrum of compound **Cou-AIE-TPP**$^{+}$.

Synthesis of the Aβ40 peptide:

Manual MW-Assisted Solid-Phase Peptide Synthesis (SPPS)

Aβ40 peptide was synthesized by a manual microwave (MW)-assisted Fmoc-SPPS procedure on a MW peptide synthesizer (*CEM, Discover Bio*) and stored at –20 °C prior to use. Wang resin (LL, 0.60 mmol/g loading density) was used to synthesize Aβ40 peptide from the C-termini to the N-termini. Fmoc-amino acid building blocks Fmoc-Gly-OH, Fmoc-Ser(tBu)-OH, Fmoc-Asn(Trt)-OH, Fmoc-Lys(Boc)-OH, Fmoc-Glu(OtBu)-OH, Fmoc-Ala-OH, Fmoc-Ile-OH, Fmoc-Leu-OH, Fmoc-Met-OH, Fmoc-Val-OH, Fmoc-Tyr(tBu)-OH, Fmoc-His(Trt)-OH, Fmoc-Gln(Trt)-OH, Fmoc-Asp(tBu)-OH, Fmoc-Arg(Pbf)-OH, and Fmoc-Phe-OH were used.

Handling of Wang Resin and Fmoc Amino Acid Building Blocks: Fmoc amino acid building blocks were stored at –20 ºC. Wang resin was stored at 4 ºC. Before opening, all the Fmoc amino acid building blocks and resins were warmed to room temperature for 20 min.

First Amino Acid Loading on Wang Resin: For the synthesis of Aβ40 peptide, the first amino acid Fmoc-Val-OH loading on Wang resin (LL, 0.60 mmol/g loading density) was achieved in a SPE cartridge with frit. The Wang resin (0.1 mmol) was swollen in DMF (2 mL) for 60 m. Next, drain the solvent off and wash with DMF (2×). Fmoc-Val-OH (5 eq), HBTU (4.9 eq.), and HOBt (5 eq.) were dissolved in 1:1 DCM/DMF (2 mL); subsequently, DIPEA (10 eq.) was mixed, and the solution was transferred in a SPE cartridge comprising the Wang resin and shaken for 3 h under N_2 bubbling. Drain the solvent, and the resin was successively rinsed with DMF (2×), DCM (2×), and MeOH (2×). Afterward Fmoc-Val-OH loading on Wang resin, the loading

density was measured by UV/vis assay of the Fmoc-dibenzofulvene deprotection product.

Estimation of the Loading Density of First Amino Acid Fmoc-Val-OH on Wang resin: The Fmoc-Val-Wang resin (5 mg) and DBU in NMP (2 mL, 2 % in NMP) were taken in a volumetric flask (10 mL). It was shaken for 30 min in a shaker, and the volumetric flask (10 mL) was filled up to the mark with CH_3CN. The solution was diluted with CH_3CN (1/12.5) and taken in an UV cuvette. The cleaved dibenzofulvene was monitored at 304 nm (ε_{304} = 7624 L mol^{-1} cm^{-1}) and contrasted with reference. The first amino acid Fmoc-Val-OH loading on the Wang resin was determined based on Lambert-Beer's law.

ρ(mmol/g) = 163.96×($A - A_0$)/m

ρ : loading density of the resin

A : absorption of a sample

A_0 : absorption of reference

m : mass of the analyzed resin in mg.

Microwave-assisted SPPS: Synthesis of Aβ40 peptide was achieved on a MW-assisted solid-phase peptide synthesizer at a 0.1 mmol scale by the Fmoc-SPPS protocol. After the final coupling, Fmoc-deprotection was executed to acquire an *N*-terminus free Aβ40 peptide, and it was stored at –20 °C prior to use.

Protocols for MW-Assisted SPPS:

1. Bubbling during the MW-assisted synthesis for all steps: on 3 sec; off 7 sec.

2. **Fmoc deprotection**: 20% piperidine/DMF; time 180 sec, power 20 W, temperature 75 ºC, delta temperature 5 ºC.

To circumvent aspartimide formation in the Fmoc deprotection step of Asp comprising sequence, 0.1 M HOBt monohydrate in the Fmoc deprotection

solution (20% piperidine/0.1 M HOBt/DMF) was utilized to diminish aspartimide development.

Washing after Fmoc-deprotection: DMF (4×), DCM (4×), and DMF (4×) to remove dibenzofulvene by-product.

3. **Coupling**: 0.5 M HBTU/0.5 M HOBt/2 M DIPEA/DMF;

General protocol: time 300 sec, power 20 W, temperature: 75 ºC, delta temperature: 5 ºC.

Double coupling was performed.

Arg (R) is vulnerable to δ-lactam formation, which considerably reduces the coupling output. Special care was taken in the case of the Arg coupling to reduce the side reactions. A modified double coupling was executed for Arg. 1^{st} coupling: 25 min at 25 °C (MW Power 0 W), next 2 min at 75 °C (MW Power 30 W); 2^{nd} coupling: 5 min at 75 °C (MW Power 30 W).

Special care for His coupling: the MW temperature was reduced to 50 °C to suppress epimerization.

Washing after coupling: DMF (3×), DCM (3×), DMF (3×)

After the final step, the resin was taken in a SPE cartridge with frit and rinsed with DMF (5×), DCM (5×), MTBE (5×), and lastly with MeOH (5×). The resins were dried in a vacuum and stored at –20 °C.

Test Cleavage from Wang Resin: To a pinch of the resin, a mixture of TFA/TIPS/EDT/H_2O (92.5/2.5/2.5/2.5 *v*/*v*/*v*/*v*) solution (2 mL) was added, and the cleavage reaction was executed by shaking the resin for 2 h at 25 °C. Next, the resin beads were filtered off, and the solvent was vaporized using N_2 stream. The Aβ40 peptide was precipitated by using cold MTBE. The MTBE suspension was centrifuged at –5 °C. The supernatant was rejected, and the

residue was washed with cold MTBE (3×) and dried to acquire the desired Aβ40 peptide, and it was stored at –20 °C prior to use.

MW-Assisted Fmoc-SPPS Protocol for Aβ40 Peptide Synthesis

Working Step	Resin	Reagents	Reaction condition
Coupling	Wang	HBTU/HOBt/DIPEA/DMF	300 sec/75 °C/20 W Double coupling was performed **Special care for the Arg coupling:** **1) 25 min/25 °C/0 W, then** **2 min/75 °C/30 W** **2) 5 min/75 °C/30 W** **Special care for the His coupling:** **The MW temperature was reduced to 50 °C**
Washing after coupling	Wang	DMF(5×), DCM(5×), DMF(5×)	
Fmoc deprotection	Wang	20% piperidine/DMF **Special care for Asp Fmoc-deprotection step: 20% piperidine/DMF with 0.1 M HOBt monohydrate**	180 sec/75 ºC/20 W
Washing after deprotection	Wang	DMF (4×), DCM (4×), DMF (4×)	
Washing after the final coupling	Wang	DMF(5×), DCM(5×), MTBE(5×), MeOH(5×)	
Final Cleavage	Wang	TFA/TIPS/EDT/H_2O (92.5/2.5/2.5/2.5 *v*/*v*)	2 h/25 °C

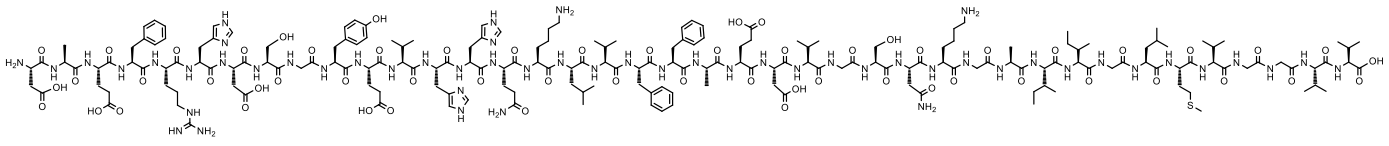

Aβ40 DAEFRHDSGYEVHHQKLVFFAEDVGSNKGAIIGLMVGGVV

The Aβ40 peptide is dissolved in ACN/H_2O and purified on a C8 column using reversed-phase HPLC. CH_3CN and H_2O gradient system containing 0.1% TFA were used to purify the peptide.

FTIR:

Aβ40 monomer: 3281 cm^{-1} (amide A region, N–H stretching), a sharp peak at 1650 cm^{-1} (amide I region, amide CO stretching), 1536 cm^{-1} (amide II region, NH bending).

Aβ40 fibril: 3290 cm^{-1} (amide A region, N–H stretching), a sharp peak at 1624 cm^{-1} (amide I region, amide CO stretching), and 1513 cm^{-1} (amide II region, NH bending).

MALDI *m/z*: Observed for $C_{194}H_{295}N_{53}O_{58}S^+$ $[M]^+$ = 4329.1560, $[M]^+$ calcd = 4329.1551

CD: The CD spectrum of Aβ40 monomer (10 μM) in deionized H2O with 1% TFE characteristically exhibits a curve with a negative peak at 198 nm that corresponds to a random coil that is transformed to a shorter wavelength positive band at 195 nm and the longer wavelength negative maxima at 217 nm after 7 days of incubation, which is characteristic for β-sheet secondary structure.

X-Ray fiber Diffraction: 4.5 Å (meridional reflection) and 10.6 Å (equatorial reflection).

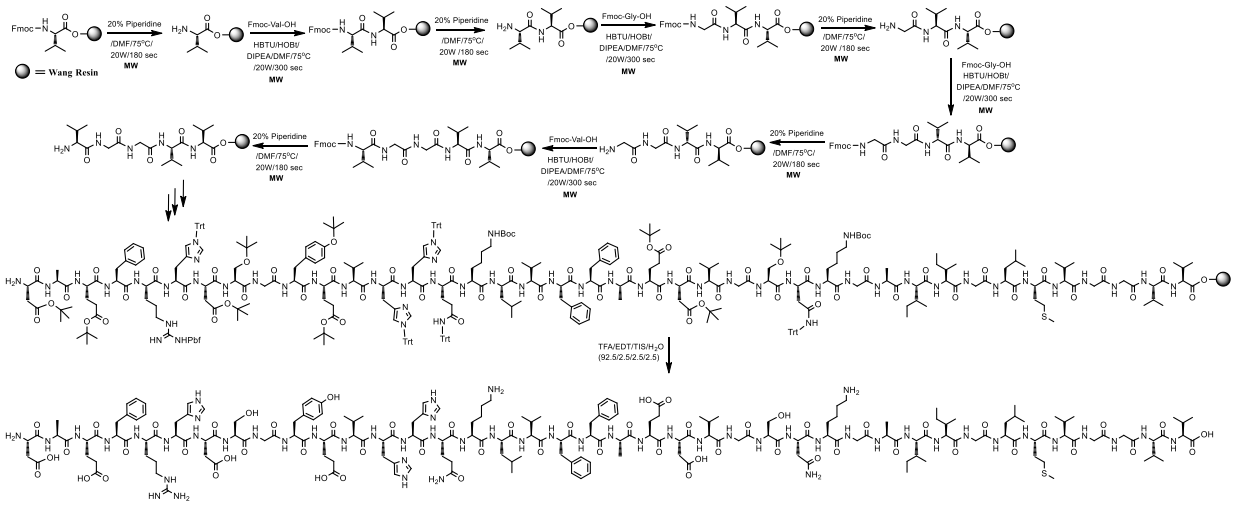

Figure 26. Microwave-assisted Fmoc-SPPS of Aβ40 on Wang resin.

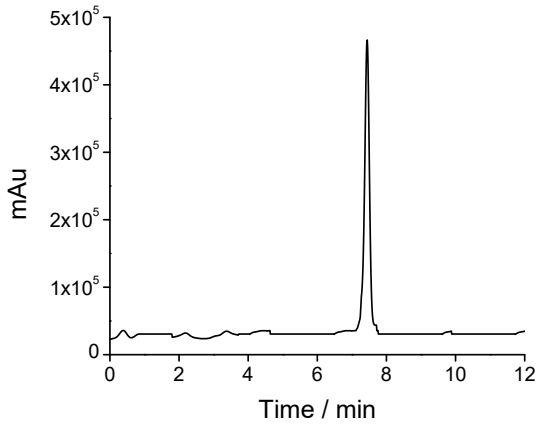

Figure 27. Analytical HPLC profile of Aβ40 peptide.

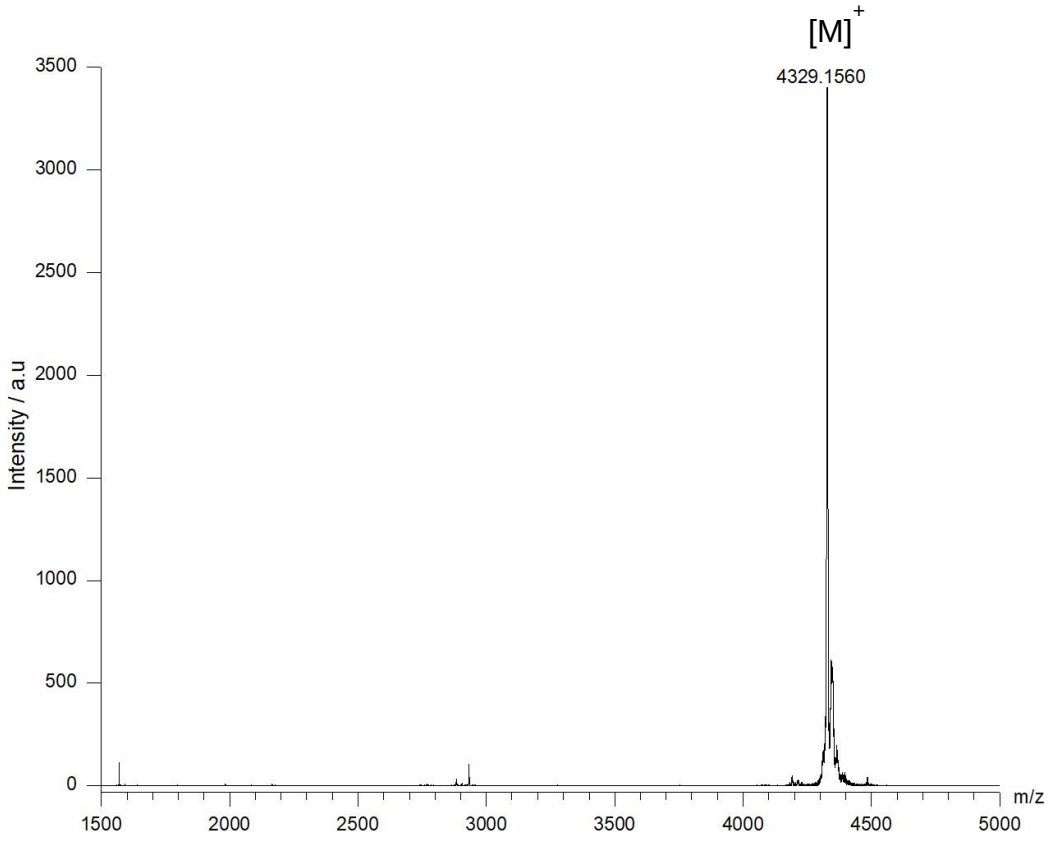

Figure 28. MALDI mass spectrum of **A*β*40** peptide.

Materials: Fmoc-amino acid building blocks: Fmoc-Gly-OH, Fmoc-Ser(tBu)-OH, Fmoc-Asn(Trt)-OH, Fmoc-Lys(Boc)-OH, Fmoc-Glu(OtBu)-OH, Fmoc-Ala-OH, Fmoc-Ile-OH, Fmoc-Leu-OH, Fmoc-Met-OH, Fmoc-Val-OH, Fmoc-Tyr(tBu)-OH, Fmoc-His(Trt)-OH, Fmoc-Gln(Trt)-OH, Fmoc-Asp(tBu)-OH, Fmoc-Arg(Pbf)-OH, Fmoc-Phe-OH, Wang Resin LL (100-200 mesh), TLC silica gel 60 F_{254}, and XTT were acquired from Merck. 4-Diethylamino-salicylaldehyde, diethyl malonate, pyridine, Phosphorus oxychloride, 2-(4-Aminophenyl)acetonitrile, 1-[Bis(dimethylamino)methylene]-1*H*-1,2,3-triazolo[4,5-*b*]pyridinium 3-oxide hexafluorophosphate (HATU), *N*,*N*-Diisopropylethylamine (DIPEA), DMF, Thioflavin T, Uranyl acetate, *N,N,N′,N′*-Tetramethyl-*O*-(1*H*-benzotriazol-1-yl)uronium hexafluorophosphate (HBTU), 1-Hydroxybenzotriazole (HOBt), Trifluoroacetic acid (TFA), Triisopropylsilane (TIPS), 1,2-Ethanedithiol, Piperidine, Ethyl iodide, Tetrabutylammonium hydroxide 30-hydrate, Hoechst 33342, all the HPLC grade solvents and spectroscopic grade solvents were bought from Sigma-Aldrich. 1,1,1,3,3,3-Hexafluoro-2-propanol (HFIP) was bought from SRL Chemicals. $CDCl_3$ was attained from Cambridge Isotope Laboratories, Inc. Rhodamine B was procured from TCI chemicals. SH-SY5Y cells were obtained from the NCCS, India. XTT, DMEM, Trypsin EDTA mixture, and FBS were procured from HiMedia Laboratories. Mitochondrion targeting commercially available dye MitoTracker Deep Red FM and Ham's F-12K (Kaighn's) medium were acquired from Thermo Fisher Scientific. JC-1 based mitochondrion membrane potential and Annexin V-FITC/PI apoptosis detection kits were procured from BD Biosciences. *Millipore* ultra-pure H_2O was used for all the experiments.

METHODS

Microwave Synthesizer: Aβ40 peptide was synthesized by a manual microwave solid phase peptide synthesizer using the Fmoc-SPPS protocol (CEM corporation, model discover bio, USA make).

NMR Spectroscopy: 1D (^{1}H and ^{13}C NMR) and 2D NMR experiments were executed on Bruker DPX300 and DPX400 MHz spectrometers at 298 K in $CDCl_3$. The manufacturers' supplied Bruker TopSpin 3.6.2 software was utilized to process the data. NMR chemical shifts were recorded in δ ppm by locking and calibration with appropriate deuterated NMR solvents.

High-Resolution Electrospray Ionization Mass Spectrometry (HRMS-ESI): A Q-Tofmicro mass spectrometer from Waters Corporation was used to record the HRMS-ESI in positive mode. Manufacturers' supplied mass application software, MassLynx V4.1, was utilized to process the data.

Matrix-Assisted Laser Desorption/Ionization Time-Of-Flight Mass Spectrometry (**MALDI-TOF MS)**: The mass of the Aβ40 protein was determined by MALDI-TOF MS using a Bruker Daltonics ultrafleXtreme instrument. Here, for the matrix preparation, α-cyano-4-hydroxy-cinnamic acid was used.

Absorption Spectroscopy: A Shimadzu UV-1800 spectrometer (double beam) with a wavelength range of 190-1100 nm was used to record the absorption spectra in various spectroscopy grade solvents. All inspections were accomplished in a quartz cuvette (1 cm path length).

Fluorescence Spectroscopy: In order to acquire fluorescence spectra in different spectroscopic grade solvents, a Horiba Jobin Yvon FluoroMax-4 spectrofluorometer operated by FluorEssence Version 3.9.0.1 software was utilized. Both the ex/em bandwidths were fixed at 5 nm.

Fluorescence Lifetime Measurement using Time-Correlated Single Photon Counting (TCSPC) Assay: The time-correlated single photon counting (TCSPC) method was utilized to achieve the fluorescence lifetimes (τ) of the synthesized Cou-AIE-TPP$^+$ fluorophore along with Cou-AIE-TPP$^+$ in the presence of Aβ40 peptide in PBS on the Horiba DeltaFlex lifetime device. The solutions of the Cou-AIE-TPP$^+$ probe and Cou-AIE-TPP$^+$ in the presence of Aβ40 peptide were distinctly excited with a 510 nm DeltaDiode laser (Horiba Scientific, model: DD-510L) to obtain the τ value. Horiba EzTime decay analysis software was used for fluorescence lifetime measurements and data analysis.

pH Meter: To prepare PBS solutions with specific pH values, a Mettler Toledo pH meter was used.

Inspection of the Aggregation-Induced Emission (AIE) Property of Cou-AIE-TPP$^+$: The AIE property of Cou-AIE-TPP$^+$ was examined by determining their fluorescence emission intensity in THF/PBS mixtures with different volume percentages (vol%) of PBS fractions. Various solutions were prepared with changing PBS volume percentages between 0−90% and the total volume of THF/PBS mixtures remained constant. The final concentration of Cou-AIE-TPP$^+$ in each sample was 2 μM. The fluorescence emission of these THF/PBS solutions was noted at λ_{ex} = 480 nm. A THF solution of Cou-AIE-TPP$^+$ is nonfluorescent but showed orange fluorescence after adding PBS due to the aggregation-induced emission of Cou-AIE-TPP$^+$.

Preparation of Aβ40 Monomers, Oligomers, Protofibrils, and Fibrils:

Aβ40 monomer was prepared by dissolving Aβ40 peptide in HFIP (concentration of the stock solution 250 μM).

For the preparation of oligomers, 1.0 mg of lyophilized Aβ40 was dissolved in 400 μL of HFIP at 25 °C and waited for 15 m. Next, D.I. H_2O (900 μL) was mixed to the resulting Aβ40 (100 μL) solution. Afterward incubation at 25 °C for an additional 15 m, the solution was centrifuged, and the supernatant was taken into a new tube to evaporate the HFIP using an N_2 stream. Next, the sample was stirred at 500 rpm for 12 h. For the protofibril preparation, it was incubated for 24 h.

To prepare Aβ40 fibrils, 1.0 mg of Aβ40 peptide was suspended in a 1% ammonium hydroxide solution (1.0 mL). The resulting solution (100 μL) was 10-times diluted using PBS buffer (pH = 7.4) and stirred at 25 °C for 5 days. The ThT fluorescence experiment and TEM analysis were applied to confirm the formation of Aβ40 fibrils.

A freshly prepared stock solution was used in every experiment.

Determination of Relative Quantum Yields of Cou-AIE-TPP$^+$ in the Presence and Absence of Aβ40 Peptide: The relative method was utilized to quantify the fluorescence quantum yields (QY) of the synthesized Cou-AIE-TPP$^+$ probe in the presence and absence of Aβ40 peptide. Here, the integrated fluorescence intensities of the synthesized Cou-AIE-TPP$^+$ probe, Cou-AIE-TPP$^+$ + Aβ40 monomers, Cou-AIE-TPP$^+$ + Aβ40 oligomers, and Cou-AIE-TPP$^+$ + Aβ40 fibrils were correlated with the reference molecule Rhodamine-B by applying the succeeding equation:

$$\Phi_f(\mathrm{x}) = \Phi_f(\mathrm{st}) \times [(A_{\mathrm{st}} \times \mathrm{F_x} \times \eta_{\mathrm{x}}^2) / (A_{\mathrm{x}} \times \mathrm{F_{st}} \times \eta_{\mathrm{st}}^2)]$$

Φ_f(st) and Φ_f(x): Fluorescence QY of the standard and synthesized Cou-AIE-TPP$^+$ probes, respectively.

A_{st} and A_{x} : Absorbance of standard and synthesized Cou-AIE-TPP$^+$ probes at λ_{ex}.

F_{st} and F_x : The integrated emission ranges underneath the modified emission spectra for the standard and synthesized Cou-AIE-TPP$^+$ probes, respectively.

η_{st} and η_x : Refractive indices of the solvents where the standard & synthesized Cou-AIE-TPP$^+$ probes were recorded, respectively. Herein, the standard and synthesized Cou-AIE-TPP$^+$ probes were dissolved in EtOH and PBS, respectively. Refractive indices, η_{EtOH} = 1.3614 and η_{PBS} = 1.335.

st : standard.

x : synthesized probe.

Φ_f (st): QY of the reference probe Rhodamine-B in EtOH = 0.49. In PBS, the relative QY (Φ_f) of the Cou-AIE-TPP$^+$ probe, Cou-AIE-TPP$^+$ + Aβ40 monomers, Cou-AIE-TPP$^+$ + Aβ40 oligomers, and Cou-AIE-TPP$^+$ + Aβ40 fibrils were determined to be 0.45, 0.47, 0.52, and 0.70, respectively.

Circular Dichroism (CD) Spectroscopy: CD spectra were acquired on a JASCO instrument (Model J-815–150S) at 25°C. Data were taken using a 1 mm quartz cuvette in the 190-260 nm range with a 0.5 nm step, 2 s collection times per step, and a 1 nm bandwidth. The CD signal from the PBS as background was corrected from the CD signal of the peptide solution in PBS. The secondary structure of Aβ40 peptide at 10 μM concentration in PBS solution was monitored at the initial stage (0 hours) and after being aged for 7 days at 37°C. The average of three spectra was taken for each measurement.

Fourier Transform Infrared Spectroscopy (FT-IR): FT-IR spectra were acquired on a PerkinElmer Spectrum Two FT-IR spectrometer from 4000 to 400 cm^{-1} at room temperature in ATR mode. The Aβ40 peptide fibrils were isolated from solution by centrifugation at 12000 rpm for ten minutes, and the secondary structure of the peptides was monitored using FT-IR. FT-IR spectra of Aβ40 monomer and Aβ40 fibrils were recorded, which signify random coil and β-sheet secondary structure, respectively.

X-Ray Powder Diffraction: The X-ray diffraction from the dried fibers of Aβ40 peptide was recorded on a Bruker D8 Advance X-ray diffractometer by Cu Kα radiation (λ = 1.5418 Å) operating at 40 kV and 40 mA.

TEM Experiments: 10 μL of freshly prepared Aβ40 monomers, oligomers, protofibrils, and fibrils in PBS solutions were pipetted out separately onto 300 mesh carbon-coated copper grids. After 2 m the solvent on the grid was cautiously blotted by a tissue paper. For negative staining, 10 μL of an aqueous solution of uranyl acetate [2 % (w/v)] was added to the grid and allowed to float for 30 s. The excess solution was shocked using a blotting paper. The sample was air dried at room temperature and kept in a desiccator for 1 day before taking TEM images on a JEOL (Model: JEM 2100F) instrument operated at 120 kV.

In Vitro Binding Assays through the Cou-AIE-TPP$^+$ Kinetic Assay: To study the fluorescence response of Cou-AIE-TPP$^+$ towards Aβ40, a solution of Cou-AIE-TPP$^+$ (1 μM) was mixed with different concentrations (0-10 μM) of Aβ40 (a final volume of 2 mL) and incubated in a PBS solution at room temperature for different times (0-200 min). The emission spectra (500-800 nm) of the mixture were measured at an excitation wavelength of 480 nm for Cou-AIE-TPP$^+$. λ_{em} of Cou-AIE-TPP$^+$ was monitored at 604 nm. The ex/em slit widths were kept at 5 nm. Three independent tests were executed for the Cou-AIE-TPP$^+$ binding kinetic assay. Error bars indicate standard deviations from the mean of three independent runs. We found that Cou-AIE-TPP$^+$ could report the nucleation (lag phase), elongation (growth phase), and saturation stages of Aβ40 fibril formation. The lag phase designated Aβ40 monomers and soluble oligomers; the elongation phase denoted early aggregates and late aggregates; and finally, the aggregation progression reached the saturation stage, where the majority of the Aβ40 peptides were converted to mature fibrils.

Thioflavin T (ThT) Kinetic Assay: A stock solution of ThT (50 μM) in PBS (pH 7.4) was made freshly with proper precaution to evade degradation from light. A solution of Aβ40 (10 μM) in 20 mmol of PBS (pH 7.4) was prepared. Aliquots of the Aβ40 peptide solution and the concentrated solution of ThT were mixed in a solution of 20 mmol PBS (pH 7.4). λ_{em} of ThT was monitored at 485 nm with λ_{ex} at 440 nm. The data were collected at 5 min intervals for 200 min. Three independent tests were executed for each ThT assay. Kinetic curves were fitted by the sigmoidal curve fitting. Error bars indicate standard deviations from the mean of three independent runs. All samples were stirred constantly by a micro magnetic stir bar. The incubation conditions were kept the same for Cou-AIE-TPP$^+$ and ThT. The ex/em slit widths were retained at 5 nm.

Competitive Binding and Displacement Assay: A displacement experiment that titrates Cou-AIE-TPP$^+$ (0 to 400 nM) against ThT (400 nM) bound Aβ40 fibrils (10 μM) is used. When Cou-AIE-TPP$^+$ is gradually added to the ThT/ Aβ40 pre-fibrillar complex in PBS (pH 7.4), ThT's fluorescence (λ_{em} = 480 nm) gradually decreases, whereas Cou-AIE-TPP$^+$'s red fluorescence intensity (λ_{em} = 604 nm) sharply increases with an increase in Cou-AIE-TPP$^+$ concentration. Before recording the fluorescence in the displacement assay, the mixture was incubated at 25 °C for 5 m. The emission intensity of ThT and Cou-AIE-TPP$^+$ was recorded under excitation at λ_{ex} = 440 nm and λ_{ex} = 480 nm, respectively.

Measurement of Binding Affinity (K_d): Pre-aggregated Aβ40 (10 μM final concentration) was mixed with various concentrations of Cou-AIE-TPP$^+$ (10, 20, 30, 40, 50, 60, 70, 80, 90, 100, 150, 200, 250, 300 nM) in PBS. The mixtures were incubated for 30 m at 25 °C. Next, the fluorescence emission intensity at 604 nm was measured at each excitation wavelength (λ_{ex} 480 nm).

Three independent experiments were accomplished. The dissociation constants (K_d) were obtained from the best-fit curve for each of the tested probe solutions.

The dissociation constant (K_d) was calculated from fluorescence titration data using the Hill-1 equation:

$$\frac{F-F_0}{F_0} = 1 + \frac{[F-F_0]\,[AIE]^n}{K_d{}^n\,[AIE]^n}$$

F and F_0 were the emission intensities of Cou-AIE-TPP$^+$ in the presence and absence of Aβ40

K_d was the dissociation constant

n was the Hill's coefficient

The relative fluorescence intensity (F/F_0) of Cou-AIE-TPP$^+$ in the absence of Aβ40 at the starting point was considered to be ~ 1.

***n*-Octanol/PBS Partition Coefficient Value of Cou-AIE-TPP$^+$:** The *n*-Octanol/PBS partition coefficient value of Cou-AIE-TPP$^+$ was calculated. To determine the partition coefficient of Cou-AIE-TPP$^+$, 1 mg of Cou-AIE-TPP$^+$ was dissolved in 2 mL of *n*-octanol. By proper dilution, the absorbance of the stock solution of Cou-AIE-TPP$^+$ in *n*-octanol was measured on a UV/vis spectrometer. The stock solution in *n*-octanol (1 mL) and an equal volume of PBS (pH 7.4) were combined and vortexed for one minute and incubated at 37 °C for one hour to attain equilibrium. The solution was centrifuged for 10 minutes at 4000 rpm in order to disperse the organic and aqueous layers. Subsequently to centrifugation, the absorbance in *n*-octanol (*A*o) part was recorded on a UV/vis spectrometer using proper dilution. The partition coefficient value is obtained by dividing the absorbance of the n-octanol layer (after mixing) by the absorbance of an aqueous PBS layer (as determined by comparing the absorbance values of the n-octanol layer before and after mixing with PBS).

Partition coefficient (P) = $(Ao)_f$ /[$(Ao)_i$ − $(Ao)_f$]

$(Ao)_i$ and $(Ao)_f$ were the initial and final absorbances in the *n*-octanol layer, respectively.

The partition coefficient (P) of Cou-AIE-TPP^+ was found to be 19.95, and the log P value was 1.3.

Diffusion-Ordered Spectroscopy (DOSY) and Diffusion by NMR: The proton diffusion-ordered NMR spectroscopy (DOSY-NMR) studies were executed on a 400 MHz Bruker NMR instrument equipped with an iProbe. To measure the diffusion coefficient of Cou-AIE-TPP^+ at 25 °C, a 5 μM concentrated solution of Cou-AIE-TPP^+ was prepared in a buffer encompassing 20 mM sodium phosphate (pH 7.4) and 20 mM NaCl. Cou-AIE-TPP^+ (5 μM) in both the absence and presence of Aβ40 (10 μM) solutions in PBS were loaded into standard 5-mm NMR tubes for the DOSY experiment. The data for diffusion measurements were collected at 25 °C with a diffusion delay time (Δ) of 50 ms, gradient pulse duration (δ) of 1.5 ms, and a gyromagnetic ratio (γ) of 26752 rad / (s*Gauss) with variable gradient strengths (gauss/cm). Data processing and analysis were executed by the Bruker TopSpin 4.3.0 software. The collective FIDs were Fourier transformed using Bruker TopSpin 4.3.0 to obtain a pseudo-2D spectrum. The diffusion coefficient was calculated by fitting the experimental data to the Stejskal-Tanner formula: $I(G_z) = I(0)*\exp[-D\gamma^2\delta^2G_z^2(\Delta - \delta/3)]*10^4$.

$I(G_z)$ and $I(0)$ = The signal intensities obtained with the respective gradient strengths of G_z and $G_z = 0$

D = Diffusion coefficient

γ = Gyromagnetic ratio

δ = Gradient pulse duration

Δ = Diffusion time

The diffusion coefficient of a Cou-AIE-TPP$^+$ (5 μM) sample in PBS was 3.11±0.14 × 10^{-10} m^2 s^{-1}, whereas the addition of Aβ40 (10 μM) to the Cou-AIE-TPP$^+$ (5 μM) sample in PBS caused a change in the diffusion coefficient of Cou-AIE-TPP$^+$ to 2.77±0.03 × 10^{-10} m^2 s^{-1}.

Isothermal Titration Calorimetry (ITC): ITC experimentation was executed on a MicroCal PEAQ-ITC microcalorimeter (Malvern). ITC measures the heat released/absorbed in a biomolecular binding incident in solution and calculates the binding affinity and thermodynamic parameters of molecular interactions in a single test. It helps to understand why the interactions happen, including the binding mechanisms. Binding affinity (K_D), reaction stoichiometry (n), enthalpy (ΔH), and entropy (ΔS) disclose the forces that dictate biomolecular interactions and can also exemplify function and mechanism at a molecular level. Aβ40 solution was made in PBS solution and filtered via a 0.2 μm syringe filter before the ITC assay. The reference cell was loaded with a PBS solution. 280 μL of Aβ40 (20 μM) in PBS was transferred into the sample cell, and 200 μM Cou-AIE-TPP$^+$ (10 times more concentrated than Aβ40) in PBS was poured into the syringe. In every test, 2 μL × 19 injections with an overall volume of 38 μL of Cou-AIE-TPP$^+$ were transferred to the Aβ40 solution with a period of 4s per injection and 150s spacing among two injections. Mixing was performed automatically by stirring the syringe at a speed of 750 rpm at 25 °C. The titrations were performed in triplicate at 25 °C, and for all the titrations, almost indistinguishable outcomes were acquired. Blank titrations were performed by injecting PBS into PBS, Cou-AIE-TPP$^+$ into PBS, and Aβ40 dilutions were subtracted from the Aβ40/Cou-AIE-TPP$^+$ titration. Binding enthalpy was achieved by fitting the amended data into an appropriate binding model. A titration plot of kcal/mol vs molar ratio (Cou-AIE-TPP$^+$/Aβ40) was developed. The upper panels show the raw data for the Aβ40/Cou-AIE-TPP$^+$

titration, and the bottom panels signify the binding isotherm by plotting integrated peak areas vs the molar ratio for titration. The subsequent isotherm is best fitted to a binding model to attain the K_D, n, ΔH, ΔS, and ΔG of interaction. The ITC data and plots were examined by MicroCal PEAQ-ITC Analysis Software to measure the heat of interaction and thermodynamic parameters.

Computational Methods:

Density functional theory (DFT): The density functional theory (DFT) calculation for Cou-AIE-TPP$^+$ was performed with Gaussian 09 W software.[43] The ground state geometries were optimized at the Becke 3-parameter exchange functional by the gradient-corrected correlation functional of Lee, Yang, and Parr (B3LYP) by the 6-31+G* basis set [B3LYP/6-31+G*]. The frontier molecular orbitals (FMOs) of Cou-AIE-TPP$^+$ were analyzed using Gaussian 09W under the B3LYP/6-31+G* level.

Molecular Docking Simulation: The obtained energy minimized structure of Cou-AIE-TPP$^+$ using B3LYP/6-31+G* was used for the molecular docking experiment. The crystal structure of Aβ40 fibrils (PDB ID: 2LMP) was achieved from the Protein Database (www.rcsb.org) and optimized by the AutoDock4.2 software.[44] Molecular docking simulation was accomplished with Autodock Vina. Figures were developed through the Discovery Studio Visualizer software package. AutoDock4.2 was exploited for molecular docking experiments with the aid of the Lamarckian procedure inside the grid box of dimensions $60 \times 60 \times 60$ Å^3 at the ligand binding pocket. The greatest docking pose of the molecules was anticipated through binding energy, inhibition constant, ligand efficiency, van der Waals forces, intermolecular energy, hydrogen bond, total internal energy, dissolve energy, torsional energy, and unbound energy.

The scoring function was written as: $\Delta G_{binding} = \Delta G_{vdW} + \Delta G_{elec} + \Delta G_{hbond} + \Delta G_{desolv} + \Delta G_{tors}$

The DFT energy-minimized conformer of the Cou-AIE-TPP^+ molecule in the Aβ40 peptide binding site was documented by .dlg file that was analyzed with the aid of AutoDockTools.

Cell Culture: SH-SY5Y was a three-time subcloned cell derived from the SK-N-SH human neuroblastoma cell line. The SH-SY5Y cell line was studied as a model for neurodegenerative disorders. A human neuroblastoma cell line SH-SY5Y was maintained in growth media encompassing DMEM:Ham′s F12 (1:1, pH 7.4), glutamine (2 mM), non-essential amino acids (1% NEAA), and 10% FBS. The SH-SY5Y cell line was preserved at 37 °C in the incubator with routine passage of 5% CO_2.

Cell Viability Assay using XTT Reagent: The cell viability test was performed on SH-SY5Y cells by 2,3-bis-(2-methoxy-4-nitro-5-sulfophenyl)-2*H*-tetrazolium-5-carboxanilide (XTT) reagent. The SH-SY5Y cells (5×10^4 cells/well) were seeded in a 96-well plate in 50% DMEM and F12K media (Invitrogen) with 10% FBS and grown to obtain > 80% confluency before treatment. SH-SY5Y cells were treated with various concentrations of Cou-AIE-TPP^+ (control, 0.5, 1.0, 2.0, 5.0, 10.0, 20.0, and 50.0 μM) and incubated for 72 h at 37 °C. After treatment, 25 μL of XTT solution with phenazine methosulfate (PMS) in 50% DMEM and F12K were mixed to each well and further incubated for 2 h at 37 °C, which was converted to H_2O-soluble highly colored formazan upon reduction in the presence of an electron mediator (dehydrogenases present in metabolically active cells). The microplate was shaken for 10 seconds, and the absorbance at 470 nm was recorded by an automated microplate reader (Thermo Fisher Scientific). The quantity of the formazan dye produced by the activity of dehydrogenases in

SH-SY5Y cells was directly proportional to the number of living SH-SY5Y cells. The SH-SY5Y cell viability was calculated based on the measured data (colorimetric assays). The consequences were reported by the following equation:

Viable cells (%) = (*A* of treated cells / *A* of untreated cells) × 100

All experiments were performed in parallel and in triplicate.

Evidence for the Accumulation of Cou-AIE-TPP$^+$ within the Live Human Neuroblastoma SH-SY5Y Cell Mitochondria Monitored through Confocal Laser Scanning Microscopy: Confocal laser scanning microscopy (CLSM) was performed to verify the accumulation of Cou-AIE-TPP$^+$ within the mitochondria of human neuroblastoma SH-SY5Y live cells. CLSM images were acquired using a Leica STELLARIS 5 platform with a HC PL APO 100×/ 1.40 OIL CS2 objective connected to a white light laser (WLL) along with an Acousto-Optical Beam Splitter (AOBS) and HyD S detector. For human neuroblastoma SH-SY5Y live cells CLSM imaging, the cells at a density of 5 × 10^4 cells/mL were seeded in a 35-mm glass-bottomed confocal dish (SPL Lifesciences, catalogue no. 200350) and permitted to obtain ~80% confluency in DMEM: F12K (1:1, pH 7.4) media at 37 °C for 24 h in a 5% CO_2 incubator. Next washing through 1× PBS, live SH-SY5Y cells were incubated with a 500 nM solution of Cou-AIE-TPP$^+$ in media for 20 min at 37 °C in a 5% CO_2 environment; subsequently, the media was discarded cautiously and washed caringly using 1× PBS. Successively, SH-SY5Y cells were incubated first with 0.2 μM MitoTracker Deep Red FM and then with Hoechst 33342 (0.1 μg mL^{-1}) for 20 and 15 min, respectively, at 37 °C in a 5% CO_2 setting. Later in the treatment process, SH-SY5Y cells were finally washed twice with media before capturing the CLSM images. Human neuroblastoma SH-SY5Y live cell

confocal images were processed by LAS X software. In the course of the live SH-SY5Y cells CLSM imaging process, 37 °C and a 5% CO_2 setting were upheld (Figure S47).

For Hoechst 33342: laser λ_{ex} = 405 nm (blue channel, detection range of emission 415-480 nm); MitoTracker Deep Red FM: laser λ_{ex} = 638 nm (Cy-5 channel, detection range of emission 650-710 nm); Cou-AIE-TPP$^+$: laser λ_{ex} = 488 nm (green channel, detection range of emission 570-630 nm).

Live SH-SY5Y Cell 3D Confocal Imaging using Synthesized Cou-AIE-TPP$^+$ Dye: For the live cell 3D picture accomplishment, the CLSM images of human neuroblastoma SH-SY5Y live cells stained with the mitochondria targeting synthesized Cou-AIE-TPP$^+$ dye and nuclear staining dye Hoechst 33342 were captured every 0.4 μm on the Z-axis by a Leica STELLARIS 5 confocal microscope. 32 frames for each channel were taken over a 10 minute period and finally rebuilt with the aid of LAS X software to acquire the live SH-SY5Y cell 3D CLSM images.

In Vitro Fluorescence Imaging of A*β*40 Fibrils using Synthesized Cou-AIE-TPP$^+$ Dye: The SH-SY5Y cells were seeded and cultured in a dish at 5 × 10^3 cells/dish for 24 h at 37 °C. Next washing through 1 × PBS, live SH-SY5Y cells were incubated with A*β*40 (10 μM) for different times at 37 °C in a 5% CO_2 atmosphere. Subsequently, the media was discarded cautiously and washed caringly using 1 × PBS. Successively, SH-SY5Y cells were incubated first with 500 nM Cou-AIE-TPP$^+$ for 20 min and then stained with ThT (5 μM) for 20 min at 37 °C in a 5% CO_2 setting. Later in the treatment process, SH-SY5Y cells were finally washed twice with media before capturing the CLSM images. Confocal images of human neuroblastoma SH-SY5Y cells treated with A*β*40 (10 μM) over 0-48 h were obtained by a Leica STELLARIS 5 confocal microscope, and the images were processed through LAS X software.

For ThT: laser λ_{ex} = 405 nm (blue channel, detection range of emission 450-500 nm); Cou-AIE-TPP^{+}: laser λ_{ex} = 488 nm (green channel, detection range of emission 570-630 nm).

Pearson's Correlation Coefficient (PCC) Determination: Pearson's correlation coefficient (PCC) is one of the classical statistical analyses in pattern recognition for matching one confocal image (green channel) with another (red channel). PC graphs can explain the extent of overlapping among two patterns in a dual-color colocalization image. PC coefficients were calculated by the examination of confocal micrographs by the LAS X software with the Quantify tool. To determine PC coefficients for CLSM images, all of the pixels having the same image coordinates were paired.

The PC coefficient (PCC) was calculated (image comprising of two channels) according to the equation:

$$PCC = \frac{\sum_i (S1_i - S1_{avg}) * (S2_i - S2_{avg})}{[\sum_i (S1_i - S1_{avg})^2 * \sum_i (S2_i - S2_{avg})^2]^{(1/2)}}$$

S1 = signal intensity of pixels (pixel i) in the 1st channel

S2 = signal intensity of pixels (pixel i) in the 2nd channel.

$S1_{avg}$ = mean values of pixels in the 1st channel

$S2_{avg}$ = mean values of pixels in the 2nd channel.

Determination of Mitochondrial Membrane Potential Alteration after Incubation with Aβ40 Over Time Using the JC-1 Assay: Amendments in mitochondrial membrane potential were measured using a lipophilic cationic JC-1 probe (mitochondrion membrane potential detection kit) on a fluorescence-activated cell sorting (FACS) flow cytometer. For healthy

mitochondria, the $\Delta\Psi_m$ value was highly negative. JC-1 dye was incorporated into the mitochondria, and the J-aggregates of JC-1 were observed. Conversely, when the membrane depolarized, the J-aggregates of JC-1 seepage from the mitochondria into the cytosol as monomers were detected. The excitation of JC-1 was 494 nm, and the emission was detected at 527 nm (green emission, JC-1 monomers) as well as at 596 nm (orange-red emission, JC-1 aggregates). The JC-1 monomers-to-aggregates emission ratio (527/596) was assessed. The greater value of this emission ratio specified larger membrane depolarization. Subsequently, after incubation of SH-SY5Y cells with Aβ40 (10 μM) over time (0-24 h), the cells were incubated with a JC-1-based mitochondrion membrane potential detection kit for 15 min using the manufacturer's supplied protocol at 37 °C in the dark. Next, $\Delta\Psi_m$ was evaluated on a FACS instrument (BD Biosciences, Mountain View, CA, USA), and the cytogram analysis was executed by the Cell Quest software (BD Biosciences). After SH-SY5Y cells were incubated with the JC-1 probe, the emission signals were scrutinized in the FITC and PE channels by a 494 nm laser.

Annexin V-FITC/PI Apoptosis Detection Assay after Incubation with Aβ40 Over Time: The extent of apoptosis was quantitatively acquired by the Annexin V-FITC/PI apoptosis assay kit by FACS. Negatively charged phosphatidylserine (PS) usually exists in the inner leaflet of a healthy cell membrane. In the event of early apoptosis, the PS is flipped from the inner to outer membrane and is exposed. FITC-conjugated Annexin V has a great affinity for PS on the apoptotic cell membrane surface and is the most sensitive biomarker to identify early apoptosis. The assay kit also comprises propidium iodide (PI) to stain the cellular DNA in necrotic cells. PI cannot penetrate the healthy or early apoptotic intact cell membrane. PI can infiltrate the late apoptotic and necrotic cell membranes and stain these cells. The cultured SH-

SY5Y cells (5×10^4 cells/well) were incubated with Aβ40 (10 μM) at various times (0-24 h). The SH-SY5Y cells were then trypsinized and rinsed with cold 1x PBS twice. Next, the cells were suspended in 1× annexin-binding buffer; subsequently, 100 μL of the solution was taken into a 5 mL culture tube. Maintaining the manufacturer's protocol, the SH-SY5Y cells were incubated with Annexin V-FITC/PI apoptosis detection assay kit solutions for 15 minutes at 25 °C in the dark. 400 μL of 1× Binding Buffer was mixed to each tube. The binding buffer in the apoptosis kit contains $CaCl_2$. After the incubation period, the samples were preserved on ice. The emissions at different time points were recorded on a BD FACSCalibur Flow Cytometer (BD Bioscience). Data were examined, and the percentage of cells that undergo early and late apoptosis was determined by BD CellQuest Pro software (BD Bioscience). A control experiment was performed without the addition of Aβ40.

Results and Discussion

Molecular Design and Synthesis:

A de novo designed unsymmetrical AIE probe Cou-AIE-TPP^+ is constructed by engineering the aromatic 2*H*-chromen-2-one motif into the bridge of electron donor (*N*,*N*-diethyl amino unit)–acceptor (π-conjugated electron-withdrawing acrylonitrile units)–donor (*N*,*N*-dialkylated amino unit) framework tethered with lipophilic cationic TPP^+ group (**Figure 29**). 7-(Diethylamino)coumarin (**1**) is synthesized via a one-pot Knoevenagel reaction between 4-(diethylamino)salicylaldehyde and diethyl malonate (**Figure 29**). The Vilsmeier-Haack synthesis of **1** produces the intermediate 7-(diethylamino)coumarin-3-carbaldehyde **(2**) (**Figures 3-6**). The condensation of compounds **2** and **5** creates compound **6,** which is hydrolyzed to obtain

compound **7** (**Figures 11-18**). Amidation of compound **7** with (2-aminoethyl)triphenylphosphonium bromide yields the target molecule Cou-AIE-TPP$^+$, which is characterized by 1D (^{1}H, ^{13}C, DEPT-135, ^{31}P) NMR, 2D COSY NMR, and HRMS (**Figures 19-25**). Cou-AIE-TPP$^+$ consists of end-capped lipophilic cationic mitochondria targeting TPP$^+$ functionality and exhibits one ^{31}P NMR peak at 23.9 ppm (**Figure 23**). The aromatic residues might exhibit π-effects and hydrophobic interactions with suitable groups at the binding site of Aβ aggregates. A control probe, Cou-AIE, lacking the lipophilic cationic TPP$^+$ functionality is constructed and characterized (**Figures 29, 7-10**). The Aβ40 peptide is synthesized using the microwave-assisted Fmoc-SPPS protocol on Wang resin (**Figure 26**). The mass of the HPLC-purified Aβ40 peptide is confirmed by MALDI-TOF MS (**Figures 27, 28**).

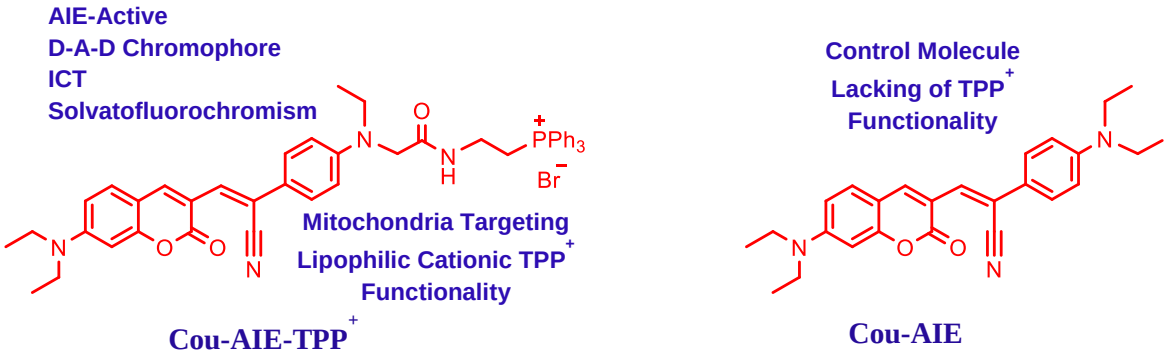

Figure 29. Chemical structures of Cou-AIE-TPP$^+$ and the control molecule Cou-AIE lacking the lipophilic cationic TPP$^+$ functionality.

Photophysical Properties:

We first investigate the photophysical characteristics of Cou-AIE-TPP$^+$; as anticipated, it exhibits excellent optical properties. Cou-AIE-TPP$^+$ displays unique solvatochromic fluorescence behaviors with an ICT mechanism among

the D and A residues in the D-A-D chromophore. The absorption spectra of Cou-AIE-TPP$^+$ display a very small shift amongst solvents with different polarities [$(\lambda_{max})_{Toluene}$ = 475 nm and $(\lambda_{max})_{PBS}$ = 480 nm], and it could be an overall result of polarity and solvation (**Figure 31a**). In contrast, the fluorescence emission wavelength exhibits a significant bathochromic shift with increasing the dielectric constant (ε) and polarity of the solvent [$(\lambda_{em})_{Toluene}$ = 517 nm and $(\lambda_{em})_{PBS}$ = 604 nm] (**Figures 30a**, **31c**, **Table 1**).[44] After photoexcitation, the ICT process results in a highly polarized excited state of Cou-AIE-TPP$^+$, and the excited state is stabilized by adjacent polar solvent molecules through noncovalent interactions, which subsequently diminishes the energy gap and exhibits solvatofluorochromism. The correlation between the λ_{em} and the dielectric constant of the solvents is linear (**Figure 31d**). The maximum Stokes shift is observed at 124 nm in aqueous PBS with a narrow abs/em bandwidth that can evade self-quenching, minimize cross-talk, and significantly enhance the imaging quality (**Figure 31b**, **Table 1**). However, this phenomenon is less significant in non-polar solvents, e.g., toluene, $CHCl_3$, etc. Moreover, Cou-AIE-TPP$^+$ is well soluble in THF and nonfluorescent but aggregates in H_2O or aqueous PBS, and the aggregated form exhibits bright orange emission (**Figure 30b**). It clearly shows that Cou-AIE-TPP$^+$ switches the emission from the "OFF" to "ON" state in a THF/PBS or THF/H_2O solvent mixture, and the emission intensity ca. 600 nm progressively increases along with a shoulder at 735 nm emission wavelength with the increase in PBS volume percent (**Figures 30b, 31e**). A 78-fold augmentation from 100% THF to a 10% THF/90% PBS mixture is observed, demonstrating the efficient AIE property of Cou-AIE-TPP$^+$. Cou-AIE-TPP$^+$ is nonfluorescent in a good solvent like THF owing to the energy dispersion in a non-radiative manner instigated by its intramolecular motion, whereas the aggregation might impede the

intramolecular motions (rotation and vibration) and result in the energy transition in the radiative pathway, responsible for the AIE effect. On the contrary, the control probe Cou-AIE lacking the lipophilic cationic TPP^+ functionality exhibits a 56-fold rise in fluorescence from 100% THF to a 10% THF/90% PBS mixture, demonstrating a mild AIE impact in comparison to Cou-AIE-TPP^+ (**Figure 32**).

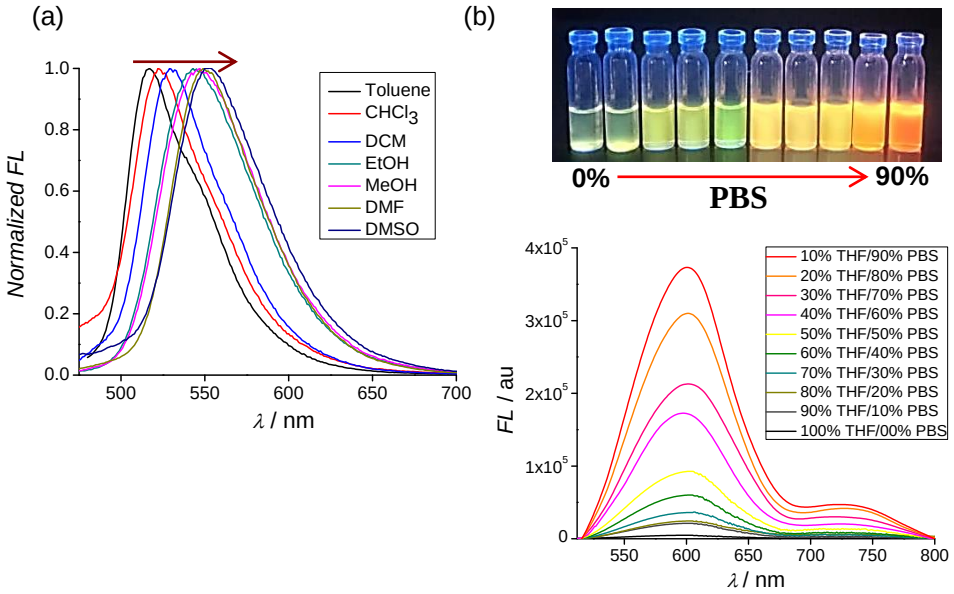

Figure 30. (a) Solvatochromic fluorescence behaviors of Cou-AIE-TPP^+. Fluorescence emission wavelength exhibits a significant bathochromic shift with increasing the dielectric constant (ε) and polarity of the solvent. (b) Fluorescence (FL) emission of Cou-AIE-TPP^+ in a THF/PBS mixture with different volume percentages (vol%) of PBS fractions (λ_{ex} = 480 nm).

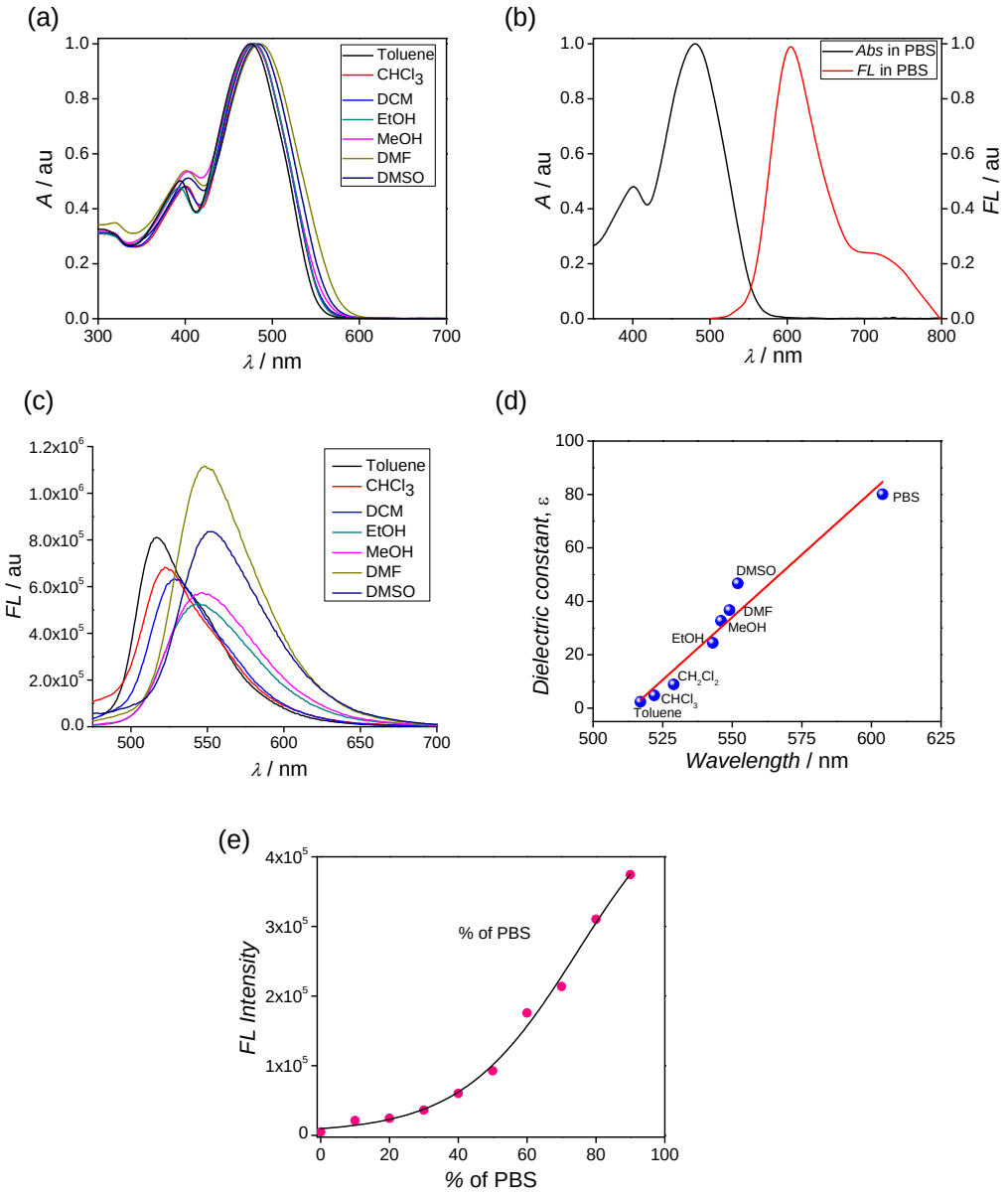

Figure 31. (a) Normalized absorption spectra of Cou-AIE-TPP^{+} in different solvents. (b) Normalized absorption and emission spectra of Cou-AIE in PBS exhibit a 124 nm Stokes shift. (c) Fluorescence emission spectra of Cou-AIE-TPP^{+} in different solvents at λ_{ex} 480 nm. (d) The correlation between the λ_{em} and the dielectric constant of the solvents. (e) Fluorescence emission intensity augmentation and AIE effect of Cou-AIE-TPP^{+} in THF/PBS mixture with different volume percentages (vol%) of PBS fractions.

Table 1. The photophysical properties of Cou-AIE-TPP^{+} in various solvents.

Solvents	Dielectric constant (ε) of Solvent	λ_{abs} (nm)	λ_{em} (nm)	Molar extinction coefficient (ε) $M^{-1}cm^{-1}$	Stokes shift ($\Delta\lambda$, nm)
Toluene	2.38	475	517	1.01×10^{5}	42
$CHCl_3$	4.81	479	522	1.78×10^{4}	43
CH_2Cl_2	8.93	478	529	1.80×10^{4}	51
EtOH	24.5	479	543	1.36×10^{4}	64
MeOH	32.7	477	546	1.87×10^{4}	69
DMF	36.7	486	549	1.42×10^{4}	63
DMSO	46.7	482	552	1.26×10^{4}	70
PBS	80.1	480	604	1.68×10^{4}	124

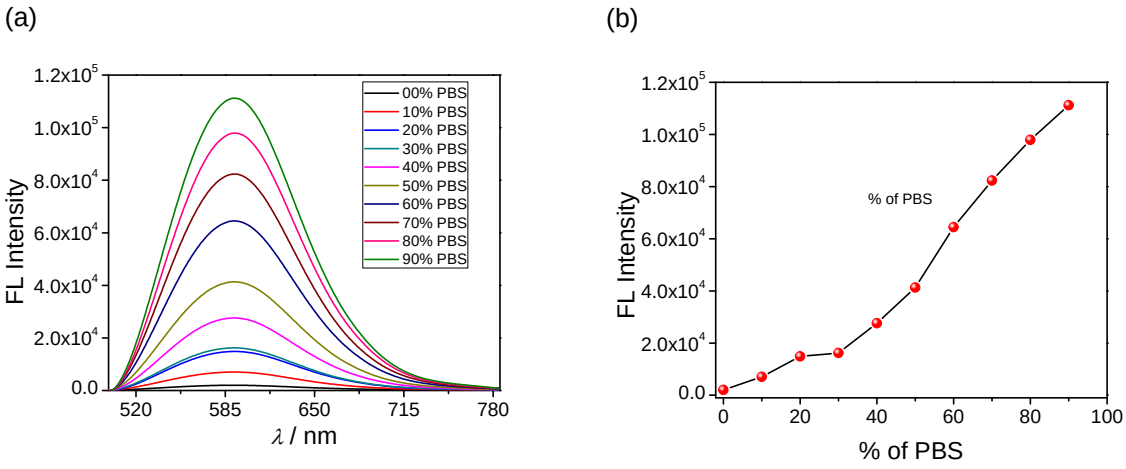

Figure 32. (a) Fluorescence spectra of the control compound Cou-AIE in THF/PBS mixture with different volume percentage (vol%) of PBS fractions. (b) Plot of the change in fluorescence intensity of Cou-AIE with the volume fraction of PBS.

Secondary Structure Determination and Morphology of Aβ40:

The secondary structural information as well as the monomers, oligomers, protofibrils, and fibril formation of Aβ40 are systematically characterized using FT-IR, CD, X-ray fiber diffraction (XRD), and TEM experiments. Initially, the FT-IR spectrum of Aβ40 exhibits a peak at 1650 cm^{-1} (amide I region) that signifies random coil structure. The FT-IR spectrum of Aβ40 fibril displays peaks at 3290 cm^{-1} (N-H stretching), 1624 cm^{-1} (amide C=O stretching), and 1513 cm^{-1} (N-H bending), signifying the construction of intermolecular H-bonded β-sheet secondary structure (**Figure 33a,b**). Initially, the CD spectrum of Aβ40 monomers (10 μM) in DI H_2O with 1% TFE shows a negative peak at 198 nm, indicative of dominating a random coil structure (**Figure 31c**). However, after 5 days, secondary structural transformation from random coil to β-sheet is established by CD. A shorter wavelength positive band at 195 nm and a longer wavelength negative peak at 217 nm, which is consistent with that of Aβ40 fibrils (**Figure 33c**). The PXRD of the Aβ40 fibril displays peaks at 4.5 Å (meridional reflection, distance between adjacent β-strands within the β-sheets) and 10.6 Å (equatorial reflection, distances of β-sheets) characteristic of a cross-β-diffraction pattern (**Figure 33d**). The Aβ40 monomers, oligomers, protofibrils, and mature fibrils acquired at 0 h, 12 h, 24 h, and 5 days, respectively, are imaged using transmission electron microscope (TEM) to verify their morphology and size (**Figures 34a-e**). The selected area electron diffraction pattern confirms the cross-β structure **(Figure 34f)**.

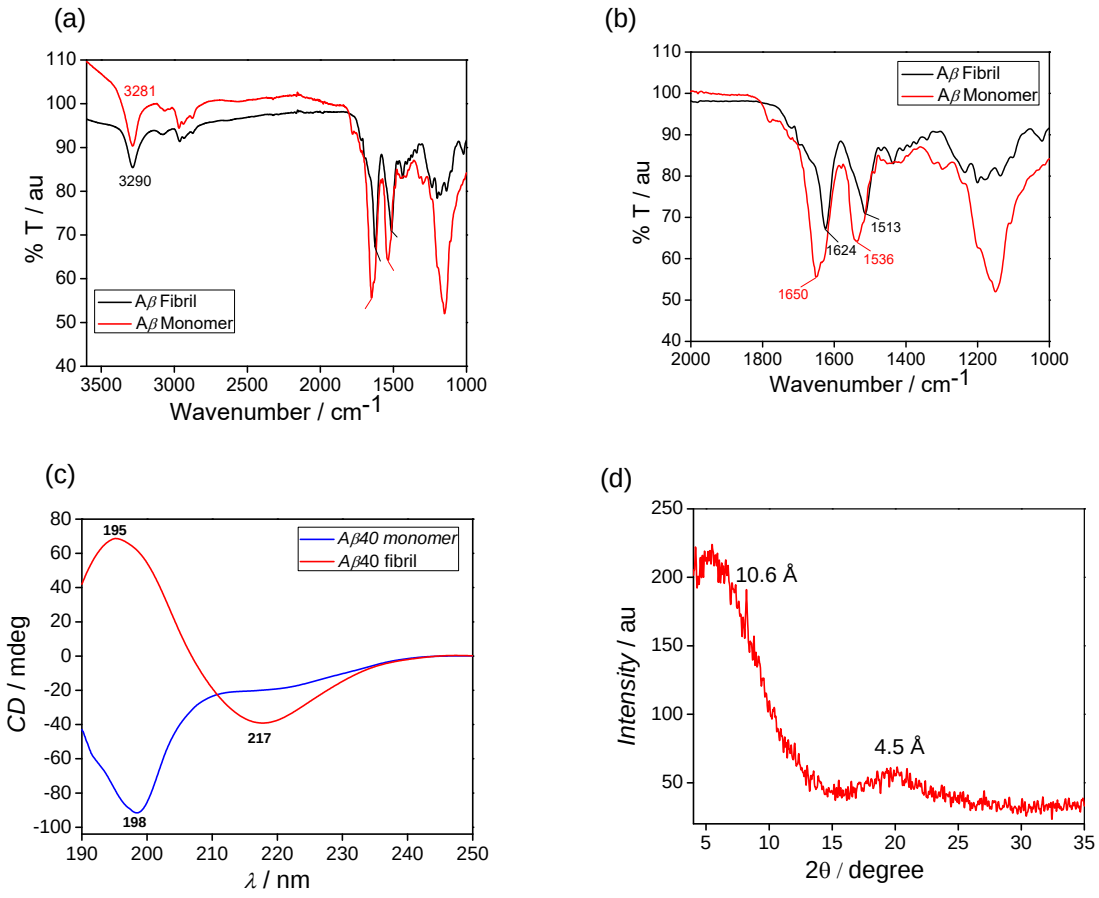

Figure 33. (a,b) FT-IR spectra of Aβ40 monomer and fibril. (c) CD spectra of Aβ40 monomers and fibrils. (d) XRD of the dried film from Aβ40 fiber.

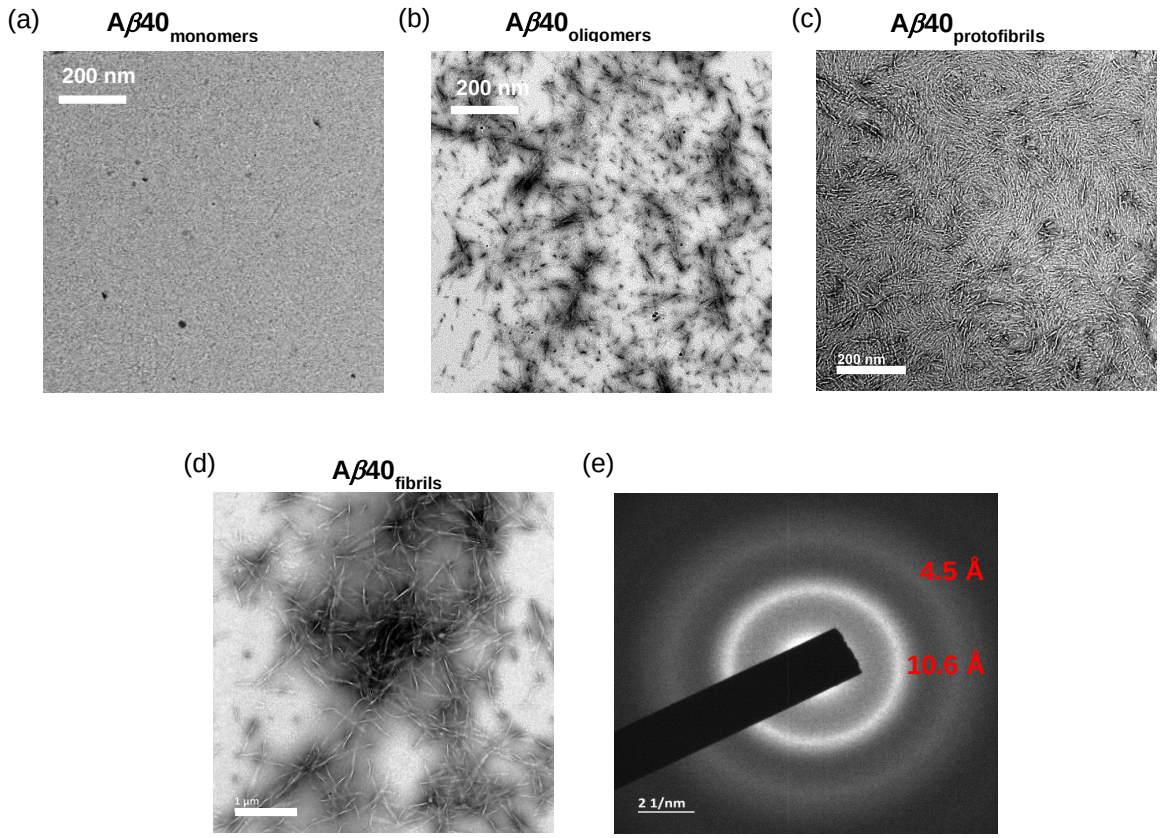

Figure 34. TEM images of Aβ40 peptide (a) monomers, (b) oligomers, (c) protofibrils, and (d) fibrils. (e) Selected area electron diffraction (SAED) pattern of Aβ40 fibril.

Monitoring of Aβ Protein Misfolding and Aggregation Kinetics Using a Targeted AIE Probe Cou-AIE-TPP$^+$:

There is an unmet need to develop extrinsic, targeted reporter probes to observe the amyloid aggregation process. We use an ex situ Cou-AIE-TPP$^+$ probe, integrating ICT-induced solvatofluorochromism with AIE phenomena, to provide comprehensive information on the Aβ40 protein misfolding and aggregation process as an alternative to ThT, the gold standard for monitoring Aβ fibril formation. The solvatofluorochromic AIE probe Cou-AIE-TPP$^+$ exhibits a remarkable inflection in its photophysics in the existence of Aβ40 aggregates. To investigate the advantages of this de novo designed Cou-AIE-TPP$^+$ probe over conventionally used ThT, the amyloid detection performance and aggregation kinetics are compared. The Cou-AIE-TPP$^+$ probe is capable of monitoring the kinetic progress of the Aβ40 fibrillation process with superior efficiency in contrast to ThT. Cou-AIE-TPP$^+$ displays very high selectivity for the Aβ40 aggregates as compared to the native monomeric form of the protein. The Cou-AIE-TPP$^+$ probe is dormant in the presence of monomeric Aβ40 forms; however, after binding to Aβ aggregates, a significant fluorescence augmentation of Cou-AIE-TPP$^+$ at 604 nm along with a shoulder at 721 nm in NIR emission wavelength is detected (**Figures 35a,b and 36a**). Though, owing to the decrease in polarity instigated via Aβ40 aggregation, the solvatochromic fluorescence probe Cou-AIE-TPP$^+$ exhibits a blue shift of 17 nm. We find that Cou-AIE-TPP$^+$ can report the nucleation (lag phase), elongation (growth phase), and saturation stages of Aβ40 fibril formation (**Figure 35b**). The lag phase designates Aβ40 monomers and soluble oligomers, the elongation phase denotes early aggregates and late aggregates; and finally, the aggregation progression reaches the saturation stage, where the majority of the Aβ40

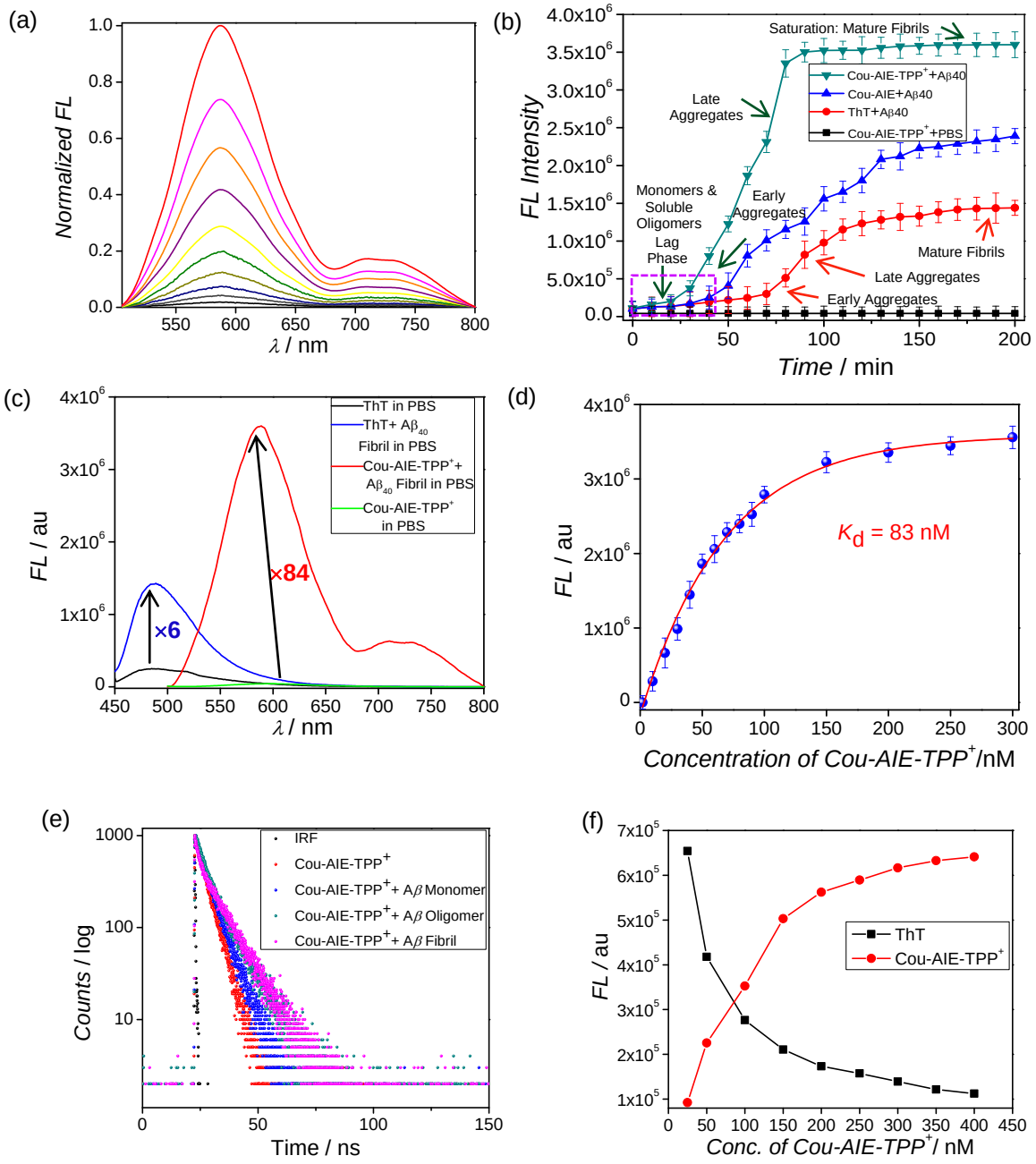

Figure 35. (a) Normalized fluorescence spectra of Cou-AIE-TPP$^+$ (1 μM) in the existence of various concentrations of Aβ40 (0-10 μM). (b) Monitoring of Aβ40 protein aggregation kinetics using a targeted AIE probe Cou-AIE-TPP$^+$ (green), a control probe Cou-AIE (blue), and the gold standard probe ThT (red). (c) Augmentation of fluorescence intensity by 84-fold

for Cou-AIE-TPP$^+$ (1 μM) and 6-fold for ThT (1 μM) after incubation with Aβ40 mature fibrils. (d) The dissociation constant (K_d = 83 nM) is determined from the plot of emission intensity change with increasing concentrations (up to 300 nM) of Cou-AIE-TPP$^+$ in Aβ40 aggregate (10 μM). Error bars denote SD of 3 measurements. (e) Fluorescence lifetime (τ) measurements of Cou-AIE-TPP$^+$ and after binding with Aβ40 monomers, oligomers, and fibrils in PBS by TCSPC technique (IRF: instrument response function). (f) Competitive binding and displacement assay of ThT with Cou-AIE-TPP$^+$ by titrating Aβ40 aggregate−ThT complex with Cou-AIE-TPP$^+$.

peptides are converted to mature fibrils. Quantitative investigation displays that the fluorescence intensity is boosted by 84-fold for Cou-AIE-TPP$^+$ after incubation with Aβ40 mature fibrils in PBS, while only a 6-fold amplification of emission intensity is detected for the gold standard probe ThT at the same conditions (**Figures 35c, 36b,c**). The kinetics of aggregation results using Cou-AIE-TPP$^+$ show approximately 1.9, 2.4, and 2.5 times augmented fluorescence intensity compared to ThT in detecting the Aβ early aggregates, late aggregates, and mature fibrils, respectively (**Figure 35b**). However, for a control experiment, a negligible fluctuation is detected for Cou-AIE-TPP$^+$ in PBS in the absence of Aβ40 over a 200 min time span. So, a fluorescence kinetics assay based on Cou-AIE-TPP$^+$ can be used to detect multiple states of Aβ protein aggregation and can be used to differentiate monomers, early aggregates, late aggregates, and mature fibrils. Furthermore, when the ThT fluorescence after binding to Aβ40 fibril is saturated, upon further addition of ThT, the fluorescence intensity of the probe is sharply decreased due to self-quenching. However, under the same condition, Cou-AIE-TPP$^+$ displays only negligible fluctuations. The binding affinity (K_d) of Cou-AIE-TPP$^+$ is quantitatively determined by a nonlinear curve fitting using the fluorescence-based saturation binding method, signifying that the synthesized Cou-AIE-TPP$^+$ probe binds tightly to the Aβ fibrils with 10.7 times higher binding

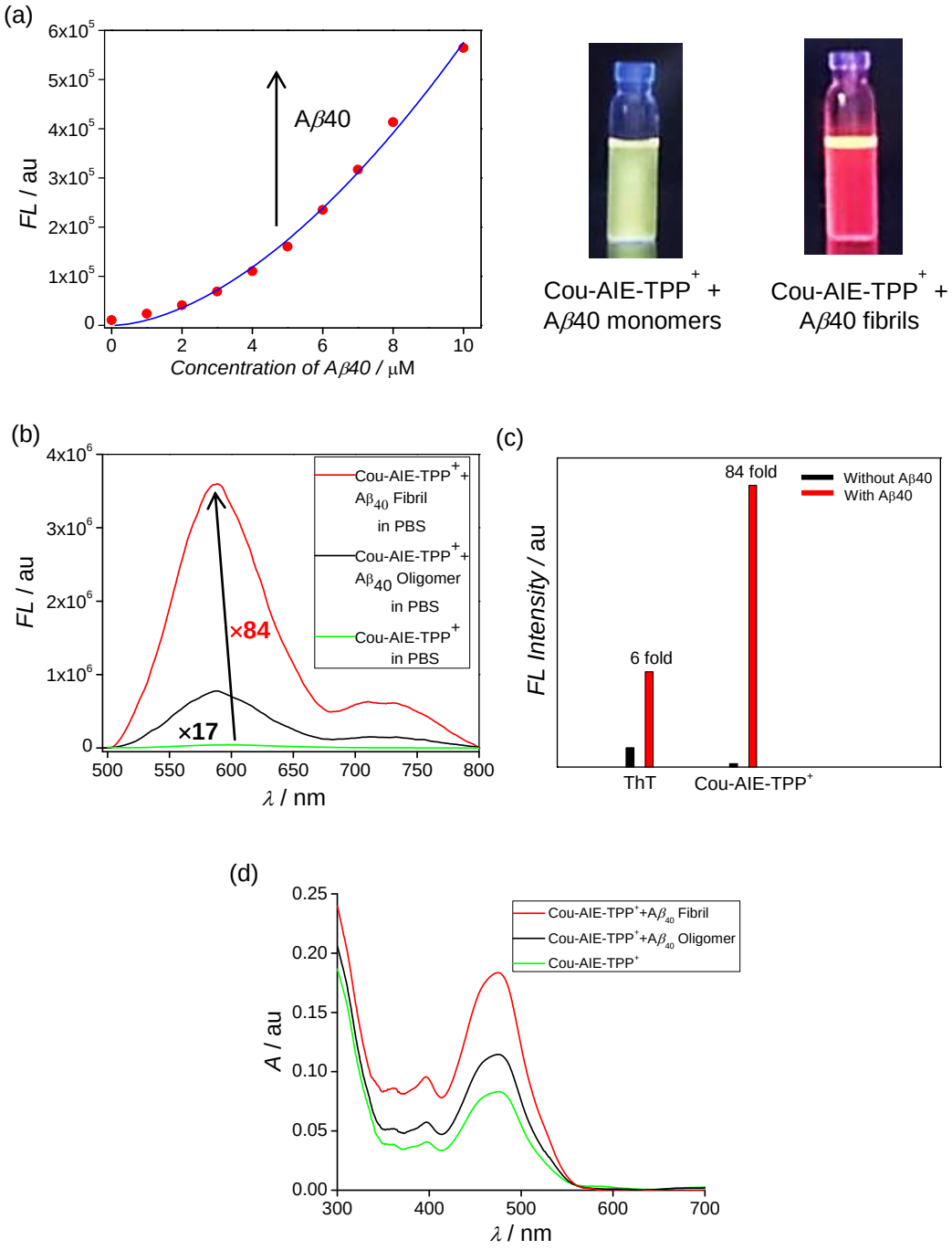

Figure 36. (a) Plot of fluorescence intensity change of Cou-AIE-TPP$^+$ versus different concentrations of Aβ40 (0-10 μM). (b) Augmentation of fluorescence intensity by 17-fold and 84-fold for Cou-AIE-TPP$^+$ (1 μM) after incubation with Aβ40 oligomers and mature fibrils, respectively, with blue shift. (c) Fluorescence emission intensity of ThT (1 μM) and Cou-AIE-TPP$^+$ (1 μM) with or without Aβ40 aggregates (10 μM). (d) Absorption spectra of Cou-AIE-TPP$^+$ and after incubation with Aβ40 oligomer and fibrils in PBS.

affinity (dissociation constant K_d = 83 nM) in comparison to ThT (K_d = 890 nM) (**Figure 35d**). The detection selectivity of the control probe Cou-AIE for Aβ40 fibril is compared to Cou-AIE-TPP$^+$. The results show that the Cou-AIE-TPP$^+$ yields a 1.5-times amplified signal in detecting Aβ fibrils relative to that of the control probe, Cou-AIE, lacking the lipophilic cationic TPP$^+$ functionality (**Figure 35b**). Moreover, Cou-AIE-TPP$^+$ senses the aggregation progression considerably earlier compared to ThT and Cou-AIE under the same condition, which signifies that Cou-AIE-TPP$^+$ can detect trace aggregated Aβ in the early incubation period (**Figure 35b**). Furthermore, the binding affinity of the control molecule Cou-AIE toward the Aβ fibrils is lower (K_d = 413 nM) in comparison to Cou-AIE-TPP$^+$, signifying that the lipophilic cationic TPP$^+$ functionality has a substantial impact on binding to the Aβ40 aggregates (**Figure 37**). It could be interpreted that Cou-AIE-TPP$^+$ accumulates into the hydrophobic pockets and is bound to the Aβ40 aggregates with the help of binding functionality, e.g., *N*,*N*′-diethylamino, TPP$^+$, aromatic π skeleton, ensuing in the diminution of conformational freedom and restriction of intramolecular motions. Moreover, the fluorescence lifetime and brightness are also augmented when the probe Cou-AIE-TPP$^+$ binds with Aβ oligomers and fibrils in comparison to monomers in PBS ($\tau_{\text{Cou-AIE-TPP+}}$ = 2.168 ns, $\tau_{\text{Cou-AIE-TPP+/Aβ fibrils}}$ = 5.648 ns) (**Figures 35e**, **36a**, **Table 2**). Such an escalation in the fluorescence lifetime is ascribed to the decrease in non-radiative progressions in the excited state of Cou-AIE-TPP$^+$ that is apparently a consequence of diminished micropolarity and enhanced microviscosity in the aggregated and fibrillar states of Aβ40. Moreover, absorption change of Cou-AIE-TPP$^+$ after binding with Aβ fibrils is also noticed (**Figure 36d**).

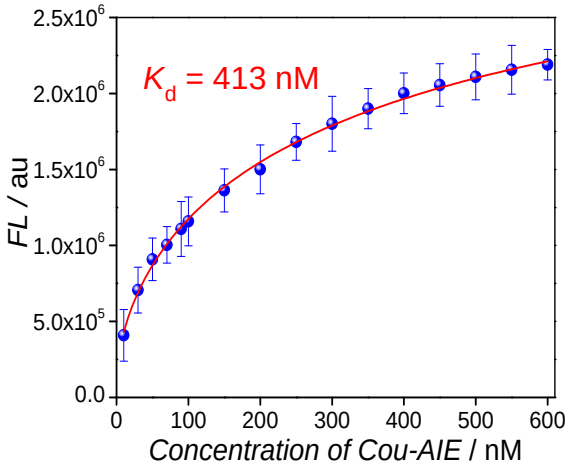

Figure 37. The dissociation constant (K_d = 413 nM) is determined from the plot of emission intensity change with increasing concentrations (up to 600 nM) of Cou-AIE in Aβ40 aggregate (10 μM). Error bars denote SD of 3 measurements.

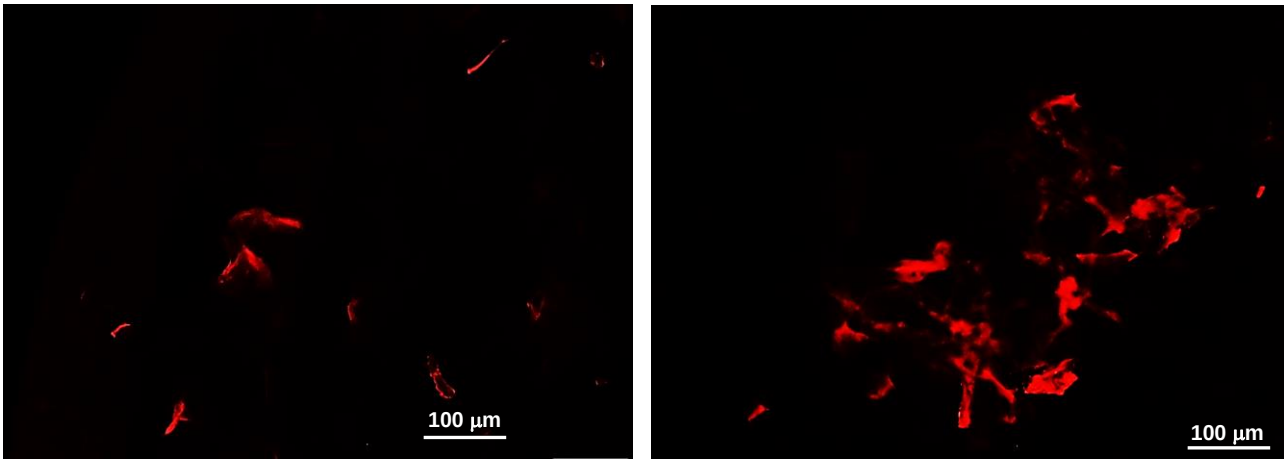

Figure 38. CLSM image of Aβ40 fibrils stained with Cou-AIE-TPP$^+$.

Bright orange-red fluorescence is detected when Aβ fibrils/ Cou-AIE-TPP$^+$ complex are exposed to UV light (**Figure 36a**). The formation of fibrils is further confirmed by CLSM of the Aβ40 fibrils stained with Cou-AIE-TPP$^+$ (**Figure 38**). Moreover, Cou-AIE-TPP$^+$ exhibits insignificant emission alteration in the existence of various amino acids and native proteins, authorizing its selectivity to Aβ40 (**Figure 45a**). The specific recognition of Aβ40 fibrils over others indicates the potential utility of Cou-AIE-TPP$^+$ as an Aβ biomarker owing to the critical structural skeleton integrating ICT-induced solvatofluorochromism with AIE phenomena and the right lipophilicity for multiple states of Aβ protein aggregation targeting.

Table 2 Relative quantum yields (QYs)[a] and fluorescence lifetimes (τ)[b] of Cou-AIE-TPP$^+$ and after binding with Aβ40 monomers, oligomers, and fibrils in PBS.

Compound	**Fluorescence Lifetime (τ / ns)**	**QY**
Cou-AIE-TPP$^+$	2.168 ± 0.126	0.45
Cou-AIE-TPP$^+$ + Aβ40 Monomers	2.253 ± 0.042	0.47
Cou-AIE-TPP$^+$ + Aβ40 Oligomers	2.981 ± 0.085	0.52
Cou-AIE-TPP$^+$ + Aβ40 Fibrils	5.648 ± 0.057	0.70

[a] Relative QYs are measured using rhodamine-B as the reference probe.

[b] τ are determined by the time-correlated single photon counting (TCSPC) technique.

Competitive Binding and Displacement Assay: **Cou-AIE-TPP$^+$ Binds Strongly to Aβ40 Aggregates and Displaces Fibril-Bound ThT**:

To acquire more information regarding the binding sites of Aβ40 aggregates for Cou-AIE-TPP$^+$, we explore a competitive binding strategy with the known amyloid probe ThT. A displacement assay that titrates ThT (400 nM)-bound Aβ40 fibrils (10 μM) with Cou-AIE-TPP$^+$ is used to acquire more insights. When Cou-AIE-TPP$^+$ (0 to 400 nM) is gradually added to the ThT/Aβ40 fibrillar complex, ThT's fluorescence at λ_{em} 480 nm progressively decreases while Cou-AIE-TPP$^+$'s red fluorescence intensity at λ_{em} 604 nm sharply increases with an increase in Cou-AIE-TPP$^+$ concentration (**Figure 35f**). It signifies that Cou-AIE-TPP$^+$ is indeed binding and displacing ThT from the ThT/Aβ40 fibrillar complex. Similar to this, when ThT and Cou-AIE-TPP$^+$ are introduced to the Aβ40 fibrils solution concurrently, ThT's fluorescent intensity is attenuated with a less than 2-fold increase while Cou-AIE-TPP$^+$'s fluorescence intensity enhances dramatically. This result indicates that Cou-AIE-TPP$^+$ would enter with ThT in the same binding site and have a stronger affinity for Aβ40 fibrils in comparison to ThT. Due to its great binding affinity and highly specific fluorescence response, Cou-AIE-TPP$^+$ offers promise for the early detection of Aβ40 aggregates.

Isothermal Titration Calorimetry (ITC):

ITC quantifies the heat released or absorbed in a biomolecular binding incident in solution and calculates the binding affinity and thermodynamic parameters of molecular interactions in a single test. The negative heat generation in the titration of Aβ40 with Cou-AIE-TPP$^+$ in ITC designates that the binding is exothermic in aqueous PBS solution and is predominantly enthalpy-driven (ΔH = –4.54 kcal/mol) (**Figure 39**). The free energy change (ΔG) is negative (ΔG =

−2.3 kcal/mol) that implies that the interactions between the Aβ40 oligomer and Cou-AIE-TPP$^+$ are spontaneous in nature.

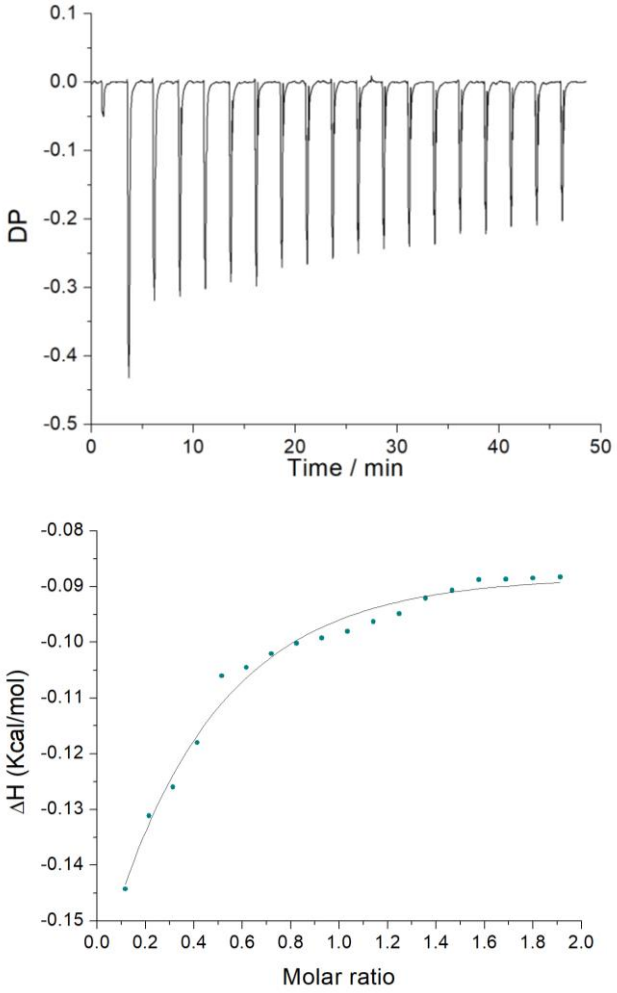

Cell conc.	Syringe conc.	N (Sites)	K_d (nM)	ΔH (kcal/mol)	TΔS (kcal/mol)	ΔG (kcal/mol)
20 µM	200 µM	1.1	107	-4.54	-2.24	-2.30

Figure 39. The upper panels show the raw data for the Aβ40/Cou-AIE-TPP$^+$ titration and the bottom panels represent the binding isotherm. The resultant isotherm is best fitted to a one site binding model to attain the binding affinity (K_d), stoichiometry (n), enthalpy (ΔH), entropy (ΔS), and ΔG of interaction.

Diffusion-Ordered Spectroscopy (DOSY) and Diffusion by NMR:

Proton diffusion-ordered NMR spectroscopy (DOSY) is utilized to scrutinize the diffusion of Cou-AIE-TPP$^+$ in solution-state inside the Aβ40 oligomers (**Figures 41, 42**). DOSY is a prevailing toolkit for inspecting molecular association via determining the diffusion coefficients of molecules that endorse us to validate the diffusion of Cou-AIE-TPP$^+$ to Aβ40 oligomers. A set of spin echo spectra is recorded with different time intervals, and signal decays are investigated to acquire the diffusion coefficients (D) (**Figure 40**). The diffusion coefficient is calculated using the relative intensities ~7.0−7.5 ppm that correspond to the aromatic hydrogens of the Cou-AIE-TPP$^+$. In comparison to free Cou-AIE-TPP$^+$ (faster diffusing species), which has a diffusion coefficient of 3.11±0.14 × 10^{-10} m^2 s^{-1}, the diffusivity of Cou-AIE-TPP$^+$ in the existence of 10 μM Aβ40 oligomer (slower diffusing complex) is considerably reduced to 2.77±0.03 × 10^{-10} m^2 s^{-1} in PBS solution. The DOSY experiment signifies that the binding of Cou-AIE-TPP$^+$ to the Aβ40 oligomer reduces the extent of Brownian molecular motion or diffusion owing to the larger construct in comparison to free Cou-AIE-TPP$^+$.

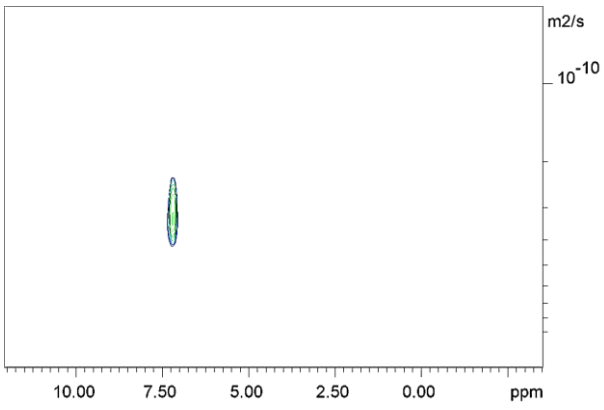

Figure 40. Diffusion coefficient of Cou-AIE-TPP^{+} (5 μM) in the existence of Aβ40 (10 μM) in PBS solution, calculated from DOSY-NMR. Free Cou-AIE-TPP^{+} (faster diffusing species) has a diffusion coefficient of 3.11±0.14 × 10^{-10} m^2 s^{-1}, and the diffusivity of Cou-AIE-TPP^{+} in the existence of Aβ40 oligomer (slower diffusing complex) is considerably reduced to 2.77±0.03 × 10^{-10} m^2 s^{-1}.

Compound	Concentration	F2 [ppm]	D (m^2/s)
Cou-AIE-TPP^{+}	5 μM	7.2	3.11e–10
Cou-AIE-TPP^{+} + Aβ40	5 μM + 10 μM	7.2	2.77e–10

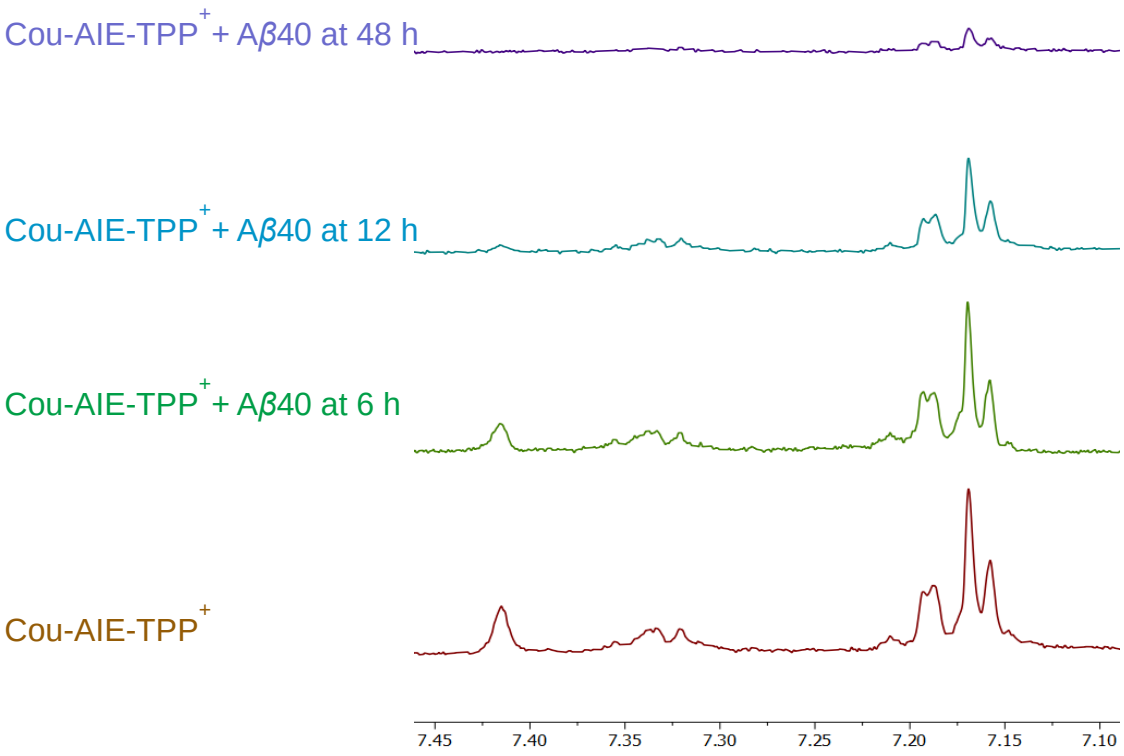

Figure 41. Relative intensities from diffusion ordered (DOSY-NMR) NMR spectra to investigate the interactions between Cou-AIE-TPP^{+} and Aβ40 at different time intervals (0-48 h). The diffusivity of Cou-AIE-TPP^{+} in the presence of 10 μM Aβ40 oligomer is considerably reduced with time in PBS solution.

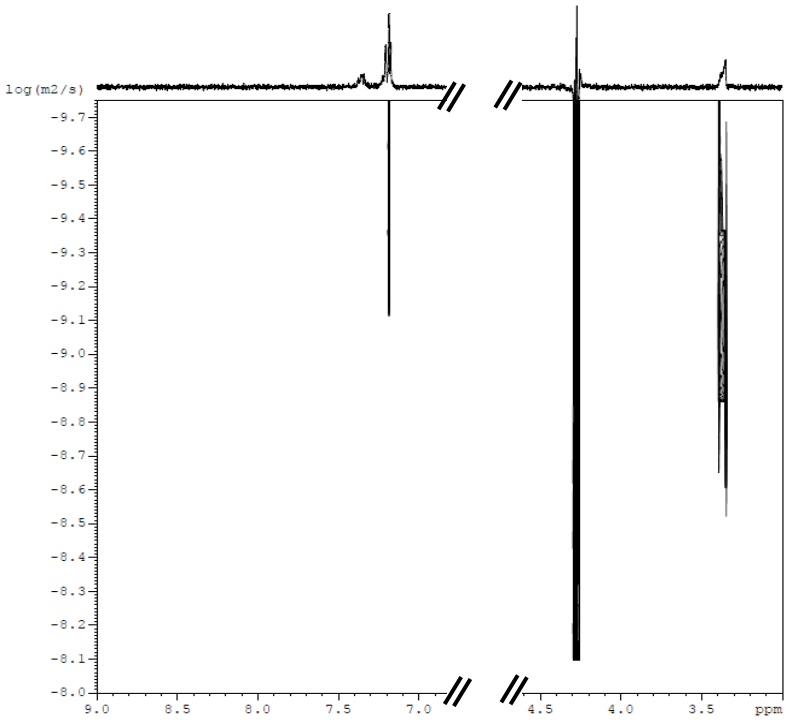

Figure 42. DOSY spectrum showing the different diffusion behavior of the protons after interactions between Cou-AIE-TPP^{+} and Aβ40. The vertical axis log (m^2 / s) represents the diffusion coefficient.

Theoretical Calculations Based on Density Functional Theory and Molecular Docking:

The DFT energy minimized structure of Cou-AIE-TPP^+ at the B3LYP/6-31G* level is used to investigate the molecular interaction with Aβ40 aggregates. The MO calculation shows that the electron density for the HOMO level is mainly localized around the electron-donating groups *N*,*N*-diethyl amino phenyl unit and *N*,*N*-dialkylated amino phenyl unit, while the LUMO lobe coefficient is larger on the electron-withdrawing acrylonitrile unit (**Figure 43**). The D-A-D structure narrows the bandgap (2.6 eV) of the Cou-AIE-TPP^+ molecule due to ICT. Such electron distribution is characteristic of the D-A-D system, which results in solvatofluorochromism. A molecular docking study is performed to further uncover the possible binding sites and molecular interactions between Cou-AIE-TPP^+ and Aβ40 fibrils. Molecular docking of the Cou-AIE-TPP^+ with Aβ40 fibril (PDB ID: 2LMQ) displays noncovalent interactions such as van der Waals interaction, conventional hydrogen bonding, carbon−hydrogen bond, σ-π interaction, π–Sulfur interaction, π-π interaction, edge-to-face or T-shape π-π interaction, alkyl-π interaction between the Gly33, Ile31, Gly37, Gly38, Val39, Met35, Ala30, Asp23, Lys28, Asn27, Ser26, Phe19, Ile 31, Ile32, and Leu17 amino acid residues of Aβ40 peptide with TPP^+, coumarin and aromatic rings, amide and lactone C=O, N of CN of Cou-AIE-TPP^+ with a docking score of −7.1 kcal/mol (**Figure 6**). The theoretical modeling suggests the presence of π-aromatic residues in the Cou-AIE-TPP^+ molecule, e.g., the π-surface of TPP^+, coumarin, and aromatic rings, play a pivotal function for the high binding affinity of the exposed hydrophobic patches of Aβ40 fibrils. The Cou-AIE-TPP^+ probe is positioned inside the tunnel along the fibril axis and has efficient Aβ40 recognition. When Cou-AIE-TPP^+ enters the hydrophobic sites and is bound to the Aβ40 fibrils, which restrict its conformational freedom, rotation,

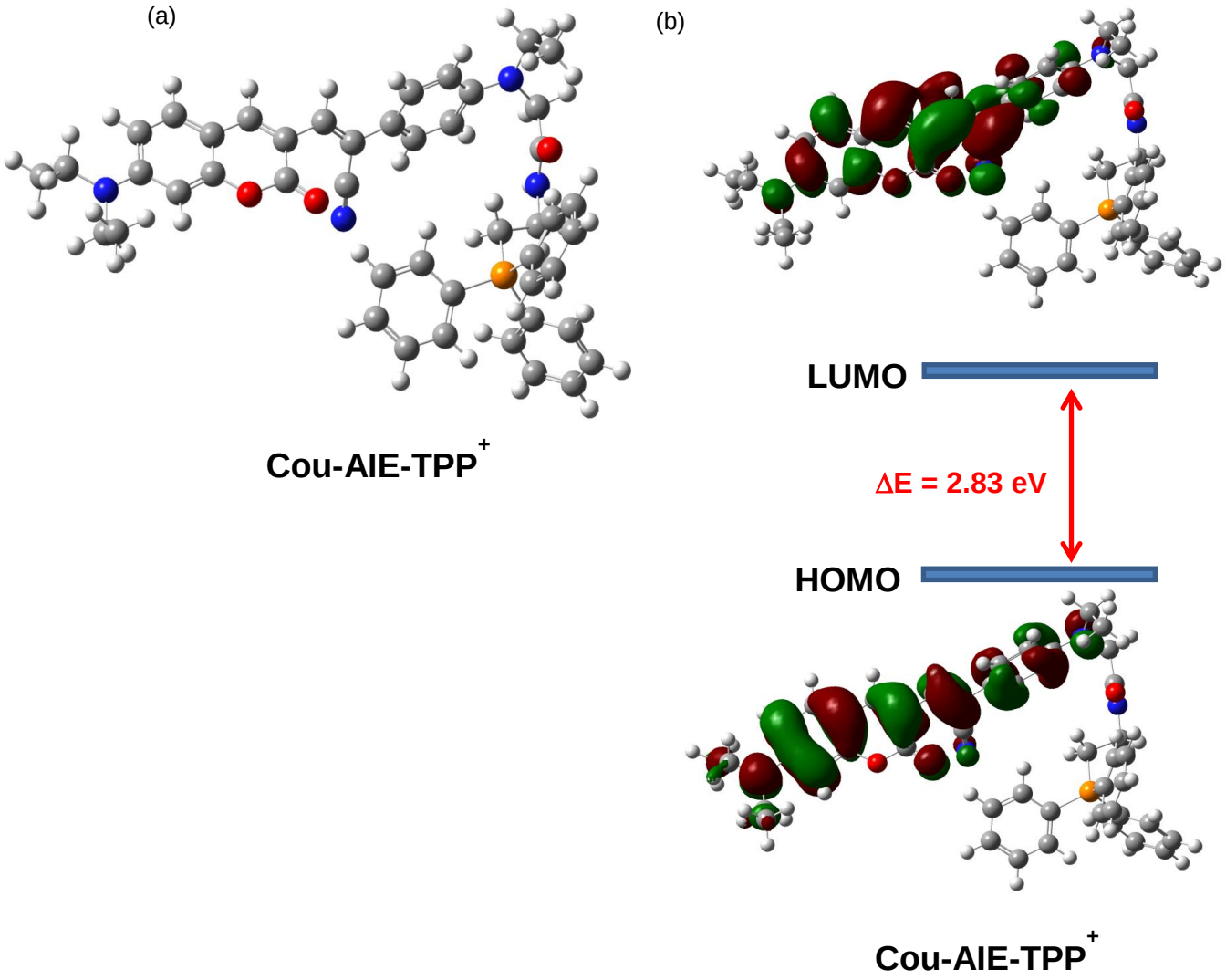

Figure 43. (a) B3LYP / 6-31G* energy optimized structure of Cou-AIE-TPP^{+}. (b) HOMO and LUMO of Cou-AIE-TPP^{+} with a HOMO-LUMO energy gap of 2.83 eV.

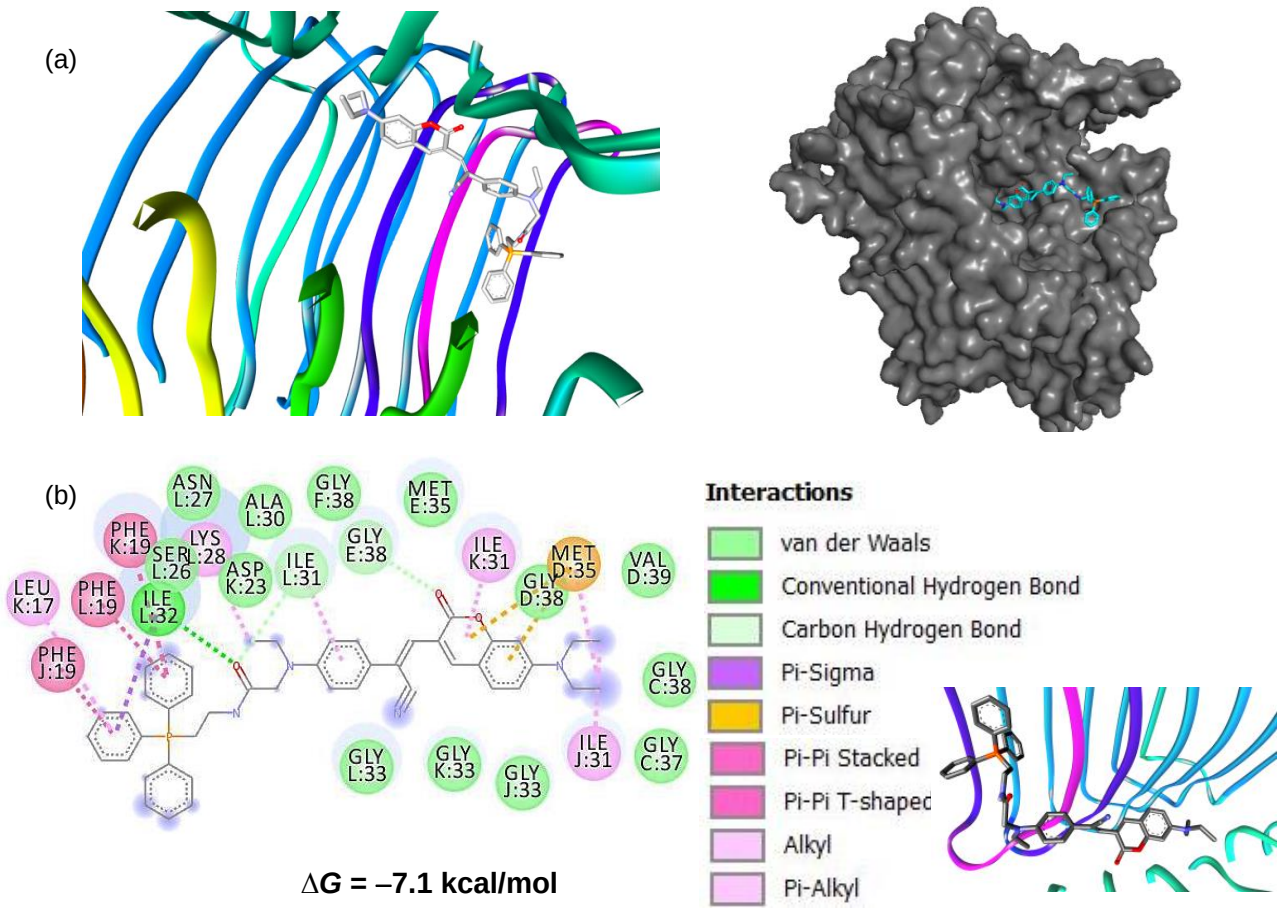

Figure 44. (a) Molecular docking and binding mode of Aβ40 fibril with Cou-AIE-TPP^{+}. Stick and surface views of the encapsulated Cou-AIE-TPP^{+} in the internal tunnel of Aβ40 fibril. (b) Binding site and noncovalent interactions of Aβ40 with Cou-AIE-TPP^{+}.

and vibration; this results in an augmentation of Cou-AIE-TPP$^+$ fluorescence. It is noteworthy that Cou-AIE-TPP$^+$ has substantially higher estimated binding affinities to Aβ40 in comparison to ThT, with much more intermolecular noncovalent interactions.

Biocompatibility and Cytotoxicity Study using Cou-AIE-TPP$^+$:

The sustained durability of Cou-AIE-TPP$^+$ in the presence of potential interferences is a crucial prerequisite for its high-performance targeted bioimaging applications. No noteworthy fluctuations are noticed in the emission of Cou-AIE-TPP$^+$ at 604 nm in addition of various cations (Na^+, K^+, Ca^{2+}) in the physiological environment (pH 7.4, 37 °C) throughout 24 h (**Figure 45a**). Additionally, Cou-AIE-TPP$^+$ is pretty stable in the existence of small reactive species, e.g., Cys, H_2O_2, ^{t}BuOOH, NO, and ClO^- in PBS (pH 7.4, 37 °C) over 24 h (**Figure 45a**). Furthermore, we have also evaluated the fluorescence variations of Cou-AIE-TPP$^+$ in the presence of a series of different amino acids, e.g., Gly, Leu, Gln, Thr, Tyr, Arg, and Lys. As illustrated in **Figure 45a**, negligible fluorescence signal fluctuations of Cou-AIE-TPP$^+$ at 604 nm are perceived in the presence of various amino acids in physiological environments (PBS, pH 7.4, 37 °C, 24 h). The specificity of Cou-AIE-TPP$^+$ for Aβ fibrils is evaluated with potentially competitive species, including insulin and lysozyme fibrils. Cou-AIE-TPP$^+$ exhibits a 6.5-fold and 3.8-fold higher binding affinity with Aβ40 fibrils in comparison to insulin and lysozyme fibrils, respectively (**Figure 45a)**. The huge augmentation in the fluorescence signal confirms the effectiveness of Cou-AIE-TPP$^+$ at a higher detection sensitivity for Aβ40 fibrils. Cell viability studies using a standard XTT assay on SH-SY5Y cells are performed. The outcome displays that there is insignificant cytotoxicity of Cou-AIE-TPP$^+$, even when the concentration is 50 μM over 72

h (**Figure 45b**). Adequate lipophilicity is requisite to achieve the blood-brain barrier

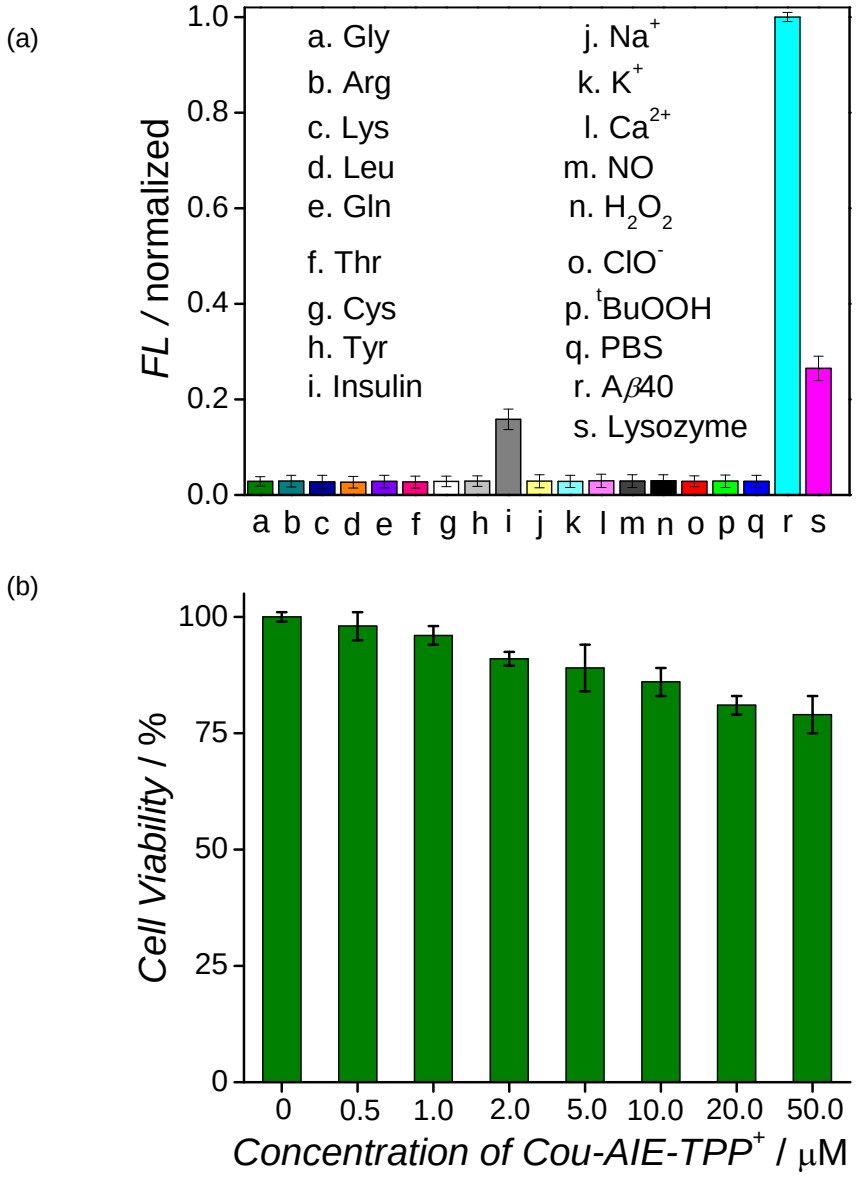

Figure 45. (a) High selectivity of Cou-AIE-TPP^{+} towards Aβ40 aggregates over other potential competitive species. Insignificant fluctuations are perceived in the emission of Cou-AIE-TPP^{+} (1 μM, λ_{em} = 604 nm) in the presence of various interferents in PBS, pH 7.4, 37 °C, 24 h. Error bars are ± SD (n = 3). (b) Cell viability of SH-SY5Y cells at different doses of Cou-AIE-TPP^{+} over 72 h exhibits negligible cytotoxicity.

(BBB) penetrability as well as substantial uptake inside the mitochondria. The BBB penetration capability is often assessed through the oil-water partition coefficient (log *P*). Experimentally, the *n*-octanol/PBS partition coefficient (log *P*) value of Cou-AIE-TPP$^+$ is determined as 1.3 by $P_{\text{octanol/PBS}} = [C]_{\text{octanol layer}}/[C]_{\text{PBS layer}}$, envisioning more reasonable lipophilicity compared to ThT (log *P* = 0.16).[26] The log *P* value suggests that the lipophilicity of Cou-AIE-TPP$^+$ is perfect to penetrate the BBB and has great potential to accumulate in the mitochondria. Considering these, we envisage that the multifunctional Cou-AIE-TPP$^+$ probe has the potential to be exploited as a harmless biomarker for targeted imaging of mitochondria and the detection of Aβ aggregates.

Mitochondria-Targeted Imaging Utilizing Cou-AIE-TPP$^+$ on a Confocal Laser Scanning Microscopy:

The lipophilic cationic TPP$^+$ functionality tethered probe Cou-AIE-TPP$^+$ is an excellent choice for targeted mitochondrial imaging owing to its exceptional biostability, noncytotoxicity, ICT-based solvatofluorochromism, AIE effect, large Stokes shift, and ultrabrightness. The subcellular localization of Cou-AIE-TPP$^+$ in human neuroblastoma SH-SY5Y live-cells is executed using CLSM. After swift internalization through the SH-SY5Y live-cell membrane, it is expected that Cou-AIE-TPP$^+$ would accumulate inside the mitochondria at a 500−1000 fold higher concentration related to the extracellular matrix ($\Delta\Psi_{\text{plasma membrane}}$ = −30 to −60 mV vs $\Delta\Psi_m$ −150 to −180 mV) in accordance with the Nernst equation, thus exhibiting the AIE effect inside the mitochondria. So, the AIE-based Cou-AIE-TPP$^+$ probe is anticipated to resolve the fluorescence quenching issue of conventional ACQ-based mitochondria targeting fluorescent biomarkers, which arises at high concentrations in an aggregation state inside the mitochondria. A colocalization experiment is performed in live SH-SY5Y cells with Cou-AIE-TPP$^+$ (500 nM) and the commercially available

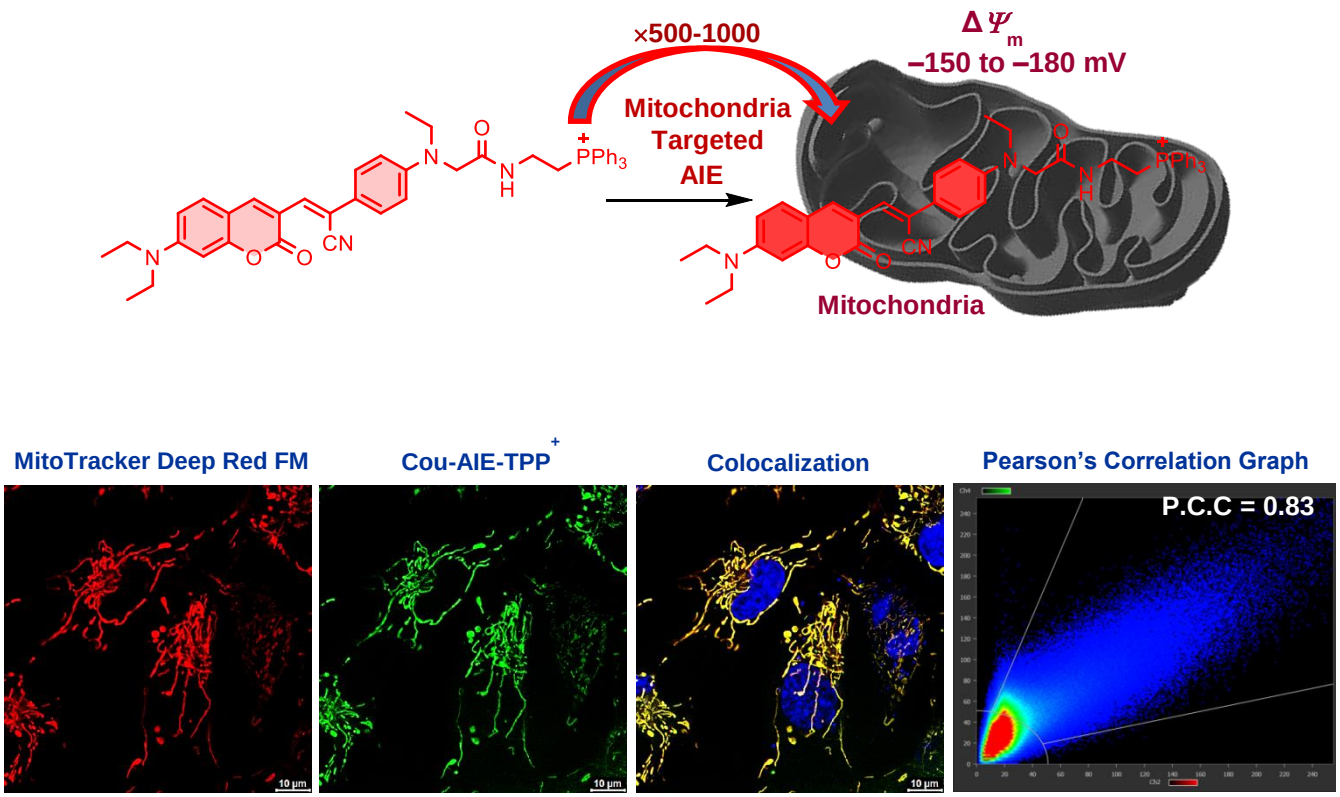

Figure 46. The lipophilic cationic Cou-AIE-TPP^{+} exhibits the AIE effect inside the mitochondria, guided by the highly negative $\Delta\Psi_m$. CLSM images of Cou-AIE-TPP^{+} colocalized with MitoTracker Deep Red FM in human neuroblastoma live SH-SY5Y cells. Hoechst 33342 (blue), MitoTracker Deep Red FM (red), and Cou-AIE-TPP^{+} (green). The colocalization scatter graph displays Pearson's correlation coefficient (PCC) of 0.83.

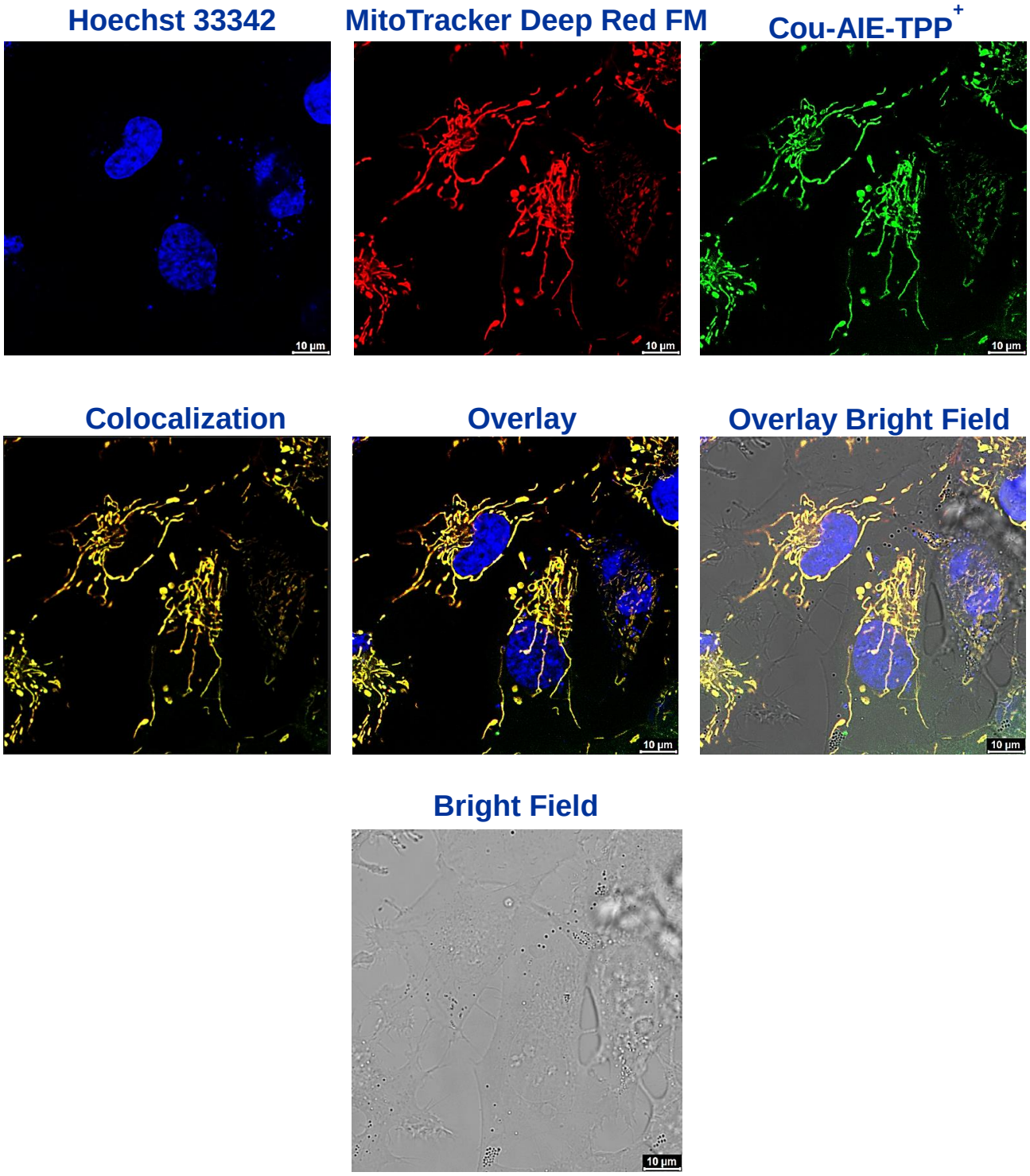

Figure 47. Confocal microscopic images of Cou-AIE-TPP^{+} colocalized with MitoTracker Deep Red FM in human neuroblastoma live SH-SY5Y cells. Hoechst 33342 (blue channel), MitoTracker Deep Red FM (red channel), and Cou-AIE-TPP^{+} (green channel).

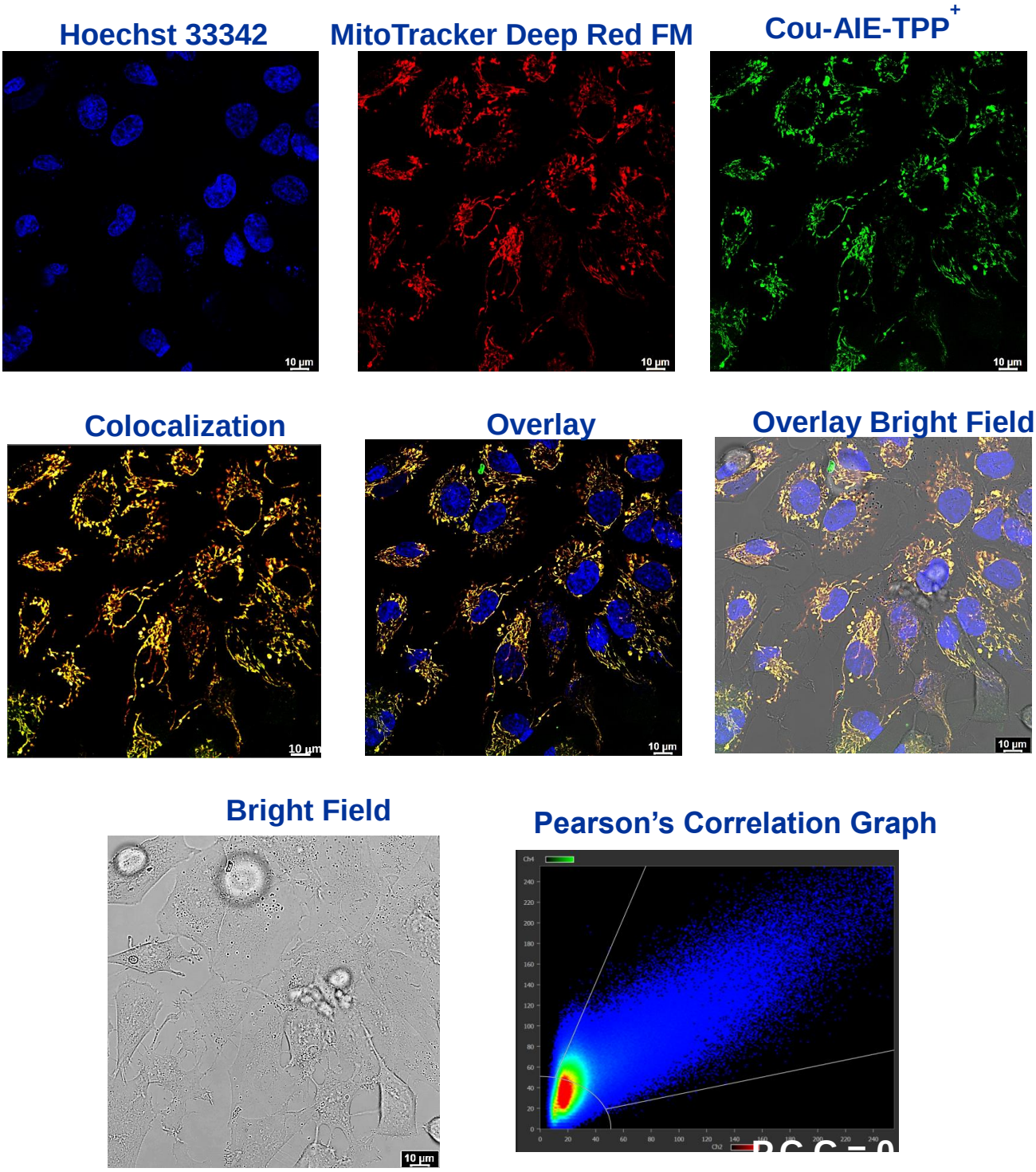

Figure 48. Confocal microscopic images of Cou-AIE-TPP^{+} colocalized with MitoTracker Deep Red FM in human neuroblastoma live SH-SY5Y cells. Hoechst 33342 (blue channel), MitoTracker Deep Red FM (red channel), and Cou-AIE-TPP^{+} (green channel). The colocalization scatter graph displays Pearson's correlation coefficient (PCC) of 0.82.

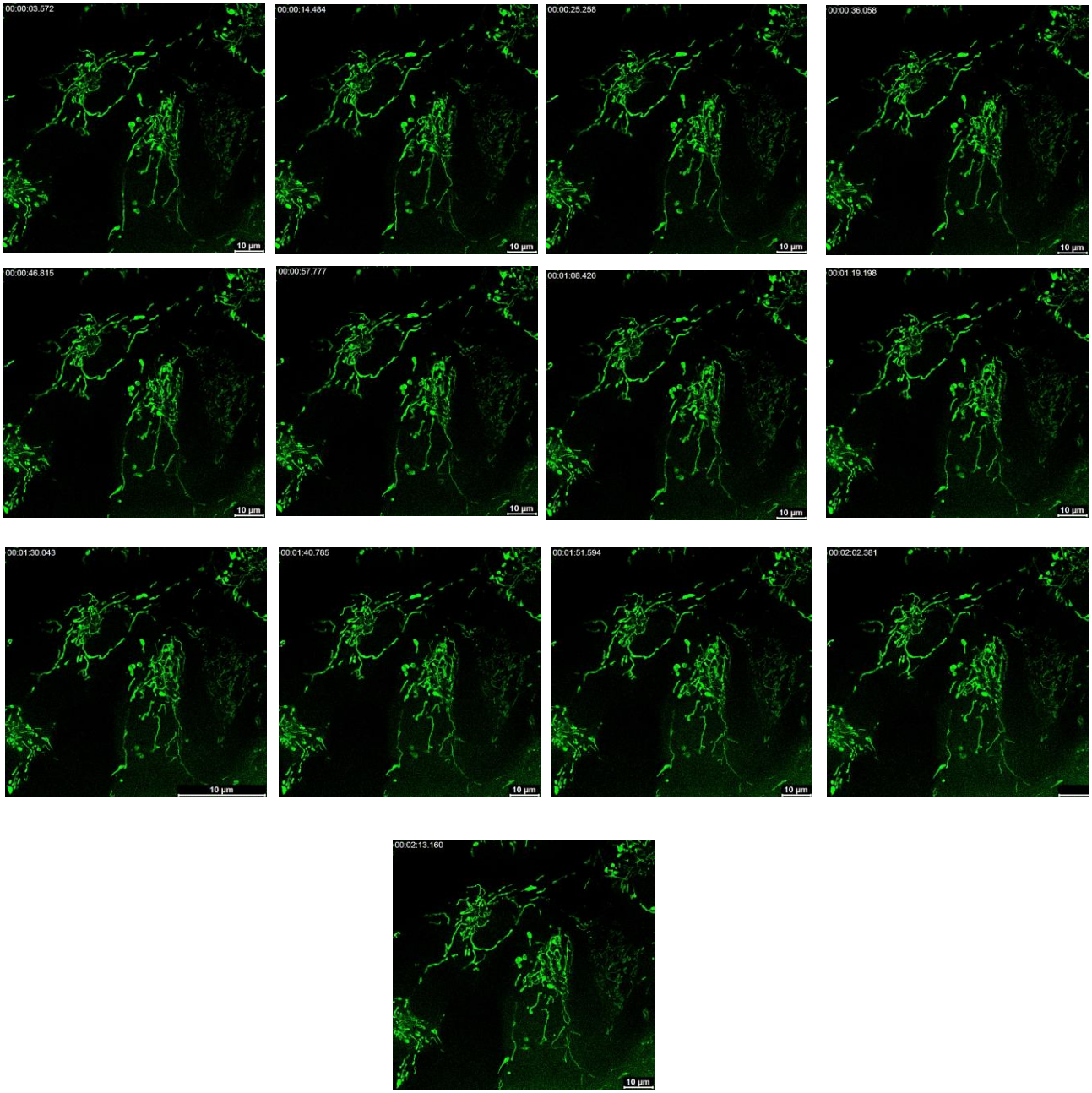

Figure 49. Real-time mitochondrial tracking inside the human neuroblastoma live SH-SY5Y cells stained with the mitochondria targeting synthesized Cou-AIE-TPP^{+} probe.

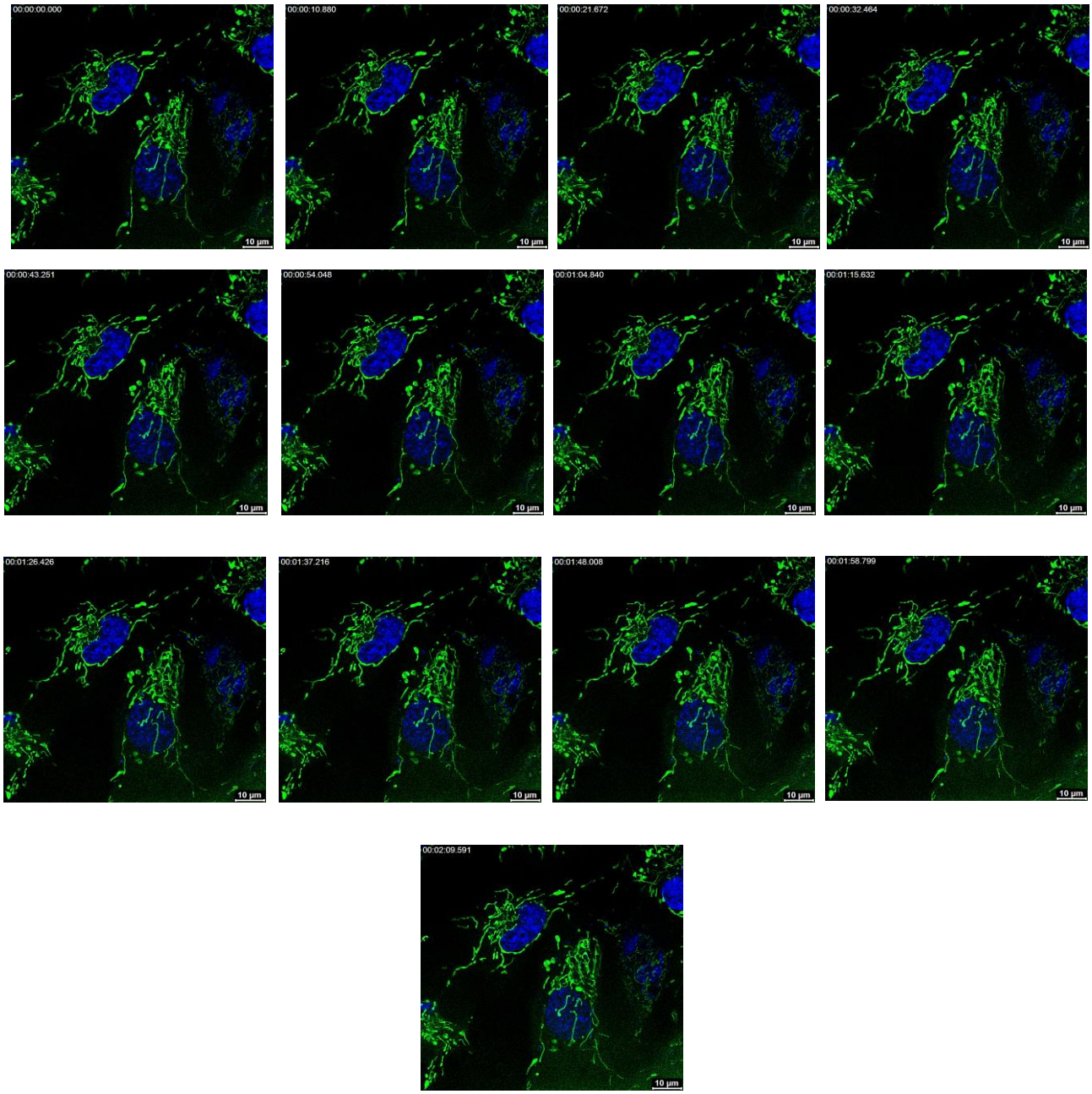

Figure 50. Real-time mitochondrial tracking inside the human neuroblastoma live SH-SY5Y cells stained with the mitochondria targeting synthesized Cou-AIE-TPP^{+} probe. Blue color signifies nuclear staining by Hoechst 33342.

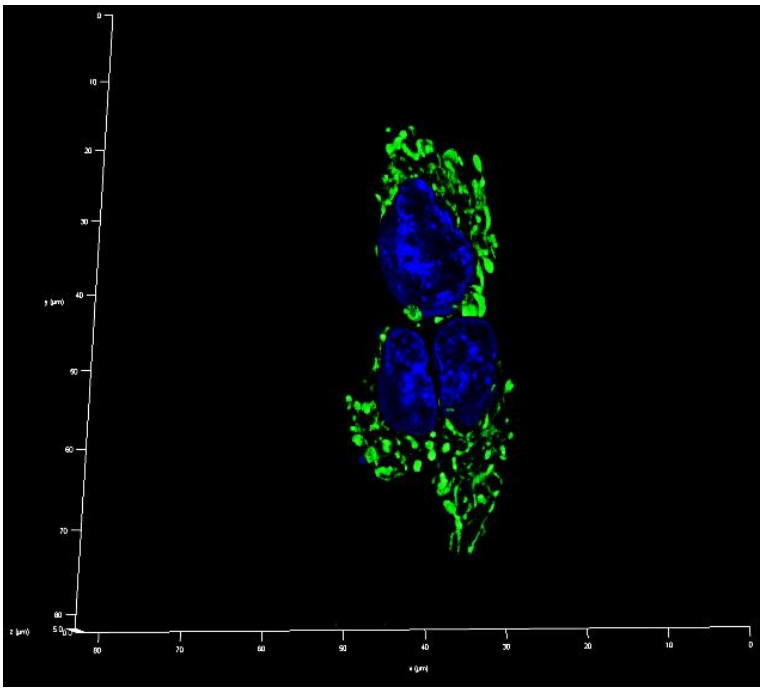

Figure 51. 3D CLSM image of the human neuroblastoma live SH-SY5Y cells stained with our synthesized mitochondria targeting Cou-AIE-TPP^{+} dye (green color). Blue color signifies nuclear staining by Hoechst 33342.

mitochondria-specific marker Mito-Tracker Deep Red. The CLSM experiment confirms that Cou-AIE-TPP^{+} localizes inside the SH-SY5Y live-cell mitochondria with a good Pearson's correlation coefficient (PCC) of 0.83 (**Figures 46, 47, 48**). Real-time mitochondrial tracking over extended periods (2.13 min) in human neuroblastoma live SH-SY5Y cells stained with the mitochondria targeting Cou-AIE-TPP^{+} probe is acquired (**Figures 49 and 50**). For live SH-SY5Y cell 3D image accomplishment, CLSM images of live cells stained with the mitochondria-selective Cou-AIE-TPP^{+} are captured every 0.4 μm on the *Z*-axis. 32 frames for distinct channels are collected over a 10 min time period to attain the live SH-SY5Y cell 3D CLSM video (**Figure 51**). It confirms that lipophilic cationic Cou-AIE-TPP^{+} molecules proficiently and

selectively accumulate inside the live SH-SY5Y cell mitochondria and exhibit an AIE effect guided by the highly negative $\Delta\Psi_m$.

Targeted Monitoring of Mitochondrial Morphology Alteration, Damage, and Dysfunction During Exogenous Aβ40-Induced Neurotoxicity:

The ability of Cou-AIE-TPP$^+$ to selectively localize in the mitochondria and exhibit the AIE effect may be an imperative tool to monitor mitochondrial morphology alteration, damage, and dysfunction during Aβ-induced neurotoxicity, which is the most early and notable hallmark of vulnerable neurons. We have monitored mitochondrial morphology alteration over time using CLSM in neuroblastoma SH-SY5Y cells are stained with mitochondria targeting Cou-AIE-TPP$^+$ (500 nM), followed by incubation with Aβ40 (10 μM). Aβ40 induces a morphological alteration of the cellular mitochondria in a time-dependent manner and is associated with perturbation of mitochondrial function, eventually resulting in neuronal cell death. Initially, elongated rod-shaped mitochondria in SH-SY5Y cells is fragmented and transformed to a spherical shape during incubation with Aβ40 over time (0-48 h) monitored through CLSM using Cou-AIE-TPP$^+$ staining (**Figure 52**). Mitochondrial fragmentation in SH-SY5Y cells after 2 h of incubation with Aβ40 (10 μM) is noticed, and spherical-shaped morphological transformation along with rod-shaped mitochondria is detected after 12 h incubation (**Figure 52a**). After 24 h of incubation of SH-SY5Y cells with Aβ40, complete transformation to the spherical morphology of mitochondria is noticed (**Figure 52a**). After 48 h of incubation of SH-SY5Y cells with Aβ40, we have noticed fatal neurotoxicity, mitochondrial damage, rupture of the cell membrane, as well as cell death and accumulation of aggregated Aβ40 fibrils in the extracellular region of SH-SY5Y cells stained with the Cou-AIE-TPP$^+$ probe, which is colocalized with ThT with a high PCC of 0.91 (**Figures 52b, 53**). However, for the control

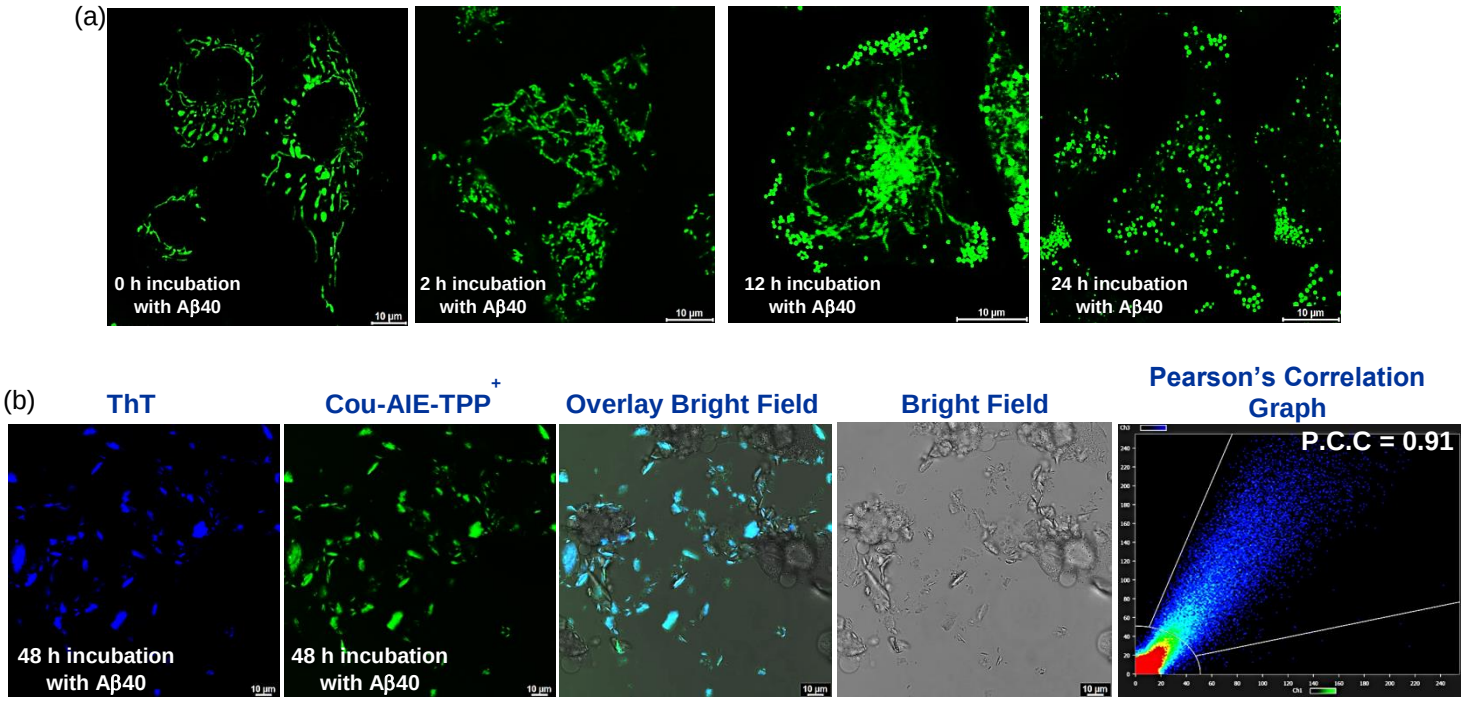

Figure 52. (a) Monitoring of mitochondrial morphology alteration and damage using CLSM in human neuroblastoma SH-SY5Y cells incubated with Aβ40 (10 μM) for 0 h, 2 h, 12 h, and 24 h, stained with Cou-AIE-TPP^{+}. (b) CLSM images of SH-SY5Y cells incubated with Aβ40 (10 μM) for 48 h, stained with Cou-AIE-TPP^{+} (green), and colocalized with Thioflavin-T (ThT) (blue). Mitochondrial damage, rupture of the cell membrane, cell death, and accumulation of the aggregated Aβ40 fibrils in the extracellular region of SH-SY5Y cells stained with the Cou-AIE-TPP^{+} probe colocalized with ThT. Colocalization scatter graph displays a PCC of 0.91.

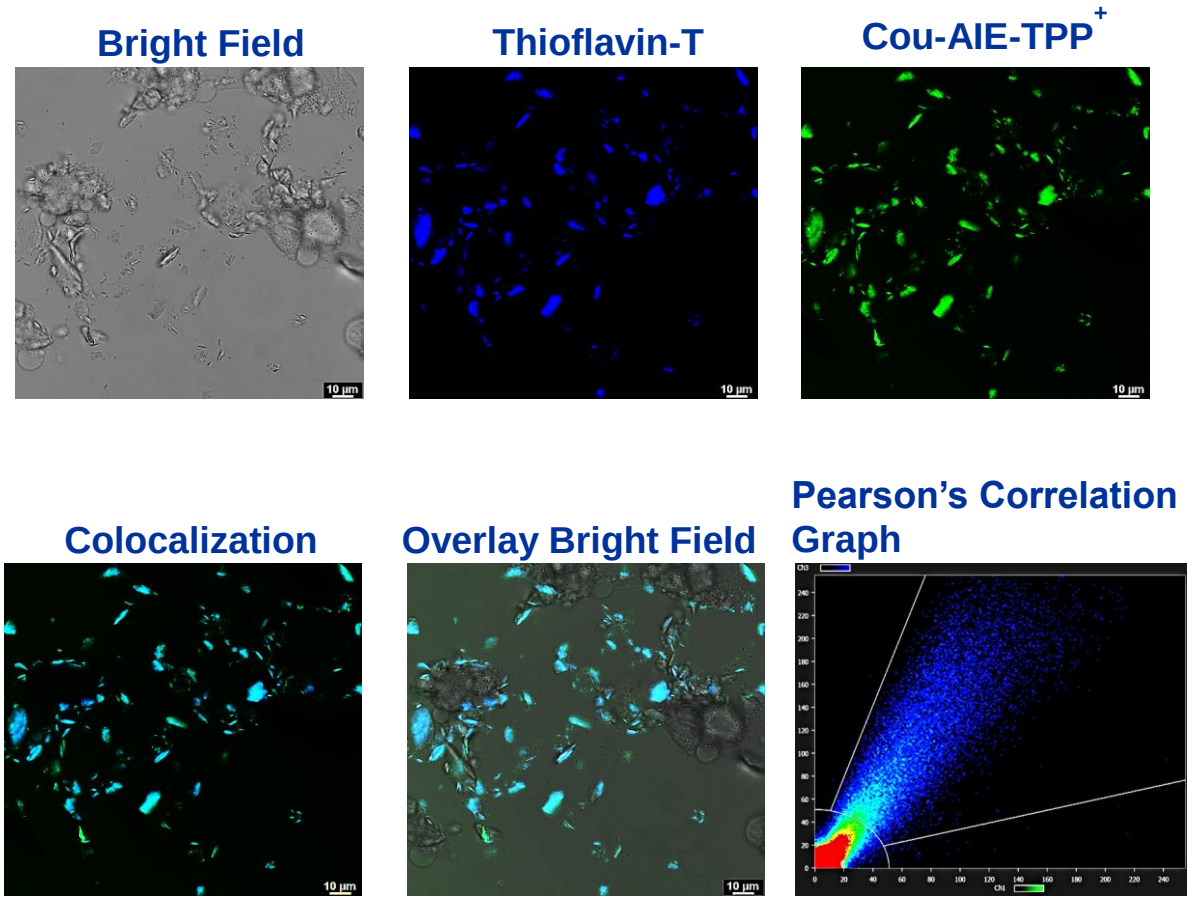

Figure 53. Confocal microscopic images of human neuroblastoma SH-SY5Y cells incubated for 48 h with Aβ40, stained with Cou-AIE-TPP$^+$, and colocalized with Thioflavin-T (ThT). ThT (blue channel) and Cou-AIE-TPP$^+$ (green channel). Colocalization scatter graph displays PCC of 0.91.

experiment without the treatment with Aβ40, we didn't observe mitochondrial morphology alteration or damage over time in SH-SY5Y cells stained with Cou-AIE-TPP$^+$. To decipher our hypothesis of mitochondrial membrane depolarization in neuroblastoma SH-SY5Y cells after incubation with Aβ40 for varying times is monitored by the JC-1-based mitochondrial membrane

potential detection kit on a fluorescence-activated cell sorting (FACS) flow cytometer. For healthy mitochondria, the $\Delta\Psi_m$ is polarized (high value), JC-1 is incorporated to the mitochondria, and the J-aggregates of JC-1 are perceived. Conversely, when the membrane depolarizes, the J-aggregates of JC-1 seepage are detected from the mitochondria to the cytosol as monomers. A substantial amendment of $\Delta\Psi_m$ in SH-SY5Y cells is noticed after treatment with Aβ40 (10 μM) over time (**Figure 54**). The percentage of depolarized mitochondria in SH-SY5Y cells increases from 2.1% (Aβ40 untreated control experiment) to 69.5% after treatment with Aβ40 (10 μM) for 24 h, which is the most early event noticed in mitochondrial dysfunction and damage, a notable hallmark of vulnerable neurons. Both early and late stages of apoptosis for SH-SY5Y cells are observed with varying times of incubation with Aβ40 by the Annexin V-FITC/PI apoptosis detection kit via FACS. In the Aβ40 untreated control experiment, 99.9% of SH-SY5Y cells are considered viable [both Annexin V and PI − Ve] (**Figure 55a**). While, with increasing incubation time with the Aβ40, there is an increase in SH-SY5Y cells facing early apoptosis (Annexin V + Ve and PI − Ve) (**Figure 55b,c**). Annexin V-FITC staining is perceived in a Ca^{2+}-dependent fashion through the recognition of negatively charged exposed phosphatidylserine (PS, typically located in the inner leaflet of the healthy plasma membrane) on the apoptotic cell, which signifies early apoptosis. At this stage, negligible PI staining is detected; moreover, the percentage of viable cells is quite high. After 24 h

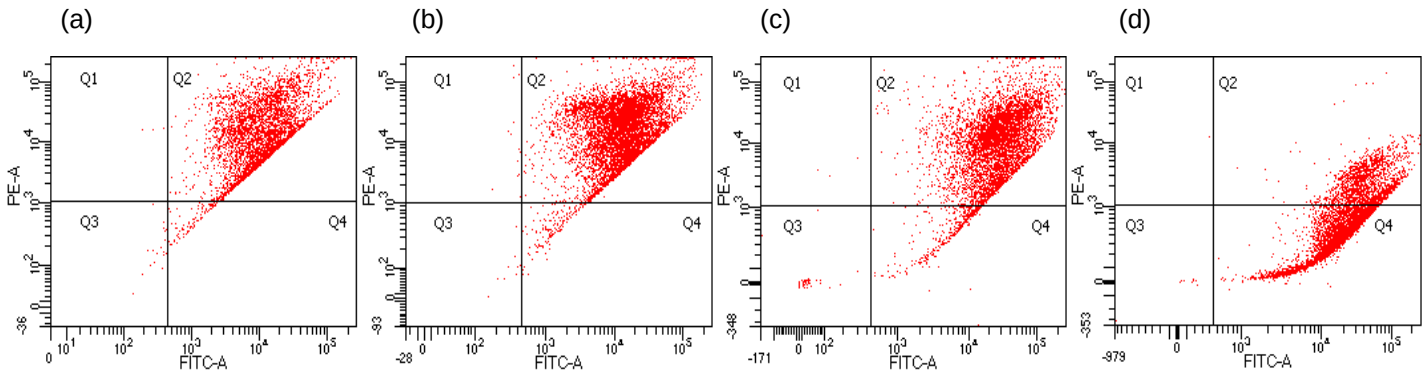

Figure 54. Mitochondrial membrane potential depolarization observed in SH-SY5Y cells utilizing the JC-1 probe. FACS experiment of SH-SY5Y cells incubated with Aβ40 (10 μM) after (a) 0 min (control experiment), (b) 6 h, (c) 12 h, and (d) 24 h. The emission intensity is examined in the FITC and PE channels utilizing a 494 nm laser. The SH-SY5Y cells with depolarized mitochondria upsurge from 2.1% (control) to 69.5% after treatment with 10 μM Aβ40.

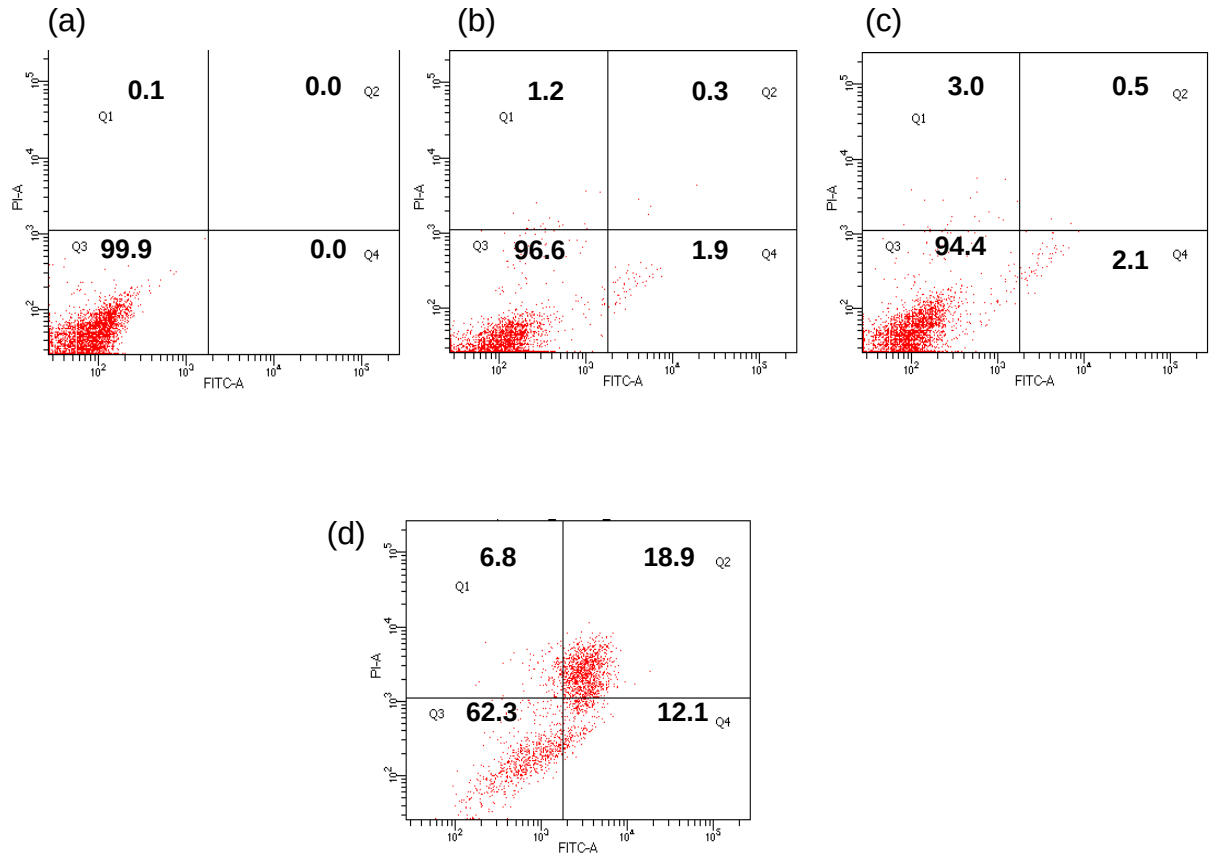

Figure 55. Time-dependent effect of Aβ40 to monitor early and late apoptosis in SH-SY5Y cells. (a) Control experiment in the absence of Aβ40. (b) Cells treated with Aβ40 (10.0 μM) after 6 h, (c) 12 h, and (d) 24 h. Lower left (Q3) quadrant denotes cell viability, both Annexin V and PI, -Ve; lower right (Q4) quadrant: Annexin V, +Ve and PI, -Ve; upper right (Q2) quadrant: Annexin V, +Ve and PI, +Ve; upper left (Q1) quadrant: Annexin V, -Ve and PI, +Ve.

incubation with Aβ40, both early (Annexin V + Ve and PI − Ve) and late (Annexin V + Ve and PI + Ve) stages of apoptosis, along with necrosis

(Annexin V − Ve and PI + Ve) are detected (**Figure 55d**). In Aβ40-induced depolarization of $\Delta\Psi_m$, the PS is exposed on the surface of the cell membrane during early apoptosis, and consequently, the mitochondrial transition pores are open, the membrane is ruptured, and mitochondrial caspase activator cytochrome c and other pro-apoptotic proteins are seeped into the cytosol, which triggers mitochondrial dysfunction and cell death via an apoptotic cascade. Furthermore, the noncovalent interaction of the Aβ40 peptide with mitochondrial proteins might also aid in induced mitochondria-targeted morphology alteration, damage, and dysfuction. These findings indicate that the mitochondria targeting de novo designed functional AIE-based solvatofluorochromic Cou-AIE-TPP$^+$ probe (λ_{em} 604 nm) is a promising switch on biomarkers for monitoring mitochondrial morphology change and damage during exogenous Aβ-induced neurotoxicity, as well as fluorescence imaging and detection of neurotoxic Aβ aggregates, which may offer imperative direction for the advancement of compelling AIE biomarkers for mitochondria targeted early stage Aβ diagnosis in the future.

Conclusion:

In conclusion, we establish that the de novo designed Cou-AIE-TPP$^+$ is an excellent ICT-induced solvatofluorochromic functional AIE probe to detect the various stages of Aβ40 aggregation along with the targeted imaging of mitochondria. The probe emits a strong fluorescence upon binding to Aβ aggregates with high binding affinity in comparison to the Aβ monomer, is capable of detecting amyloid aggregation kinetics, and is superior to the gold standard probe ThT. The lipophilic cationic Cou-AIE-TPP$^+$ probe selectively accumulates inside the live neuroblastoma cell mitochondria and exhibits the

AIE effect inside the mitochondria due to the highly negative $\Delta\Psi_m$. Additionally, the effective live-cell penetration, mitochondrial target selectivity and real-time monitoring ability, adequate lipophilicity, ultrabrightness, biocompatibility, and negligible cytotoxicity of Cou-AIE-TPP^+ make it extremely suitable for sensing and imaging of neurotoxic Aβ oligomers in the complicated cellular environment. After 48 h of incubation of neuroblastoma cells with Aβ40, fatal neurotoxicity, mitochondrial damage, and accumulation of aggregated Aβ40 fibrils in the extracellular region of SH-SY5Y cells stained with the Cou-AIE-TPP^+ probe are detected. It can be used to study mitochondrial morphology alteration, damage, and dysfunction in Aβ-induced neurotoxicity, recognize and image neurotoxic Aβ fibrils, and may offer imperative guidance for the advancement of compelling AIE biomarkers for mitochondria targeted early diagnosis of Alzheimer's disease in the future.

Cartesian coordinates and total energies (Hartrees) of B3LYP/6-31+G* energy minimized structure of Cou-AIE-TPP^{+}

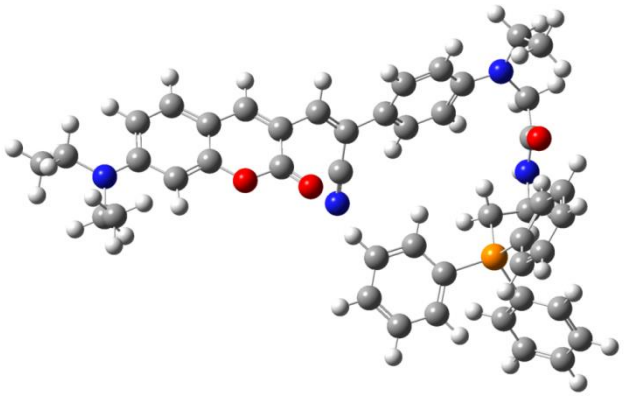

Charge = 1 Multiplicity = 1

C	-6.5614	-4.8343	0.
C	-6.6116	-6.1736	-0.0001
C	-5.2432	-6.8535	-0.0001
C	-4.0689	-6.1875	0.
C	-4.0192	-4.7574	0.0001
C	-5.1989	-4.095	0.0001
N	-8.0025	-6.9213	0.
C	-9.2735	-6.1251	-0.0002
C	-8.2119	-8.4109	0.0002
C	-6.9944	-9.3502	0.001
C	-10.5753	-7.0365	0.0009
O	-2.8997	-6.8732	-0.0001
C	-1.6441	-6.2762	-0.0001
C	-1.4289	-4.7728	0.0002
C	-2.5908	-4.0437	0.0003

O	-0.7009	-7.0451	-0.0004
C	0.1194	-4.0448	0.
C	1.3949	-4.6296	-0.001
C	2.8106	-3.8091	-0.0015
C	4.0157	-4.437	-0.0081
C	5.3674	-3.6498	-0.0056
C	5.361	-2.3056	0.0092
C	4.0277	-1.7001	0.0181
C	2.8603	-2.3649	0.0087
N	6.6669	-1.4597	0.0351
C	7.9773	-2.2217	-0.005
C	6.765	0.1212	0.1802
C	5.5546	1.1851	-0.0037
N	5.8978	2.5457	-0.1437
C	5.0461	3.7995	-0.675
C	4.1617	4.9516	0.3502
O	4.4069	0.7935	-0.1915
C	9.2715	-1.322	0.0041
C	1.527	-6.0436	-0.0005
N	1.6382	-7.1914	-0.0001
P	2.6791	5.6398	-0.5092
C	3.781	7.2454	-0.0576
C	3.3859	8.5503	-0.099
C	4.0236	9.7573	0.0543
C	5.3085	9.6901	0.1441

C	5.9159	8.3491	0.1027
C	5.2046	7.2068	0.0329
C	0.9683	6.5505	-0.227
C	-0.3034	6.1764	-0.4911
C	-1.4561	6.9178	-0.2059
C	-1.3429	8.1699	0.1311
C	-0.1016	8.6556	0.2017
C	0.8941	7.8352	0.0738
C	1.9672	4.0138	0.1419
C	2.5473	2.8414	0.2763
C	1.7949	1.6025	0.3091
C	0.4927	1.6254	0.1446
C	-0.0796	2.8259	0.1816
C	0.6804	3.8695	0.2297
H	7.04659	0.25179	1.20419
H	7.44463	0.39272	-0.60036
H	-7.47048	-4.26996	0.00001
H	-5.2139	-7.9231	-0.00018
H	-5.19115	-3.02503	0.00017
H	-9.28689	-5.58958	0.92605
H	-9.28748	-5.59098	-0.92725
H	-8.7078	-8.61263	0.92664
H	-8.70687	-8.61301	-0.92665
H	-6.09579	-8.76934	0.00133
H	-7.02055	-9.96725	0.87476

H	-7.01968	-9.96761	-0.87254
H	-10.28891	-8.06746	0.00159
H	-11.15649	-6.82719	0.87458
H	-11.15704	-6.82851	-0.87272
H	-2.53891	-2.97496	0.00052
H	0.11425	-2.97481	0.00076
H	4.04085	-5.50668	-0.01525
H	6.29631	-4.18077	-0.01566
H	3.97883	-0.63133	0.03348
H	1.94463	-1.81132	0.00877
H	8.01122	-2.78333	0.90512
H	7.98629	-2.72873	-0.9472
H	6.08722	2.80985	0.802
H	5.7822	4.41133	-1.15325
H	4.27175	3.34225	-1.25483
H	3.79181	4.38966	1.18225
H	4.82326	5.77657	0.51346
H	8.98866	-0.29063	0.03831
H	9.86395	-1.55805	0.86328
H	9.84044	-1.50657	-0.88311
H	2.33977	8.65852	-0.29598
H	3.49305	10.68556	0.09616
H	5.90755	10.571	0.24439
H	6.98318	8.2778	0.12959
H	5.71077	6.26418	0.04542

H	-0.44189	5.2255	-0.96175
H	-2.42119	6.45945	-0.2644
H	-2.19872	8.77712	0.34026
H	0.0681	9.70005	0.36051
H	1.84731	8.28958	0.24649
H	3.61285	2.80024	0.36463
H	2.29953	0.67226	0.46692
H	-0.07479	0.73157	-0.01007
H	-1.14498	2.92478	0.17174
H	0.14887	4.78779	0.36796

Total Energy = –2536.433839

References

1. Knopman, D. S.; Amieva, H.; Petersen, R. C.; Chételat, G.; Holtzman, D. M.; Hyman, B. T.; Nixon, R. A.; Jones, D. T. *Nat. Rev. Dis. Primers* **2021**, *7*, 33.
2. van der Flier, W. M.; de Vugt, M. E.; Smets, E. M. A.; Blom, M.; Teunissen, C. E. *Nat. Aging* **2023**, *3*, 494–505.
3. Pospich, S.; Raunser, S. *Science* **2017**, *358*, 45−46.
4. Selkoe, D. J. *Nat. Med*. **2011**, *17*, 1060−1065.
5. Scheltens, P.; Strooper, B. D.; Kivipelto, M.; Holstege, H.; Chételat, G.; Teunissen, C. E.; Cummings, J.; van der Flier, W. M. *Lancet* **2021**, *397*, 1577−1590.
6. Ismail, Z.; Creese, B.; Aarsland, D.; Kales, H. C.; Lyketsos, C. G.; Sweet, R. A.; Ballard, C. *Nat. Rev. Neurol*. **2022**, *18*, 131−144.
7. Barron, D. P.; Guo, Z. *Chem. Sci*. **2024**, *15*, 46−54.
8. An, J.; Kim, K.; Lim, H. J.; Kim, H. Y.; Shin, J.; Park, I.; Cho, I.; Kim, H. Y.; Kim, S.; McLean, C.; Choi, K. Y.; Kim, Y.; Lee, K. H.; Kim, J. S. *Nat. Commun*. **2024**, *15*, 1004.
9. Hardy, J.; Selkoe, D. J. *Science* **2002**, *297*, 353−356.
10. Cha, M-Y.; Han, S-H.; Son, S-M.; Hong, H-S.; Choi, Y-J.; Byun, J.; Mook-Jung, I. *PLoS ONE* **2012**, *7*, e34929.
11. Ke, J.; Tian, Q.; Xu, Q.; Fu, Z.; Fu, Q. *Drug Discovery Today* **2021**, *26*, 1991−2002.

12. Zhua, X.; Perryc, G.; Smitha, M. A.; Wanga, X. *J Alzheimers Dis*. **2013**, *33*, S253–S262.
13. Smith, M. A.; Perry, G.; Richey, P. L.; Sayre, L. M.; Anderson, V. E.; Beal, M. F.; Kowall, N. *Nature* **1996**, *382*, 120–121.
14. Qian, K.; Bao, X.; Li, Y.; Wang, P.; Guo, Q.; Yang, P.; Xu, S.; Yu, F.; Meng, R.; Cheng, Y.; Sheng, D.; Cao, J.; Xu, M.; Wu, J.; Wang, T.; Wang, Y.; Xie, Q.; Lu, W.; Zhang, Q. *ACS Nano* **2022**, *16*, 11455–11472.
15. McKay, N. S.; Gordon, B. A.; Hornbeck, R. C.; Dincer, A.; Flores, S.; Keefe, S. J.; JosephMathurin, N.; Jack, C. R.; Koeppe, R.; Millar, P. R.; et al. *Nat. Neurosci*. **2023**, *26*, 1449–1460.
16. Higuchi, M.; Iwata, N.; Matsuba, Y.; Sato, K.; Sasamoto, K.; Saido, T. C. *Nat. Neurosci*. **2005**, *8*, 527–533.
17. Therriault, J.; Schindler, S. E.; Salvadó, G.; Pascoal, T. A.; Benedet, A. L.; Ashton, N. J.; Karikari, T. K.; Apostolova, L.; Murray, M. E.; Verberk, I.; et. al. *Nat. Rev. Neurol*. **2024**, *20*, 232–244.
18. Bandara, N.; Sharma, A. K.; Krieger, S.; Schultz, J. W.; Han, B. H.; Rogers, B. E.; Mirica, L. M. *J. Am. Chem. Soc*. **2017**, *139*, 12550−12558.
19. Aliyan, A.; Cook, N. P.; Martí, A. A. Chem. Rev. **2019**, *119*, 11819−11856.
20. Venkatesh, Y.; Marotta, N. P.; Lee, V. M.-Y.; Petersson. E. J. *Chem. Sci*. **2024**, *15*, 6053−6063.
21. Sun, L.; Cho, H.-J.; Sen, S.; Arango, A. S.; Huynh, T. T.; Huang, Y.; Bandara, N.; Rogers, B. E.; Tajkhorshid, E.; Mirica, L. M. *J. Am. Chem. Soc*. **2021**, *143*, 10462−10476.
22. Levine, H. *Protein Science* **1993**, *2*, 404−410.
23. Needham, L.-M.; Weber, J.; Varela, J. A.; Fyfe, J. W. B.; Do, D. T.; Xu, C. K.; Tutton, L.; Cliffe, R.; Keenlyside, B.; Klenerman, D.; et. al. *Chem. Sci*. **2020**, *11*, 4578–4583.
24. Hou, S. S.; Yang, J.; Lee, J. H.; Kwon, Y.; Calvo-Rodriguez, M.; Bao, K.; Ahn, S.; Kashiwagi, S.; Kumar, A. T. N.; Bacskai, B. J.; Choi, H. S. *Nat. Biomed. Eng*. **2023**, *7*, 270–280.
25. Fu, W.; Yan, C.; Guo, Z.; Zhang, J.; Zhang, H.; Tian, H.; Zhu, W.-H. *J. Am. Chem. Soc*. **2019**, *141*, 3171–3177.
26. Miao, J.; Miao, M.; Jiang, Y.; Zhao, M.; Li, Q.; Zhang, Y.; An, Y.; Pu, K.; Miao. Q. *Angew. Chem. Int. Ed*. **2023**, *62*, e202216351.
27. Ji, X.; Cai, Y.; Dong, X.; Wu, W.; Zhao, W. *Nanoscale*, **2023**, *15*, 9290–9296.
28. Chen, W.; Young, L. J.; Lu, M.; Zaccone, A.; Ströhl, F.; Yu, N.; Schierle, G. S. K.; Kaminski, C. F. *Nano Lett*. **2017**, *17*, 143–149.
29. Duo, Y.; Luo, G.; Zhang, W.; Wang, R.; Xiao, G. G.; Li, Z.; Li, X.; Chen, M.; Yoon, J.; Tang, B. Z. *Chem. Soc. Rev*. **2023**, *52*, 1024–1067.
30. He, W.; Kwok, R. T. K.; Qiu, Z.; Zhao, Z.; Tang, B. Z. *J. Am. Chem. Soc*. **2024**, *146*, 5030–5044.
31. Kumar, M.; Hong, Y.; Thorn, D. C.; Ecroyd, H.; Carver, J. A. *Anal. Chem*. **2017**, *89*, 9322−9329.

32. Wang, Y.-L.; Fan, C.; Xin, B.; Zhang, J.-P.; Luo, T.; Chen, Z.-Q.; Zhou, Q.-Y.; Yu, Q.; Li, X.-N.; Huang, Z.-L.; Li, C.; Zhu, M.-Q.; Tang, B. Z. *Mater. Chem. Front*. **2018**, *2*, 1554−1562.
33. Wang, H.; Li, Q.; Alam, P.; Bai, H.; Bhalla, V.; Bryce, M. R.; Cao, M.; Chen, C.; Chen, S.; Chen, X.; Chen, Y.; et. al. *ACS Nano* **2023**, *17*, 14347–14405.
34. Xu, L.; Gao, H.; Zhan, W.; Deng, Y.; Liu, X.; Jiang, Q.; Sun, X.; Xu, J-J.; Liang, G. *J. Am. Chem. Soc*. **2023**, *145*, 27748−27756.
35. Hong, Y.; Meng, L.; Chen, S.; Leung, C. W. T,; Da, L-T.; Faisal, M.; Silva, D-A.; Liu, J.; Lam, J. W. P.; Huang, X.; Tang. B. Z. *J. Am. Chem. Soc*. **2012**, *134*, 1680−1689.
36. Yan, C.; Dai, J.; Yao, Y.; Fu, W.; Tian, H.; Zhu, W.-H.; Guo, Z. *Nat. Protoc*. **2023**, *18*, 1316–1336.
37. Hou, T.-T.; Tang, Y.-H.; Zhang, Z.-Y. Li, Z.-J.; Wang, Y.-L. *J. Innovative Opt. Health Sci*. **2023**, *16*, 2330009.
38. Hu, Q.; Gao, M.; Feng, G.; Liu, B. *Angew. Chem. Int. Ed.* **2014**, *53*, 14225–14229.
39. Wang, J.; Shangguan, P.; Chen, X.; Zhong, Y.; Lin, M.; He, M.; Liu, Y.; Zhou, Y.; Pang, X.; Han, L.; et.al. *Nat. Commun*. **2024**, *15*, 705.
40. Das, R. S.; Maiti, D.; Kar, S.; Bera, T.; Mukherjee, A.; Saha, P. C.; Mondal, A.; Guha, S. *J. Am. Chem. Soc*. **2023**, *145*, 20451–20461.
41. Zielonka, J.; Joseph, J.; Sikora, A.; Hardy, M.; Ouari, O.; Vasquez-Vivar, J.; Cheng, G.; Lopez, M.; Kalyanaraman, B. *Chem. Rev*. **2017**, *117*, 10043−10120.
42. Wan, W.; Zeng, L.; Jin, W.; Chen, X.; Shen, D.; Huang, Y.; Wang, M.; Bai, Y.; Lyu, H.; Dong, X.; Gao, Z.; Wang, L.; Liu, X.; Liu, Y. *Angew. Chem. Int. Ed*. **2021**, *60*, 25865– 25871.
43. Frisch, M. J.; Trucks, G. W.; Schlegel, H. B.; Scuseria, G. E.; Robb, M. A.; Cheeseman, J. R.; Scalmani, G.; Barone, V.; Mennucci, B.; Petersson, G. A. et al. Gaussian 09W Revision D.01, Gaussian, Inc., Wallingford CT, USA, 2009.
44. Morris, G. M.; Goodsell, D. S.; Pique, M. E.; Lindstrom, W. L.; Huey, R.; Forli, S.; Hart, W. E.; Halliday, S.; Belew, R.; Olson, A. J.; User Guide, AutoDock Version 4.2, Scripps Research, 2012.

Chapter 5

Summery and Outlook

As the most basic components in all living things, proteins are involved in nearly every biological function. Proteins can, however, become misfolded as a result of mutations, or modifications to the cellular microenvironment. Proteins can gather into a highly structured architecture known as amyloid fibrils if these misfolded proteins manage to evade the cellular regulatory system that typically eliminates the misfolded proteins. Amyloid fibril deposition in tissue has been associated with multiple disorders, including Alzheimer's disease (AD). To provide the best available treatments, a detailed understanding of the illness progression and the construction of improved diagnostic tools are required.

In this thesis, we developed new research tools and methods for the detection and inhibition of protein aggregates that caused AD. These developments have possible applications in the diagnosis of these diseases as well as therapeutics.

This thesis is an overview of the literature reports how fluorescence spectroscopy has aided in our understanding of amyloid self-assembly and to summarize many of the probes that have been developed to scrutinize these aggregates, with particular attention to recent developments.

Many trials have shown mixed results, and not all treatments have led to meaningful cognitive improvements. Some therapies can cause adverse effects, including inflammation in the brain. The best window for intervention might be early in the disease process, but detecting Alzheimer's at that stage can be challenging. Research is ongoing, and new therapies are continually being developed to address these challenges and better target Aβ in Alzheimer's disease.

The novel observations of this thesis are:

- We have designed self-assembled myristoyl-KPGPK lipopeptide-based biocompatible nanovesicles, which can inhibit amyloid fibrillation made by the transmembrane GxxxGxxxGxxxG motif of Aβ-protein and human myelin protein zero as well as reduce their neurotoxicity. We have used a MW-assisted SPPS procedure to make myristoyl-KPGPK and GxxxGxxxGxxxG motif peptide quickly and efficiently.

  We have designed and synthesized an aggregation-induced emission (AIE) probe Cou-AIE-TPP^+ for selective detection of neurotoxic amyloid-β aggregates. The probe exhibits biocompatibility, noncytotoxicity, and a huge Stokes shift (124 nm in PBS). Cou-AIE-TPP^+ has respectable fluorescence augmentation inside the aggregated Aβ40 in comparison to monomeric Aβ40 with high binding affinity (K_d = 83 nM) to Aβ40 aggregates, is capable of detecting the kinetics of amyloid aggregation, and is superior to the gold standard probe thioflavin T. Cou-AIE-TPP^+ (λ_{em} 604 nm) can selectively target and image neuronal cell mitochondria, and is useful to monitor mitochondrial morphology alteration and damage during Aβ40-induced neurotoxicity.

List of Publications and Research Works Included In the Thesis:

As a First Author:

1) Construction of Self-Assembling Lipopeptide-Based Benign Nanovesicles to Prevent Amyloid Fibril Formation and Reduce Cytotoxicity of GxxxGxxxGxxxG Motif. **Tapas Bera**, Pranab Chandra Saha, Tanima Chatterjee, Samiran Kar and Samit Guha*. *Bioconjugate Chem.* **2022**, *33*, 1201–1209.

2) A Mitochondria Targeting, De Novo Designed, Aggregation-Induced Emission Probe for Selective Detection of Neurotoxic Amyloid-β Aggregates. **Tapas Bera**, Aniruddha Mondal, Samiran Kar, Ayan Mukherjee, Somenath Banerjee, and Samit Guha*. *J. Mater. Chem. B*, **2024,** doi: 10.1039/d4tb01337a.

List of Publications and Research Works Not Included In the Thesis:

1) Design of an Acidic pH-Activated NIR Fluorescent Convertible Rhodamine-Hemicyanine Probe-Peptide Conjugate for Living Cancer Cell Active Targeted Selective Tracking of Lysosomes. Ayan Mukherjee, Samiran Kar, Shreya Das, **Tapas Bera**, Aniruddha Mondal, Arunima Sengupta, and Samit Guha*. *Chem. Eur. J*. **2024**, *30*, e202402146.

2) Design of Water–Soluble Rotaxane-Capped Superparamagnetic, Ultrasmall Fe_3O_4 Nanoparticles for Targeted NIR Fluorescence Imaging in Combination with Magnetic Resonance Imaging. Rabi Sankar Das, Debabrata Maiti, Samiran Kar, **Tapas Bera**, Ayan Mukherjee, Pranab Chandra Saha, Aniruddha Mondal, and Samit Guha*. *J. Am. Chem. Soc.* **2023**, *145*, 20451–20461.

3) Live-cell mitochondrial targeted NIR fluorescent covalent labeling of specific proteins using a dual localization effect. Pranab Chandra Saha, Rabi Sankar Das, Shreya Das, Nayim Sepay, Tanima Chatterjee, Ayan Mukherjee, **Tapas Bera**, Samiran Kar, Maitree Bhattacharyya, Arunima Sengupta, and Samit Guha*. *Bioconjugate Chem.* **2023**, *34*, 1407–1417.

4) C-Terminal Lipidation of SARS-CoV-2 Fusion Peptide Reinstates Superior Membrane Fusion Catalytic Ability. Avijit Sardar, **Tapas Bera**, Santosh Kumar Samal, Nikesh Dewangan, Mithila Kamble, Samit Guha, and Pradip K Tarafdar*. *Chem. Eur. J*. **2023**, *29*, e202203034.

5) Acidic pH-Triggered Live-Cell Lysosome Specific Tracking, Ratiometric pH Sensing, and Multicolor Imaging by Visible to NIR Switchable Cy-7 Dyes. Ayan Mukherjee, Pranab Chandra Saha, Samiran Kar, Pampa Guha, Rabi Sankar Das, **Tapas Bera,** and Samit Guha*. *ChemBioChem* **2023**, *24*, e202200641.

6) Construction of Red Fluorescent Dual Targeting Mechanically Interlocked Molecules for Live Cancer Cell Specific Lysosomal Staining and Multicolor Cellular Imaging. Rabi Sankar Das, Ayan Mukherjee, Samiran Kar, **Tapas Bera**, Shreya Das, Arunima Sengupta, and Samit Guha*. *Org. Lett*. **2022**, *24*, 5907–5912.

7) Acidic pH-Activatable Visible to Near-Infrared Switchable Ratiometric Fluorescent Probe for Live-Cell Lysosome Targeted Imaging. Ayan Mukherjee, Pranab Chandra Saha, Rabi Sankar Das, **Tapas Bera**, and Samit Guha*. *ACS Sens.* **2021**, *6*, 2141–2146.

8) Supramolecular Dipeptide-Based Near-Infrared Fluorescent Nanotubes for Cellular Mitochondria Targeted Imaging and Early Apoptosis. Pranab Chandra Saha, **Tapas Bera**, Tanima Chatterjee, Jayeeta Samanta, Arunima Sengupta, Maitree Bhattacharyya, and Samit Guha*. *Bioconjugate Chem.* **2021**, *32*, 833–841.

PRESENTATION / PARTICIPATION IN INTERNATIONAL / NATIONAL SYMPOSIUM / CONFERENCES:

1) Poster presentation "***Self-Assembling Lipopeptide-Based Benign Nanovesicles to inhibit Amyloid Fibril Formation***" presented at International Seminar on Recent Advances in Chemistry and Materials Sciences (RACMS-2022) organised by INDIAN CHEMICAL SOCIETY (ICS). (Date-30-31 July and 2-3August)

2) Poster presentation "***Construction of Self-Assembling Lipopeptide-Based Benign Nanovesicles to Prevent Amyloid Fibril Formation and Reduce Cytotoxicity of GxxxGxxxGxxxG Motif*** " presented at National Conference on Material Chemistry for Better Tomorrow – 2023 organised by Department of Chemistry, Asutosh College. (Date-20.12.2023)